

AD-A171 508

DTIC/ROC-86/047

**DAVID W. TAYLOR NAVAL SHIP
RESEARCH AND DEVELOPMENT CENTER**

Bethesda, Maryland 20814-6030



**AN EXPERIMENTAL INVESTIGATION OF WALL PRESSURE FLUCTUATIONS
BENEATH NON-EQUILIBRIUM TURBULENT FLOWS**

by

Theodore Maurice Farabee

**DTIC
ELECTE
SEP 0 8 1985**

APPROVED FOR PUBLIC RELEASE: DISTRIBUTION IS UNLIMITED.

A dissertation submitted to the faculty
of the School of Engineering and Architecture
of the Catholic University of America in partial
fulfillment of the requirements for the degree
Doctor of Philosophy

**SHIP ACOUSTIC DEPARTMENT
RESEARCH AND DEVELOPMENT REPORT**

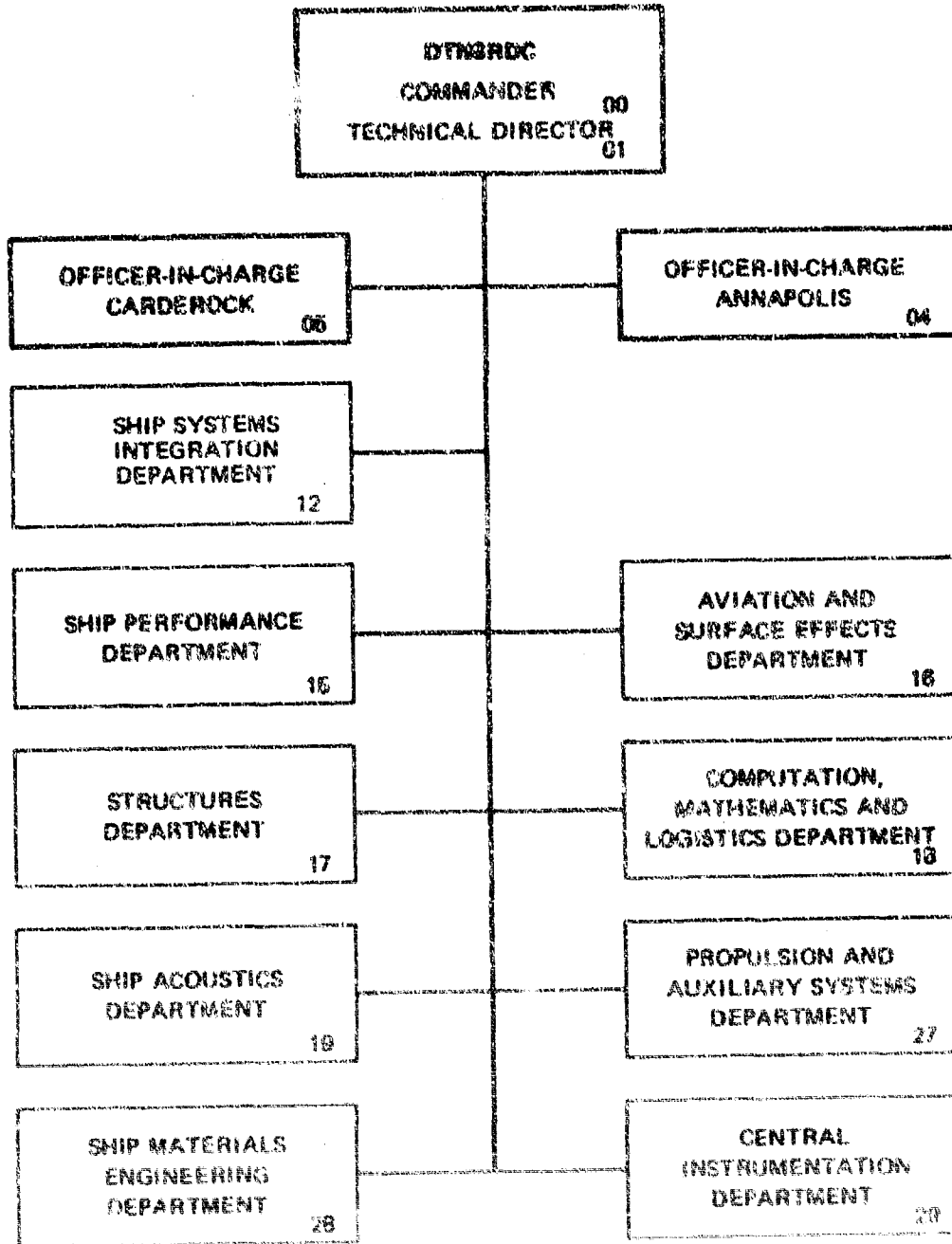
May 1985

DTIC/ROC-86/047

AN EXPERIMENTAL INVESTIGATION OF WALL PRESSURE FLUCTUATIONS
BENEATH NON-EQUILIBRIUM TURBULENT FLOWS

DTIC FILE COPY

MAJOR DTNSRDC ORGANIZATIONAL COMPONENTS:



SECRETARY OF THE INTERIOR - For classified documents, follow the procedures in 50 USC 552a, Executive Order 12958 Sections 1.7 and 1.8, and Executive Order 12958 Section 1.9. For unclassified documents, follow the procedures in 50 USC 552a, Executive Order 12958 Section 1.7 and 1.8, and Executive Order 12958 Section 1.9. For unclassified documents, follow the procedures in 50 USC 552a, Executive Order 12958 Section 1.7 and 1.8, and Executive Order 12958 Section 1.9.

AD-A171508

REPORT DOCUMENTATION PAGE

1a REPORT SECURITY CLASSIFICATION UNCLASSIFIED		1b RESTRICTIVE MARKINGS	
2a SECURITY CLASSIFICATION AUTHORITY		3 DISTRIBUTION / AVAILABILITY OF REPORT	
2b DECLASSIFICATION / DOWNGRADING SCHEDULE			
4 PERFORMING ORGANIZATION REPORT NUMBER(S) DTNSRDC-86/047		5 MONITORING ORGANIZATION REPORT NUMBER(S)	
6a NAME OF PERFORMING ORGANIZATION David Taylor Naval Ship R&D Center	6b OFFICE SYMBOL (If applicable) Code 1942	7a NAME OF MONITORING ORGANIZATION	
6c ADDRESS (City, State, and ZIP Code) Bethesda, Md. 20084-5000		7b ADDRESS (City, State, and ZIP Code)	
8a NAME OF FUNDING/SPONSORING ORGANIZATION David Taylor Naval Ship R&D Center	8b OFFICE SYMBOL (If applicable) Code 19	9 PROCUREMENT INSTRUMENT IDENTIFICATION NUMBER	
6c ADDRESS (City, State, and ZIP Code) Bethesda, Md., 20084-5000		10 SOURCE OF FUNDING NUMBERS	
		PROGRAM ELEMENT NO None	PROJECT NO None
		TASK NO None	WORK UNIT ACCESSION NO None
11 (Include Security Classification) AN EXPERIMENTAL INVESTIGATION OF WALL PRESSURE FLUCTUATIONS BENEATH NON-EQUILIBRIUM TURBULENT FLOWS			
12 PERSONAL AUTHOR(S) Farabee, Theodore Maurice			
13a DATE OF REPORT	13b TIME COVERED FROM TO	14 DATE OF REPORT (Year, Month, Day) 1986 May	15 PAGE COUNT
16 SUPPLEMENTARY NOTATION A dissertation submitted to the faculty of the School of Engineering and Architecture of the Catholic University of America in partial fulfillment of the requirements for the degree Doctor of Philosophy			
17 COSATI CODES		18 SUBJECT TERMS (Continue on reverse if necessary and identify by block number)	
GROUP	SUB-GROUP	Wall pressure fluctuations, flow noise, hydroacoustics, non-equilibrium boundary layer, perturbed flow, turbulence, backward-facing step	
19 ABSTRACT (Continue on reverse if necessary and identify by block number) Wall pressure fluctuations beneath a non-equilibrium turbulent boundary layer were studied experimentally. The objective of the investigation was to better understand the process by which turbulent boundary layer flows produce wall pressure fluctuations. The approach was to study the statistics of both the wall pressure field and velocity field for a non-equilibrium turbulent boundary layer, produced by passing a flow over a back- ward-facing step, and then to identify turbulent structures in the flow that contribute to the source terms of the wall pressure field. Detailed velocity and wall pressure measurements were also obtained for an equilibrium flow to provide a basis of comparison for the perturbed flow results. ———— The experiments were conducted in a low noise wind tunnel for velocities ranging from 50 to 95 ft/sec. The two-dimensional backward-facing step had a step height (h)			
(Continued)			
20 DISTRIBUTION / AVAILABILITY OF ABSTRACT <input checked="" type="checkbox"/> UNCLASSIFIED UNLIMITED <input type="checkbox"/> SAME AS RPT <input type="checkbox"/> DTIC USERS		21 ABSTRACT SECURITY CLASSIFICATION UNCLASSIFIED	
22a NAME OF RESPONSIBLE INDIVIDUAL Theodore Maurice Farabee		22b TELEPHONE (Include Area Code) (202) 227-1731	22c OFFICE SYMBOL Code 1942

UNCLASSIFIED

SECURITY CLASSIFICATION OF THIS PAGE

(Block 19 continued)

of 0.5-inch and the boundary layer thickness at the top of the step was approximately 2 step heights. Cross-spectral density measurements of the wall pressure fluctuations were obtained for both streamwise and transverse separations using small, flush-mounted, pinhole microphones at several downstream positions. Velocity data were obtained using both a single and a x-wire anemometer at several downstream locations. The velocity data consisted of measurements of the mean-velocity and turbulence intensity (u' , v' , $u'v'$) profiles, and measurements of the frequency spectrum of the streamwise (u) and vertical (v) components of velocity at various positions in the boundary layer.

The velocity measurements show that the boundary layers downstream of reattachment are marked by the presence of a disturbance layer, consisting of highly energized flow, that is the remnants of the free-shear layer that formed when the flow separated at the top of the step. This disturbance layer propagates away from the wall and decays in level as it convects downstream.

Near reattachment the entire boundary layer is highly disturbed, but by $x/h=16$ the near wall region ($y^+ < 100$) has recovered to an equilibrium flow condition. However, full recovery of the outer flow region takes much longer and will not occur until the disturbance layer has fully propagated across the boundary layer. It is estimated that full recovery will not occur until an $x/h \approx 250$.

The wall pressure statistics for the perturbed flow are characterized by the presence of the disturbance layer. Levels of fluctuating wall pressure are very high near reattachment. The frequency spectra show that these high levels are associated with an excess of low frequency energy. This low frequency energy excess decreases in the downstream direction, but even at $x/h=72$ is still greater than the spectral levels for the equilibrium flow and never fully recovers within the streamwise range of the measurements. Furthermore, these components were found to scale on disturbance layer variables. Hence, the source of the low frequency excess in the wall pressure fluctuations is the disturbance layer.

The high frequency wall pressures were found to scale on inner variables, and as such, recovered to an equilibrium flow condition quite rapidly. This places the source of high frequency wall pressures in the inner layer of the boundary layer.

The cross-spectral properties of the wall pressure field show that for the perturbed flow the low frequency components are coherent over a much greater distance than the coherence lengths measured for the equilibrium flow. The convective phase speeds of the low frequency components track the location of the disturbance layer in the boundary layer.

For both the perturbed and equilibrium flow, it was found that the boundary layer suppresses wall pressure components below an $\omega \delta^*/U_o \leq 0.3$. This cutoff frequency is also the frequency at which the wall pressure spectrum is a maximum for the equilibrium flow.

A simplified analytical model for the wall pressure frequency spectrum, which is a function of the measured velocity statistics, confirmed that the primary source for the low frequency wall pressures was the disturbance layer.

UNCLASSIFIED

SECURITY CLASSIFICATION OF THIS PAGE

TABLE OF CONTENTS

	Page
LIST OF TABLES	vi
LIST OF FIGURES	vi
ACKNOWLEDGMENTS	xi
NOMENCLATURE	xiii
ABSTRACT.....	xvii
ADMINISTRATIVE INFORMATION	xviii

CHAPTER

1 INTRODUCTION

1.1 Background	1
1.2 Review of the Problem Area	3
1.2.1 Features of the Disturbed Flow (Backward-facing Step)	4
1.2.2 Literature Review- Disturbed Flow Studies ...	4
1.2.3 Literature Review- Wall Pressure Studies	10
1.3 Objectives of the Research	22

2 THEORETICAL FORMULATIONS

2.1 Statistical Functions for Turbulence	25
2.2 Equations for Wall Pressure	29
2.2.1 Poisson Equation for Pressure	29
2.2.2 Solutions to Poisson Equation for Wall Pressure	31
2.2.3 Source Term Identification	36
2.3 Measured Statistical Functions	37

3 EXPERIMENTAL ARRANGEMENT AND METHODOLOGY

3.1 Wind Tunnel	40
3.1.1 Construction Details	40
3.1.2 Test Wall	43
3.1.3 Performance Characteristics	44
3.2 Pressure Measurements	46
3.3 Velocity Measurements	49
3.3.1 Anemometer Systems	49
3.3.2 Hot Wire Traverse	50
3.3.3 Hot Wire Data Acquisition and Processing	51
3.4 Spectral Data	53
3.4.1 Acquisition and Processing	53
3.4.2 Error Analysis in Spectral Measurements	55



for	
&I	<input checked="" type="checkbox"/>
ed	<input type="checkbox"/>

Availability Codes

Dist	Avail and/or Special
A-1	

	Page
4 EXPERIMENTAL RESULTS FOR VELOCITY MEASUREMENTS	
4.1 Introduction	61
4.2 Onset and Equilibrium Boundary Layers	62
4.2.1 Mean Velocity Profiles	62
4.2.2 Turbulence Intensity Profiles	64
4.2.3 Spanwise Uniformity of the Boundary Layers ..	65
4.2.4 Criteria for an Equilibrium Boundary Layer ..	65
4.3 Mean Velocity and Turbulence Measurements	67
4.3.1 Mean Velocity Profiles	67
4.3.2 Turbulence Profiles	69
4.3.3 Correlation Coefficient and Mixing Length Profiles	72
4.4 Velocity Spectra	75
4.4.1 Presentation Format for Spectral Data.....	75
4.4.2 Velocity Spectra for Equilibrium Flow.....	77
4.4.3 Velocity Spectra at Downstream Locations	80
4.4.4 Length Scales	81
4.5 Discussion of the Structure of the Flow	84
4.5.1 Physical Features of the Step Flow	84
4.5.2 Propagation of the Disturbance Layer	87
4.5.3 Spectral Data	92
4.5.4 Summary	97
5 EXPERIMENTAL RESULTS FOR WALL PRESSURE FLUCTUATIONS	
5.1 Introduction	121
5.2 Root-Mean-Square of Pressure Fluctuations	122
5.2.1 RMS Pressure Fluctuations	122
5.2.2 Resolution Errors in Pressure Measurements ..	123
5.3 Spectral Features of Wall Pressure Fluctuations for Equilibrium Flow	124
5.3.1 Frequency Spectra	124
5.3.2 Cross-Spectral Measurements	127
5.3.3 Streamwise Coherence	129
5.3.4 Streamwise Convection Velocity	134
5.3.5 Transverse Coherence and Phase	136
5.3.6 Discussion	13
5.4 Spectral Features of Wall Pressure Fluctuations for Non-Equilibrium Flow	142
5.4.1 Frequency Spectra	142
5.4.2 Streamwise Coherence	147
5.4.3 Convection Velocity	151
5.4.4 Transverse Coherence	153
5.4.5 Summary	154

	Page
6 VELOCITY-PRESSURE RELATIONSHIPS	
6.1 Introduction	179
6.2 Analytical Source Terms	179
6.3 Burst Event Process	187
7 SUMMARY AND CONCLUSIONS	
7.1 Summary of Accomplishments	191
7.2 Major Conclusions	192
7.3 Concluding Remarks	194
REFERENCES	196
APPENDIX A - HOT WIRE ERROR ANALYSIS	204
APPENDIX B - TABULATED PROFILE DATA	213

LIST OF TABLES

		Page
4.1	Boundary Layer Properties	98
5.1	Values of RMS Pressure	155

LIST OF FIGURES

1.1	Features of the Flow Over a Backward-Facing Step	24
3.1	Schematic of CUA Wind Tunnel	56
3.2	Wind Tunnel Contraction Section and Static Wall Pressure Data	57
3.3	Diagram of Test Wall	58
3.4	Comparison of Wall Pressure Spectra With Background Noise	58
3.5	Block Diagram of Microphone System	59
3.6	View of Test Plate Showing Measurement Positions	59
3.7	Block Diagram of Hot Wire Traverse and Data Acquisition System	60
4.1	Mean Velocity Profiles (Wall Law) for Equilibrium Flows	99
4.2	Turbulence Intensity Profiles for Equilibrium Flows	99
4.3	Mean Velocity Profiles (Wall Law) at $x/h = -2$ and $z/h = 0, -6, +6$	100
4.4	Mean Velocity Profiles (Wall Law) at $x/h = 54$ and $z/h = 0, -6, +5$	100
4.5	Streamwise Velocity Spectra for Equilibrium Flows	101
4.6	Mean Velocity Profiles at Downstream Locations	102
4.7	Mean Velocity Profiles (Wall Law) at Downstream Locations	102
4.8	Streamwise Variations in Boundary Layer Properties	103

	Page
4.9 Streamwise Variations in Clauser Parameter	103
4.10 Streamwise Variations in Skin Friction Coefficient	104
4.11 Turbulence Intensity Profiles for Equilibrium Flows	104
4.12 Comparison of Turbulence Profiles with Klebanoff (1955) (a) Turbulence Intensities; (b) Turbulence Stress ...	105
4.13 u'/U_0 Profiles at Downstream Locations (single wire)	106
4.14 u'/U_0 Profiles at Downstream Locations (x-wire)	106
4.15 v'/U_0 Profiles at Downstream Locations	107
4.16 Turbulence Stress Profiles at Downstream Locations	107
4.17 Turbulence Stress Correlation Coefficient Profiles	108
4.18 Mixing Length Profiles at Downstream Locations	108
4.19 Velocity Spectra for Equilibrium Flow (a) u spectra; (b) v spectra	109
4.20 Velocity Spectra at Fixed Downstream Location (x/h=10) (a) u spectra; (b) v spectra	110
4.21 Velocity Spectra at Fixed Downstream Location (x/h=24) (a) u spectra; (b) v spectra	111
4.22 Velocity Spectra at Fixed Downstream Location (x/h=54) (a) u spectra; (b) v spectra	112
4.23 Velocity Spectra at Fixed Wall Position (y=0.03-inch) (a) u spectra; (b) v spectra	113
4.24 Velocity Spectra at Fixed Wall Position (y=0.1-inch) (a) u spectra; (b) v spectra	114
4.25 Velocity Spectra at Fixed Wall Position (y=0.4-inch) (a) u spectra; (b) v spectra	115
4.26 Velocity Spectra at Fixed Wall Position (y=0.8-inch) (a) u spectra; (b) v spectra	116
4.27 Velocity Spectra at Fixed Wall Position (y=1.5-inch) (a) u spectra; (b) v spectra	117

	Page
4.28(a) Profiles of Streamwise Integral Length Scale, L_1	118
4.28(b) Profiles of Vertical Integral Length Scale, L_2	118
4.29 Downstream Propagation of Disturbance Layer	119
4.30 Mean Velocity Profiles Plotted Versus \sqrt{y}	119
4.31 Location of Disturbance Layer	120
4.32 Decay of Disturbance Layer	120
5.1 RMS Wall Pressure Fluctuations at Downstream Locations	156
5.2 Comparison of RMS Pressure Fluctuations for Equilibrium Flows	156
5.3 Wall Pressure Spectra For Equilibrium Flows	157
5.4 Wall Pressure Spectra Scaled on Outer Variables (Equilibrium Flow)	157
5.5 Wall Pressure Spectra Scaled on Inner-Outer Variables (Equilibrium Flow)	158
5.6 Wall Pressure Spectra Scaled on Inner Variables (Equilibrium Flow)	158
5.7 Streamwise Coherence for Equilibrium Flow ($U_0=51$ ft/sec)	159
5.8 Streamwise Coherence for Equilibrium Flow ($U_0=93$ ft/sec)	159
5.9 Convection Velocity for Equilibrium Flow ($U_0=51$ ft/sec)	160
5.10 Convection Velocity for Equilibrium Flow ($U_0=93$ ft/sec)	160
5.11 Spanwise Coherence for Equilibrium Flow ($U_0=51$ ft/sec)	161
5.12 Spanwise Coherence for Equilibrium Flow ($U_0=93$ ft/sec)	161
5.13 Streamwise Coherence versus $\omega\delta^*/U_c(\omega,\xi)$ (Equilibrium Flow)	162

	Page
5.14 Streamwise Coherence for Selected Frequencies (Equilibrium Flow)	162
5.15 Plot of Dimensionless Wavenumber versus Strouhal Number (Equilibrium Flow)	163
5.16 Wall Pressure Spectra at Downstream Locations	164
5.17 Wall Pressure Spectra Scaled on Inner-Outer Variables ...	164
5.18 Collapse of Speed Variations for Wall Pressure Spectra Using Inner-Outer Variables	165
5.19 Wall Pressure Spectra Scaled on Step Variables	165
5.20 Wall Pressure Spectra Scaled on Disturbance Variables ...	166
5.21 Wall Pressure Spectra Scaled on Inner Variables	166
5.22 Streamwise Coherence at Downstream Location ($x/h=10$)	167
5.23 Streamwise Coherence at Downstream Location ($x/h=24$)	167
5.24 Streamwise Coherence at Downstream Location ($x/h=54$)	168
5.25 Comparison of Non-Equilibrium and Equilibrium Coherence Data	168
5.26 Streamwise Coherence for 200 Hz Component	169
5.27 Streamwise Coherence for 300 Hz Component	169
5.28 Streamwise Coherence for 500 Hz Component	170
5.29 Streamwise Coherence for 1,000 Hz Component	170
5.30 Streamwise Coherence versus Strouhal Number (Non-Equilibrium Flow)	171
5.31 Convection Velocity at Downstream Location ($x/h=10$)	171
5.32 Convection Velocity at Downstream Location ($x/h=24$)	172
5.33 Convection Velocity at Downstream Location ($x/h=54$)	172
5.34(a) Convection Velocity for 200 Hz Component (Non-Equilibrium Flow)	173
5.34(b) Convection Velocity for 300 Hz Component (Non-Equilibrium Flow)	173

	Page
5.34(c) Convection Velocity for 500 Hz Component (Non-Equilibrium Flow)	174
5.35(a) Dimensionless Wavenumber versus Strouhal Number at $x/h=10$ for Non-Equilibrium Flow	175
5.35(b) Dimensionless Wavenumber Versus Strouhal Number at $x/h=24$ for Non-Equilibrium Flow	175
5.36 Spanwise Coherence at Downstream Location ($x/h=10$)	176
5.37 Spanwise Coherence at Downstream Location ($x/h=24$)	176
5.38 Spanwise Coherence at Downstream Location ($x/h=54$)	177
5.39 Spanwise Coherence for 200 Hz Component	177
5.40 Spanwise Coherence for 300 Hz Component	178
5.41 Spanwise Coherence for 500 Hz Component	178
6.1 Source Term Distribution Within the Boundary Layer	190
6.2 Mean Velocity Gradient Within the Boundary Layer	190
A.1 Hot Wire Geometry and Velocity Components	212
A.2 Comparison of Turbulence Intensities From Integrated Velocity Spectra to Results from Hot Wire Analysis Program	212

ACKNOWLEDGMENTS

This thesis effort could not have been possible without the many contributions that I have received from my colleagues and friends. To them I wish to express my sincere appreciation.

I would like to express appreciation to my many colleagues at the David W. Taylor Naval Ship Research & Development Center who have helped me in my professional career. Of these people special appreciation goes to Dr. DeMetz and Messrs. Geib and Mathews. They have not only willingly given of their technical skills but have also been close personal friends. For this I am grateful. Dr. DeMetz has been instrumental in my overall career development. He showed me that an endeavor, such as a program of doctoral research, is indeed possible. Mr. Mathews has provided me with a strong background in signal processing that has been invaluable in my research. Mr. Geib has taught me the importance of detail in the conduct of an experimental investigation which has greatly enhanced my research capabilities. A note of thanks also goes to Dr. Cole who, over the last year, has been very helpful by participating in lively discussions on my research effort.

The generous support of the Ship Acoustics Department at DTNSRDC is gratefully acknowledged. The successful conduct of this research effort is due in part to the Extended Term Training program within the Department which allowed me to participate in the research efforts at the University. I hope their investment in my training proves worthwhile. I also appreciate the funding that the Office of Naval Research provided to the University, as part of the Selected Research Opportunities program in Hydro-acoustics, which allowed the University to conduct research in an area pertinent to my thesis work.

I wish to express special appreciation to my dissertation director, Professor Casarella. He has not only provided me with technical guidance throughout my academic career but has also always treated me as a colleague and a friend. Professor Casarella has spent endless hours working with me on this research and is the one who receives most of the credit for its successful completion. I hope that he has gotten as much out of this research effort as I have.

I am grateful to Drs. Clark and von Kerczek for taking time from their busy schedules to act as readers for this dissertation. My involvement with them has proved to be very stimulating. I also wish to express my gratitude to the many people at the University for their help and cooperation during the course of this research effort.

My last expressions of appreciation go to my family. I wish to thank my mother and father for the support they have given me throughout my life. Finally, I thank my son, Joshua, for the time with me that he has foregone. I hope that this thesis partly explains where I have been over the past few years.

NOMENCLATURE

C_f	skin friction coefficient
C_{fm}	skin friction coefficient from Ludwig-Tillman formula
C_1	exponential decay coefficient for streamwise coherence
C_2	exponential decay coefficient for transverse coherence
d	diameter of pinhole microphone
f	frequency (Hz)
G	Clauser parameter, $G=(U_o/u^*) \cdot (H-1)/H$
h	step height
H	boundary layer shape factor (δ^*/θ)
i	$\sqrt{-1}$
K	$\sqrt{k_1^2+k_2^2}$
k_1	streamwise wavenumber
k_2	transverse wavenumber
\vec{k}	planar wavenumber, $\vec{k}=(k_1,k_2)$
k_o	ω/U_o
l_m	mixing length
L_1	streamwise integral length scale
L_2	vertical integral length scale
P	total pressure
P_o	mean pressure
p'	fluctuating pressure
P_{RMS}	root-mean-square of fluctuating pressure
q	dynamic head, $q=1/2\rho U_o^2$
$q(\vec{x},t)$	general turbulence function
Q	source term
\hat{Q}	spectral form of source term
R, R_i	correlation functions
R_2	vertical correlation function
R_{12}	Reynolds shear stress, $R_{12}=-\overline{u'v'}/\overline{u' \cdot v'}$
R_θ	momentum thickness Reynolds number
\vec{r}	dummy position vector
$S(y)$	wall pressure source term distribution
t	time variable
u	fluctuating streamwise velocity component
u'	root-mean-square of u
\vec{u}	fluctuating velocity vector, $\vec{u}=(u,v)$
$U, \bar{u}(y)$, or \bar{u}	mean streamwise velocity at position y away from wall
U_o	free-stream reference velocity
\vec{U}	Mean velocity vector, $\vec{U}=(U,V)$

U_c	convection velocity
u^*	shear velocity
u^+	u/u^*
$\overline{u'v'}$	Reynolds shear stress
v	fluctuating vertical velocity
v'	root-mean-square of v
V	mean vertical velocity
w	fluctuating transverse velocity
W	mean transverse velocity
x	streamwise direction
x_r	streamwise location of flow reattachment
\vec{x}	position vector, $\vec{x}=(x,y,z)$
X	$(x-x_r)/h$
y	vertical direction
y^+	y expressed in wall units, $y^+=yu^*/\nu$
z	transverse (lateral) direction
$\langle \rangle$	time average
Γ	pressure field coherence function
γ^2	coherence squared, $\Gamma=\sqrt{\gamma^2}$
δ	boundary layer thickness, where $U=0.99U_0$
δ^*	boundary layer displacement thickness
δ_0	boundary layer thickness at separation
δ_d	location of disturbance layer away from wall
n	separation distance in transverse direction
θ	boundary layer momentum thickness
$\theta(\omega, \xi)$	phase of wall pressure cross-spectrum
κ	von Karman constant, $\kappa=0.41$
Λ	vertical correlation coefficient
λ_1, λ_2	streamwise and vertical microscales, respectively
λ_3	turbulence scale (taken as $\lambda_3=L_2$)
μ	fluid viscosity
ν	fluid kinematic viscosity
ξ	separation distance in streamwise direction
$\vec{\xi}$	separation vector (planar), $\vec{\xi}=(\xi, n)$
π	3.14159...
ρ	fluid density
τ	delay time
τ_0, τ_w	wall shear stress
Φ	spectral function
$\Phi(\omega)$	frequency spectrum
Φ_p	wall pressure spectrum

ϕ_u, ϕ_v	velocity spectrum of u and v components, respectively
$\tilde{\phi}$	first-moment spectral density normalized by mean-square value $\tilde{\phi} = \omega \phi_1(\omega) / u_1'^2$
ϕ_o	moving axis spectrum
ϕ_1	k_1 spectrum
ϕ_3	k_3 spectrum
ω	angular frequency $\omega = 2\pi f$
ω_b	burst event frequency
ω_m	frequency of peak in wall pressure spectrum

ABSTRACT

Wall pressure fluctuations beneath a non-equilibrium turbulent boundary layer were studied experimentally. The objective of the investigation was to better understand the process by which turbulent boundary layer flows produce wall pressure fluctuations. The approach was to study the statistics of both the wall pressure field and velocity field for a non-equilibrium turbulent boundary layer, produced by passing a flow over a backward-facing step, and then to identify turbulent structures in the flow that contribute to the source terms of the wall pressure field. Detailed velocity and wall pressure measurements were also obtained for an equilibrium flow to provide a basis of comparison for the perturbed flow results.

The experiments were conducted in a low noise wind tunnel for velocities ranging from 50 to 95 ft/sec. The two-dimensional backward-facing step had a step height (h) of 0.5-inch and the boundary layer thickness at the top of the step was approximately 2 step heights. Cross-spectral density measurements of the wall pressure fluctuations were obtained for both streamwise and transverse separations using small, flush-mounted, pinhole microphones at several downstream positions. Velocity data were obtained using both a single and a x-wire anemometer at several downstream locations. The velocity data consisted of measurements of the mean-velocity and turbulence intensity (u' , v' , $u'v'$) profiles, and measurements of the frequency spectrum of the streamwise (u) and vertical (v) components of velocity at various positions in the boundary layer.

The velocity measurements show that the boundary layers downstream of reattachment are marked by the presence of a disturbance layer, consisting of highly energized flow, that is the remnants of the free-shear layer that formed when the flow separated at the top of the step. This disturbance layer propagates away from the wall and decays in level as it convects downstream.

Near reattachment the entire boundary layer is highly disturbed, but by $x/h=16$ the near wall region ($y^+ < 100$) has recovered to an equilibrium flow condition. However, full recovery of the outer flow region takes much longer and will not occur until the disturbance layer has fully propagated across the boundary layer. It is estimated that full recovery will not occur until an $x/h=250$.

The wall pressure statistics for the perturbed flow are characterized by the presence of the disturbance layer. Levels of fluctuating wall pressure are very high near reattachment. The frequency spectra show that these high levels are associated with an excess of low frequency energy. This low frequency energy excess decreases in the downstream direction, but even at $x/h=72$ is still greater than the spectral levels for the equilibrium flow and never fully recovers within the streamwise range of the measurements. Furthermore, these components were found to scale on disturbance layer variables. Hence, the source of the low frequency excess in the wall pressure fluctuations is the disturbance layer.

The high frequency wall pressures were found to scale on inner variables, and as such, recovered to an equilibrium flow condition quite

rapidly. This places the source of high frequency wall pressures in the inner layer of the boundary layer.

The cross-spectral properties of the wall pressure field show that for the perturbed flow the low frequency components are coherent over a much greater distance than the coherence lengths measured for the equilibrium flow. The convective phase speeds of the low frequency components track the location of the disturbance layer in the boundary layer.

For both the perturbed and equilibrium flow, it was found that the boundary layer suppresses wall pressure components below an $\omega\delta/U_0 \leq 0.3$. This cutoff frequency is also the frequency at which the wall pressure spectrum is a maximum for the equilibrium flow.

A simplified analytical model for the wall pressure frequency spectrum, which is a function of the measured velocity statistics, confirmed that the primary source for the low frequency wall pressures was the disturbance layer.

ADMINISTRATIVE INFORMATION

This work is a dissertation submitted to the Faculty of the School of Engineering and Architecture of the Catholic University of America in partial fulfillment of the requirements for the degree Doctor of Philosophy and has been reproduced, with minor modifications, as a David W. Taylor Naval Ship Research and Development Center (DTNSRDC) report. The major portion of the research was conducted at the Catholic University of America while the author was on Extended Term Training from the Ship Acoustics Department. At the time of the research effort the University was funded by the Office of Naval Research as part of a more extensive Selected Research Opportunities program in Hydroacoustics administered by Dr. M. Reischman. Funding for the publication of this report has been obtained from the Hydroacoustics Task of the 6.2 Block Program at DTNSRDC.

CHAPTER 1

INTRODUCTION

1.1 Background

The fluctuating wall pressure field that develops beneath a turbulent boundary layer as it flows over a surface has received extensive analytical and experimental attention in the past. A majority of this interest arises from the fact that the unsteady surface pressures are a source of surface excitation that can lead to unwanted noise and vibrations. Lately there has been a renewed interest in studying wall pressure fluctuations in an attempt to understand better the turbulence processes that occur in wall bounded flows. In these studies the large scale excursions that are detected in the wall pressure signature are related to possible burst-sweep events in the inner boundary layer.

The analytical studies have attempted to understand the relationship between the large and small scale turbulence structures in the flow and how they induce wall pressures. The direction of the experimental studies has been towards measuring the statistical properties of the wall pressure field and then relating them to turbulence structures that are known to exist in the flow. These investigations have led to a fairly conclusive understanding of the relationship between fluctuating velocities and surface pressures, as well as the importance of the wall pressure field as a forcing function acting on the surface. This level of understanding, however, is restricted to classical, equilibrium types of flow.

For the case of perturbed (non-equilibrium) flows, little is presently known about the fluctuating velocity field and pressure field. These type of flows are fairly common in practical configurations such as, in turbomachinery, on high lift airfoils, along the walls of diffusers and over irregular surfaces. The physical structure of these turbulent flows can become highly complex. For example, the flow can go

through a separation and reattachment process in which the velocity field becomes energized and then goes through a slow evolutionary relaxation period, eventually returning to an equilibrium flow. It is hypothesized in this investigation that by studying the wall pressure field that develops beneath such an energized flow a better understanding can be obtained of the process by which velocity fluctuations produce surface pressure fluctuations. Furthermore, information of this type will also greatly advance the understanding of flow induced surface vibrations for practical flow/structure geometries.

Flow over a two-dimensional backward-facing step has a well-defined region of separation and reattachment and, as such, has been used by many investigators as a generic perturbed flow. Recent doctoral investigations (Eaton (1980) and Pronchick (1983)) have performed detailed studies of the turbulent structure in the separation-reattachment region and to a limited extent in the downstream relaxation region. These studies were restricted to the physical features of the flow field. This investigation extends that work by experimentally investigating both the velocity and wall pressure fluctuations for the turbulent flow downstream of reattachment. Comparisons of the spatial and temporal statistics of the velocity and wall pressure fields for this perturbed flow will be made to those measured for an equilibrium flow. Special attention will be given to the evolutionary characteristics of the wall pressure field in the relaxation region.

In the following section a literature review of backward-facing step work as well as other investigations on disturbed flows will be given in which the basic features of such a flow are described. After that, a literature review covering what are considered to be the more important wall pressure fluctuation studies will be given. This includes both analytical and experimental studies. Finally the specific objectives of this study will be given.

1.2 Review of the Problem Area

1.2.1 Features of the Disturbed Flow (Backward-facing Step)

The non-equilibrium flow field that was selected for this study was the flow that develops downstream of reattachment of flow over a backward-facing step. This flow is easy to obtain and has the advantage of a fixed point of separation. The flow becomes highly energized by the separation and reattachment process. In order to understand the type of energized flow that is being studied some details of the development of the flow in the separated and reattaching regions need to be reviewed. This has been the subject of many extensive studies.

The characteristic features of flow over a backward-facing step are illustrated schematically in figure 1.1. This complex flow field can be described in terms of five overlapping flow zones. In zone I a fully developed equilibrium turbulent boundary layer flows along the top of the step. At the edge of the step the boundary layer separates forming a free-shear layer. This free-shear layer grows, by an entrainment process, as it moves downstream until its growth brings it in contact with the downstream wall. At this reattachment point a portion of the flow is directed upstream, into the recirculation region where it eventually gets entrained by the free-shear layer, while the remaining flow continues on its downstream path. The impingement and splitting of the shear layer, at reattachment, produces high levels of turbulence activity. Immediately downstream of reattachment the attached shear flow is highly energized and has the characteristics of an attached free-shear layer. As this energized flow convects downstream it undergoes a relaxation and redevelopment process, eventually becoming an equilibrium turbulent boundary layer. Zones IV and V are the regions of interest in this study.

1.2.2. Literature Review- Disturbed Flow Studies

Flow over a backward-facing step has been the subject of many experimental investigations. A majority of these investigations have dealt specifically with details of the flow in the free-shear layer and reattachment regions with the objective of developing computer codes that are capable of accurately calculating flow fields downstream of separation and reattachment. While studies of this type are not immediately pertinent, since they typically do not address the flow in the relaxation zone, they do provide information on the energized nature of the attached boundary layer. These details are needed in order to understand how the energized flow, in zone IV, redevelops as it convects downstream.

Eaton and Johnston (1981a) provide the most current review article describing research on subsonic turbulent flow reattachment. In that review they refer to and compare results from approximately 20 separate investigations. They compare reattachment locations, locations and magnitudes of Reynolds stresses, turbulence intensity profiles, and mean velocity profiles. In the summary they recommend specific investigations that should be conducted in order to resolve remaining questions. The discussions deal primarily with the flow field upstream of the redevelopment region.

Tani, Matsusaburo and Komoda (1961) investigated flow over various backward-facing steps of different step height. They presented measurements of static surface pressure, mean velocity profiles, turbulence intensity profiles, and Reynolds stress profiles obtained on top of the steps and at various downstream locations. The farthest downstream measurement location was at an x/h of 15. They found the static pressure distributions to be rather insensitive to changes in step height and approaching boundary layer thickness. The base pressure is nearly constant for all conditions tested and the pressure rise at reattachment increases slightly as the step height is increased. The maximum in the turbulence and shear stress profiles are initially located at the dividing streamline of the free-shear layer but deviate outward as reattachment is approached. They state that the turbulence

and shear stress, formed in the mixing region of the free-shear layer, decreases downstream of the reattachment location and that a new system of turbulence and shear stress moves upward into the reattached layer, eventually forming a fully developed boundary layer with a maximum in turbulence located near the wall.

Bradshaw and Wong (1972) investigated turbulent flow over a backward-facing step to study the complicated nature of the flow in the reattachment region. They showed how this flow resulted in a slow, non-monotonic return of the attached shear layer to an ordinary boundary layer state. Previous experiments that dealt with flow over surface discontinuities that produce a separated/reattached boundary layer were reviewed and compared to their results. The various flows were categorized according to the strength of perturbation applied to the initially thin shear layer as a weak perturbation, a strong perturbation, or an overwhelming perturbation. The strength of the perturbation was classified by the value of h/δ_0 , where h is the step height and δ_0 is the boundary layer thickness at separation; $h/\delta_0 \ll 1$ being a weak perturbation, $h/\delta_0 \approx 1$ being a strong perturbation, and $h/\delta_0 \gg 1$ being an overwhelming perturbation. They concluded that the large scale eddies, which are formed in the free-shear layer and produce much of the shear stress, are torn in two at reattachment and that this accounted for the rapid decrease in turbulent shear stress immediately downstream of reattachment. Just downstream of reattachment the flow bears little resemblance to any sort of a thin shear layer. After reattachment an internal boundary layer which follows a logarithmic law behavior, grows out from the surface. The outer-layer structure was found to relax back to an ordinary boundary layer very slowly. Even at the last data station, located at 52 step heights downstream, the turbulent properties of the boundary layer were not that of an ordinary turbulent boundary layer. These conclusions were drawn from measurements of mean velocity profiles, wall shear stress, turbulence intensity profiles, and Reynolds stress profiles.

Kim, Kline and Johnston (1978) experimentally and numerically studied the flow over a backward-facing step. The experiments were conducted using two different step heights; a 1.5-inch step and a 1-inch step installed in the wall of a 3-inch wide wind tunnel. This arrangement gave area expansion factors (step height to upstream tunnel width) of 0.5 and 0.33 for the two steps. Static pressure, mean velocity profiles, turbulence intensity profiles, Reynolds stress profiles, and intermittency profiles were measured out to $x/h=16$. Tufts were used to visualize the flow field. Reattachment of the separated shear layer was found to be an unsteady phenomena, fluctuating upstream and downstream of the mean reattachment point by approximately one step height. It was suggested that in the reattachment zone large eddies are not only split, as proposed by Bradshaw and Wong, but some move alternately back and forth producing the unsteady reattachment fluctuations. Flow in the recirculation region was found to be highly turbulent. It was pointed out that the recirculated flow is entrained by the free-shear layer as it grows downstream which is a quite different process than occurs for a plane mixing layer which entrains quiescent non-turbulent fluid. This enhances the turbulent activity of the free-shear layer. Turbulence intensities and turbulence shear stresses were found to be a maximum in the reattachment zone. Downstream of reattachment these quantities rapidly decayed but the total flow structure returned very slowly to that of an equilibrium boundary layer flow. The inner layer adjusts rapidly while the outer layer, which is dominated by large scale eddies, adjusts very slowly. This results in the mean flow profile dropping below the log-law line at the center of the profile.

Eaton and Johnston (1980) (also Eaton (1980)) investigated the reattaching turbulent shear layer downstream of a backward-facing step. Specific attention was given to the large scale turbulent structures present in the flow. Mean velocity profiles, turbulence intensity profiles, Reynolds stress profiles, and wall static pressures were

measured. A pulsed-wire anemometer, a thermal tuft and a pulsed-wall probe were developed to allow measurements to be made in the highly turbulent, frequently reversing, flow field near reattachment. Standard anemometry and pitot tube techniques are highly inaccurate for measurements in these types of flow fields. Laminar, transitional and turbulent boundary layer flows at separation were studied. For all cases the turbulence intensity decayed rapidly in the reattachment zone with the decay beginning one to two step heights upstream of reattachment. The reattaching shear layer had growth rates and turbulence intensity profiles that were similar to those measured for a plane-mixing layer with identical initial conditions. Large spanwise vortices were shown to be present in the shear layer originating from a laminar inflow but not present for the turbulent inflow. Flapping of the shear layer was found to cause back and forth movement of the impingement point and is believed to be the primary contributor to low frequency unsteadiness in the reattachment region.

Chandrsuda and Bradshaw (1981) obtained detailed measurements of the reattaching flow and of the downstream developing flow for flow over a backward-facing step. A thin laminar boundary layer at separation was used to ensure that the free-shear mixing layer was fully developed prior to reattachment in order to uncouple effects associated with separation from those at reattachment. Triple products of turbulence were measured and the farthest downstream measurements were made at 16 step heights downstream of the step. Rapid changes in turbulence quantities were observed in the reattachment region. The dramatic decreases in Reynolds stress and triple products were suggested to be due to confinement of the large eddies, developed in the mixing layer, as the flow approaches the wall. The mean velocity profiles, when plotted in a log-law format, were found to dip below the standard logarithmic law reportedly due to the flow scaling on a roughly constant length scale, as does a free-shear layer, instead of a length scale that is proportional to wall distance. The dip persisted to the last measurement location exhibiting the persistence of the abnormally large

length scale. The Reynolds stress coefficient was a maximum in the mixing layer and decreased after reattachment and remained lower than values for an ordinary boundary layer. From measurements of the flow intermittency interface position they concluded that there is no evidence of large increases in the reattachment region associated with large eddies alternately moving upstream and then downstream as was suggested by Kim et al. (1978). The turbulence measurements showed that the flow was far from being a self-preserving boundary layer even at the most downstream position they measured.

Pronchick (1983) studied the flow downstream of a backward-facing step in a water channel using both hydrogen bubble flow visualization techniques and a two-component laser-doppler system. Large three-dimensional eddies, generated in the free shear layer were identified by flow visualization. These eddies had a wide distribution of sizes and their trajectories exhibit a wide dispersion. An eddy, as it passed through the reattachment region would follow one of two paths: the eddy would strongly interact with the wall, resulting in a loss of coherence and formation of back flow, or the eddy would pass through the reattachment region with little loss of coherence. The downstream outer flow was seen to consist of a broad spectrum of eddy sizes and the large eddies were seen to persist for many boundary layer thicknesses downstream. Readjustment to an equilibrium layer was quite slow. Reynolds stress and triple products in the outer flow region initially increased and then rapidly decreased as the flow passed through the reattachment zone. For the flow near the wall these quantities remained nearly constant throughout the reattachment zone. The last measurement point was 16 step heights downstream of the step.

Troutt, Scheelke and Norman (1984) studied the spanwise turbulence structures in a two-dimensional separated flow formed by flow over a backward-facing step. The importance of large scale vortices in both the separated and reattached regions of the flow were discussed and it was suggested that the vortex dynamics of these large-scale structures is primarily responsible for time-averaged features of the flow that are

measured. These large-scale structures persisted as far downstream as the last measurement station, 16 step heights downstream of the step. The rapid decrease in turbulence energy and Reynolds stress that occurs at reattachment was suggested to be due to a halt in vortex-pairing activity brought on by the presence of the wall at reattachment. The large length scales that Chandrsuda and Bradshaw (1981) attributed to the cause of the dip in the mean velocity profiles were also associated with the large-scale vortices formed in the free-shear layer.

Boundary layer redevelopment downstream of changes in surface condition has characteristics that are common to the boundary layer development downstream of reattachment for flow over a backward-facing step. Smits and Wood (1985) address many of these issues in a review article on the response of turbulent boundary layers to sudden perturbations. These similarities are discussed next.

Antonia and Luxton (1971a,b) experimentally studied the response of a turbulent boundary layer to a step change in surface roughness from a smooth wall condition to a rough wall condition. They also studied the changes that occur when there is a change in surface roughness from rough-to-smooth (1972). They found that although both flows are characterized by the growth of an internal layer the two flows were fundamentally different. The growth rate of the internal layer for the rough-to-smooth surface change was slower than for the smooth-to-rough change and at the last measurement station the former flow was still far from being self-preserving yet the latter flow was nearly self-preserving.

The response of a turbulent boundary layer to passage over a short length of surface roughness was investigated by Andreopoulos and Wood (1982). A roughness length of approximately three boundary layer thicknesses was used and measurements included the mean velocity, all Reynolds stresses, and triple products. Flow over the roughness strip induced the growth of two internal layers: the first layer, beginning at the start of the roughness strip grew very rapidly, fully extending through the boundary layer within about 13 boundary layer thickness downstream of the strip. The second layer started at the downstream end

of the strip and grew very slowly and had barely penetrated to the outer layer by the last measurement station at 55δ downstream. Turbulence intensities in the region of the wall increased abruptly over their smooth wall values immediately downstream of the strip. These levels slowly decayed downstream but were still larger than the smooth inflow values at the last measurement position. The Reynolds stress exhibited a strong peak at the downstream edge of the roughness strip and the peak propagated outward and decays in the downstream direction. On the other hand the Reynolds stress coefficient changed very little. The overriding feature of the measurements is that even at the last measurement position the flow was still not completely relaxed to that of an ordinary boundary layer. This is similar to what is observed in changes of surface roughness from rough-to-smooth. In all such cases, the high levels of shear stress that are developed in the outer layer must decay before a fully developed boundary layer profile can be established.

The above cited investigations studied in great detail many aspects of perturbed flows particularly flow over a backward-facing step. For the step flow, they have led to a fair understanding of the turbulence processes that occur in the separated/reattaching regions of the flow. However, with the noted exception of the work by Bradshaw and Wong (1972) very few of the studies have specifically addressed the features of the flow field in the downstream relaxation region where the flow is slowly redeveloping and relaxing from an energized state to an ordinary boundary layer state.

1.2.3 Literature Review- Wall Pressure Studies

Kraichnan (1956) provided one of the earliest analytical studies of pressure fluctuations at the wall beneath a turbulent boundary layer. His analytical approach is the same as that which will be presented in Chapter 2. Kraichnan derived a Poisson equation for the unsteady pressure in a turbulent field by combining the continuity equation with the divergence of the incompressible Navier-Stokes equation. To solve the Poisson equation he performed a time-planar Fourier transform of the

Poisson equation, in planes of homogeneity (parallel to wall), to obtain an equation for pressure that is a linear inhomogeneous ordinary differential equation with constant coefficients. The wavenumber-frequency spectral density of the wall pressure fluctuations was thus expressed in terms of a double integral over the velocity fluctuations throughout the boundary layer. Next Kraichnan formulated a mirror flow model of the turbulence structure in a boundary layer which he used to obtain quantitative estimates for the levels of the wall pressure fluctuations. He estimated that the major contributions came from mean shear-turbulence interactions and that the mean square pressure fluctuations should be approximately six times the mean wall shear stress. From his model Kraichnan was also able to estimate the force that would be imparted to a rectangular section of wall area by the fluctuating pressures. A final observation by Kraichnan, which is still open to discussion today, is that the integral of the pressure correlation over the wall must vanish and that the total mean square force per unit area exerted on the wall by the pressure fluctuations must be zero.

Using an approach similar to that of Kraichnan, Lilley and Hodgson (1960) investigated wall pressure fluctuations for flat plate type flows and also examined pressure fluctuations due to a wall jet flow. They supported their analytical work with direct comparisons to experimental data they obtained for both types of flow. Lilley and Hodgson also extended the Kraichnan model by including the separate effects of large eddy structures, as suggested by Townsend, and by allowing for the convection of eddies.

Willmarth and Wooldridge (1962) obtained the first high quality wall pressure measurements as a function of space-time variables. They made combined spatial and temporal cross-correlation measurements of the wall pressure field beneath a thick turbulent boundary layer and showed that pressure fluctuations convected downstream with the flow. The convection velocity was shown to be frequency dependent with the low frequency pressure fluctuations having the highest convection speed. They also showed that a typical pressure-producing eddy, whether it be

of large or small wavelength, decays and vanishes after traveling a distance of approximately six wavelengths. Both the transverse and longitudinal length scales of the pressure fluctuations were of the order of the boundary layer displacement thickness.

Corcos (1963) addressed the issue of spatial resolution errors arising in the measurement of wall pressure fluctuations with finite sized transducers. Using the experimental results of Willmarth and Wooldridge (1962) Corcos established correction relationships that can be used to correct various types of pressure measurements for the spatial resolution errors that occur due to the finite size of the transducer that is used to make the measurements. He provided correction curves (or functions) for the frequency spectrum, cross-spectral density, and for space-time correlation measurements.

Bull (1967) obtained both broad and narrow-band space-time correlations of the wall pressure field beneath a turbulent boundary layer. It is noted that narrow-band spatial correlation measurements are the same as cross-spectral density measurements. These measurements provided information on both the spatial and frequency scales that comprise the fluctuating wall pressures. Bull concluded that the structure of the wall pressure field is produced by contributions from pressure sources within the boundary layer with a wide range of convective velocities. The wall pressure field was viewed as being composed of two families of convected wavenumber components. The first, a group of high wavenumber components, is associated with turbulent motion in the constant stress region of the boundary layer and are longitudinally coherent over convected distances proportional to their wavelengths. These components were also found to be coherent laterally over distances proportional to their wavelength. This resulted in the pressure field coherence, for these higher wavenumber components, scaling on similarity variables. The second family of convected wavenumber components was of lower wavenumber, having wavelengths greater than twice the boundary layer thickness. These lower wavenumber components lost coherence more or less independently of wavelength and

were associated with large scale turbulence motion in the outer part of the boundary layer. Bull also used the measured convective velocities of the pressure field as an indication of where in the flow field the pressure source terms are located.

Landahl (1967) modeled a turbulent boundary layer as a wave-guide and obtained calculations for the streamwise cross-spectral density of the surface pressure fluctuations. His approach was to numerically solve the nonhomogeneous Orr-Sommerfeld equation for a turbulent boundary layer and assume that the least damped eigenvalues of the problem would be the dominant sources of the wall pressure field. His results for the pressure cross-spectral density for a flat plate boundary layer flow were in good agreement with the experimental results of Willmarth and Wooldridge (as interpreted by Corcos (1964)). The streamwise coherence exhibited the similarity scaling that was found by Bull to exist for the higher wavenumber components and the calculated streamwise decay rates agreed well with the experimental results. The calculated convection velocities, however, were found to be too low by approximately 30%. Good agreement for the convection velocities could be obtained if a viscosity 80 times as large as the experimental value was used in the analysis. The conclusion was that accurate convection velocity calculations require that the damped Orr-Sommerfeld disturbances propagate in a flow with pre-existing fluctuations. Computations incorporating this effect were not made. A final aspect of the analytical study was the confirmation of the separability hypothesis in which the complete pressure cross-spectrum can be expressed in terms of the product of a separate streamwise and transverse terms.

Willmarth and Tu (1967) proposed a qualitative model in which the turbulence structure in the flow is correlated with the wall pressures. They used earlier measurements by Willmarth and Wooldridge (1963), and new measurements of the space-time correlations between the wall pressure fluctuations and various velocity components to develop the model. The model associates intense pressure fluctuations with the

stretching of vorticity produced by viscous stresses in the sublayer. The vortex stretching results in the diffusion of a disturbance away from the wall as it convects downstream.

Wills (1970) measured filtered spatial correlations (cross-spectra) of the wall pressure field beneath a turbulent boundary layer and spatially transformed the measurements to obtain a wavenumber-frequency spectrum. He also presented the data in the form of a wavenumber-phase velocity spectrum which directly shows the distribution of energy over the range of phase velocities for each wavenumber. Pressure data presented in these forms are particularly useful. The effects of transducer size can be seen as a simple lack of response to the higher wavenumber components of the pressure field. Wills found that the distribution of pressure energy over the range of phase velocities at all wavenumbers is approximately a normal distribution with a standard deviation of 0.14. He defined a mean convection velocity that was associated with the peak-energy velocity at a constant value of streamwise wavenumber. This mean convection velocity varied from a maximum value of $0.9U_0$ at a $k_1\delta$ of 1.2 to an asymptotic value of $0.55U_0$ at higher values of $k_1\delta$. It was suggested that these variations in mean convection velocity demonstrated that the largest eddies extend over the whole width of the boundary layer and are convected with speeds that are typical of the outer flow while the small-scale, high wavenumber eddies are located nearer the wall where the boundary layer velocities are lower. At the lowest wavenumbers the mean convection velocity appears to decrease from the maximum value. Wills suggested that perhaps this effect was due to experimental inaccuracies even though this same trend was also reported by Bradshaw (1967) for measurements in an adverse pressure gradient flow.

Blake (1970) investigated the wall pressure fluctuations beneath a rough wall flow as well as a smooth wall flow. He was one of the first to use the pinhole microphone as a small area pressure sensor. Both broadband spatial correlations and cross-spectral density measurements of the wall pressure fluctuations were made. Blake found that the convection velocities, measured by the cross-spectrum method, decreased

sharply at low frequency. This was in disagreement with the results of Bull (1967). Blake attributed the differences to the rather wide frequency bandwidth Bull used to make his measurements. The coherence decay rates for the smooth wall case were in general agreement with Bull's decay rates. Blake found that for smooth wall flows the high frequency pressure fluctuations scaled on inner flow variables and the low frequency end of the pressure spectrum scaled on combined inner-outer variables. It was found that roughness height influenced the medium and very small-scale turbulence structure and the separation between roughness elements affected the very large scale turbulence structure.

Elliott (1972) measured static pressure fluctuations within a turbulent boundary layer. These measurements were made in the atmospheric boundary layer that developed on a tidal flat and on a taxiway of an abandoned airport using an especially constructed circular disk transducer. Surface pressure measurements and pressure-velocity correlation measurements were made. The pressure had a well defined shape that did not change with height above the surface. The large scale pressure fluctuations were in phase with the downstream velocity fluctuations.

Emmerling, Meier and Dinkelacker (1973) obtained space-time maps of the instantaneous pressure field beneath a turbulent boundary layer. These measurements were made by photographing the fringe patterns produced by turbulent flow over a reflective, flexible wall in a wind tunnel. The flexible wall was constructed by stretching a rubber foil over a rigid base which had 650 holes, of approximately 0.1-inch diameter, drilled in it. This arrangement produced 650 individual wall mounted mirrors that each acted as a Michelson-interferometer. The fringe patterns produced by pressure induced deflections of each mirror were photographically recorded and later read by hand to obtain maps of the instantaneous structure of the pressure field. Convection velocities for various wall pressure events ranged from $0.39U_0$ to $0.82U_0$. Pressure extremes that are over five times the RMS pressure

observed. Regions of high amplitude pressure were found to occur with a mean occurrence frequency of 67 Hz. This frequency was very close to the expected rate at which near-wall burst events occur in the flow field.

Panton and Linebarger (1974) calculated the one-dimensional wavenumber (streamwise wavenumber) spectrum of pressure fluctuations beneath equilibrium turbulent boundary layers. They numerically solved the Poisson equation for wall pressure, following the development of Kraichnan (1956), by using empirical models for the turbulence velocity source terms in the equation. The form for the vertical velocity correlation that was assumed included an anisotropy factor. An interesting feature of their work is that they showed the contributions to the total pressure, as a function of wavenumber, that come from the various regions of the boundary layer. The inner-inner portion of the boundary layer dominates the contributions at the highest wavenumbers. When contributions come entirely from the wall layer and log region, a universal overlap region in the pressure spectrum existed. This overlap region started at a $k_1 \delta \approx 20$ and ended at about $k_1 \nu / u^* \approx 0.5$. The presence of an overlap region can be argued following the same dimensional arguments that are used to show the presence of an overlap region for the mean flow velocity profile. Within the overlap region the wavenumber spectrum should scale as k^{-1} . Interestingly, the contributions to the low wavenumber components come from the wake region, yet the contribution to the lowest wavenumber components come from the middle region of the boundary layer.

Burton (1974) experimentally investigated the connection between the intermittent turbulent activity near the wall and wall pressure fluctuations. This was the first attempt to study the relationship between the sublayer burst events and fluctuating wall pressures. Simultaneous measurements were made of streamwise velocity, streamwise wall shear stress, and fluctuating wall pressure. There was no significant relationship found between wall pressure occurrences and either sweep or ejections in the sublayer. In fact, it was suggested that most large pressure fluctuations originate from random occurrences

outside the sublayer. These conclusions were made with some reservation since vertical velocity measurements were not also made. It was suggested that this term may be quite important for ejections but was not thought to play an important role in sweeps.

Chase (1980) developed an analytical model for the wavenumber-frequency spectrum of turbulent boundary layer wall pressures. The objective of his modeling was to provide a description of the pressure spectrum that is valid for both the convective (high wavenumber) components and for the low wavenumber components. Chase used the Poisson equation formulation given by Kraichnan (1956) and modeled the fluctuating velocities as similar boundary layer waves as suggested by Morrison and Kronauer (1969). An analytical expression for the pressure spectrum was obtained containing adjustable constants that were evaluated using experimental data. Chase's model agrees well with experimental results and even predicts that the convection speed will rapidly decrease at low frequency and that the pressure coherence will drop off rapidly at low values of the similarity variable.

Meecham and Tavis (1980) obtained expressions for the pressure variances throughout a turbulent boundary layer flow by solving the Poisson pressure equation using idealized models for the turbulence functions. They obtained expressions for the pressure variances that require only a specification of the mean flow and turbulence distributions throughout the boundary layer. Their near-wall results for a canonical boundary layer agreed favorably with measurements of the wall pressures for a flat plate turbulent boundary layer.

Thomas and Bull (1983) conditionally sampled wall pressure fluctuations beneath a turbulent boundary layer on a basis of the high frequency activity in both the pressure field and the velocity field. They identified a characteristic wall pressure pattern that is associated with the burst-sweep cycle of events in the near wall region of the flow. The convective speed of the identified pressure pattern is $0.67U_0$ and the pattern spans a streamwise distance of approximately three displacement thickness. They concluded from the phase

relationships between the pressure and velocity during a burst, that the pressure gradient imposed on the wall is not responsible for initiating the burst process. In fact, the pressure pattern at the onset of a burst is favorable and not adverse as would be needed to initiate the burst process.

Schewe (1983) obtained wall pressure measurements beneath a turbulent boundary layer using small, non-pinhole, pressure transducers. Measurements were also obtained using large size transducers. Schewe found that the size of the transducer affected the probability density distributions of the wall pressure fluctuations that were measured. It was concluded that the smallest transducer was small enough to resolve accurately the small scale structure in the wall pressure field. Schewe also presented pressure spectra and showed pressure patterns measured at the wall by averaging the wall pressure signal when the instantaneous pressure exceeded a high threshold.

Blake (1984) provides an extensive review of research that has been done in the area of aero- and hydro-acoustics as it applies to ship applications. He reviewed the experimental and analytical work that has been done on understanding turbulence and wall pressure fluctuations. This work has since been rewritten and is currently in press as a commercial publication (Academic Press). This text provides the most comprehensive review that is available on the subject of flow noise.

All of these cited wall pressure studies have been made for what are essentially equilibrium flat plate types of flow. Hence, there is a lot known about wall pressure fluctuations beneath an equilibrium turbulent boundary layer. The subject of wall pressure fluctuations for non-equilibrium turbulent boundary layers is less well understood. This lack of understanding stems partly from the complexities of the turbulence structure of non-equilibrium flows and from the many different ways that a non-equilibrium flow can be developed.

Consequently, a wide range of wall pressure fields are obtained. Two typical ways of developing a non-equilibrium turbulent boundary layer are; 1) impose a strong pressure gradient on the flow, and 2) perturb the flow by passing the flow over a surface mounted obstacle which causes the flow to separate and reattach. There are many types of surface geometries that can be used to produce a non-equilibrium flow and the specific details of the resulting wall pressures will depend strongly on the type of surface/flow geometry that is used. A number of the non-equilibrium flow studies that addressed the issue of wall pressure statistics are cited below.

Hubbard (1957) briefly reviewed self-generated noise produced by airflow over aerodynamic surfaces. He observed that the noise levels inside a body of revolution increased by 10 dB when a small ring was attached to the nose section. Hubbard stated that fatigue damage, by skin panel vibrations, has been experienced when there are protuberances, such as spoilers, located on an aerodynamic surface and that noise levels in the interior spaces of aircraft are more intense when discontinuities exist on the outside aerodynamic surfaces.

Schloemer (1967) measured the cross-spectral properties of the wall pressure fluctuations for both mild adverse and mild favorable turbulent flow. Direct comparisons of these results were made to measurements for an equilibrium flow condition. The adverse gradient caused an increase in the low frequency content of the wall pressure spectrum while the favorable gradient caused a sharp decrease in the high frequency portion of the wall pressure spectrum. Generally, the pressure field convection velocities were higher for the favorable gradient and lower for the adverse gradient. The decay rate for the streamwise coherence was higher for the adverse gradient and lower for the favorable gradient, and no differences were found for the decay rate for the lateral coherence.

Fricke and Stevenson (1968) measured the wall pressure fluctuations in the separated flow region downstream of a surface mounted fence. The position of flow reattachment was found to coincide closely with the position of maximum mean square surface pressure and maximum pressure levels were about eight times that found in a equilibrium turbulent boundary layer. Pressure data were obtained to 50 fence heights downstream of the fence and the pressure spectra were found to change considerably with distance behind the fence.

Greshilov, Evtushenko and Lyamshev (1969) experimentally investigated the wall pressure fluctuations downstream of a wall mounted projection (ramp) on a smooth wall in a water tunnel. Flow separated at the top of the ramp and formed a free-shear layer that reattached at 5-6 projection heights downstream. Pressure fluctuations were found to be highest at the point of flow reattachment. In the separated flow region the wall pressure fluctuations did not contain much high frequency energy.

Fricke (1971) presented measurements of wall pressure spectra and mean square wall pressure levels for separated flows. This work was an extension of his earlier work (Fricke and Stevenson (1968)). The objective of the work was to produce a flow model that could predict mean square wall pressure levels from flow properties. The efforts were concentrated in predicting wall pressure levels in the separated region of the flow. Fricke found that the wall pressure fluctuations in subsonic flows can be an order of magnitude higher than for non-separated flows. He found that the source of the wall pressure fluctuations in the separated flow region is in the outer shear layer and not the recirculating flow region. He states that the wall pressures are correlated throughout the separated flow region and are convected downstream at a convection velocity ranging from $0.6U_0$ to $1.0U_0$.

Mabey (1972) provided a review article on wall pressure fluctuations beneath separation bubbles for subsonic flows. He concluded that maximum mean square wall pressure fluctuations always occur in the reattachment region and are fairly insensitive to changes

in Reynolds number for many bubble type separations. Additionally, the frequency spectra near reattachment, when scaled on a frequency parameter based on bubble length, were very similar for all of the bubble type separations reviewed.

Elswick (1975) measured the cross-spectral properties of the wall pressure fluctuations downstream of various types of surface mounted irregularities. The surface irregularities consisted of backward- and forward-facing steps, half round rods and quarter round rods. He found that the cross-spectral properties of the wall pressure field were quite different from those for an unperturbed type of flow.

Vlasov, Ginevskii, Karavosov and Frankfurt (1979) investigated the velocity and wall pressure fluctuations in the flow-separation zone behind a fence type spoiler. An interesting feature of their work is the space-time correlation measurements that were made for the wall pressures and for the streamwise velocity component. They concluded from the correlation measurements that coherent structures exist in the pressure field which persist over relatively large streamwise distances.

Cherry, Hillier and Latour (1984) measured the fluctuating velocity and wall pressure for an unsteady separated and reattaching flow formed by flow over a two-dimensional flat plate with a rectangular leading-edge. The flow separated at the leading edge of the plate and reattached some five plate thickness downstream of the leading edge of the plate. It was shown that, throughout the separated flow region, a low frequency motion could be detected and that this motion was associated with a slow flapping of the shear layer. The wall pressure spectra in the separated flow region had an absence of high frequency energy while downstream of reattachment, the wall pressure spectra were rich in high frequency fluctuations. Overall, the frequencies of the wall pressure fluctuations were found to scale on reattachment length.

Farabee and Casarella (1984, 1985) investigated the wall pressure field upstream and downstream of both forward- and backward-facing steps. It was found that these types of flow perturbations produced large amplitude, low frequency pressure fluctuations. The maximum RMS

wall pressure levels for the forward-facing step were ten times larger than the no-step levels and the backward-facing step levels were five times the no-step levels. At flow reattachment there existed a region of coherent, highly energized, velocity fluctuations located near the wall. Further downstream this energized region decayed in level. Even as far downstream of the backward-facing step as 72 step heights the effects of the separation/reattachment process were still evident in the wall pressure spectra.

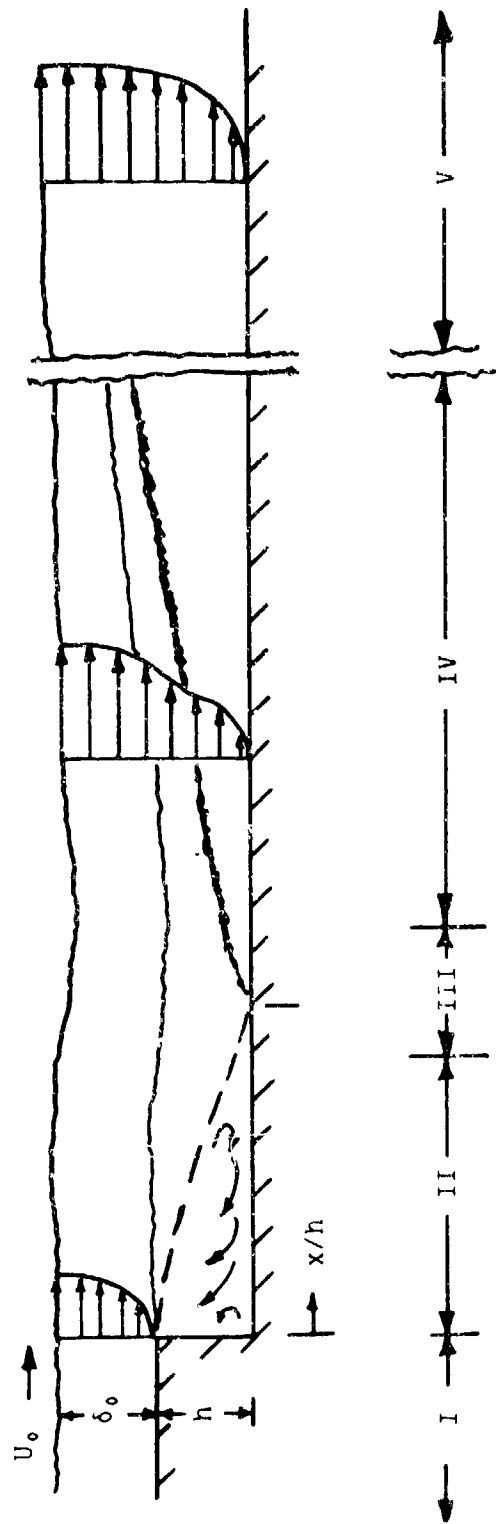
1.3 Objectives of the Research

The objective of this research effort was directed at understanding the mechanisms by which turbulent boundary layers produce wall pressure fluctuations. The overall approach was to study the velocity fluctuations and wall pressure fluctuations for both an equilibrium turbulent flow, for which the relationship between the flow turbulence and the induced wall pressure is partly understood, and for a perturbed, non-equilibrium flow. A non-equilibrium flow is used because it has highly distinct turbulence characteristics which produce unique wall pressures. By evaluating the relationships between the measured velocities and wall pressures, using the techniques developed for equilibrium flow, a better understanding can be obtained of how turbulence velocity activity is related to the unsteady wall pressures. In addition, both the velocity and wall pressure data will greatly add to the limited data base that exists for non-equilibrium flows.

The specific objectives of this study are:

1. To extend the data base by obtaining velocity and wall pressure statistics for an equilibrium flow, and a non-equilibrium flow that undergoes relaxation within the streamwise extent of the measurements.
2. To compare the equilibrium flow velocity statistics to the non-equilibrium flow statistics to determine how the perturbed turbulent boundary layer relaxes back to an equilibrium condition.
3. To evaluate the pressure cross-spectra to determine the distinct regions of the boundary layer that are the major sources of wall pressure.

4. To examine scaling laws for the equilibrium and non-equilibrium wall pressure spectra.
5. To use the measured velocity statistics to estimate regions of the boundary layer that are primary contributors to the wall pressure fluctuations.
6. To examine an analytical model of the wall pressure field, which utilizes the velocity statistics, for comparing the source locations from the data.



ZONES

$x/h < 0$ I - Upstream Equilibrium Turbulent Boundary Layer

$0 < x/h \leq 6$ II - Separated Flow Zone

$6 \leq x/h \leq 8$ III - Reattachment Zone

$8 \leq x/h \leq 100$ IV - Redevelopment Zone

$x/h \geq 100$ V - Downstream Equilibrium Turbulent Boundary Layer

Figure 1.1 Features of the Flow Over a Backward-Facing Step

CHAPTER 2

THEORETICAL FORMULATIONS

In this Chapter various theoretical relationships are developed that will be used in the interpretation and analysis of the experimental data. The first are the statistical functions of turbulence for the velocity and pressure fluctuations. Secondly, the equation for fluctuating pressures in a turbulent flow will be developed. Then, this will be evaluated to obtain an equation for the wall pressure field. Lastly, the specific statistical functions that are measured are described.

2.1 Statistical Functions for Turbulence

Turbulence quantities are random functions of both space and time. This requires that descriptions of turbulence be given in terms of statistical functions of the variables of interest. The variables of primary interest in this study are the pressure and velocity, each given by $p(\vec{x}, t)$ and $\vec{u}(\vec{x}, t)$, respectively, with the velocity being a three component vector ($\vec{u}=(u, v, w)$). The statistical functions that are used in this text to describe the properties of these turbulence quantities are: a) mean-square value (variance), b) covariance, c) (single-point) frequency spectrum, and d) cross-spectral density. The definition of each of these statistical quantities will next be given as well as the relationships between these functions and other statistical functions of turbulence. In depth discussions of statistical functions can be found in Batchelor (1967) for the case of homogeneous turbulence, and in Bendat and Piersol (1971, 1980) for general random functions.

Consider a general random turbulence quantity $q(\vec{x}, t)$. The position vector $\vec{x}=(x, y, z)$ is given by the streamwise component x , the component normal to the wall y , and the lateral (transverse) component z , and is a function of the time variable t . The most general space-time statistical function is the cross-correlation function given as

$$R_{q_1 q_2}(\vec{x}, \vec{x}', t, t') = \langle q_1(\vec{x}, t) q_2(\vec{x}', t') \rangle, \quad (2.1)$$

where the braces indicate an appropriate statistical average (which is a

time average in this study). If $q(\vec{x}, t)$ is a stationary function of time then $R_{q_1 q_2}$ is a function of only the time difference, $\tau = t' - t$, giving

$$R_{q_1 q_2}(\vec{x}, \vec{x}', \tau) = \langle q_1(\vec{x}, t) q_2(\vec{x}', t + \tau) \rangle. \quad (2.2)$$

If $q(\vec{x}, t)$ is homogeneous then $R_{q_1 q_2}$ is not a function of the position vector but a function of only the separation vector $\vec{\xi} = \vec{x}' - \vec{x}$, giving

$$R_{q_1 q_2}(\vec{\xi}, \tau) = \langle q_1(\vec{x}, t) q_2(\vec{x} + \vec{\xi}, t + \tau) \rangle. \quad (2.3)$$

If, additionally $q(\vec{x}, t)$ is isotropic then $R_{q_1 q_2}$ is only a function of the magnitude of the separation vector, $r = |\vec{\xi}|$, giving

$$R_{q_1 q_2}(r, \tau) = \langle q_1(\vec{x}, t) q_2(\vec{x} + \vec{r}, t + \tau) \rangle. \quad (2.4)$$

Equilibrium boundary layer flows are found to be (generally) stationary and homogeneous in planes parallel to the boundary. As such, the cross-correlation of the wall pressure is given by

$$R_{p_1 p_2}(\vec{\xi}, \tau) = \langle p_1(\vec{x}, t) p_2(\vec{x} + \vec{\xi}, t + \tau) \rangle \quad (2.5)$$

where $\vec{\xi} = (\xi, \eta)$ with $\xi = x' - x$ and $\eta = z' - z$. The auto-correlation of the wall pressure field is found by setting $\vec{\xi} = 0$ in equation (2.5),

$$R_{p_1 p_2}(\tau) = \langle p_1(\vec{x}, t) p_2(\vec{x}, t + \tau) \rangle. \quad (2.6)$$

The spatial correlation is given by setting $\tau = 0$ in equation (2.5),

$$R_{p_1 p_2}(\vec{\xi}) = \langle p_1(\vec{x}, t) p_2(\vec{x} + \vec{\xi}, t) \rangle. \quad (2.7)$$

The variance of the wall pressure field is given by setting $\tau = 0$ and $\vec{\xi} = 0$,

$$P_{RMS} = R_{p_1 p_2}(0, 0) = \langle p_1^2(\vec{x}, t) \rangle. \quad (2.8)$$

For the velocity field $\vec{u}(\vec{x}, t)$, the above relationships are similarly defined, except the spatial separation vector is three dimensional and cross-correlations can be formed between different velocity components. The one such cross-correlation that will be used later is the covariance between u and v , given as

$$R_{uv}(y) = R_{uv}(y, 0) = \langle u(y, 0) v(y, 0) \rangle. \quad (2.9)$$

This correlation is also termed the turbulence Reynolds shear stress.

Statistical functions (2.5)-(2.9) are for a stationary and homogeneous random field. The velocity and pressure field downstream of the step are highly non-homogeneous near the step and, as will be shown later, are still non-homogeneous as far downstream as 72 step heights. The downstream velocity and pressure fields are, however, stationary over a long time-average. The inhomogeneity of the fields requires that correlation functions of the form of equation (2.2) be used. The turbulence fields are inhomogeneous in only the streamwise direction allowing the position vectors to be expressed as functions of the streamwise coordinate x/h . In this coordinate system equation (2.2) is

$$R_{q_1 q_2}(x/h, \vec{\xi}, \tau) = \langle q_1(x/h, t) q_2(x/h + \vec{\xi}, t + \tau) \rangle, \quad (2.10)$$

Similarly, the pressure cross-correlation is

$$R_{p_1 p_2}(x/h, \vec{\xi}, \tau) = \langle p_1(x/h, t) p_2(x/h + \vec{\xi}, t + \tau) \rangle, \quad (2.11)$$

and the pressure auto-correlation is

$$R_{p_1 p_2}(x/h, 0, \tau) = \langle p_1(x/h, t) p_2(x/h, 0, \tau) \rangle. \quad (2.12)$$

The variance of the pressure field is not affected by the inhomogeneity, but can be expressed in terms of the $\vec{x}=(x/h, y, z)$ coordinate system as

$$p_{RMS}^2 = \langle p^2(x/h, t) \rangle. \quad (2.13)$$

The cross-correlation provides a complete description of the second-order statistics, expressed in space-time variables, of a random field. Often it is more convenient to describe a random field in terms of spectral variables (\vec{k}, ω) , where \vec{k} is the wavenumber vector and ω is the frequency ($\omega=2\pi f$). Note that the space-time variables (\vec{x}, t) and the wavenumber-frequency variables (\vec{k}, ω) are Fourier pairs. Relationships for the various spectral functions are found as Fourier transforms of the correlation functions given above.

First, consider a stationary and homogeneous random field. The wavenumber-frequency spectrum $\Phi(\vec{k}, \omega)$ of the random field $q(\vec{x}, t)$ is found as

$$\Phi(\vec{k}, \omega) = \frac{1}{(2\pi)^4} \iint_{-\infty}^{\infty} R_{q_1 q_2}(\vec{\xi}, \tau) \exp^{-i(\vec{k} \cdot \vec{\xi} - \omega \tau)} d\vec{\xi} d\tau \quad (2.14)$$

This expresses the wavenumber and frequency distribution of the mean-square of the random field $q(\vec{x}, t)$. The cross-spectral density of $q(\vec{x}, t)$ is found as

$$\Phi(\vec{\xi}, \omega) = \frac{1}{2\pi} \int_{-\infty}^{\infty} R_{q_1 q_2}(\vec{\xi}, \tau) \exp^{i\omega\tau} d\tau \quad (2.15)$$

and the frequency spectrum of q is

$$\Phi(\omega) = \frac{1}{2\pi} \int_{-\infty}^{\infty} R_{q_1 q_2}(\tau) \exp^{i\omega\tau} d\tau \quad (2.16)$$

or

$$\Phi(\omega) = \int_{-\infty}^{\infty} \Phi(\vec{k}, \omega) d\vec{k} = \Phi(\vec{\xi}=0, \omega).$$

Finally, the pressure variance p_{RMS}^2 is given as

$$p_{RMS}^2 = \int_{-\infty}^{\infty} \Phi(\omega) d\omega. \quad (2.17)$$

In the case of a homogeneous pressure field ($\vec{\xi}=(\xi, \eta)$ and $\vec{k}=(k_1, k_2)$)

$$\Phi_p(\vec{k}, \omega) = \frac{1}{(2\pi)^2} \iint_{-\infty}^{\infty} R_{p_1 p_2}(\vec{\xi}, \tau) \exp^{-i(\vec{k} \cdot \vec{\xi} - \omega\tau)} d\vec{\xi} d\tau \quad (2.18)$$

$$\Phi_p(\vec{\xi}, \omega) = \frac{1}{2\pi} \int_{-\infty}^{\infty} R_{p_1 p_2}(\vec{\xi}, \tau) \exp^{i\omega\tau} d\tau, \quad (2.19)$$

$$\Phi_p(\omega) = \frac{1}{2\pi} \int_{-\infty}^{\infty} R_{p_1 p_2}(\tau) \exp^{i\omega\tau} d\tau = \int_{-\infty}^{\infty} \Phi_p(\vec{k}, \omega) d\vec{k} = \Phi_p(\vec{\xi}=0, \omega), \quad (2.20)$$

and

$$p_{RMS}^2 = \int_{-\infty}^{\infty} \Phi_p(\omega) d\omega. \quad (2.21)$$

Equivalent spectral functions for the velocity field exist when expressed for constant values of y . Complete four-dimensional spectral functions for the velocity field are possible since the spatial function is three dimensional.

The wavenumber-frequency spectrum of the inhomogeneous pressure field is not the simple function given by equation (2.18). Romanov (1985) addressed the issue of inhomogeneous (nonuniform) pressure fields and showed that the wavenumber-frequency spectrum is a function of two

wavenumbers in the direction of inhomogeneity. For discussion purposes a "locally" valid wavenumber-frequency spectrum $\Phi'(x/h, \vec{k}, \omega)$ will be defined as

$$\Phi'_p(x/h, \vec{k}, \omega) = \frac{1}{(2\pi)^3} \iint_{-\infty}^{\infty} R_{p_1 p_2}(x/h, \vec{\xi}, \tau) \exp^{-i(\vec{k} \cdot \vec{\xi} - \omega \tau)} d\vec{\xi} d\tau \quad (2.22)$$

Transformation of (2.22) over x/h gives what is essentially the dual wavenumber spectrum of Romanov. The spectral functions that are related to transforms over the stationary variable τ are still valid. These functions are given as,

$$\Phi_p(x/h, \vec{\xi}, \omega) = \frac{1}{2\pi} \int_{-\infty}^{\infty} R_{p_1 p_2}(x/h, \vec{\xi}, \tau) \exp^{i\omega \tau} d\tau \quad (2.23)$$

$$\Phi_p(x/h, \omega) = \frac{1}{2\pi} \int_{-\infty}^{\infty} R_{p_1 p_2}(x/h, \tau) \exp^{i\omega \tau} d\tau \quad (2.24)$$

$$p_{RMS}^2(x/h) = \int_{-\infty}^{\infty} \Phi_p(x/h, \omega) d\omega. \quad (2.25)$$

2.2 Equations for Surface Pressure

2.2.1 Poisson Equation for Pressure

Consider the flow of an incompressible fluid with constant density and viscosity along a smooth surface. The motion of the fluid is governed by the Navier-Stokes and continuity equations,

$$\frac{D\vec{U}}{Dt} = \frac{-1}{\rho} \nabla P + \nu \nabla^2 \vec{U} \quad (2.26)$$

$$\text{and} \quad \nabla \cdot \vec{U} = 0 \quad (2.27)$$

where $D/Dt = (\partial/\partial t + \vec{U} \cdot \nabla)$, $\vec{U} = (U, V, W)$ is the velocity vector, P is the pressure, and ν is the kinematic viscosity of the fluid. The divergence of (2.26) gives

$$\nabla \cdot \partial \vec{U} / \partial t + \nabla \cdot (\vec{U} \cdot \nabla) \vec{U} = - \frac{1}{\rho} \nabla^2 P + \nu \nabla \cdot \nabla^2 \vec{U} \quad (2.28)$$

The order of operations in the first term can be switched and thus set equal to zero from (2.27). Next consider the last term in (2.28).

Expand the Laplacian as

$$\nabla \cdot (\nabla^2 \vec{U}) = \nabla \cdot [\nabla(\nabla \cdot \vec{U}) - \nabla \times (\nabla \times \vec{U})]$$

The first term is zero due to continuity and the second term will be identically zero since it is the divergence of the curl of a vector. Consequently, (2.28) is now

$$\nabla \cdot (\vec{U} \cdot \nabla) \vec{U} = - \frac{1}{\rho} \nabla^2 P$$

which can be written

$$\nabla^2 P = -\rho \partial^2 (U_i U_j) / \partial x_i \partial x_j \quad (2.29)$$

If the terms on the right-hand-side are considered to be known then (2.29) is a Poisson equation for the total pressure. Note that the pressure is produced exclusively by inertial forces of the turbulence flow.

To obtain an equation for the fluctuating pressures introduce a Reynolds decomposition for the variables in (2.29). That is, assume the pressure and velocity are the sum of a mean and a fluctuating term, given as

$$\vec{U} = \vec{\bar{U}} + \vec{u}'$$

$$\text{and} \quad P = P_0 + p'.$$

With these substituted into equation (2.29) we have

$$\nabla^2 P_0 + \nabla^2 p' = -\rho \partial^2 [\bar{U}_i \bar{U}_j + \bar{U}_i u'_j + u'_i \bar{U}_j + u'_i u'_j] / \partial x_i \partial x_j \quad (2.30)$$

To eliminate $\nabla^2 P_0$, average (2.30) over time, to get a mean value equation, and replace $\nabla^2 P_0$ with this equation. In averaging (2.30) the terms that are linear in fluctuation go to zero leaving

$$\nabla^2 P_0 = -\rho \partial^2 [\bar{U}_i \bar{U}_j + \overline{u'_i u'_j}] / \partial x_i \partial x_j. \quad (2.31)$$

Now replace $\nabla^2 P_0$ in (2.30) with (2.31) to get

$$\nabla^2 p' = -\rho \partial^2 [2\bar{U}_i u'_j + \overline{u'_i u'_j} - \overline{u'_i u'_j}] / \partial x_i \partial x_j. \quad (2.32)$$

With (2.27)

$$\partial^2 [2\bar{U}_i u'_j] / \partial x_i \partial x_j = 2 \frac{\partial \bar{U}_j}{\partial x_j} \frac{\partial u'_i}{\partial x_i}$$

which upon substitution into (2.32) gives

$$\nabla^2 p' = -\rho [2 \frac{\partial \bar{U}_j}{\partial x_j} \frac{\partial u'_i}{\partial x_i} - \partial^2 (u'_i u'_j - \overline{u'_i u'_j}) / \partial x_i \partial x_j].$$

For boundary layer flows, it is assumed that

$$U_1 = (U(y), 0, 0)$$

and $u'_1 = (u, v, w)$

giving, finally

$$\nabla^2 p' = -\rho \left[2 \frac{\partial U}{\partial y} \frac{\partial v}{\partial x} - \partial^2 (u_i u_j - \overline{u_i u_j}) / \partial x_i \partial x_j \right]. \quad (2.33)$$

Again, if the terms on the right-hand-side of (2.33) are taken to be known source terms, then (2.33) is a Poisson equation for the fluctuating pressures in a boundary layer flow.

The first source term in (2.33), $2[(\partial U / \partial y)(\partial v / \partial x)]$, results from interaction of the mean shear gradient $(\partial U / \partial y)$ with turbulence $(\partial v / \partial x)$ in the flow. This source term is called the mean shear-turbulence term. The remaining terms result from interactions of turbulence with turbulence and are termed the turbulence-turbulence source terms. Most estimates place the contributions from the turbulence-turbulence terms at less than 6% of the mean-square value of the pressure, and as such, most analyses drop these terms and consider only the mean shear-turbulence term.

2.2.2 Solutions to Poisson Equation for Wall Pressure

The solution to equation (2.33) on the wall is not a difficult mathematical problem, as will be shown. However, quantitative results are limited by the extent of knowledge that exists for the source terms. Unfortunately, these terms are not well understood and are generally modeled using somewhat limited empirical information. Irrespective of these issues, the solution of (2.33) provides good qualitative insight as to what regions of the boundary layer contribute to the generation of wall pressure fluctuations.

Two different approaches to solving equation (2.33) have been followed in the literature. The first approach obtains an equation for the pressure as a function of space-time variables while the second approach obtains the pressure as a function of the spectral variables, wavenumber and frequency. If one is interested in, say, the mean-square pressure or the pressure cross-correlation, then the former development would be preferred. But, if interest is in spectral descriptions of the

pressure field, then the latter development is preferred. Both equations form a set that are Fourier pairs.

Since we seek spectral functions of the wall pressure field, the solution to (2.33) in terms of spectral variables is needed. However, it is informative to initially review the solution to (2.33) in terms of (physical) space-time variables.

For convenience, collectively write the source terms as a source density $q(\vec{x}, t)$ and drop the prime on the pressure (since fluctuating pressures are implied). With this (2.33) becomes

$$\nabla^2 p(\vec{x}, t) \Big|_{y=0} = -q(\vec{x}, t). \quad (2.34)$$

The solution to (2.34) is obtained by using an appropriate Green's function which satisfies the boundary conditions. This has been discussed in detail by Kraichnan (1956), Lilley and Hodgson (1960), and Meecham and Tavis (1980). Details of the solution to (2.34), following this approach, will not be given except to note that difficulties arise in evaluating the boundary conditions for the pressure and that this problem will also arise following the spectral approach. The solution to (2.34) for the pressure at the wall is (Lilley and Hodgson (1960))

$$p(\vec{x}, t) \Big|_{y=0} = \frac{1}{2\pi} \int_{y>0} \frac{q(\vec{r}, t)}{|\vec{x} - \vec{r}|} d\vec{r} \quad (2.35)$$

where \vec{r} is a dummy position vector in the half space above the plate (bounded by $y=0$). Equation (2.35) shows that contributions to the wall pressure come from all regions of the boundary layer but that contributions are weighted by the $|\vec{x} - \vec{r}|$ term which diminishes contributions far from the measurement point $\vec{x}=(x, 0, z)$. Equation (2.35) does not show explicitly the relative importance of the frequency content of the source terms. This is provided by the spectral approach.

Solutions to (2.33) in terms of spectral variables have been obtained by Kraichnan (1956), Panton and Linebarger (1974), and Chase (1980). Additionally, Blake (1984) provides an extensive review of the research that has been done to date on the subject of wall pressure fluctuations (as well as general hydro- and aero-acoustics research). The procedures for solving (2.33) will now be reviewed.

Consider (2.34) to be a governing equation and recall that $\vec{x}=(x,y,z)$, where for a constant value of y , x and z form a plane parallel to the surface. With the assumption that the flow is homogeneous in planes parallel to the surface, (2.34) can be Fourier transformed over the spatial variables in the x and z directions. Assuming that the flow is stationary, (2.34) can be Fourier transformed over time to get a governing equation that is a function of frequency. After these (three) Fourier transformations of equation (2.34) we have

$$\nabla^2 \hat{p} = \hat{Q} \quad (2.36)$$

where

$$\hat{p} = p(k_1, k_3, y, \omega) = \frac{1}{(2\pi)^3} \iiint_0^\infty p(\vec{x}, t) e^{-(k_1 x + k_3 z - \omega t)} dx dz dt \quad (2.37)$$

and

$$\hat{Q} = \hat{Q}(k_1, k_3, y, \omega) = \frac{1}{(2\pi)^3} \iiint_0^\infty q(\vec{x}, t) e^{-i(k_1 x + k_3 z - \omega t)} dx dz dt \quad (2.38)$$

which are the associated time-planar Fourier transforms of the wall pressure and source terms. These transformations model the source terms as wave-like structures in planes that are parallel to the surface. The requirement that the source terms (as well as pressure) be homogeneous in planes parallel to the surface is generally valid for equilibrium flows in which the boundary layer growth is slow. However, this condition is not met for the non-homogeneous flow downstream of a step. The consequences of a streamwise inhomogeneity will depend on the severity of the inhomogeneity. It will be assumed that discussions of pressure source terms are still valid for the flow downstream of a step.

Expand the Laplacian of \hat{p} to get

$$\nabla^2 \hat{p} = -K^2 \hat{p} + \partial^2 \hat{p} / \partial y^2 \quad (2.39)$$

where $K^2 = k_1^2 + k_3^2$. With this equation (2.36) becomes

$$\partial^2 \hat{p} / \partial y^2 - K^2 \hat{p} = -\hat{Q}. \quad (2.40)$$

Equation (2.40) is a linear, inhomogeneous, ordinary differential equation with constant coefficients. A solution to (2.40) is readily written as

$$\hat{p}(\vec{k}, y, \omega) = A_1 e^{Ky} + B_1 e^{-Ky} + \frac{1}{K} \int_{y' > 0} e^{-K|y'-y|} \hat{Q}(\vec{k}, y', \omega) dy' \quad (2.41)$$

where $\vec{k} = (k_1, k_2)$.

The pressure must remain bounded requiring that $A_1 = 0$. The value of B_1 is obtained by evaluating the normal derivative of the pressure at the wall. For the moment it will be said that, to first approximation, the normal gradient of pressure at the wall is zero, giving $B_1 = 0$. Equation (2.41), evaluated at the surface, is thus given as

$$\hat{p}(\vec{k}, 0, \omega) = \frac{1}{K} \int_{y > 0} e^{-Ky} \hat{Q}(\vec{k}, y, \omega) dy. \quad (2.42)$$

With regard to the second boundary condition, Kraichnan (1956) estimated the contributions to the wall pressure fluctuations that would come from this term and determined that it would be small enough to neglect. He pointed out that this term is equivalent to a surface dipole oriented in the plane of the surface. Meecham and Tavis (1980) also estimated the contributions that would come from this term, which they explicitly called a drag term (dipole), and found it to be negligible. Recently, Haj Hariri and Akylas (1985) re-addressed this question and found that except for the very lowest wavenumbers this term is negligible.

Equation (2.42) gives the fluctuating wall pressure as a function of wavenumber and frequency. The quantity that is of interest is the pressure spectral density. Using the relationship (Dowling and Ffowcs-Williams (1983))

$$\Phi_p(\vec{k}, \omega) = \langle \hat{p}^*(\vec{k}, 0, \omega) \hat{p}(\vec{k}', 0, \omega') \rangle / [\delta(\vec{k}' - \vec{k}) \delta(\omega' - \omega)] \quad (2.43)$$

where $\Phi_p(\vec{k}, \omega)$ is the pressure spectral density, \hat{p}^* is the complex conjugate of \hat{p} and $\delta(\vec{k}' - \vec{k})$ is the Dirac delta function, the pressure spectral density can be written as

$$\Phi_p(\vec{k}, \omega) = \frac{1}{K^2} \iint_0^\infty e^{-(K(y+y'))} \hat{Q}^*(\vec{k}, y, \omega) \hat{Q}(\vec{k}, y', \omega) dy dy'. \quad (2.44)$$

For discussion purposes it will now be assumed that the mean shear-turbulence term is dominant, allowing the turbulence-turbulence term to be dropped. With this assumption the source density $q(\vec{x}, t)$ is given as

$$q_{\text{mst}}(\vec{x}, t) = 2 \rho \frac{\partial U}{\partial y} \frac{\partial v}{\partial x} \quad (2.45)$$

which has a time-planar Fourier transform

$$\hat{Q}_{\text{mst}}(\vec{k}, y, \omega) = 2 \rho \frac{\partial U}{\partial y} k_1 \hat{v}(\vec{k}, y, \omega) \quad (2.46)$$

where $\hat{v}(\vec{k}, y, \omega)$ is the time-planar Fourier transform of the fluctuating normal velocity (again $\vec{k}=(k_1, k_2)$). Introducing (2.46) into (2.44) gives

$$\Phi_p(\vec{k}, \omega) = 4 \rho^2 (k_1/K)^2 \iint_0^\infty e^{-K(y+y')} \frac{\partial U}{\partial y} \frac{\partial U}{\partial y'} \Phi_v(\vec{k}, \omega, y, y') dy dy' \quad (2.47)$$

where $\Phi_v(\vec{k}, \omega, y, y')$ is the cross-spectral density of the normal component of fluctuating velocity between wall planes y and y' . If the source terms were homogeneous in all the spatial directions then a complete (four-dimensional) Fourier transform could have been performed and then the wall pressure spectral density would be found by integrating over the spatial Fourier component normal to the wall.

In review, the approximations that have been made leading to (2.47) are: 1) incompressible flow, 2) constant viscosity and density fluid, 3) boundary layer approximations, 4) normal gradient of pressure is zero at the wall, 5) turbulence is stationary, and 6) turbulence is homogeneous in planes parallel to the surface. One final approximation that will further simplify the use of (2.47) is that the velocity cross-spectrum can be approximated as being equal to a planar spectral density times a vertical correlation term,

$$\Phi_v(\vec{k}, \omega, y, y') = \Phi_v(\vec{k}, \omega, y) R_2(y; y-y') \quad (2.48)$$

where $R_2(y; y-y')$ expresses the correlation of the turbulence eddies at location y to those at location y' . Introducing (2.48) into (2.47) gives

$$\begin{aligned} \Phi_p(\vec{k}, \omega) = 4 \rho^2 (k_1/K)^2 \iint_0^\infty e^{-K(y+y')} \frac{\partial U}{\partial y} \frac{\partial U}{\partial y'} \\ \times R_2(y; y-y') \Phi_v(\vec{k}, \omega, y) dy dy'. \end{aligned} \quad (2.49)$$

Equation (2.49) is the final solution to the Poisson equation for pressure with which we will work. It expresses the wavenumber-frequency spectrum as a function of the fluctuating velocity field. The pressure

cross-spectral density is obtained from (2.49) by

$$\phi_p(\vec{k}, \omega) = \int_{-\infty}^{\infty} \phi_p(\vec{k}, \omega) e^{i(\vec{k} \cdot \vec{\xi})} d\vec{\xi} \quad (2.50)$$

and the frequency spectral density is obtained by

$$\phi_p(\omega) = \int_{-\infty}^{\infty} \phi_p(\vec{k}, \omega) d\vec{k}. \quad (2.51)$$

2.2.3 Source Term Identification

Equation (2.49) is quite formidable; the pressure spectral density is equal to a double integral over the y spatial coordinate of the planar cross-spectral density of the vertical velocity component, between wall distances y and y'. To date, solutions to (2.49) have been obtained only for highly idealized estimates of the velocity cross-spectrum. These solutions do reflect the salient features of the pressure spectrum, particularly in the region of convective wavenumbers ($k_1 \approx \omega/U_0$).

What can be readily obtained from (2.49) is an idea of what regions of the flow field are major contributors to the wall pressure fluctuations. Consider the velocity cross-spectrum to be a density function that describes the distribution of turbulent eddies (size, speed and magnitude) throughout the boundary layer, then the remaining terms within the integral are weighting functions which determine the impact these eddies will have at the wall.

The first term within the integral is an exponential, attenuation function. For a given wavenumber disturbance K the pressure is obtained from regions of the flow field $y < K^{-1}$. High wavenumber components must originate from velocity structure near the wall while low wavenumber components can result from structure further out in the flow. The next terms are the mean velocity gradient which are not a function of the spectral variables (\vec{k}, ω). In the viscous sublayer these terms are constant ($\partial U / \partial y \approx u_*^2 / \nu$); in the log-law region these terms are proportional to y^{-1} , and in the outer layer these terms are small. The third term represents the vertical distance over which an eddy is correlated. Blake (1984) approximates this to be equal to the integral

scale of the vertical velocity fluctuations which is roughly equal to the distance the eddy is from the wall. The last term within the integral is the eddy density distribution function. A final term that bears some significance is the (k_1/K) term in front of the integral. This term increases the contributions from the k_1 fluctuations and results in the pressure cross-spectrum having smaller streamwise length scales than transverse length scales.

In the previous Chapter a general review of studies dealing with wall pressure fluctuations was given. Of the studies cited, the following specifically address the issue of modeling wall pressure fluctuations from velocity statistics: 1) Kraichnan (1956), 2) Lilley and Hodgson (1960), 3) Panton and Linebarger (1974), 4) Chase (1980), 5) Meecham and Tavis (1980), and 6) Blake (1984).

2.3 Measured Statistical Functions

Many types of statistical functions have been discussed in this Chapter. It is not possible, in a realistic sense, to measure all of these functions. The difficulty in measuring a statistical function increases geometrically with the order of the function. The highest order statistical function that is measured in this work is the two-dimensional cross-spectral density of the wall pressure fluctuations (3-dimensional function (ξ, ω)). The statistical functions of the wall pressure fluctuations and velocity fluctuations that are measured will be discussed.

Measurements were made of both the mean and fluctuating components of the streamwise and normal velocities. The mean and root-mean-square values of each component were obtained. These are given as

$$U = \langle u(t) \rangle \quad (2.52a)$$

$$V = \langle v(t) \rangle \quad (2.52b)$$

$$\text{and} \quad u' = \sqrt{\langle u^2(t) \rangle} \quad (2.53a)$$

$$v' = \sqrt{\langle v^2(t) \rangle} \quad (2.53b)$$

where the capital letters denote mean values and the primes denote root-mean-square values. The braces are a time average and $u(t)$ and $v(t)$ are, respectively, the instantaneous streamwise and normal components of

velocity. Additionally the turbulence Reynolds stress $\overline{u'v'}$ was obtained, where

$$\overline{u'v'} = \langle u'(t)v'(t) \rangle. \quad (2.54)$$

The frequency spectral density of each velocity component was obtained ($\phi_u(\omega)$ and $\phi_v(\omega)$). Values of u' and v' were also calculated by integrating the associated frequency spectrum using (2.21).

Cross-spectral density measurements were made of the fluctuating wall pressures. Generally, the pressure cross-spectrum is denoted by $\phi_p(\omega, \xi)$ where $\xi = (\xi, \eta)$ is the separation vector between measurement positions. Experimentally $\phi_p(\omega, \xi)$ was obtained by assuming a separability between the streamwise and transverse components of the cross-spectrum. This is expressed as $\phi_p(\omega, \xi) = \phi_p(\omega, \xi) * \phi_p(\omega, \eta)$ where $\phi_p(\omega, \xi)$ is the streamwise cross-spectrum and $\phi_p(\omega, \eta)$ is the transverse cross-spectrum. In addition to the cross-spectrum, the frequency spectrum, $\phi_p(x/h, \omega)$, was also obtained at each measurement position. The cross-spectra for the non-equilibrium flow are also functions of the streamwise coordinate x/h . This dependence has not been explicitly shown to simplify the nomenclature. Root-mean-square values of the pressure, $p_{RMS}(x/h)$, were calculate at each measurement location using (2.21).

The cross-spectral density is a complex function for a convecting field. As such, the pressure cross-spectrum is expressed in terms of a normalized magnitude $\Gamma(\omega, \xi)$ and a phase $\theta(\omega, \xi)$. The normalized magnitude that is used is given as

$$\Gamma_p(\omega, \xi) = \sqrt{\frac{\phi_p^*(\omega, \xi) \phi_p(\omega, \xi)}{\phi_{p_1}(\omega) \phi_{p_2}(\omega)}} \quad (2.55)$$

and is referred to in the literature as the coherence function (Bendat and Piersol (1971, 1980)). The phase function is given as

$$\theta(\omega, \xi) = \tan^{-1} \left[\frac{I_m(\phi_p(\omega, \xi))}{R_e(\phi_p(\omega, \xi))} \right] \quad (2.56)$$

where R_e and I_m mean the real and imaginary parts of the cross-spectrum.

For a propagating, or convecting, field the phase of the (narrow-band) cross-spectrum has been shown (Blake (1984)) to be proportional to the convective speed $U_c(\omega, \xi)$ of the field. The relationship between measured phase and convection velocity is given as

$$U_c(\omega, \xi) = \omega \xi / \theta(\omega, \xi). \quad (2.57)$$

In review, for the velocity field the following measurements were obtained: 1) mean velocity U , 2) root-mean-square velocities (variances) u' and v' , 3) turbulence Reynolds stress $\overline{u'v'}$, and 4) velocity frequency spectra $\Phi_u(\omega)$ and $\Phi_v(\omega)$. For the pressure field the following measurements were made: 1) root-mean-square (variance) p_{RMS} , 2) pressure frequency spectrum $\Phi_p(\omega)$, and 3) the pressure cross-spectrum $\Phi_p(\omega, \xi)$ expressed in terms of the coherence $\Gamma(\omega, \xi)$ and the convection velocity $U_c(\omega, \xi)$. The coherence for both the streamwise and transverse cross-spectra was obtained. The details of measuring these statistics will be given in Chapter 3.

CHAPTER 3

EXPERIMENTAL ARRANGEMENT AND METHODOLOGY

3.1 Wind Tunnel

This first phase of this investigation was to refurbish the wind tunnel to provide a facility in which boundary layer flow noise measurements could be made. Such a facility must have low background acoustic noise levels, a low freestream turbulence intensity level, low levels of facility vibration, and a fully developed turbulent boundary layer flow along its test wall. Originally the wind tunnel was a non-return flow facility driven by an axial fan located at the tunnel exit. This configuration was excessively noisy, and there were serious concerns about the boundary layers that developed along the walls of the tunnel. During the refurbishing the only components of the original facility that were kept were the turbulence management screens and the electric drive motor and controller.

3.1.1 Construction Details

Figure 3.1 shows a schematic of the refurbished facility. The major design features of the facility are: 1) a turbulence management section located at the tunnel inlet, 2) a contraction section with an area contraction ratio of 16:1 that occurs over a distance of 10 feet, 3) a 2x2 ft test section that is 8-ft long, 4) a small angle (7°) diffuser section that is acoustically treated, 5) in-line acoustic mufflers located upstream and downstream of the blower, 6) a low speed centrifugal blower driven with a pulley arrangement by a 20 hp dc motor, and 7) ducting of the exhaust flow back into the wind tunnel room allowing an open loop recirculation of the flow.

The turbulence management section consisted of 6-inch thick honeycomb followed by four bronze screens and then followed by 2 cheese cloth screens. The screens are stretched tight on wooden frames and are spaced at approximately 3-inch intervals. The first screen is located approximately 3-inches downstream of the end of the honeycomb. The inside faces of the screen frames were kept as smooth as possible to minimize flow disturbances. A metal screen was placed at the very inlet of the tunnel to act as a filter for any possible airborne trash.

The contraction section was especially designed to provide a gradual acceleration of the flow preventing regions of local separation. Figure 3.2 shows a diagram of the contraction section and includes measurements of the static pressure distribution obtained along one wall of the contraction section. The contraction section was made from sections of thick steel plate that were rolled to a specified contour and then welded together at the four corners to form the rectangular cross section. Both vertical walls were made from a single sheet of steel. The top and bottom were made from a sheet of steel formed by welding together two pieces of steel that were side pieces left over from the pattern used to obtain the two wall pieces. Circumferential frames, spaced at approximately 3-ft intervals, were welded around the outside of the contraction section to reduce low frequency drumming. After receiving the contraction section from the manufacturer extensive grinding, filling with body filler, and sanding were done to obtain a very smooth and continuous finish to the inside of the contraction section. Special care was given to the test wall side of the contraction.

The test section is an 8-ft long 2x2 ft square rectangular section. All pieces of the test section are made removable allowing a high degree of flexibility in test configuration. The wall opposite the test wall is made from a continuous sheet of 5/8-inch thick Plexiglas which allows viewing of the experiment. The floor is constructed from three sections of 3/4-inch Plexiglas. The center section of the floor was removed and replaced by the hot wire traverse mechanism when velocity measurements were being made. The roof consists of 5 sections of 3/4-inch Plexiglas. Access to inside the tunnel is gained by removing one of the two large roof sections. All hardware attaching the Plexiglas pieces to the tunnel frame are located outside the tunnel circuit to minimize flow disturbances. The inside corners and joints between pieces are filled with modeling clay to reduce leaks that can produce loss in flow speed and background noise. The test wall is described in detail in a later section.

The diffuser section has a square cross-section with an expansion angle of 7-degrees. It is constructed from #11 gauge perforated steel sheet (1/8-inch holes, 3/16-inch staggered spacing) backed by 4-inch Fiberglas duct lining (40% porosity). This is encased in a sealed wood casing to prevent air leaks. The objective of the Fiberglas backed perforated metal is to reduce acoustic noise. The diffuser exits out of the wind tunnel room, through a cinder block wall, into an adjoining room that housed the blower and motor assembly. A section of 6-inch thick honey-comb is placed at the very end of the diffuser section.

In-line acoustic mufflers are placed upstream and downstream of the blower. The mufflers are 52-inch square and 6-ft long and are commercially available products (Aeroacoustic Fan Silencer). They are placed in the tunnel circuit to help minimize acoustic noise.

The upstream muffler is soft coupled to the blower inlet. Similarly the blower outlet is soft coupled to the right-angle turning vanes. The blower and motor assembly are mounted as a unit to a pad which is isolation mounted to a concrete pad by large springs. The blower and motor were isolation mounted and located in a separate room to help minimize acoustic noise and vibration coupling to the tunnel circuit.

The blower is a 16 blade, low speed, up-draft centrifugal blower built by Buffalo Forge Corporation. It is driven by a 20 hp dc motor by a multiple pulley belt arrangement. Motor speed is controlled by a SCR feedback system located in the motor room with a hand held control box located near the tunnel test section (recently, a 25 hp motor and a new controller were installed which provides stable operation at lower speeds).

The air that is drawn through the tunnel is exhausted into the tunnel room allowing for continued recirculation of the tunnel room air. This greatly reduces the time it takes for the air temperature to stabilize and allows the tunnel room to be closed during tunnel operations.

3.1.2 Test Wall

The test wall consists of a fixed upstream section and a removable downstream section. The upstream wall is constructed from a single 3-ft piece of 1/2-inch thick aluminum plate that is securely bolted to the tunnel frame using 1-inch thick spacers. The inside surface was carefully polished to give a very smooth finish. The downstream edge was milled to provide a square edge. This edge formed the backward facing step. Figure 3.3 shows a diagram of the test wall section along with some of the geometry used to describe transducer locations.

Two different downstream test plates were used. For the equilibrium flow study, the wood plate used in the study of Farabee and Casarella (1984) was used. This plate has a mahogany surface backed by plywood. It was mounted flush with the aluminum plate with the smooth mahogany surface facing the flow. The joint between the two plates was filled using a polyester body filler compound that was sanded smooth. The transducer holes that existed in the plate from the earlier study were used for the equilibrium flow study. This arrangement located the pressure measurements at a position six inches downstream of the edge of the aluminum plate.

The downstream plate for the backward-facing step work was constructed from a piece of 1/2-inch thick particle board covered on both sides by a thick laminate of hard plastic veneer. This plate overlapped behind the aluminum plate to give a 1/2-inch step. The 1/2-inch step was carefully maintained downstream by using spacers between the test plate and the tunnel frame. An 8:1 up ramp was placed at the end of the test plate to return to the 2x2 ft dimension at the start of the diffuser section.

The veneer covering was selected since it provided a hard durable surface that could easily be drilled and sanded and still be made to have a smooth surface. All of the pressure transducer holes (in excess of 100) were pre-drilled in the test plate prior to installing the plate in the tunnel. This included the holes for the desired streamwise separations at each of the six downstream (cluster) positions as well as the holes for the transverse separations at each of these streamwise locations. Initially, all of these holes were immediately filled with

polyester body filler and sanded smooth. A final thin covering with a lacquer based putty was applied to the holes and this was sanded smooth using crocus cloth to yield a very smooth finish. The plate surface was then polished using a hard paste automotive wax. Before each hole was used for a measurement of the wall pressure the putty filler was carefully drilled out and the plate surface was again polished to ensure that the surface was smooth.

After measurements at a particular location were completed the open transducer hole was again filled and smoothed in the same manner as described above. In order to minimize the time spent filling and smoothing transducer holes, the measurements were made at the most downstream positions first and then progressed upstream. The previously used holes were temporarily covered with a small piece of transparent tape. At the end of each set of measurements the pieces of tape were removed and all open holes were again filled and smoothed. At all times extensive care was taken to prevent wall disturbances associated with flow over the many transducer holes in the wall.

3.1.3 Performance Characteristics

The objective in refurbishing the wind tunnel was to obtain a facility in which boundary layer related hydro-acoustic research could be performed. In order to perform such work a fully developed equilibrium turbulent boundary layer was needed in a low noise (acoustic), low turbulence intensity facility. These objectives were met as discussed below and will be shown in more detail in Chapters 4 and 5. Additional discussions on the facility performance are also given by Hasan, Casarella and Rood (1985).

In order to obtain fully developed turbulent flow at the start of the test section, two boundary layer trips were used. Each trip consisted of a piece of 0.032-inch diameter wire (piano wire) glued to the wall of the contraction section. One wire was located 2-ft 11-inch upstream of the start of the test section and the other wire was located 1-ft upstream of the start of the test section. The latter trip is located 375 trip heights upstream of the start of the test section and 1500 trip heights upstream of the step. The fully developed character

of the boundary layer along the test wall and its consistency with the classical flat plate data will be described in Chapter 4.

The acoustic performance of the tunnel is good above 50 Hz. Figure 3.4 shows a comparison of a wall pressure spectrum with a pressure spectrum measured using a 1/2-inch nose cone microphone located in the center of the tunnel test section. Clearly the wall pressure spectrum below 50 Hz is contaminated by facility noise which is also picked up by the freestream microphone. The source of this noise is not known but it is low enough in frequency not to be a major concern in this study. Also shown in figure 3.4 is a wall pressure spectrum obtained with a flush-mounted microphone that is covered over with a thin piece of flat stock. This blocks the transducer from responding to hydrodynamic pressures and gives a direct measure of the vibration induced response of the microphone. The vibration induced levels are well below those produced by the pressure fluctuations. Hence, above 50 Hz the facility is considered to be a low noise facility. All wall pressure data below 50 Hz are discarded.

The free-stream turbulence intensity in the tunnel is less than 0.2% over a wide range of flow speeds. This is documented in the turbulence intensity profiles given in Chapter 4 and in Hasan et al. (1985).

Tunnel speed was monitored by measuring the pressure drop between a ring of static taps located at the start of the contraction section and a ring located 6-inches upstream of the start of the test section. The pressure drop was measured using a 1-psi range (CGS) electronic manometer. This pressure drop was calibrated against the pressure drop measured with a pitot tube located along the tunnel centerline to provide a simple relationship that could be used to determine tunnel speed from the contraction section pressure drop. During the experiments the tunnel was run at constant values of dynamic head. Hence, the specific speed for nominally the same runs varied slightly, but the actual speeds were accounted for in all analyses.

3.2 Pressure Measurements

In order to minimize spatial averaging effects, wall pressure measurements were made using a flush-mounted pinhole microphone. This technique is commonly used to obtain wall pressure measurements for high Reynolds number flows (Blake (1970)). The pinhole microphone system provides a high sensitivity transducer that has a relatively small sensing area.

The microphone is a Bruel and Kjaer (B&K) Model 4138, 1/8-inch condenser microphone. The pinhole arrangement is obtained by replacing the standard protective cap with a blank cap in which a 1/32-inch diameter hole has been drilled in the center. The blank caps are obtained from B&K with the 1/32-inch diameter hole already drilled in them (machining hole for cutting the screw threads that hold the cap onto the microphone cartridge). The microphone and cap assembly are mounted flush to the test wall giving a wall pressure transducer that has a 1/32-inch diameter active sensing area.

The free-field acoustic response of a 1/8-inch microphone is nominally flat out to 80 KHz. However, the pinhole cap and microphone assembly form a Helmholtz resonator which greatly reduces the flat response range of the pinhole microphone. Using the physical dimensions quoted by the manufacturer for the 1/8-inch microphone and protective cap, the frequency of the Helmholtz resonance was calculated to be approximately 26 KHz for a 1/32-inch pinhole cap arrangement. This frequency is very sensitive to the enclosed volume which depends on how far the blank cap screws onto the microphone cartridge. A comparison calibration was performed and showed that the Helmholtz frequency occurred at approximately 25 KHz. Wall pressure measurements are thus limited to frequencies below 25 KHz. Wall pressure data above 20 KHz is not shown. As will be shown later, even with a 1/32-inch diameter sensing area, at the Reynolds numbers of the current experiments, spatial averaging by the transducer is a problem for the higher frequency data (above 10 KHz).

Figure 3-5 shows a block diagram of the complete microphone system. The 1/8-inch microphones are connected to Model 2633 preamplifiers using Model UA160 (and UA0160) 1/8-inch to 1/4-inch adapters. The

preamplifiers are powered by either Model 2803 (ac powered) or Model 2804 (dc powered) power supplies. The fluctuating pressure signals are amplified using Ithaco Model 451 post amplifiers that have switch selective high-pass filters. The amplified and filtered signals were monitored on an oscilloscope while on line spectral analysis was performed using a Nicolet Scientific Corporation Model 660A Dual Channel FFT Analyzer. For selected runs pressure data were recorded on a Lockheed Store 4D 1/4-inch tape recorder using FM electronics with a 20 KHz bandwidth.

The closest spacing that can be obtained between transducers is limited by the diameters of the microphone preamplifiers. Model 2633 preamplifiers are 1/4-inch in diameter which fixed the smallest spatial separation at 1/4-inch. A smaller preamplifier is not commercially available.

The sensitivity of the transducer systems were measured at the start and end of each day, and after major changes, using a B&K Model 4220 Pistonphone. There was little change in sensitivity for a given system. The sensitivities measured each day were used to calculate the pressure levels. Nominal sensitivities for the pressure transducers were approximately -181 dB re 1v/ μ Pa. Phase differences between transducer channels were found to be negligible for signals introduced to the input section of the power supplies. Phase differences arising in the transducer and preamps are not thought to be a serious problem, which is partly supported by the nearly zero phase angles measured for the transverse separation data.

Special microphone holders were machined from a resilient plastic material. The holders had a wide flange at one end that sat flat on the back of the test plate keeping the microphone at a right angle to the plate thus ensuring a flush fit between the microphone face and the test plate. Plastic set screws in the plastic holders held the microphones in place once correctly positioned. A track arrangement attached to the back of the test plate allowed the holders to be clamped in place at any location. The microphones were made flush to the flow surface by first extending the microphones out slightly (into the flow if the tunnel were

on) and then using the thin edge of a piece of feeler gauge material to push it back flush with the surface. The set screws were then lightly tightened to hold the microphone in place. If a seam would be felt between the blank cap and the adjacent test plate, clay was carefully placed around the (1/8-inch diameter) seam to give a completely smooth surface. Most positions required the use of the clay filler. When not being used, the microphones were kept in a sealed can containing silica gel to prevent possible moisture problems with the microphones.

Figure 3.6 shows a plan view of the test plate which illustrates some of the nomenclature used for the pressure measurements. There are six primary measurement positions downstream of the step ($x/h = 10, 16, 24, 36, 54$ and 72). At each of these primary positions 17 streamwise pressure transducer holes were pre-drilled and a series of 10 holes along a lateral line were pre-drilled. The streamwise holes gave streamwise transducer separations ranging from 1/4-inch to 24-inch and the lateral holes gave transverse separations that ranged from 1/4-inch to 4-inch. During the course of a set of measurements, at a given cluster position, the upstream pressure transducer was kept fixed at the specified x/h position ($x=0$) and the downstream transducer was sequentially moved from hole-to-hole to obtain the described streamwise separation, ξ . After all the streamwise data was measured the procedure was repeated but with the second transducer placed in the holes along the transverse line to get the desired transverse separations, η . At each cluster position (x/h) there is a whole series of measurements with varying streamwise separation, ξ , and a whole series with varying transverse separations η . The maximum separation that could be obtained at cluster positions $x/h > 36$ was limited by the length of the tunnel. At $x/h = 72$ the maximum streamwise separation was limited to $\xi = 2$ -inch.

A similar procedure was used for the equilibrium flow pressure measurements. For these measurements there was only one cluster position, located six inches downstream of the interface between the aluminum and the wood test plates, and closer spaced holes were provided for. The equilibrium flow measurements were not limited by the length of the tunnel.

3.3 Velocity Measurements

3.3.1 Anemometer Systems

Two different sets of hot wire anemometry equipment were used during the course of this investigation. The equilibrium flow measurements were made using a TSI Model 1210-T1.5 single element sensor with one channel of a TSI Model 1050-2C anemometry system. Boundary layer traverses for the equilibrium measurements were made using a DISA Model 55H01 traversing mechanism controlled by a DISA Model 52B01 sweep drive unit and driven by a DISA Model 52C01 External stepper motor. The guide tube for the traverse protruded through a hole drilled in the test plate downstream of the measurement location. Mean and mean-square values of the hot wire signal were obtained by manually reading a TSI Model 1076 True RMS voltmeter at each position. The voltmeter was set for a 100 second integration time.

Sensor linearization coefficients supplied by the factory were used and the linearization was checked over the speed range of the tunnel. Spectral analysis of the velocity signal was performed by passing the linearized signal through the signal conditioner to suppress the dc component and then passing it through the Ithaco post amplifiers for final amplifications prior to being passed to the Nicolet 660A spectrum analyzer.

For the backward-facing step measurements both a single and a x-wire probe were used. The single wire sensor was a TSI Model 1218-T1.5 boundary layer probe. The x-probe sensor was a DISA Model 55P63. Both sensors were driven by DISA Model 55M10 bridges and the bridge voltages were linearized using DISA Model 55D10 linearizers. The linearizing exponential coefficient was selected as the coefficient that gave a 2:1 output voltage ratio for a 2:1 velocity ratio. The 2:1 velocity ratio was always taken as 90:45 ft/sec, which spanned the velocity ranges that could occur for a given profile. A more detailed (8 point) linearization check was occasionally made. The x-wire probe was visually aligned to be square with the flow prior to linearization. Further discussions of the x-wire measurements can be found in Chapter 4.

The TSI Model 1210-1.5 sensor used for the equilibrium flow measurements and the TSI Model 1218-11.5 boundary layer probe used for the single wire backward-facing step measurements had an active sensing length of 0.050-inch and a wire diameter of 1.5×10^{-4} -inch. The DISA Model 55P63 x-wire probe has sensor wire lengths of 0.050-inch, diameters of 2.0×10^{-4} -inch, and wire separation distances of approximately 0.050-inch.

3.3.2 Hot Wire Traverse

A computer controlled traverse was used to remotely position the hot wire for the velocity measurements with the backward-facing step configuration. The traverse is built onto a large test plate that is bolted in place of the tunnel floor when velocity measurements are to be obtained. The traverse plate is self contained; it houses the lead screws, support bearings, all of the drive hardware, and the two stepper motors that provide the remote motions in a direction normal to the test wall and in a direction laterally (z-direction). The stepper motors turn high precision lead screws which in turn move an airfoil shaped strut that serves as a hot wire holder. With the high precision lead screws a single step corresponded to a motion of 0.001-inch. In this study the lateral motion drive was disconnected and lateral motion, as well as motion in the streamwise direction, were obtained by manually turning the appropriate lead screws. Hence, only motion normal to the test wall was left to remote control.

Figure 3-7 shows a block diagram of the hot wire traverse and data acquisition system. Overall traverse control is handled by a PDP 11/23 microcomputer. Traverse motion requests are sent over a serial interface line to a stepper motor controller box (Rockwell International AIM-65 Basic) which controls the motion of the stepper motors. The microcomputer monitors the controller box position read-out to ensure that the requested position is obtained. The traverse system has no absolute reference. A reference was obtained by manually positioning the hot wire to a known distance from the wall and then zeroing the motor controller system. This was done every time the traverse was moved either laterally or streamwise.

Velocity profiles could only be made over the streamwise extent of the test wall covered by the traverse. The extent of the traverse motion in the streamwise direction ranged from approximately 24-inches upstream of the step to approximately 30-inches downstream of the step. It was not possible to obtain velocity information at the farthest downstream location ($x=36$ -inches or $x/h=72$). The furthest downstream position for which velocity information was obtained is $x/h=54$.

3.3.3 Hot Wire Data Acquisition and Processing

Included in figure 3-7 is a block diagram of the hot wire data acquisition system. The core system is a high speed data acquisition system manufactured by Data Translation Corporation. It uses a PDP 11/23 CPU with 256 KBytes of RAM, has an extended instruction set, a memory management system, and a hardware floating point processor. Analog to digital conversion is performed with an 8 channel, 12-bit converter (LDT 3382) that has a maximum continuous sampling rate of 200,000 points per second when writing to RAM or a 100,000 points per second sampling rate when writing to the hard disk. The sampling rate is controlled by a separate programmable clock (LDT 2769). The system incorporates a 1 megabyte floppy disk and a 35.6 megabyte hard disk (Winchester) that is set up to continuously record digital data at a rate of 100,000 points per second without data loss. Additional features of the system are a high speed D/A board, a VT102 terminal fitted with REGIS graphics capability, and an Okidata graphics printer.

Data acquisition and processing programs were written in Fortran IV and used special device driver software purchased from Data Translation (CPLIB software package) to control the operation of the various boards. The A/D boards are configured to digitize voltages over the range of ± 10 volts. The output amplifiers on the linearizers were adjusted to give a maximum voltage of approximately 8 volts. The complete linearized signal (mean and fluctuating) was input to the digitizer. For single wire measurements, only one A/D channel was used and for the x-wire measurements, two A/D channels were used.

The data acquisition and processing algorithm is as follows. Individual blocks of 2000 sample points were obtained at a time. Typically a sampling rate of 20,000 points per second was used and the

A/D was run in a "burst" mode to minimize delay times between A/D channels (appropriate for the x-wire only). For the x-wire measurements the data blocks from the two sensor elements were appropriately summed and subtracted to obtain data blocks representative of the u and v components. The mean value and variance of the u and v data blocks were calculated and the covariance between the u and v blocks was calculated. These terms were then stored and a new block of data was obtained and similarly processed. Typically 40 such data blocks were used to obtain the final statistical averages. The final averages were stored on the hard disk and also printed out on the dot-matrix printer. After completing data acquisition at a particular wall position a command is given to move to a new wall location and the process is started over again. A similar procedure was followed for the single wire data processing routine except only one block of A/D data was obtained at a time and only mean and variances were computed.

The profile data were transferred to an IBM PC for additional analysis and plotting. The single wire profile data was used to calculate various boundary layer parameters. An integration of the mean velocity profile, using a combination of Simpson rule and Trapezoidal integration, was used to calculate the boundary layer displacement thickness, δ^* , and momentum thickness, θ . The boundary layer thickness, δ , defined at the point where $u/U_0=0.99$, was estimated using a 3-point interpolation of the profile data at the edge of the boundary layer. Values of shear velocity (or wall shear stress) were obtained using a best fit log-law method similar to that proposed by Kline et. al. (1967).

To obtain spectral data the two signals from the x-wire were analog summed/subtracted, using a TSI Model 1015C correlator, to obtain a u and a v component signal. These two signals were then directly passed into the Nicolet 660A spectrum analyzer for processing. Only single point velocity statistics were obtained.

3.4 Spectral Data

3.4.1 Acquisition and Processing

All of the spectral data was obtained using a Nicolet Scientific Corporation Model 660A Dual Channel FFT processor. Within the analyzer, data for each channel is simultaneously sampled by separate A/D's at a rate of 2.56 times the selected frequency range. Anti-aliasing filters are in-line in front of the A/D's to prevent aliasing of high frequency components in the incoming signal. Blocks of 1024 time points are acquired and standard Fourier algorithms are used to transform the data. The number of ensembles that are averaged together to form a final spectrum is continuously selectable. Typically 1000 ensembles were used for the pressure data and 500 ensembles for the velocity data. The basic spectral functions that are computed by the analyzer are the two auto-spectra (one per input channel) and the complex cross-spectrum between the two channels. The analysis bandwidth for a given frequency range is found by dividing the selected frequency range by 400.

Data was typically obtained for a series of frequency ranges in order to satisfy the need for both narrow-band cross-spectral information and for high frequency auto-spectrum information. Pressure spectra were generally measured for frequency ranges of 500 Hz, 2,000 Hz, and 20,000 Hz and the velocity spectra were measured for these same ranges plus a 50,000 Hz range. All of the spectral data were recorded on a Nicolet Model 160C data recorder (floppy disk system) and selected data were plotted on a digital plotter.

The spectral data stored on the 160C was transferred to an IBM PC for post processing. The post processing consisted of converting the raw voltage spectra into absolute pressure (or velocity) spectra, using the appropriate transducer sensitivities and amplifier gains, and then assembling the data from the individual frequency ranges into a single frequency spectrum. This was done for both the auto- and cross-spectra for the pressure data and for the auto-spectra for the velocity spectra.

Additional post processing was performed on the (combined) pressure cross-spectra. At high frequencies the cross-spectra become incoherent. The cross-spectra for each condition were reviewed and the frequency at which the coherence was consistently below a value of 0.05 was marked

and all cross-spectral data above that frequency was eliminated. Due to the facility noise limitations the data below 50 Hz was also eliminated.

The phase of the pressure cross-spectrum obtained with streamwise separated transducers is interpreted as a convection velocity (equation (2.57)). In order to directly use the phase spectrum to calculate convection velocities the phase spectrum must be "unwrapped" to eliminate the 2π ambiguities that exist in the measured phase. The phase is obtained as the arc tangent of the imaginary part of the cross spectrum divided by the real part. Increments of 2π ambiguity occur after each complete rotation in the cross-spectrum phase plane and that must be accounted for in the post processing. The phase was unwrapped by first using the slope of the phase ($d\theta/df$) at 100 Hz to estimate the convection velocity at this frequency. This convection velocity was used to calculate the expected phase angle at 100 Hz which was then compared to the actual measured phase to determine the number of 2π increments that had to be added to the measured phase. The appropriate number of increments were added to give the unwrapped phase at 100 Hz from which the actual convection velocity was also calculated. The convection velocity at 100 Hz was then used as an estimate of the convection velocity at the two neighboring frequency points. This was used to calculate an estimated phase to be compared to the measured phase to determine the number of 2π ambiguities that occurred. These ambiguities were added to the measured phase to get a final phase which was used to get the actual convection velocity. This value of convection velocity was then used as the estimated value for the next frequency point and the procedure repeated. The validity of this procedure is borne out by the behavior of the convection velocity data which smoothly increases for small values of separation, where there are no 2π ambiguities, to large values of separation where there are many increments of 2π that must be unwrapped.

3.4.2 Error Analysis in Spectral Measurements

Standard formulas for statistical errors in spectral estimates can be found in Bendat and Piersol (1980). For a relatively broad-band spectrum, like the pressure or velocity spectrum, bias errors are generally second order when compared to random errors. The normalized random error for an auto-spectrum is given as

$$\epsilon[\hat{\phi}] = 1/\sqrt{n_d} \quad (3.1)$$

where n_d is the number for averages.

Similarly the normalized random error for the coherence and the phase can be estimated to be

$$\epsilon[\hat{\gamma}^2] = \frac{\sqrt{2}[1-\gamma^2]}{\gamma \sqrt{n_d}} \quad (3.2)$$

$$\epsilon[\hat{\Delta\theta}] = \frac{\sqrt{1-\gamma^2}}{\gamma \sqrt{2n_d}} \quad (3.3)$$

where γ^2 is the coherence squared, $\hat{\Delta\theta}$ is the phase uncertainty measured in radians and the top hat indicates the estimated (measured) functions. To use equation (3.2) or (3.3) the estimated values are substituted in for the unknown actual values (unhatted).

For the auto-spectrum estimates the 1000 averages gives a random error of 0.032. This gives a measured estimate with a 95% confidence interval of $\pm 6\%$. The errors for the coherence and phase are not easily quantified since they are functions of the true coherence between the two signals. As can be seen from (3.2) and (3.3) the only way to decrease the random errors in the cross-spectrum estimators is to increase the number of averages. 1000 averages were selected in order to reduce the random errors that occur for the estimators. Obviously a realistic limit exists as to how many averages can be taken since the total processing time increases as the number of averages increases. For the Nicolet 660A, the 1000 averages required a data processing time of approximately 5 minutes per spectrum.

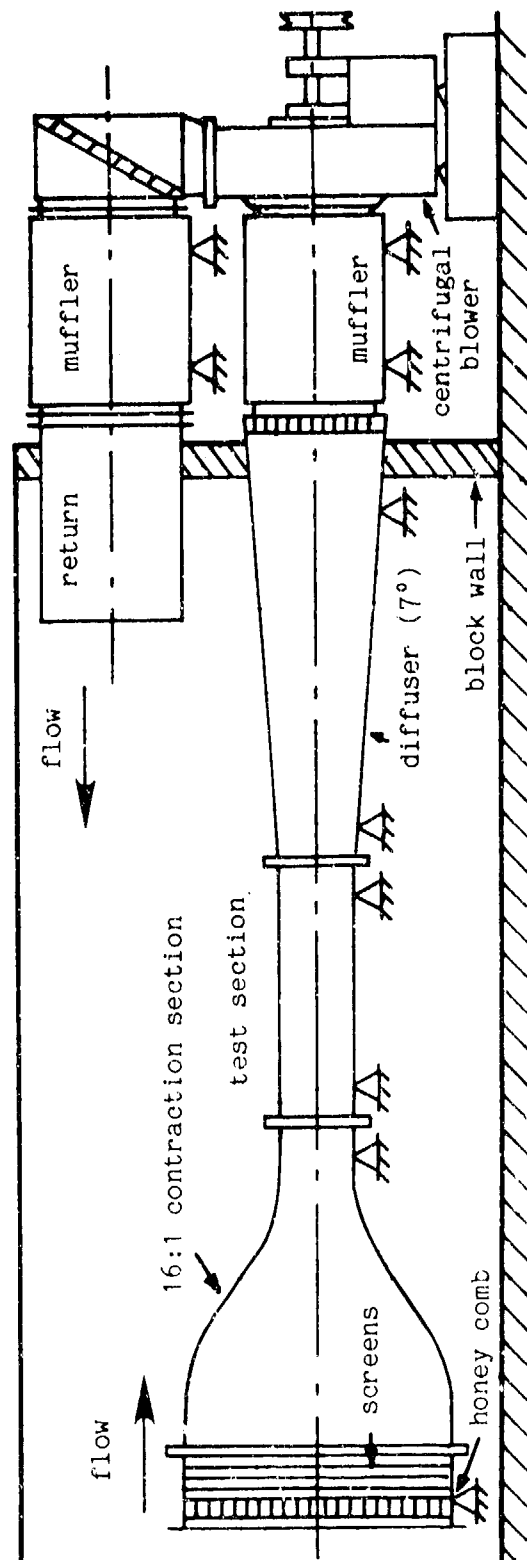
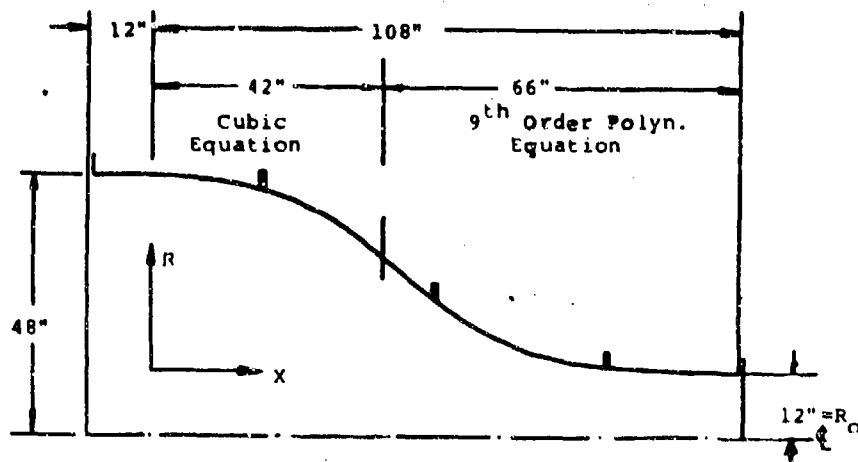


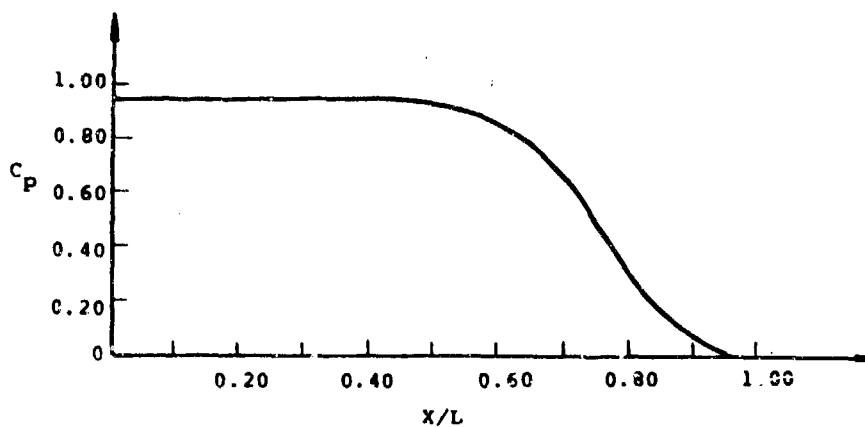
Figure 3.1 Schematic of CUA Wind Tunnel



Contraction Profile

--- Cubic Equation: $R = 36 - 4.426 \cdot 10^{-3} X^2 - 8.865 \cdot 10^{-5} X^3$

--- 9th Order Eqn.: $\frac{R+R_0}{R_0} = 1 + 84y^9 - 189y^8 + 108y^7$ Where $y = \frac{132-x}{120}$



Static Pressure Distribution

Figure 3.2 Wind Tunnel Contraction Section
and Static Wall Pressure Data

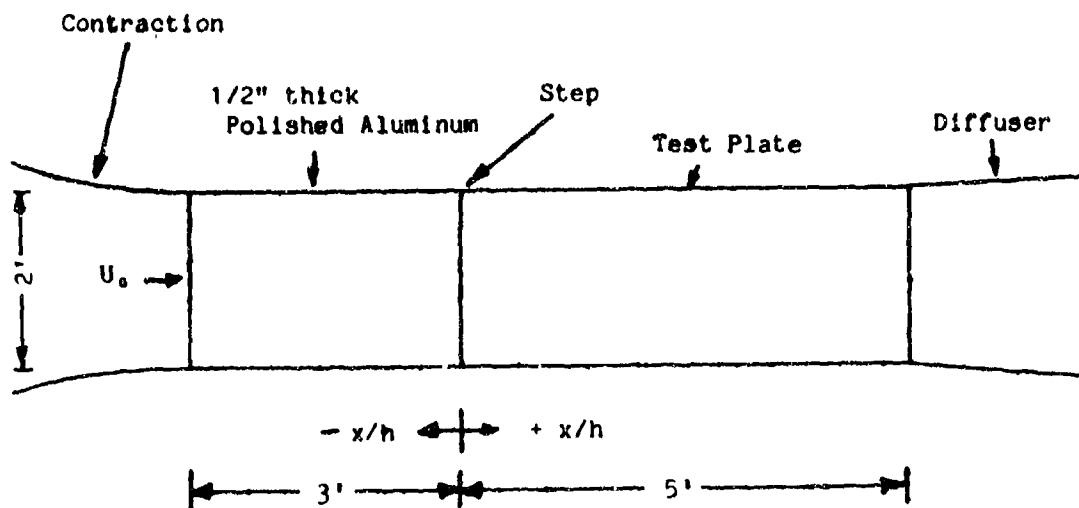


Figure 3.3 Diagram of Test Wall

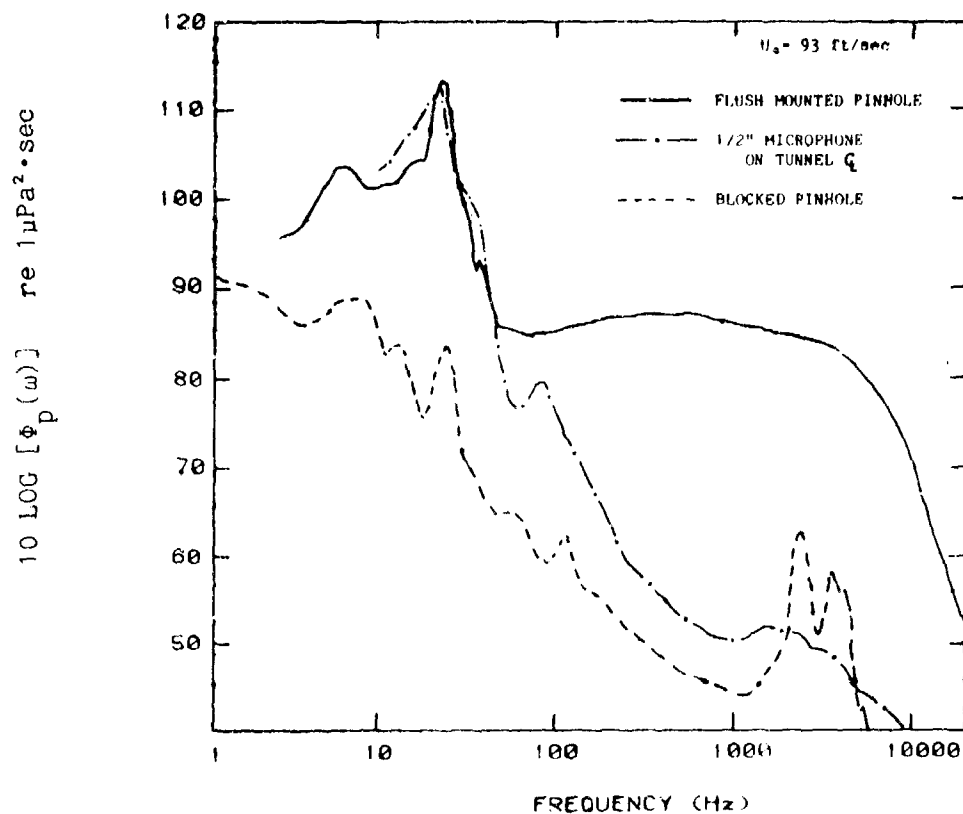


Figure 3.4 Comparison of Wall Pressure Spectra with Background Noise

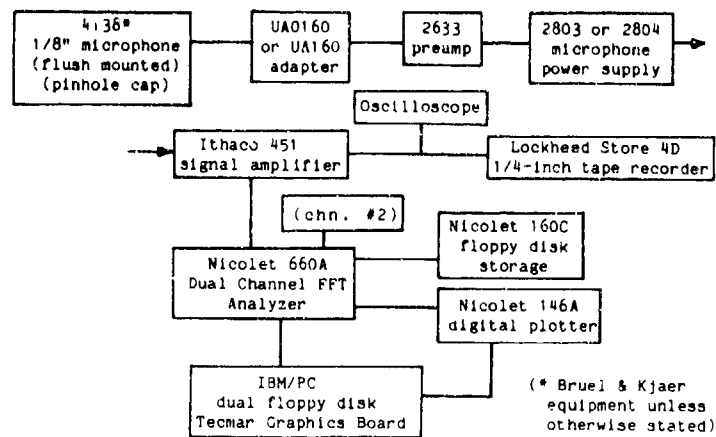


Figure 3.5 Block Diagram of Microphone System

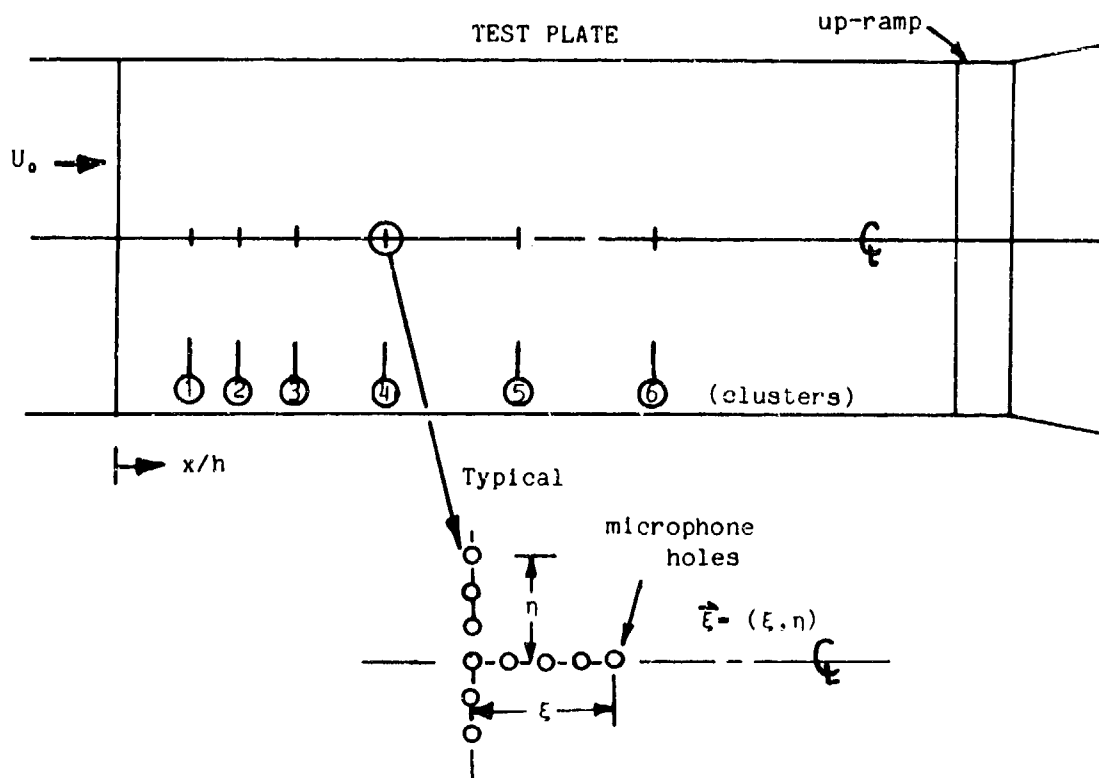


Figure 3.6 View of Test Plate Showing Measurement Positions

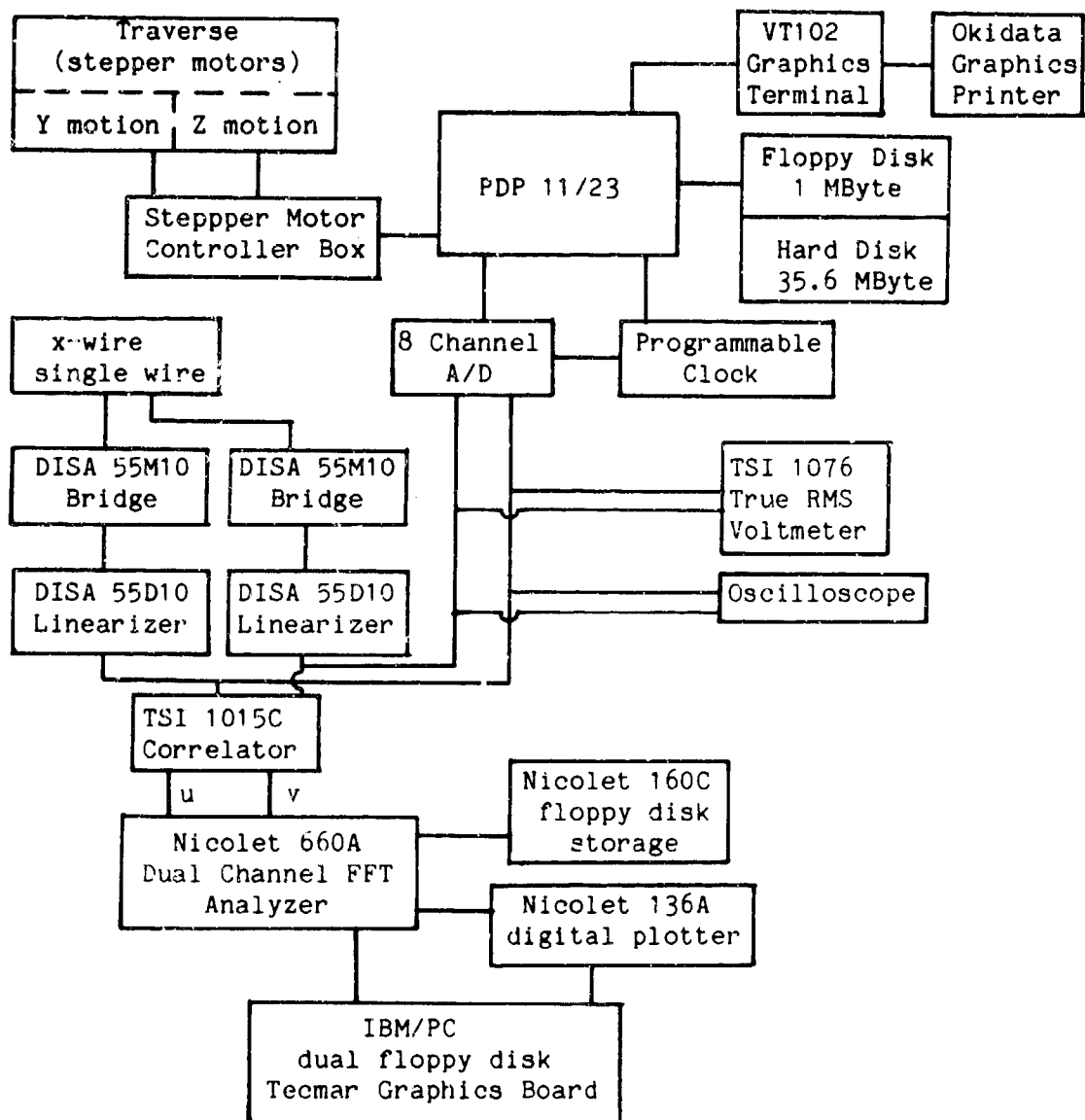


Figure 3.7 Block Diagram of Hot Wire Traverse and Data Acquisition System

CHAPTER 4

EXPERIMENTAL RESULTS FOR VELOCITY MEASUREMENTS

4.1 Introduction

This chapter presents the experimental results of the measurements made in the flow field of the backward-facing step. The objective of these measurements was to obtain turbulence data for a non-equilibrium boundary layer that would be used in identifying sources, within the boundary layer, of fluctuating wall pressures. By relating characteristics of the wall pressure field to the structure of the turbulent flow a better understanding will be obtained of how turbulence generates unsteady surface forces.

Measurements were made of the fully developed onset boundary layer and of the boundary layer downstream of reattachment, at 10, 16, 24, 36 and 54 step heights downstream of the step. Mean velocity profiles, turbulence intensity profiles of both the u and v components of velocity, Reynolds stress profiles, and frequency spectra of the u and v components were all measured at these locations. Data were obtained using both a single and a x-wire anemometer. Typically measurements were made at two speeds, nominally 50 and 80 ft/sec. In the discussions that follow, data are presented for the lower speed runs. However, various flow parameters measured for the higher speed are given in table 4.1. Velocity spectra were obtained at a speed of nominally 82 ft/sec.

Velocity measurements are made much closer to the wall with the single wire anemometer than with the x-wire anemometer. As such, all mean velocity data that are presented are measured with the single wire anemometer. In most cases when reference is made to streamwise turbulence intensities it is for data measured with the single wire anemometer.

Measurements of the mean velocity profile and turbulence intensity profile were also made for the equilibrium flow on a smooth flat plate using a single wire anemometer. The equilibrium flow condition, in

contrast to the onset boundary layer, was obtained by shimming out the downstream wall to be flush with the upstream wall. Data for this condition were obtained at 50.8 and 93.3 ft/sec.

All backward-facing step measurements, except those made to check spanwise uniformity, were made along the tunnel centerline. The step height was set at 1/2-inch for this study. Measurements for the equilibrium flow condition were made along a line 1-inch (spanwise) above the test wall centerline. This allowed the use of a line of pre-existing holes for the pressure measurements.

4.2 Onset and Equilibrium Boundary Layers

The characteristics of the boundary layer that is onset to the backward facing step are important in establishing the flow field that develops downstream of separation. This has been discussed in detail by Bradshaw and Wong (1972), Eaton and Johnston (1981), and by Cheun, Toy and Moss (1983), to cite but a few. For this study, since we are not interested in the details of the separation/reattachment process, no attempt was made to modify the upstream flow so as to obtain a prescribed boundary layer state at the step. Instead, the boundary layer that naturally formed at the step edge was used. Similarly, the boundary layer that was studied for the equilibrium flow condition was the one that naturally existed. For both these flows, a fully developed "ordinary" turbulent boundary layer was sought. Velocity measurements were obtained for both the onset and equilibrium boundary layers to fully document their turbulence characteristics and to provide the boundary layer scaling parameters that are needed in interpreting the fluctuating pressure data.

4.2.1 Mean Velocity Profiles

Velocity measurements were obtained at two upstream locations ($x/h = -12, -2$) for the step study, and at what would be an $x/h = 12$ (if the step were present) for the equilibrium flow study. The mean velocity profiles that were obtained for these three positions are shown in figure 4.1 plotted using inner variable scaling. The quantity u^* is the shear velocity which is determined using a best log-law fit technique. Included in figure 4.1 are lines representing the linear-law and log-law

dependencies that should exist for the velocity profiles near the wall. The dimensionless constants in the log-law relationship that are used ($\kappa=0.41$ and $B=4.9$) are those used by Clauser (1956) which give,

$$u^+ = 2.44 \ln(y^+) + 4.9 \quad (4.1)$$

where, $u^+ = U/u^*$ and $y^+ = yu^*/\nu$.

The different regions of a boundary layer are also shown in this figure. The sublayer covers the range $0 < y^+ \leq 5$, the buffer layer extends from $5 < y^+ < 40$, and the log-law region extends from $40 < y^+$ to $y \leq 0.2\delta$. These three regions comprise the inner layer of the boundary layer. The outer layer covers the region $y/\delta \geq 0.2$.

The profiles in figure 4.1 collapse on the log-law line and merge smoothly to the linear-law line nearest the wall. There is slight scatter in the equilibrium flow profile measurements in the linear-law region but the overall behavior is excellent. Measurements for all three profiles extend down to the region of the viscous sub-layer ($y^+ < 5$). The extended data region over which there is a good fit, and the manner in which the data merges smoothly into the linear-law region, all reflect the quality of the data and the fact that the boundary layers at these locations are classical equilibrium flows. At large values of y^+ the equilibrium profile has a stronger or more pronounced wake region than the onset flows. This is consistent with the higher Reynolds number of this flow. The momentum thickness Reynolds number for the equilibrium flow is 33% larger than that for the boundary layer at $x/h = -12$ (see table 4.1 for boundary layer properties).

The boundary layer properties measured for the upstream positions and equilibrium flow are also characteristic of a fully developed (ordinary) turbulent boundary layer. The boundary layer at $x/h = -2$ is slightly thinner than at the $x/h = -12$ position. This results from the slightly favorable pressure gradient that exists immediately upstream of the step. Pressure gradient data was obtained but is not discussed.

4.2.2 Turbulence Intensity Profiles

Turbulence intensity profiles of the upstream and equilibrium flow boundary layers were measured and are shown in figure 4.2. In this figure, the root-mean-square values of fluctuating velocity are normalized by the value of shear velocity and plotted against y^+ . The measurements were made with a single wire anemometer and are fluctuations in the streamwise velocity component.

As in the mean velocity profiles, there is good agreement among the profiles with no distinguishable differences between the profiles measured at $x/h = -12$ and -2 . The overall behavior of the turbulence intensity profiles is the same as reported in the literature. Streamwise velocity fluctuations increase away from the wall, peak at $y^+ = 15$, then slowly decrease until the edge of the boundary layer where the fluctuations rapidly drop to the turbulence levels of the free-stream flow.

The peak value of turbulence intensity that is measured can be limited by the finite size of the hot wire used. Fluctuations in velocity in the very near wall region are characteristically small scale and can not be accurately resolved by a sensor that is larger than the length scale of the fluctuations. Eckelmann (1974) used commercially available hot-film anemometers to investigate the wall region of a fully developed turbulent channel flow, using oil as the fluid medium. For this experiment the sensor was only two y^+ in length due to the large sublayer that developed. Eckelmann obtained a peak u'/u^* value of 2.8 which occurred at $y^+ = 13$. Willmarth and Sharma (1984) constructed especially small hot wires with which turbulence intensity measurements were made. These wires were on the order of $0.3y^+$ in length. A peak u'/u^* value of 3 was measured at a position of $y^+ = 13$.

The hot wire length for the present data is approximately $55 y^+$ units. The peak value of turbulence intensity that is measured is approximately 2.4 and it occurs at approximately $y^+ = 16$. These values are in good agreement with those reported in the literature considering the physical size of the wires relative to the boundary layer viscous

scales. It is interesting to note that the peak turbulence intensities occur in the overlap region between the inner-law and log-law regions where viscous and turbulence shear stresses are approximately equal.

4.2.3 Spanwise Uniformity of the Onset Boundary Layer

The spanwise uniformity of the boundary layers at $x/h=-2$ and at $x/h=54$ was checked by comparing mean velocity profiles measured at three spanwise positions at each of the streamwise locations. Figure 4.3 shows the mean velocity profiles measured at $x/h=-2$ for the spanwise locations $z/h=0, -6$, and 6 . Positive z is measured up from the centerline of the test wall. The mean velocity profiles measured at $x/h=54$ for spanwise positions $z/h=0, -6$, and 5 are shown in figure 4.4.

The comparison between profiles in figure 4.3 is excellent and shows no spanwise variations in the onset flow, at least to the extent that spanwise variations can be identified by comparisons of mean velocity profiles. The profiles in figure 4.4 also compare well, exhibiting only a small amount of scatter at the measurement location nearest the wall. Microphone mounting holes were located along the $z/h=0$ and $z/h=6$ lines at various streamwise positions. The holes, when not used for pressure measurements, were filled with polyester body filler (automotive body filler) and sanded smooth then covered with a second layer of lacquer material and again sanded smooth. Along the $z/h=0$ line there were some 70 such filled holes upstream of the $x/h=54$ measurement position. Upstream of the $x/h=-2, z/h=0$ position there were 4 filled holes. The $z/h=5$ line was selected for one of the spanwise checks since there were no holes along this line and it would provide a check on the effect these holes might have on the boundary layer profiles. The profiles show no effect due to the filled holes.

4.2.4 Criteria for an Equilibrium Boundary Layer

The characteristics of the onset boundary layer play a key role in determining the flow field that develops downstream of the step. For this investigation it was desired to have a fully developed turbulent boundary layer flow as the onset flow. Hussain (1983) reviewed initial conditions for a flow and established seven characteristics that a flow must have in order to be considered a fully developed turbulent boundary

layer. These seven required characteristics are: 1) a mean profile of proper shape and a shape factor of about 1.4, 2) a mean profile with a log-law and wake region present when plotted in log-law variables with there being an adequate extent to the log-law region, and 3) a wake strength that is appropriate for the Reynolds number of the flow; 4) a peak in the turbulence intensity profile of $u'/u^* = 2.5 \pm 10\%$, 5) with the intensity profile peak being located at $y^+ = 15$, and 6) a monotonic decrease in u' to the free-stream value; and 7) a broadband continuous u' spectrum that contains an inertial subrange.

Characteristics 1-6 have already been shown to exist in the boundary layers upstream of the step and for the equilibrium boundary layer. Figure 4.5 shows spectra of the velocity fluctuations measured at $x/h = -12$ and for the equilibrium boundary layer. Measurements at $x/h = -12$ are the u component of fluctuating velocity obtained from the x-wire. The equilibrium spectrum was obtained with a single wire anemometer. Measurements obtained at $y/\delta = 0.22$, 0.44 , and 0.66 are shown for the boundary layer at $x/h = -12$ and spectra obtained at $y/\delta = 0.23$ and 0.46 are shown for the equilibrium flow. In this figure, the measured frequency spectra are converted to wavenumber spectra using $\Phi(k) = \omega\Phi(\omega)/k$ and normalized by the local turbulence intensity. The frequency axis is displayed as a wavenumber axis ($k = \omega/U_0$). The spectra for both boundary layers are continuous and broadband. The spectra exhibit, in the mid-wavenumber range, a region that scales as $k^{-5/3}$. This, as will be discussed later, is characteristic of the inertial subrange for the turbulence energy spectrum.

Hence, in terms of the criteria or characteristics proposed by Hussain, the boundary layer upstream of the step and the boundary layer for the equilibrium flow were fully developed (ordinary) turbulent boundary layers. Furthermore, the flows upstream and downstream of the step were two-dimensional, at least over a 6-inch spanwise region along the test wall centerline.

4.3 Mean Velocity and Turbulence Measurements

4.3.1 Mean Velocity Profiles

Mean velocity profiles were measured with the single wire anemometer at downstream locations $x/h = 10, 16, 24, 36$ and 54 ; all of these positions are downstream of reattachment ($x_p = 6h$). Only the profiles measured at 50 ft/sec will be shown but boundary layer parameters for all the measured profiles are given in table 4.1. The Reynolds number based on step height is $13,021$ for the 50 ft/sec runs. Figure 4.6 shows the measured profiles plotted versus distance from the wall (U/U_0 vs. y/h). Included in this figure is the profile measured upstream at $x/h = -12$. In figure 4.7, the profiles are plotted using inner-law variables. In both figures the profile origins are sequentially shifted and in figure 4.7 a log-law line for each profile is given.

The profiles have features that are notably different from an equilibrium flow profile. These differences are similar to those reported by other investigators. At the first downstream location, $x/h = 10$, there is a region of strongly retarded flow extending throughout the boundary layer. Further downstream, the region of retarded flow slowly fills out. By the last measurement station, $x/h = 54$, the profile begins to approach an equilibrium shape. The boundary layer redevelopment begins immediately after reattachment with a more pronounced recovery for the flow nearest the wall. This recovered wall region grows outward from the wall in the downstream direction.

Figure 4.7 best displays the manner in which the downstream boundary layers deviate from an equilibrium flow. These profiles have three distinguishing features which change with downstream position. The first feature is the wall region over which the boundary layer follows a log-law scaling. At $x/h = 10$ this region is very short, extending out to a $y^+ = 120$. The log-law region increases with downstream location and at $x/h = 54$ extends out to approximately $y^+ = 250$ which is typical of an equilibrium boundary layer. The second notable feature in the profiles is the dip below the log-law line that marks the end of the log-law scaling. The location of the dip also moves away from the wall

for positions further downstream. The last feature is the strength of the outer flow or wake region. At $x/h=10$ there is a very marked deviation of the profile from the log-law line in the wake region which, for an equilibrium flow, would be indicative of flow in a strong adverse pressure gradient. The strength of the outer flow region decreases rapidly downstream and by $x/h=54$ the wake region is more typical of that for an equilibrium flow. These features show that just downstream of reattachment the flow is highly energized and that the flow relaxes and undergoes a redevelopment downstream.

The mean velocity profiles in figure 4.7 exhibit characteristics that are similar to those of Bradshaw and Wong (1972) who obtained measurements as far downstream as $x/h=52$. Bradshaw and Wong show a more pronounced dip in the log-law region and a weaker wake region than is found in this data. The profiles of Kim et al. (1978), although made out to only $x/h=16$, are in closer agreement to those in figure 4.7 for similar x/h locations.

These differences are partly a result of the difference in methods used to specify values of wall shear stress. Bradshaw and Wong used a Preston tube to obtain values of wall shear stress. The present study used the method of Kline et al. (1967) which is a Clauser plot type of technique in that the value of wall shear stress is selected as the value which best fits the profile to a log-law line. The range of measurement points that follow the log-law line depends to a certain extent on the value of wall shear stress that is selected. By selection of a different value of wall shear stress the strength of the dip can be increased, but at the expense of the wake region. Kim et al. used a similar "best fit" technique to obtain values of wall shear stress. Another probable reason for the differences in dip and wake strengths is in the differences in initial conditions (δ_0/h). Kim et al. (1978) had an initial condition of $\delta_0/h=1.0$, which is closer to that of this investigation ($\delta_0/h=2.0$) than to Bradshaw and Wong ($\delta_0/h=0.1$). This conclusion is further supported by the study of Adams, Johnston and Eaton (1984) who investigated the effect of δ_0/h on downstream velocity

profiles and showed that for an initial condition of $\delta_0/h=1.0$ there is a much stronger wake region than for initial conditions of $\delta_0/h=0.03$ or 0.04 . The dip for the $\delta_0/h=1.0$ profile, however, was only slightly less than for either the $\delta_0/h=0.3$ or 0.04 profiles.

Boundary layer parameters were calculated from the mean velocity profiles and are given in Table 4.1. Values of skin friction coefficient C_{fm} calculated using the Ludwig-Tillman formula ($C_{fm}=0.246 \cdot 10^{-.678H} \cdot R_\theta^{-.268}$) are tabulated for each profile. Included are the values obtained for the equilibrium boundary layers and for the boundary layer measured as part of the spanwise uniformity check.

The variations of the boundary layer parameters with streamwise location are shown in figures 4.8-4.10. Both δ^* and δ decrease rapidly between $x/h=10$ and $x/h=16$ and then slowly increase. The values of δ at $x/h=54$ are nearly twice the values at $x/h=-12$. The shape factor decreases monotonically downstream and at $x/h=54$ has returned to the value measured upstream. The Clauser parameter is very large at $x/h=10$ but rapidly decreases downstream. At reattachment C_f must be zero since this is a point of flow impingement. Starting at zero C_f rises rapidly until $x/h=24$ where the rise becomes less rapid but still pronounced. There is no reason to expect the skin friction coefficient to return to the upstream value. It is worth noting how well the Ludwig-Tillman formula predicts the measured values of C_f , even just downstream of reattachment.

4.3.2 Turbulence Profiles

Profiles of the streamwise normal stresses, u'/U_0 (u' is the RMS value of u as defined in Chapter 2) were obtained with both the single and x-wire anemometers. Vertical (wall-normal) normal stress profiles, v'/U_0 , and turbulence shear stress profiles, $-\overline{u'v'}/U_0^2$, were obtained with the x-wire anemometer. Profiles of u'/U_0 and v'/U_0 were also obtained by integrating the u and v frequency spectra.

Figure 4.11 shows a comparison of the u'/U_0 profiles obtained at $x/h=-12$ for the two anemometer setups along with a profile obtained by Klebanoff (1955). The measurements reported by Klebanoff were obtained in a 3-inch boundary layer that had been artificially thickened by

roughness in order to minimize transducer resolution errors. The boundary layer at $x/h=-12$ was 0.9-inch thick. The single wire profile agrees quite well with the Klebanoff profile except in the outer part of the boundary layer where the levels do not decrease as rapidly as the Klebanoff profile. This variation in the outer layer region of the boundary layer may be a result of differences in wake strength between the two boundary layers or possibly due to the differences in free-stream turbulence intensity between facilities.

The profile results for the x-wire are not completely in agreement with Klebanoff. Over almost the entire extent of the boundary layer the x-wire measures lower values of u'/U_0 . Only at the outer edge of the boundary layer does the profile agree with the single wire profile. This same trend of lower levels is evident in the v'/U_0 profiles shown in figure 4.12(a). In this figure both the u and v profiles are compared to the profiles of Klebanoff. At large values of y/δ the v' profile converges with the u' profile and the levels, at $y/\delta > 1.5$, are approximately $u'/U_0 \approx 0.003$, which is the order of the turbulence intensity in the free-stream. A peculiar feature of the v'/U_0 profile is the increase in level that occurs as the wall is approached while just the opposite trend is seen in the profile of Klebanoff. Turbulence stress profiles, $-\overline{u'v'}/U_0^2$, measured at the upstream position are shown in figure 4.12(b) compared to the profile obtained by Klebanoff. The same trend of low values of measured turbulence levels is present. The stress levels are presented as a quadratic term while the normal turbulence stresses (RMS velocities) are presented linearly so the differences in the turbulence stress profiles are larger.

A review (presented in Appendix A) of hot wire response characteristics and signal interpretation was conducted in order to determine the sources of these differences. Errors in the processing of the hot wire signals, at the output of the linearizers, are considered not to be a factor since good agreement was obtained between the turbulence levels obtained with the computer data reduction system and integrations of the velocity spectra. Errors due to electronic

responses of the two anemometry channels were found to be less than 2%. The major sources of error seem to be 1) excessive spatial averaging of the velocity fluctuations due to the finite size of the hot wire, particularly in the case of the x-wire for which there is a large measurement volume, and 2) deviations from the sum/difference decomposition relationship that was assumed for the u and v components of a x-wire. Correcting the measured levels for these errors is considered to be questionable since such corrections require a priori knowledge of the true turbulence field. For the type of complex flow field that exists downstream of reattachment, this is not available. The objective in measuring the turbulence levels was to obtain a qualitative understanding of the features of the turbulent velocity field in the relaxing flow regime. Consequently, it is assumed that these features are not altered by these errors so the measured (uncorrected) turbulence profiles are presented and discussed.

Measured profiles of u'/U_0 , v'/U_0 , and $\overline{u'v'}/U_0^2$ are shown in figures 4.13-4.16. The u'/U_0 profiles obtained with the single wire anemometer are given in figure 4.13 while the data presented in figures 4.14-4.16 were obtained with the x-wire. The qualitative features between the single wire and the x-wire profiles of u'/U_0 (figures 4.13 and 4.14, respectively) are the same. Only the data measured at 50 ft/sec is presented in graphical form but a complete listing of all data is given in Appendix B.

All of the turbulence stress profiles follow the same general trends. The level of stress for any given profile peaks at some location in the profile but this peak value continually decreases in level in the downstream direction. In addition, the location of the peak moves away from the wall with downstream direction.

There are three distinct regions in the individual profiles. The first is the near wall region given as $y/\delta < 0.02$. Measurements in this region could only be obtained with the single wire anemometer since the minimum wall position that could be reached with the x-wire is $y = 0.025$ -inch ($y^+ = 50$). In this region the profiles exhibit a local peak in turbulence stress at $y^+ = 18$ which is at the same location as the peak

for the equilibrium flows. This peak in u'/U_0 shows that at all of the measurement locations the wall region has developed to the point of establishing a buffer region which is the region of maximum u' production in an equilibrium boundary layer. However, this region is not necessarily the region of maximum u' downstream of reattachment. The second region of the profiles is away from the wall region where the turbulence quantities again reach a local maximum level. This region is bounded roughly by $0.02 < y/\delta < 0.9$. In this region, for a given x/h location, all of the stresses peak at the same y/δ location. The location of the peak propagates away from the wall in the downstream direction. Along with this propagation, the magnitude of the peaks decreases. By $x/h=54$ a specific peak is no longer evident but a broader region of excessive turbulence levels can be seen compared to the upstream profile ($x/h=-12$). At $x/h=16$ the level of the u'/U_0 peak has decreased to approximately the level of the peak in the buffer layer. Peaks in the turbulence stress profiles shown in figure 4.16 are more evident than those in the RMS velocity profiles since they are presented in quadratic form. The final region of the turbulence profiles is the outer flow region, $y/\delta > 0.9$. Here, with the exception of the $x/h=10$ profiles, the turbulence levels collapse on y/δ . At $x/h=10$ there is an extensive region of low turbulence activity in the outer flow. This region is essentially removed at $x/h=16$ by the rapid reduction in boundary layer thickness that occurs.

4.3.3 Correlation Coefficient and Mixing Length Profiles

Turbulence stress is a measure of the vertical transport of streamwise momentum that occurs in the flow. This is the primary mechanism for the production and maintenance of turbulence itself. Values of turbulence stress do not however, indicate the fraction of total turbulence activity that is associated with this transport. The turbulence stress correlation coefficient $R_{12} = -\overline{u'v'}/(u' \cdot v')$, is a measure of this fraction. R_{12} may also be interpreted as a measure of the level of coherent turbulence activity. As an example, typical levels of R_{12} in a well organized plane mixing layer can be on the order

of 0.7 while the highest values obtained in an equilibrium turbulent boundary layer are only about 0.5. Clearly the plane mixing layer contains more coherent activity than the anisotropic boundary layer.

Profiles of R_{12} are shown in figure 4.17. The origin for each profile is sequentially shifted up in figure 4.17. It should be noted that x-wire measurement errors are a minimum for this type of data presentation since, to first order, the measurement errors, which are present in both the RMS values and turbulence stresses, are canceled out. The highest correlation coefficients are obtained for the $x/h=10$ profile in a localized region of $0.11 < y/\delta < 0.22$. These peak values are higher than the coefficients for the profile at $x/h=-12$ indicating a slightly more organized turbulence structure within the inner region of the boundary layer. Correlation coefficients at $x/h=-12$ have a nearly constant value of 0.37 to 0.4 throughout most of the boundary layer. This corresponds to the values reported in the literature (0.44 to 0.5) if probe interference effects are accounted for (Kassab et al. (1985)). The profiles of R_{12} for $x/h > 10$ all have the same general shape. Below $y/\delta=0.3$ the values of R_{12} are slightly less than for the $x/h=-12$ profile, but above this position the values are similar.

Bradshaw and Wong (1972) point out that the higher values of turbulence stress, measured downstream of reattachment, are inconsistent with the local equilibrium formula

$$dU/dy = (\tau/\rho)^{1/5}/(\kappa y), \quad (4.2)$$

where κ is the von Karman constant, which holds for the log-law region of an equilibrium boundary layer. In this formula κy is assumed to be the turbulence mixing length (l_m). In order for (4.2) to hold for the downstream flow a mixing length larger than κy must be used. The dipping of the mean velocity profiles below the log-law line is a result of this large length scale. Furthermore, at reattachment the turbulence length scale should be that of the upstream mixing layer which has a nearly constant value. This nearly constant mixing length scale is larger than κy and will persist for some distance downstream. This

places a dominant, constant value, mixing length near the wall. As such, slightly downstream of reattachment the boundary layer turbulence length scale will increase more rapidly with wall distance than κy .

Values of turbulence mixing length were calculated for the profiles downstream of reattachment using the equation

$$l_m^2 = -\overline{u'v'} / (dU/dy)^2 \quad (4.3)$$

and are shown in figure 4.18. Mean velocity gradients were estimated from the single wire profile by

$$dU/dy \approx 0.5[(U_2 - U)/(y_2 - y) + (U - U_1)/(y - y_1)]$$

where y_2 and y_1 are the adjacent points above and below the location at which the derivative is evaluated. The mixing lengths, in the region $y/\delta < 0.2$ where the log-law scaling should hold, is larger for all downstream locations than for the values measured at $x/h = -12$. A portion of this is due, as discussed earlier, to the low values of turbulence stress that were measured particularly for the profile at $x/h = -12$. With this in mind and considering the errors that are inherent in numerically differentiating data the best that can be said about this near wall region is that at $x/h = 10$ the turbulence length scale increases more rapidly than κy .

There are three trends in the mixing length profiles that bear noting: 1) for locations $x/h > 10$ the mixing length increases at a rate that is proportional to κy out to $y/\delta \approx 0.2$, which is further out in the boundary layer than the $l_m \approx \kappa y$ range for an equilibrium boundary layer; 2) at $x/h = 16$ and $x/h = 24$, the mixing length peaks at $y/\delta \approx 0.2$ (which is slightly before the peak in the turbulence stress) and then decreases to a nearly constant value (that is x/h location dependent); and 3) the mixing length in the outer flow region increases in the downstream direction and at $x/h = 54$ is slightly higher than the generally reported equilibrium value ($l_m \approx 0.08$). The peak in l_m , that is evident at $x/h = 16$ and $x/h = 24$, is also reported by Etheridge and Kemp (1978).

The peaking of the profiles ($x/h = 16$ and $x/h = 24$) indicate that the length scales in the mid region of the profiles are greater than those in the outer flow region, which suggests that there are multiple length

scales in the flow that are not present for an equilibrium flow. The outer flow structure is the last to adjust to changes in the overall flow structure.

4.4 Velocity Spectra

Velocity spectra were measured at various positions throughout the boundary layer at the same streamwise locations for which velocity profiles were measured. The objective in measuring the spectra was to obtain information on the frequency content of the turbulent velocity fluctuations. This information identifies the turbulence scales that are present thus providing a better understanding of the turbulence processes that occur in the flow. The spectral information will also be compared to the surface pressure spectra in order to identify possible wall pressure source regions within the boundary layer. One-dimensional time spectra of the u and v components of fluctuating velocity were measured by passing the summed and subtracted x-wire signals into a two channel narrow-band spectrum analyzer. The summing/subtraction process was performed with an analog correlator. Details of the analysis procedures are given in Chapter 3.

4.4.1 Presentation Format for Spectral Data

The velocity spectra are shown in figures 4.19-4.22 and figures 4.23-4.27. Figures (a) are the spectra for the u (streamwise) component and figures (b) the v (vertical) component. Each of the figures 4.19-4.22 present spectra obtained at a fixed x/h . In each figure, spectra obtained at $y=0.03, 0.1, 0.4, 0.8, 1.0$ and 1.5 -inch are shown (except where noted). These same spectra are replotted in figures 4.23-4.27 where each figure shows spectra obtained at the same wall distance as a function of x/h . The first set of spectra show the variations in the turbulence spectrum across the boundary layer at fixed streamwise locations while the second set of figures show the streamwise evolution of the spectra measured at fixed locations from the wall. Both perspectives of the spectral information provide interesting insight into the turbulence structure of the flow field.

The spectra are presented as a dimensionless spectral function $\bar{\Phi}(\omega)$, defined as,

$$\bar{\Phi}_1(\omega) = 10 \cdot \log[\omega \Phi_1(\omega) / u_1'^2] \quad (4.4)$$

where $u_1 = u_1(u, v)$,

and are plotted against (logarithmic) frequency ($f = \omega / 2\pi$). Definitions for $\Phi(\omega)$ are given in Chapter 3.

The specific presentation format that was selected for the velocity spectra is quite arbitrary. A number of different formats were compared and the form given above was selected as being most illustrative. This format normalizes the spectrum by the total mean-square fluctuation level ($u_1'^2$) and presents it as a first-moment spectral density ($\omega \Phi(\omega)$).

Perry and Abell (1975) used this spectral function as a matter of convenience since they obtained spectra using constant-percentage bandwidth filters (instead of using an FFT procedure that provides a constant bandwidth spectrum as in this study). Bradshaw (1971) suggested that data presentation in this format might be advantageous since it displays the relative contribution each frequency range makes to the overall mean-square value since $\omega \Phi(\omega) d(\log \omega) = \Phi(\omega) d\omega$. Samuel and Joubert (1974), as well as Bullock et al. (1978), presented velocity spectra in this format to emphasize the differences between measurements at different wall locations. Strickland and Simpson (1975) state that the peak in the first-moment spectral density of the streamwise velocity fluctuations occur due to a statistically periodic turbulence phenomena which they argue is the "bursting" phenomena that occurs near the wall.

Presenting the spectral data in the form of this spectral function was considered most illustrative for two reasons; it reduces the amplitude range of each spectrum, and it emphasizes the variations in spectral shape that occur in the region where contribution to the mean-square value are largest. Use of this spectral function is purely a matter of convenience and is not a suggestion of the scaling dependence for velocity spectra.

Each of the velocity spectra that will be presented is a composite of four individually obtained spectra (500 Hz, 2 kHz, 20 kHz, and 50 kHz range analysis spectra) assembled into a single spectrum. It is also

assumed that frequency spectra, $\phi_1(\omega, y)$, can be transformed to equivalent one-dimensional wavenumber spectra, $\phi_1(k_1, y)$, by using Taylor's hypothesis, $k_1 = \omega/U_c$, which gives

$$\phi_1(k_1, y) = U_c \phi_u(\omega, y) \quad (4.5)$$

where the convection velocity, U_c , is taken to be the local mean velocity at $U(y)$. All spectra were measured at a reference velocity of approximately 82 ft/sec. In order to see clearly each individual spectrum there is a 5 dB shift down in origin between spectra starting with the second spectrum in each figure.

4.4.2 Velocity Spectra for Equilibrium Flow

The closest wall position that x-wire measurements could be made at was 0.025-inch ($y^+ = 45$). This places the closest measurement at the edge of the buffer region and within the log-law region but still too far from the wall to measure the peak turbulence stress levels that occur at $y^+ = 18$ (see figure 4.13). The furthest distance from the wall at which spectra are presented is $y = 1.5$ -inch ($y^+ = 1600$ to 2700) which is in the wake region of the velocity profile. In general, positions $0.1 \leq y \leq 0.4$ -inch are considered to be in the log-law region while positions $y \geq 0.8$ -inch are in the wake region. In all the spectral data to be presented, the very high frequency portions of the velocity spectra are limited by hot wire size effects. These limitations occur above the frequency region of primary interest in this study. Included in many of the figures is a line with a $k^{-5/3}$ slope. This line represents the slope that $\phi_1(\omega, y)$ would follow if it scaled as $k^{-5/3}$.

Figures 4.19(a) and 4.19(b) show the velocity spectra (u and v) obtained at $x/h = -12$, which is for an equilibrium turbulent boundary layer. Near the wall, at $y = 0.025$ -inch ($y^+ = 40$), $\tilde{\phi}_u(\omega)$ exhibits two weak peaks, one at approximately 100 Hz and the other at 800 Hz. At $y = 0.1$ -inch ($y^+ = 180$) the $\tilde{\phi}_u(\omega)$ is nearly flat over the 100-1000 Hz range indicating a ω^{-1} (or k^{-1}) dependence to the turbulence spectrum. $\tilde{\phi}_v(\omega)$, at all y positions, is more band-limited than $\tilde{\phi}_u(\omega)$ and the maximum values of $\tilde{\phi}_v(\omega)$ occur at higher frequencies indicating v is composed of smaller scale fluctuations than is u .

The frequency characteristics of the velocity spectra are interpreted as indication that specific turbulence phenomena are present or occurring in the equilibrium flow. Before any description of the velocity spectra in the downstream region is given, a discussion of the types of frequency dependence that occur for turbulence spectra is in order. This will be helpful in identifying regions of the flow field where expected scaling occurs.

The double peak in $\tilde{\Phi}_u(\omega)$ near the wall is also reported by others; for example, the double peak is in the data of Perry and Abell (1975) and in the data of Bullock et al. (1978). Bullock et al. (1978) argue that the dual peaks are not due simply to two mixing processes that are present in the boundary layer with variations in the spectrum resulting from variations in the magnitude of each contributor at a given y position. Instead, they suggest an interpretation based on a stochastic wave model of turbulence that follows the analysis of Morrison and Kronauer (1969).

A more "classical" view of the turbulence process that is used to describe spectral characteristics of turbulence is termed the "energy cascade" process. It is based on a spectral treatment of turbulence as opposed to one based on wave-mechanics. The description of high Reynolds number turbulence in terms of an energy cascade has turbulence energy being generated at low wavenumbers where the spatial scales are of the order of the systems that are generating the turbulence (plate length, step height, etc.). This energy is transferred (cascaded), by inertial forces, to higher wavenumbers where the turbulence energy is dissipated by viscous forces. At high enough Reynolds numbers, the separation between the low and high wavenumber regions will be large and the high wavenumber region will be isotropic and independent of the character of the production process which can be highly anisotropic.

For flows of this type, there exists a region of wavenumbers where the large-scale (low wavenumber) spectrum overlaps the high wavenumber isotropic (Kolmogorov) spectrum producing an inertial subrange of wavenumbers. The inertial subrange is a spectral equivalent of the log-law region in a boundary layer where there is an overlap between the

viscous dominated near-wall region and the outer flow region which scales on flow length scales. The inertial subrange of wavenumbers is not directly affected by either the turbulence production mechanisms or the dissipation mechanisms. This energy transfer process, from wavenumber to wavenumber, is termed the "cascade process" and is discussed in detail in Tennekes and Lumley (1972), Batchelor (1967), and Hinze (1975).

If the appropriate conditions that are necessary for the existence of an inertial subrange are met (Tennekes and Lumley (1972)) then the three-dimensional wavenumber spectrum of the turbulence, in the inertial range of wavenumbers should scale as $k^{-5/3}$. Tennekes and Lumley (1972) show that in the inertial subrange the one-dimensional Eulerian time spectrum should scale as $\omega^{-5/3}$. That is, Taylor's hypothesis can be used with the measured (one-dimensional) turbulence frequency spectrum to establish the wavenumber dependence of the energy spectrum.

In order for an inertial subrange to exist, the turbulence Reynolds number must be high. Tchen (1954) showed that for boundary layer flows, away from the wall, in the log-law region of the mean velocity profile, the classical $k^{-5/3}$ scaling could be observed in the inertial wavenumber range. However, very near the wall in the buffer region, where the mean velocity gradient is large, the spectrum in the inertial wavenumber range reflects the influence of the production process, namely the mean velocity gradient (dU/dy), and that the spectrum in this range scales as k^{-1} . It is interesting to note that Bullock et al. (1978) also obtained a k^{-1} dependence to their near wall data ($200 < y^+ < 500$) which they attributed as being due to the predominance of the lower frequency peak (u wave) that was present in the spectral data. Nevertheless, the frequency of the velocity spectra can be used to gain insight to the turbulence structure of the flow field.

4.4.3 Velocity Spectra at Downstream Locations

The first location downstream of reattachment for which velocity spectra were obtained is $x/h=10$. The spectral functions measured there are shown in figures 4.20(a) and 4.20(b). This position is approximately four step heights downstream of reattachment. For the measurement nearest the wall, $y=0.03$ -inch, $\tilde{\Phi}_u(\omega, y)$ exhibits only a single peak centered at approximately 300 Hz in contrast to the equilibrium flow ($x/h=-12$). For the measurement at $y=0.1$ -inch ($y^+=150$) and $y=0.4$ -inch ($y^+=600$) $\tilde{\Phi}_u(\omega, y)$ shows an inertial wavenumber range ($k^{-5/3}$ scaling) which extends over nearly a full decade. The peak in the $\tilde{\Phi}_u(\omega, y)$ remains at approximately the same frequency with increasing wall distance. $\tilde{\Phi}_v(\omega, y)$ for the position $y=0.03$ -inch is nearly identical to that at $x/h=-12$. Away from the wall $\tilde{\Phi}_v(\omega, y)$ flattens out displaying a broad region of equal contribution to v' . At $y=0.8$ -inch the peak of $\tilde{\Phi}_v(\omega, y)$ is at a lower frequency than for locations nearer the wall and a low frequency bulge has developed (approximately 320 Hz).

The spectral functions obtained at $x/h=24$ are shown in figures 4.21(a) and 4.21(b). Nearest the wall ($y=0.03$ -inch) $\tilde{\Phi}_u(\omega, y)$ is flattening out and just beginning to show signs of the development of the higher frequency bump that is present in the $x/h=10$ near-wall spectrum. At greater distances from the wall $\tilde{\Phi}_u(\omega, y)$ exhibits a well defined inertial range of wavenumbers characteristic of a high turbulence Reynolds number flow. The inertial range begins at the peak of $\tilde{\Phi}_u(\omega, y)$ and extends out to higher frequencies.

At $x/h=54$, the furthest downstream location at which velocity information was obtained, the u spectra at the wall have almost completely recovered to an equilibrium condition as shown in figure 4.22(a). Even the spectrum at $y=0.2$ -inch is starting to develop an equilibrium shape. The spectra of the outer flow clearly show a $k^{-5/3}$ region. The v spectrum at $y=0.2$ -inch is now showing a low frequency bulge. This bulge builds in strength further out from the wall. These spectra show a band of turbulence energy that shifts with increasing y

from a high frequency to a lower frequency. At $y=0.8$ -inch this lower frequency bulge is the peak in $\bar{\phi}_v(\omega, y)$ and is thus the major contributor to the v fluctuations.

Having shown the variations in spectral content that occur across the boundary layer the variations in spectral content as a function of streamwise location, at the same wall distance, will be shown. This allows the streamwise evolution of the turbulence spectrum that occurs at a given wall distance to be seen more clearly. These are shown in figures 4.23 through 4.27.

Downstream of reattachment the recovery of a double peak character in the near-wall measurements of $\bar{\phi}_u$ is very evident. This is shown in figure 4.23(a). In addition, the development of an inertial region where the spectra $\bar{\phi}_u$ scale as $k^{-5/3}$ can be seen quite clearly. For example, at $y=0.4$ -inch, the inertial region is first obtained at $x/h=10$ and is present to the last measurement location (see figure 4.25(a)). At $y=0.8$ -inch this region does not begin to be present until $x/h=24$ but extends downstream to $x/h=54$ (see figure 4.26(a)). $\bar{\phi}_v(\omega, y)$ measured nearest the wall maintains the same spectral shape for all streamwise locations. The v spectra further away from the wall show the same general trend of being broader in frequency content downstream of reattachment.

4.4.4 Length Scales

The purpose in examining the spectral features of the velocity fluctuations is to obtain a measure of the spatial scales that are present in the turbulence field. This amounts to a description of the distribution of eddy sizes that make up the fluctuations. The transformation between fluctuations in time (frequency) and eddy size is made using Taylor's hypothesis. With this approach, the frequency spectra that have been presented can also be viewed as wavenumber spectrum or an eddy size spectrum of the eddies that are convected past the measurement location. The same transformation can be used to obtain various turbulence length scales from the frequency spectrum measurements.

The integral length scale of turbulence, L_1 , is defined as the integral of the broadband spatial correlation function over all separation distances,

$$L_1 = \int_0^{\infty} R_1(r) dr \quad (4.6)$$

where, $R_1(r)$ is the correlation function.

This length scale is interpreted to be a measure of the "typical" eddy size of the energy-containing eddies that compose the turbulence field (Bradshaw (1971)). Relation (4.6) can be expressed in terms of the frequency spectrum as,

$$L_1 = \lim_{\omega \rightarrow 0} \left[\frac{U_c \phi_1(\omega)}{\pi u_1'^2} \right] \quad (4.7)$$

where U_c is the eddy convection speed, which is taken here to be the local mean velocity (see Hinze (1975) or Blake (1984) for detailed discussions). The overall validity of expression (4.7), in light of the actual definition (4.6), can be questioned since the use of a Taylor's hypothesis implies that the temporal and spatial scales are simply equated by a single convection velocity and that this convection velocity is not frequency dependent and does not account for dispersive effects of the flow field. Additional problems in using (4.7) arise in obtaining the value of the spectrum in the limit of zero frequency.

Regardless, relation (4.7) does define an integral scale of the turbulence field which is on the order of the length scale of the energy-containing eddies. Values of L_1 and L_2 , the streamwise and vertical length scales respectively, were computed from the $\phi_1(\omega, y)$ spectra by using a 10 point ($f \leq 12.5$ Hz) least square fit extrapolation to obtain the value of the spectrum at zero frequency. These values are shown in figures 4.28(a) and 4.28(b) normalized by boundary layer displacement thickness and plotted against the wall distance in units of displacement thickness.

The streamwise length of the energy containing eddies is always less than the boundary layer thickness ($\delta \approx 8\delta^*$) but greater than δ^* . L_1 increases away from the wall and is larger than L_2 . Downstream of

reattachment L_1/δ^* continually increases in the streamwise direction but is always less than the values for the upstream equilibrium flow. The vertical length scale is a maximum at about $2\delta^*$ to $3\delta^*$. The fact that L_2 is always smaller than L_1 is additional evidence that the v spectra is more dominated by higher frequency components than is the u spectra. Downstream of reattachment the peak in the L_2 profiles moves away from the wall with downstream position. At $x/h=54$, L_2/δ^* is approximately the same as the upstream (equilibrium) values except near the wall. The presence of the wall seems to be limiting the vertical size of the energy-containing eddies. However, at the closest wall positions L_2 is greater than the wall distance ($L_2/\delta^* > y/\delta^*$).

Since there is an integral length scale representative of the size of the energy-containing eddies, there is also a length scale that provides a measure of the smallest eddy sizes that are present in the turbulence. This scale is termed the Taylor microscale and was originally equated to a dissipation length scale of the turbulence. Tennekes and Lumley (1972) point out that this length scale does not actually represent the scale at which turbulence is dissipated since it is derived using a velocity scale that is not relevant to the dissipative eddies. This length scale does, however, provide a measure of the smaller scale eddies that are present. The microscale, λ_1 , can be obtained from the frequency spectrum as,

$$\frac{1}{\lambda_1^2} = \frac{1}{U_1^2 U_c^2} \int_0^\infty \omega^2 \Phi_1(\omega) d\omega \quad (4.8)$$

where $U_c = U(y)$ (see Hinze (1975) and Blake (1984)).

Values of λ_1 were calculated from the spectra using equation (4.8) and were found to be essentially a constant for each of the two microscales (u and v microscales). This indicates that the smallest length scales that were measured were not controlled by a viscous limit in the flow but by the finite size of the hot wire. The highest frequency portions of the velocity spectra are thus in error due to spatial averaging effects. If the microscale is accepted as being the smallest scale that was measured then it can be used to estimate the

high frequency limit of the velocity data. With this the u spectra are not valid above approximately 8,000 Hz and the v spectra are in error above approximately 12,000 Hz. (These limits do not affect the interpretations of the data since the phenomena that is of interest and discussed occurs below these frequencies.) The values of the microscales are smaller than the integral length scales showing that the small scale limit, imposed by the size of the hot wire, does not bias the measurement of the energy-containing eddies.

4-5 Discussion of the Structure of the Flow

4.5.1 Physical Features of the Step Flow

The objective of this study is to experimentally investigate the wall pressure field beneath a non-equilibrium turbulent boundary layer and identify turbulence structures in the flow that contribute to the source term of the wall pressure field. Fully developed turbulent boundary layer flow over a backward-facing step was selected as the flow geometry to provide the non-equilibrium or perturbed boundary layer. At reattachment the flow is highly energized and this energized state persists far downstream. This energized flow undergoes extensive relaxation and redevelopment as it moves downstream. It is this relaxation region that is of primary interest in this investigation.

Details of the separation and reattachment process, in the vicinity of the step, are not specifically addressed in this investigation. However, certain details of this process must be known in order to understand the characteristics of the non-equilibrium (perturbed) boundary layer that is to be studied.

Extensive research has been conducted on flow over backward-facing steps to better understand the details of the turbulent flow. Most notable are the studies conducted at Stanford University (Kim, Eaton, Pronchick, Westphal, and Adams in the references) and those conducted under P. Bradshaw at Imperial College, London. From these studies a fairly consistent description can be given of the development of the flow field and this will briefly be described.

The boundary layer that exists at the top of the step separates as it passes over the edge forming a free-shear layer. At separation the state of the onset boundary layer (laminar/turbulent) and the thickness of the boundary layer, relative to the step height, are important initial conditions that can influence the development of the free-shear layer (Bradshaw and Wong (1972), Chandrusda and Bradshaw (1981), and Eaton and Johnston (1981b)).

The free-shear layer grows through entrainment as it convects downstream. Similarities are made between the free-shear layer that forms and that of a plane mixing layer. The degree of similarity depends strongly on the initial conditions at separation. One important difference between this free-shear layer and a plane mixing layer is that the fluid that is entrained beneath the free-shear layer is not quiescent, as it is for a plane mixing layer, but is recirculating flow from the reattachment point. This recirculated flow increases the turbulence levels in the free-shear layer. Initially, turbulence stresses in the free-shear region are highest along the dividing streamline of the flow. As the shear layer grows and starts to feel the presence of the downstream wall the dividing streamline rapidly curves towards the wall. The line of maximum turbulence stresses, however, move towards the wall more slowly, thus deviating from the dividing streamline.

The location at which the free-shear layer "reattaches" is unstable due to unsteadiness in the flow. This causes the reattachment point to fluctuate in the streamwise direction. This produces a "region" of reattachment, instead of a point, which is approximately two step heights wide.

At reattachment, the inner region of the velocity profile has some of the characteristics of an attached, newly forming boundary layer, while the outer region of the boundary layer has the characteristics of the outer region of the upstream flow. A major new feature of the inner layer of the velocity profile is a region of high turbulence activity produced by the attached free-shear layer.

There are rapid changes in the turbulence structure of the flow field at reattachment. Vortical motions in the approaching free-shear layer are rotated and distorted as the reattachment region is approached. This distortion results in a rapid redistribution of turbulence energy (Etheridge and Kemp (1978)). The large scale eddies in the free-shear layer, which produce much of the turbulent shear stress, are brought near the wall where the turbulence motion is confined. These eddies are torn in two near reattachment as the flow splits into an upstream moving flow and a downstream moving flow. This results in a rapid reduction in turbulence activity and reduction in turbulence length scale. Immediately downstream of reattachment the flow is a greatly distorted form of the upstream free-shear layer. Due to these effects, the turbulence mixing length near the wall increases faster than κy near the wall as shown in figure 4.18.

Downstream of reattachment, this region of high turbulence slowly decays and propagates away from the wall. It requires many step heights of downstream redevelopment before the disturbance decays and the non-equilibrium boundary layer returns to an ordinary boundary layer condition. Figure 4.29 is a diagram of the flow over a backward-facing step illustrating some of these details.

These features are present in the velocity data of the current investigation. Few of the previous backward-facing step studies have addressed the details of the flow far downstream of reattachment. The furthest downstream location at which velocity information was obtained in this study is $x/h=54$. At this location, the flow still has not relaxed to an ordinary state. It is estimated that a downstream distance of over 100 step heights is needed before an equilibrium flow conditions will occur.

It will be argued in this discussion that the non-equilibrium condition of the flow field is a result of the placement of a region of highly turbulent flow, namely the free-shear layer, near the wall and that this region grows away from the wall in a manner that is, in many ways, analogous to the growth of an internal or disturbance layer after

a step change in surface roughness. Full boundary layer recovery will not occur until this layer has fully propagated through the existing boundary layer.

4.5.2 Propagation of the Disturbance Layer

As stated earlier, the boundary layer redevelopment downstream of reattachment has characteristics that are similar to the redevelopment of a turbulent boundary layer after a step change in surface roughness. In the near wall region both flows have a "disturbance layer" with turbulence stress levels that are markedly different from those for the flow away from the wall. This wall region of high stress propagates outward as the flow convects downstream. Boundary layer redevelopment will not be complete until the internal layer has propagated all the way through the original boundary layer.

The response of turbulent boundary layers to changes in surface roughness have been studied by: 1) Antonia and Luxton (1971 a,b), for a change from smooth-to-rough; 2) Antonia and Luxton (1972), for a rough-to-smooth change; 3) Andreopoulos and Wood (1982), for a nearly impulsive change in surface roughness. For configurations 1) and 3) the step change increases the turbulence stress at the wall, while for configuration 2) the turbulence wall stress is reduced after the step change. In configuration 3), with an impulse change in roughness obtained by a short region of wall roughness, the region of increased wall stress occurs over a short streamwise distance. For this configuration, the downstream flow contains two disturbance or internal layers, one developing from the smooth-to-rough change and the other from the rough-to-smooth change. This flow has characteristics that are rather unique from either of the one way surface roughness changes of configurations 1) and 2).

The turbulence characteristics downstream of reattachment are most similar to those for configuration 2), a rough-to-smooth step change in surface roughness. Both flows initially have a highly stressed boundary layer that redevelops downstream over a smooth wall. However, there are certain characteristics of configuration 3), the impulsive change in roughness, that are similar to the backward-facing step flow. The flow

for an impulsive change also has development of a highly stressed layer but, in this case the highly stressed flow is not as well developed as the rough-to-smooth change since it only develops over a short streamwise distance.

Obviously the strength of the perturbation that is introduced to a turbulent boundary layer by the placement of a mixing layer near the wall is much stronger than that caused by a change in surface roughness (excluding the case of very large roughness which then is similar to flow over steps). Furthermore, for flow over a backward-facing step the region of maximum stress does not begin at the wall but at a position close to the wall (at $x/h=10$ the wall position of maximum $\overline{u'v'}$ is $y/h=0.5$). The outer flow region at reattachment is also different from that of an equilibrium boundary layer.

In the following discussion, the characteristics of turbulence profiles measured downstream of reattachment will be compared to those obtained for both the rough-to-smooth and impulsive changes in surface roughness.

The turbulence profiles shown in figures 4.13-4.16 exhibit a region of excess turbulence activity that moves away from the wall in the downstream direction. Decay of the turbulence activity accompanies the outward propagation. This region of high turbulence stresses is the remnants of the attached free-shear layer. At $x/h=10$ the region is fairly narrow and is located at $y/h=0.5$. As it propagates away from the wall it broadens and decays. By $x/h=54$ a specific peak is not obvious but the center of the excess stress region is at approximately $y/h=1.4$.

The turbulence profiles show an actual propagation of the high stress layer across the boundary layer, as opposed to there being increased stress levels throughout the boundary layer which decay in level from the wall outward. At $x/h=10$ the turbulence levels in the outer part of the boundary layer are lower than they are further downstream supporting the statement that the disturbance layer propagates away from the wall as it convects downstream.

These characteristics are similar to those obtained by Andreopoulos and Wood (1982) for an impulsive change in surface roughness (figure 8 in the reference). For both flows, a region of excess stress propagates across the boundary layer. Andreopoulos and Wood termed this phenomena a "stress bore", borrowing a term applied to a similar phenomena that occurs following an impulse of convex surface curvature. Another interesting similarity is the variation of the turbulence stress correlation coefficient. The coefficients are remarkably constant (at $R_{12}=0.4$) increasing only slightly away from the wall as do the coefficients in this investigation (figure 4.17). The decay rates of the region of excess turbulence stress in the impulsive change investigation will be shown later to be similar to those of the current investigation.

In the study of Antonia and Luxton (1972), a rough-to-smooth step change in surface roughness, the region of excess turbulence stress is not as dramatic as for an impulsive change in surface roughness. However, many of the features of the boundary layer development downstream of the surface change compare favorably to those downstream of reattachment. Antonia and Luxton also pointed out the similarities that exist between a rough-to-smooth flow and flow over a surface fence between. They attributed the similarities to the fact that both flows experience a decreased rate of strain after the perturbation.

The mean velocity profiles downstream of the step change in surface roughness (Antonia and Luxton (1972)) follow the same development pattern as the profiles of figure 4.7; initially the extent of the wall region that scales on a log-law behavior is very limited and the outer flow has a strong wake-like character. Downstream the log-law region grows and at the most downstream position ($x=46$ -inch), the log-law region extends over about one decade. Antonia and Luxton found that for this type of flow the additive constant in the log-law relationship is not a constant but varies from a value of approximately 15, immediately aft of the step change, to a value of 6.9, at the last measurement station, which is still larger than the universal value of 4.9. (This leaves in question the values of wall shear stress that are obtained

assuming a universal type of log-law relationship near the wall). At their last measurement position ($x/\delta=16$) the flow was still far from being self-preserving. The values of skin friction coefficient, although reduced below the rough wall value, continually increased downstream. The boundary layer shape factor decreased with downstream position. These are the same trends found in the current investigation (figures 4.8-4.10).

Antonia and Luxton (1972) found that the mean velocity profiles, when plotted in the form of U/U_0 versus $y^{1/2}$, followed a half-power line near the wall and then followed another half-power line, but of different slope, further out in the boundary layer. Although they state that there does not seem to be any physical basis for plotting the profiles in these coordinates they used plots of this form to locate the edge of the disturbance layer that grows out from the step change in surface roughness (this plotting technique is actually borrowed from their earlier work on smooth-to-rough step changes, Antonia and Luxton (1971b), where it does have technical merit). They define the outer edge of the disturbance layer as the position where the two half-power lines intersect. Using this technique they established that the disturbance layer grew at the rate of $\delta_d = 10.3 \cdot x^{0.43}$ (inches).

This plotting technique was applied to the profiles downstream of reattachment as shown in figure 4.30. There are two regions in each profile that scales as $y^{1/2}$. δ_d is taken as the point of intersection of the lines drawn through the $y^{1/2}$ regions. The values of δ_d obtained in this manner are plotted, in figure 4.31 against a dimensionless streamwise distance downstream of reattachment, $X=(x-x_r)/h$. By plotting against X , one assumes that the internal layer begins at reattachment. Included in figure 4.31 are the locations of the peaks in the turbulence shear stress profiles. The values of δ_d follow a $\delta_d/h = 0.22 \cdot X^{0.47}$ line quite well. The locations of peak turbulence shear stress also follow this line but are located slightly above the the edge of the internal layer.

The $x^{0.47}$ growth rate is very similar to the rate of $x^{0.43}$ for the rough-to-smooth step change obtained by Antonia and Luxton (1972). Antonia and Luxton (1971a) also obtained an internal growth rate of $x^{0.5}$ after an upstanding smooth-to-rough step change in surface roughness. However, when the top of the roughness elements were shifted down to being flush with the upstream smooth wall a growth rate of $x^{0.8}$ was obtained (Antonia and Luxton (1971b)).

It is interesting to look at where in the velocity profiles the disturbance layer is located. The locations of the disturbance layer are marked with an "x" in each profile of figure 4.6 and are flagged in each profile of figure 4.7. The edge of the disturbance layer generally corresponds to a position prior to the start of the wake region. The region that dips below the log-law line is within the disturbance layer. Similar comparisons with the mixing length plots show that δ_d corresponds to the location where l_m becomes constant. Since δ_d is below the peak stress position, the large mixing lengths that are measured for $y/\delta < 0.2$ are due more to a reduced dU/dy than to high levels of shear stress since the shear stress has yet to peak at this y position.

The location of δ_d does not correlate with any specific trend in the plots of streamwise integral length scale (L_1). The location of δ_d , however, is generally close to the location of the peak in the vertical length scale (L_2). Upstream of $x/h=24$ δ_d is just below the L_2 maximum and downstream of $x/h=24$ it is just above the maximum.

Using the disturbance layer growth rate given in figure 4.31 an estimation can be made of the downstream distance that is needed for the flow to return to a fully equilibrium state. Assuming that the boundary layer thickness remains constant at the $x/h=54$ value (approximately 1.5-inch) further downstream, then it will take approximately $250h$ before $\delta_d/\delta=1$. This is a rough estimation which surely exceeds the range of applicability of the δ_d data fit but does demonstrate the order of magnitude that is needed for full recovery of the boundary layer.

An estimation of the decay rate of the turbulence stresses was obtained by plotting the maximum stress levels as a function of streamwise position. All of the stress levels (Q) were normalized by the value of stress (Q_{ref}) at $x/h=10$ and plotted against X/X_0 ($X_0=X$ at $x/h=10$, where $X=(x-x_p)/h$) as shown in figure 4.32. This allows a direct comparison of the decay rate of all stresses. The RMS velocity profiles downstream of $x/h=24$ were too broad to ascertain the location of their peak, so the peak was always taken as the y value where the turbulence shear stress peaked. Values of $\overline{u'v'}$, u'^2 and v'^2 from the x-wire and values of u'^2 from the single wire are all included in the plot. Also included are peak values taken from the turbulence stress profiles of Andreopoulos and Wood (1982) for the flow downstream of the impulse change in surface roughness. The peak values in that investigation followed the growth of the internal layer associated with the rough-to-smooth change. Data from that study are normalized in the manner described above using as a reference the first shear stress profile for which there is a discernible peak. All of the data follow a $X^{-1/2}$ decay rate quite well. This, interestingly, is also the decay rate for a plane wake. The spreading rate for a plane wake $X^{1/2}$, is also close to the propagation rate measured for the disturbance layer.

4.5.3 Spectral Data

The spectral data provide additional information on the structure of turbulence in the relaxing flow. Features of the u spectra are different from those for the v spectra. The u spectra have characteristics that reflect the passage of a region of highly turbulent flow across the boundary layer. These features are not explicitly seen in the v spectra but instead spectral variations associated with a shift of turbulence energy, with increasing wall distance, from high frequency to low is seen in the v spectra.

There are two distinct features in the $\Phi_u(\omega, y)$ plots that warrant attention. The results in the region near the wall (for example figure 4.23(a), $y=0.03$ -inch) show a double peak in the spectra which is only

found at specific streamwise locations; and a spectral region where $\Phi_u(\omega, y)$ scales as $\omega^{-5/3}$. This second region is identifiable at most downstream locations away from the wall.

Consistent with the earlier discussion the spectra measured at $x/h \approx 12$ (figure 4.19(a)) show a double peak near the wall which shifts to a ω^{-1} slope region slightly further out from the wall. Far from the wall, there is a spectral region that scales as $\omega^{-5/3}$. Near the wall, in the buffer layer, the kinetic energy production term, $\overline{u'v'} \cdot dU/dy$, is large due to the large dU/dy term. This precludes establishing an inertial range of wavenumbers in which the turbulence spectrum scales as $k^{-5/3}$. Tchen (1954) has shown that in this region the spectrum of turbulence should scale as k^{-1} (ω^{-1}).

It is apparent in the data that downstream of reattachment the spectra contain extended regions of $k^{-5/3}$ scaling that are associated with the high stress layer. Figure 4.23(a) (spectra at $y=0.03$ -inch) shows that $\Phi_u(\omega, y)$ at $x/h=10$ has a limited region that scales as $\omega^{-5/3}$ but further downstream the spectra flatten out and by $x/h=36$ have returned to a spectral shape similar to that measured upstream. Of the spectra in this figure the disturbance layer is nearest the wall for the $x/h=10$ spectrum ($\delta_d \approx 0.23$ -inch). This result shows that the turbulence Reynolds number of the disturbance layer is high enough to produce an inertial wavenumber range even near the wall. Hence, the vertical distance over which the high stress layer has an influence extends to near the wall (see figure 4.16). However, by $x/h=16$, the naturally growing sublayer has developed enough for the dU/dy term to again be dominant near the wall, preventing a $k^{-5/3}$ scaling.

As shown above, the near wall region returns to an equilibrium condition fairly rapidly. This is evident in both the profiles and velocity spectra. Rapid recovery is a result of two effects. First, turbulence length scales in the wall region are typically small while at the same time the turbulence production rate is large which makes the adjustment time in the wall region very short. Secondly, the disturbance layer moves away from the wall taking the source of highly

turbulent activity with it. If the high stress region were not to propagate away from the wall the recovery time for the wall region would be longer.

Figure 4.24(a) show the spectra at $y=0.1$ -inch for various downstream locations. In these data, the upstream spectrum scales as ω^{-1} near the peak of $\bar{\psi}_u(\omega, y)$, which is the frequency region that contributes the greatest percent of the mean-square fluctuation. For the downstream locations $x/h=10$ through $x/h=24$, there is a spectral region that scales as $k^{-5/3}$. This region, which is representative of an inertial range of wavenumbers, starts immediately after the peak in the spectral function. Further downstream this spectral region scales closer to $k^{-4/3}$. The same trends are seen for the $y=0.4$ -inch spectra (figure 4.25(a)) except that the region of $k^{-5/3}$ scaling is strongly evident further downstream. The disturbance layer is located at about $y=0.4$ -inch at $x/h=24$. Again, the broad range of x/h locations for which there is a spectral region of $k^{-5/3}$ scaling is indicative of the spatial extent of the high stress layer.

At $y=0.8$ -inch (figure 4.26(a)) the regions of strong $k^{-5/3}$ have moved even further downstream such that both the $x/h=10$ and $x/h=16$ spectra scale at a rate less than $k^{-5/3}$. This also results in an apparent shift of energy content to lower frequency. The edge of the disturbance layer is below this y location for all x/h but still influences the spectra for $x/h>24$.

By $y=1.5$ -inch (figure 4.27(a)) the spectra at all x/h locations show a reduction in spectral bandwidth. This y location is less than δ at $x/h=10$, approximately equal to δ at $x/h=54$ and greater than δ for all other locations. However, δ is defined as the $0.99U_0$ location which is still within the intermittent outer flow region. The broader shape of the spectra at $x/h=10$ and 54 is due to strong intermittent flow that occurs at this location in the boundary layer. No inferences can be made about the influence of the high stress layer from these spectra. The spectral shapes at $y=1.5$ -inch are similar to those obtained by Cherry et al. (1984) in the outer flow region of a boundary layer

downstream of a separated/reattached flow. Interestingly the peak in their furthest downstream spectrum occurs at approximately the same ω/U_0 as the peaks in $\tilde{\phi}_u(\omega, y)$ shown in figure 4.27(a).

The discussion of the v spectra centers on the variations that occur in three frequency regions: a high frequency region, ($f > 1000$ Hz); a mid-frequency region, ($100 \leq f \leq 1000$ Hz); and a low frequency region, ($f < 100$ Hz). In contrast to the u fluctuations, the v fluctuations have a spectrum that is shifted to higher frequencies with increasing downstream distance. The spectral levels of the v fluctuations are never larger than the u levels but the downstream spectral content of the v fluctuations is richer in higher frequency components. This occurs at the expense of reduced spectral levels at low frequency. The v spectra depend more on wall location than on the presence of the high stress layer in the flow.

At a fixed streamwise location, in moving from the wall out, the spectral content of the v fluctuations slowly shifts from the high frequency region to the mid-frequency region while the levels in the low frequency region initially increase and then decrease. This behavior is demonstrated in figure 4.21(b) ($x/h=24$). A composite plot of all y location spectra would show a predominate band of turbulence energy that slowly sweeps from high frequency to lower frequency as wall distance is increased. However, at $y=1.5$ -inch, which is generally beyond the edge of the boundary layer (δ), the v spectra have the same band-limited character as the u spectra and peak at the same frequency, of approximately 200 Hz (depending on x/h location, see figure 4.27(b)).

At the closest wall position ($y=0.03$ -inch, figure 4.23(b)) each of the spectra at the downstream x/h location are similar in shape except that the high frequency region decreases in level slightly with increasing x/h . At $y=0.1$ -inch (figure 4.24(b)) the $x/h=-12$ spectrum was the highest spectrum in the high frequency region. The spectrum at $x/h=10$ is the lowest in the high frequency region and at all further downstream locations the spectra are equal in level but below that of the upstream spectrum. In the mid-frequency region the spectrum at

$x/h=10$ is highest and this level decreases with increasing x/h . This is consistent with the rapid recovery of the wall region that is seen in the u spectra.

The streamwise variations in the v spectra at $y=0.4$ and 0.8 -inch (figures 4.25(b) and 4.26(b)) are similar. The high frequency region for the downstream spectra are about equal and below that for the upstream spectrum. The downstream mid-frequency regions are higher than for the upstream spectrum. The low frequency part of the spectra slowly increase with downstream location.

The most distinguishing feature of the v spectra is the shift toward lower frequency with increased wall distance. No specific correlation with the high stress layer could be found that would explain this trend. The low frequency bulge that characterizes this shift is not seen in the upstream spectra and is thus assumed to be associated with flow over the step. The shift to lower frequency away from the wall is consistent with the view that large scale disturbances are present in the flow, due to the separation and reattachment process, and that the vertical size of these disturbances is limited by the presence of the wall. Basically, the vertical extent of a given disturbance can not be greater than the distance it is from the wall. As you move further from the wall the disturbances that are present can be larger. These larger disturbances are measured as lower frequency fluctuations.

This contention is partly supported by the plots of vertical integral length scale that also increased away from the wall. The lack of correlation with the location of the region of high stress is probably due to the wall distance limitations being a stronger criteria than the physical location of the disturbance source in the flow for the v fluctuations.

It should be pointed out that the spectra are normalized by the mean-square of the fluctuations so that in dimensional units the velocity spectrum at the location of the high stress layer will have maximum levels. In this regard, all of the spectra reflect the presence of the high stress region. What has been discussed is the variations in spectral content that occur with wall distance and streamwise location.

4.5.4 Summary

In summary, the reattachment process places a highly turbulent, highly energized region of flow near the wall. This region initially has characteristics that are remnants of the original mixing layer. Downstream this region propagates away from the wall. As it propagates it also decays in level. Recovery of the boundary layer to an equilibrium condition will not occur until the layer has fully propagated across the boundary layer. Recovery of an equilibrium condition occurs fairly rapidly near the wall where the memory period of turbulence is short due to the high levels of turbulence production and small turbulence scales. The outer region of the flow recovers much more slowly.

As shown by the u spectra the high stress layer is a region in the flow where the turbulence Reynolds number is locally high. u spectra measured in the vicinity of the high stress layer show a broad spectral region that scales as $k^{-5/3}$, characteristic of a high turbulence Reynolds number flow. The v spectra on the other hand do not show this region. Instead the v spectra show a shift in energy content from high to mid-frequency with wall distance.

Table 4.1 - Boundary Layer Properties

x/h	U_0 (ft/sec)	δ (inch)	δ^* (inch)	θ (inch)	H	u^*/U_0	G	$C_f \times 10^3$	$C_{fm} \times 10^3$
-12	81.5	0.918	0.132	0.101	1.31	0.0411	5.776	3.378	3.514
-12	50.4	0.875	0.130	0.097	1.34	0.0435	5.838	3.778	3.863
-2	50.4	0.789	0.114	0.084	1.36	0.0444	5.915	3.950	3.911
(z/h= 0)									
-2	50.4	0.724	0.109	0.079	1.37	0.0443	6.095	3.919	3.894
(z/h= 6)									
-2	50.4	0.709	0.104	0.076	1.36	0.0446	5.976	3.987	3.968
(z/h=-6)									
10	82.1	2.048	0.261	0.178	1.47	0.0325	9.880	2.109	2.253
10	50.4	1.804	0.269	0.176	1.53	0.0329	10.461	2.167	2.466
16	82.2	1.015	0.191	0.135	1.41	0.0382	7.597	2.914	2.785
16	50.6	1.131	0.219	0.150	1.46	0.0381	8.203	2.909	2.868
24	81.4	1.199	0.208	0.155	1.34	0.0389	6.521	3.031	2.996
24	50.2	1.275	0.219	0.157	1.40	0.0398	7.120	3.168	3.119
36	81.7	1.389	0.213	0.161	1.33	0.0389	6.338	3.033	3.023
36	50.4	1.293	0.216	0.160	1.36	0.0404	6.502	3.271	3.294
54	82.1	1.536	0.206	0.160	1.28	0.0406	5.447	3.289	3.237
54	50.6	1.472	0.225	0.171	1.31	0.0415	5.763	3.449	3.451
54	50.4	1.627	0.219	0.166	1.32	0.0415	5.856	3.442	3.448
(z/h= 0)									
54	50.4	1.360	0.207	0.155	1.33	0.0413	6.028	3.409	3.452
(z/h= 5)									
54	50.4	1.397	0.218	0.162	1.34	0.0410	6.222	3.366	3.351
(z/h=-6)									
Equil. Flow	93.3	1.095	0.169	0.124	1.36	0.0379	6.936	2.867	2.871
Equil. Flow	50.8	1.097	0.177	0.128	1.38	0.0403	6.828	3.255	3.229

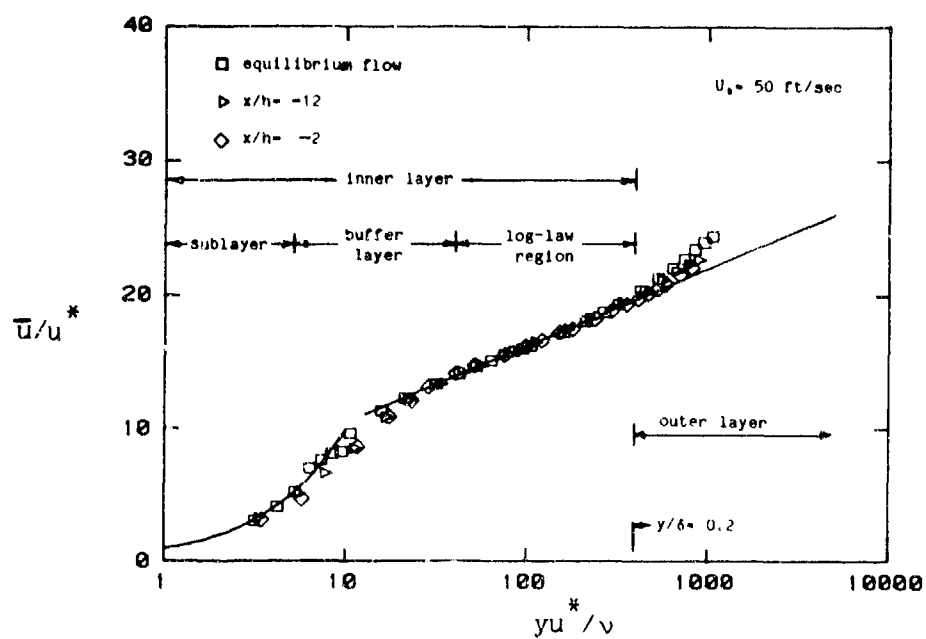


Figure 4.1 Mean Velocity Profiles (Wall Law) for Equilibrium Flows

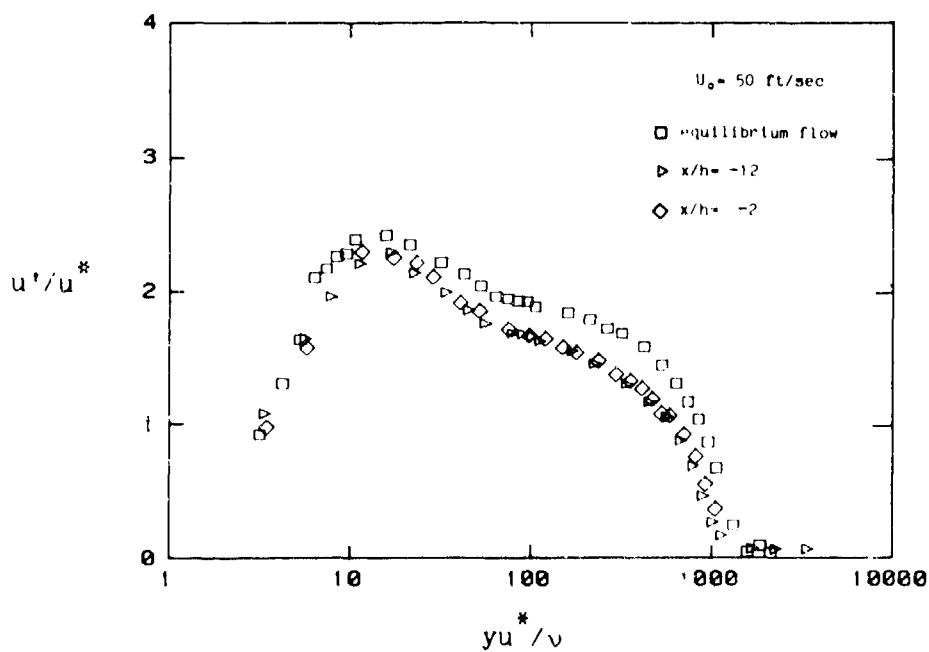


Figure 4.2 Turbulence Intensity Profiles for Equilibrium Flows

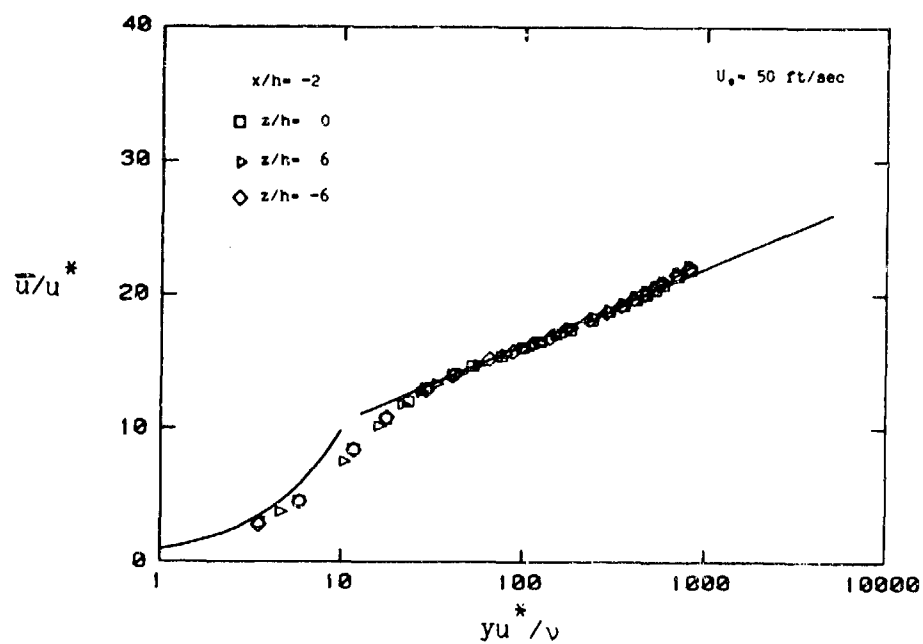


Figure 4.3 Mean Velocity Profiles (Wall Law)
at $x/h = -2$ and $z/h = 0, -6, +6$

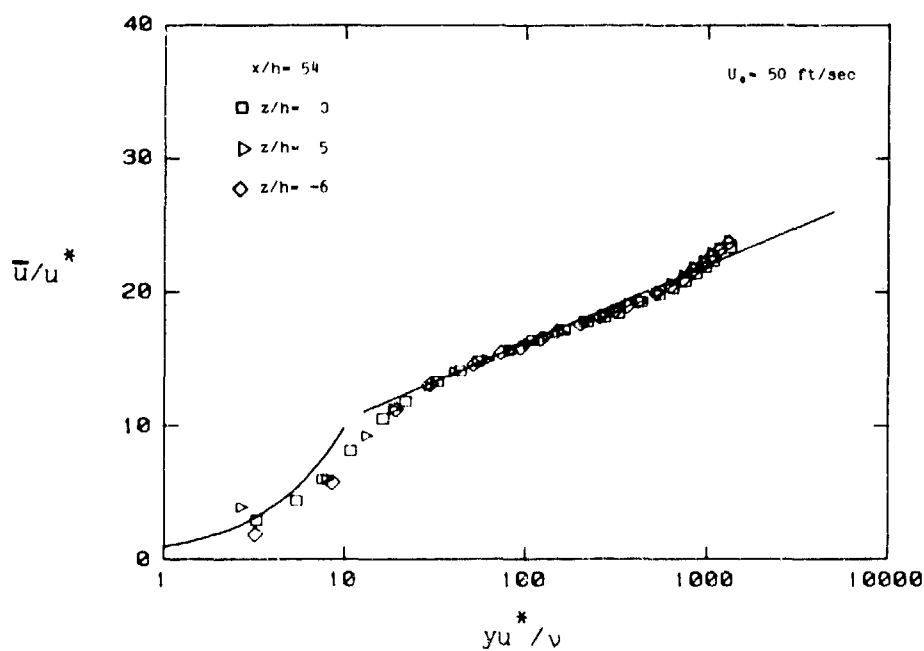


Figure 4.4 Mean Velocity Profiles (Wall Law)
at $x/h = 54$ and $z/h = 0, -6, +5$

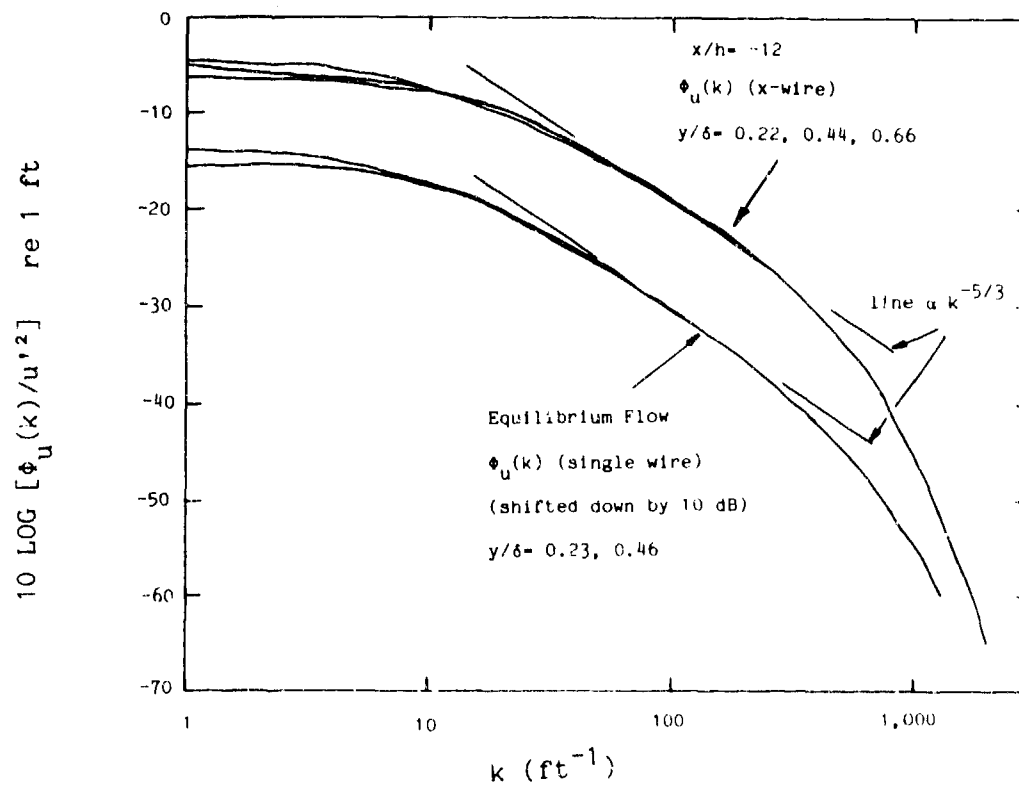


Figure 4.5 Streamwise Velocity Spectra for Equilibrium Flows

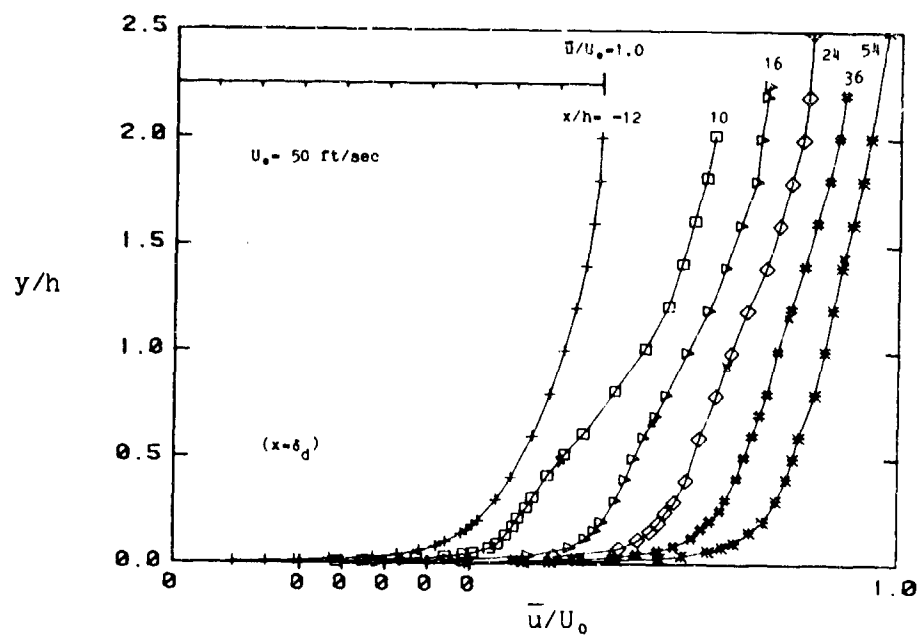


Figure 4.6 Mean Velocity Profiles at Downstream Locations

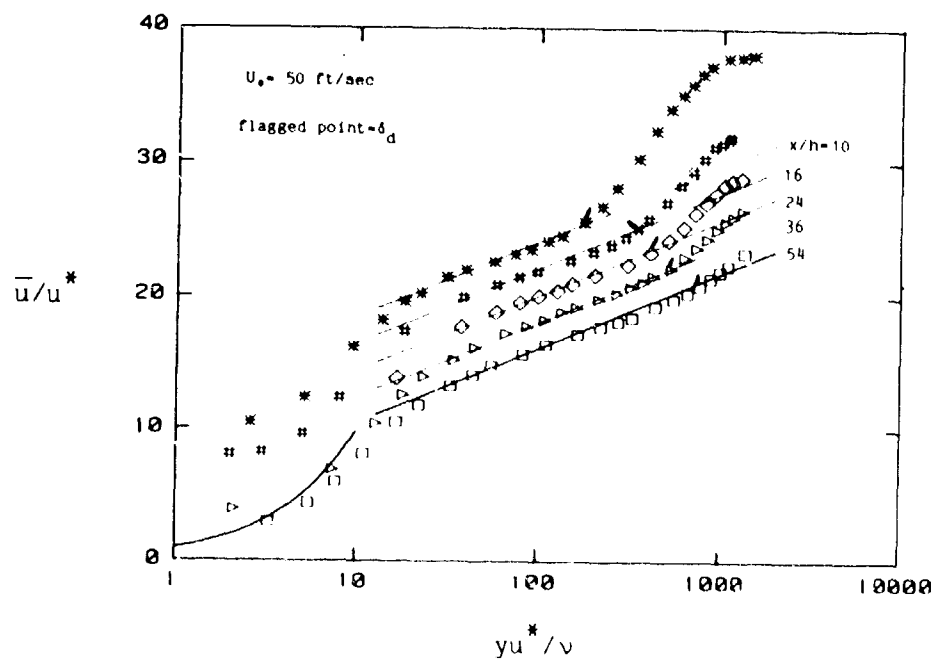


Figure 4.7 Mean Velocity Profiles (Wall Law) at Downstream Locations

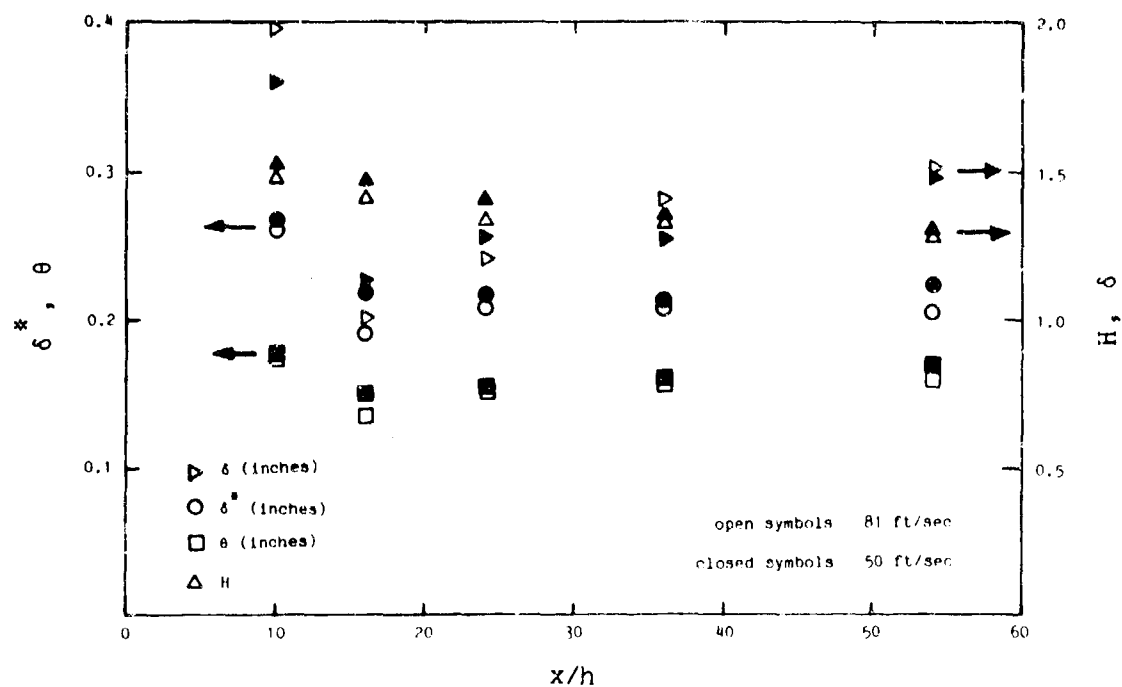


Figure 4.8 Streamwise Variations in Boundary Layer Properties

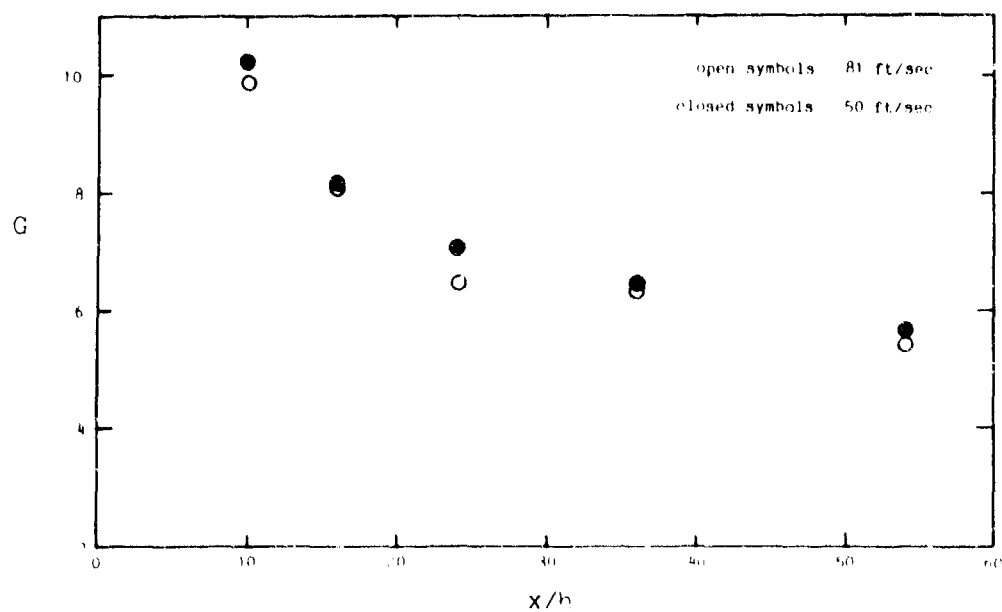


Figure 4.9 Streamwise Variations in Clauser Parameter

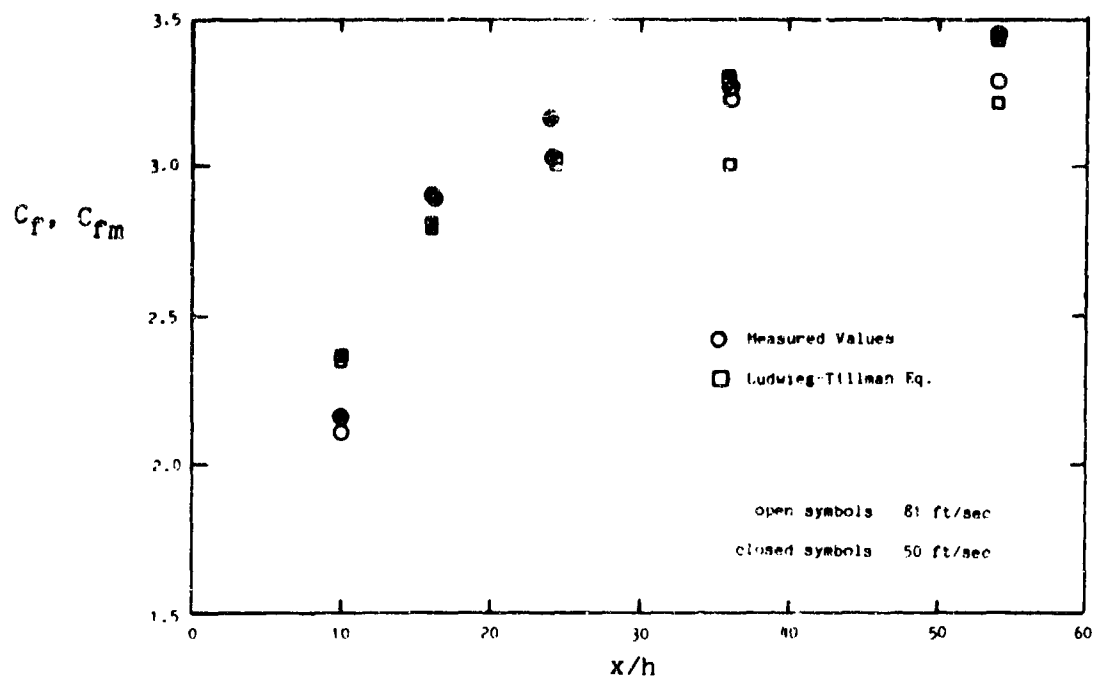


Figure 4.10 Streamwise Variations in Skin Friction Coefficient

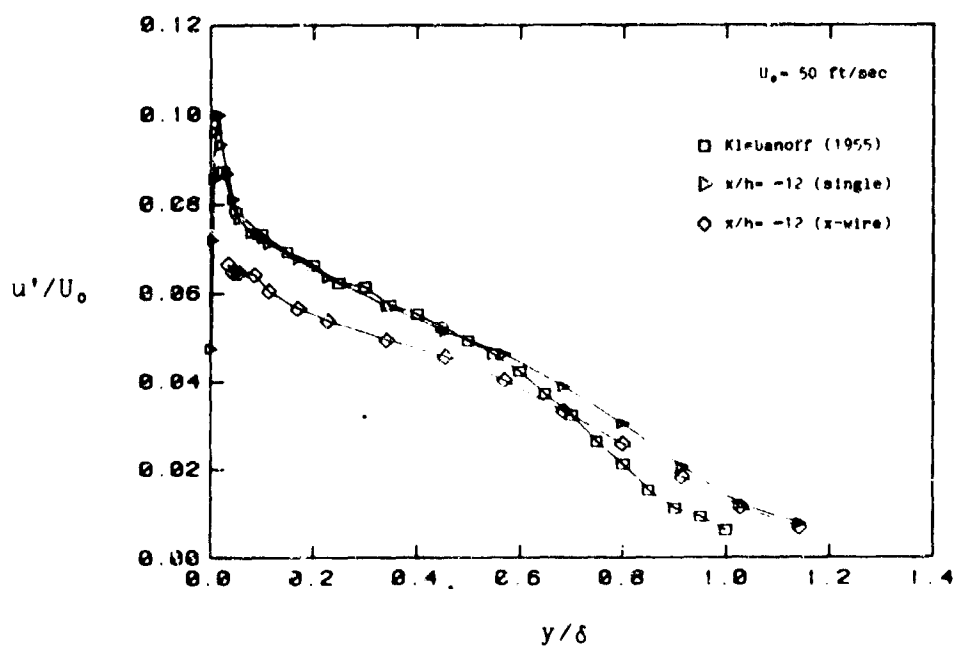


Figure 4.11 Turbulence Intensity Profiles For Equilibrium Flows

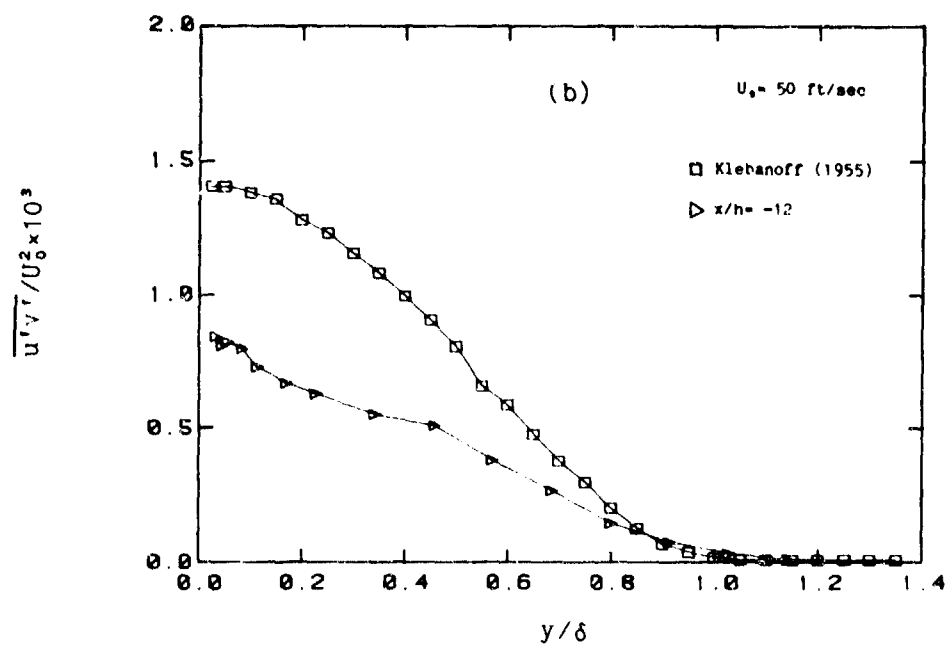
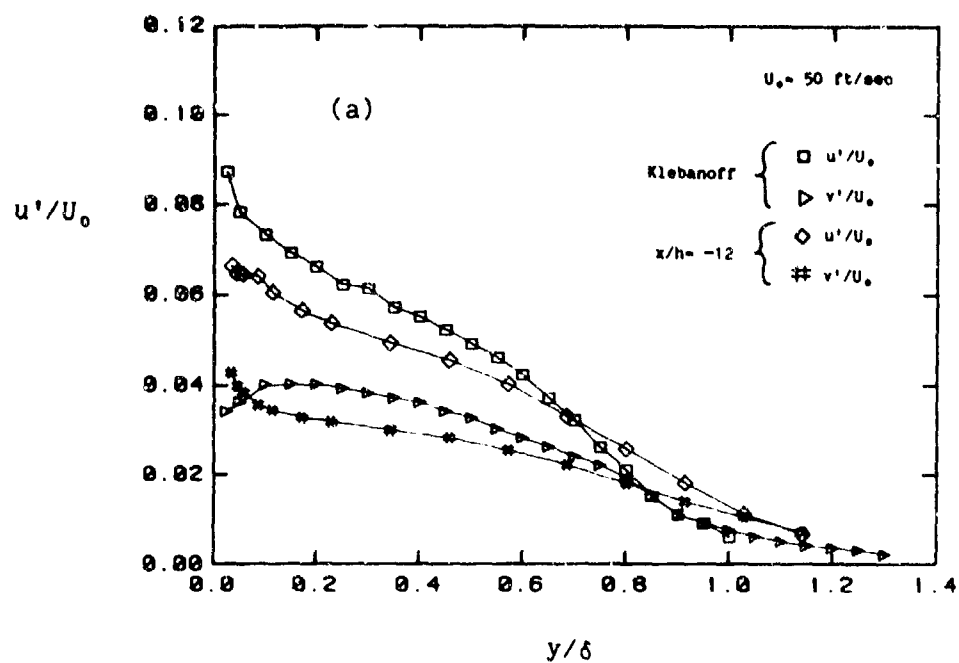


Figure 4.12 Comparison of Turbulence Profiles with Klebanoff (1955)
(a) Turbulence Intensities; (b) Turbulence Stress

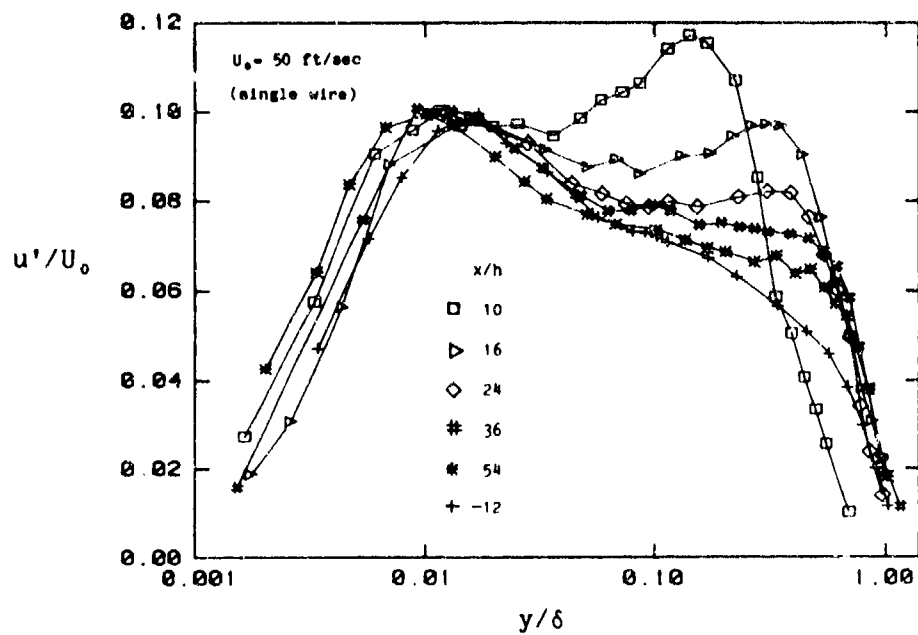


Figure 4.13 u'/U_0 Profiles at Downstream Locations (single wire)

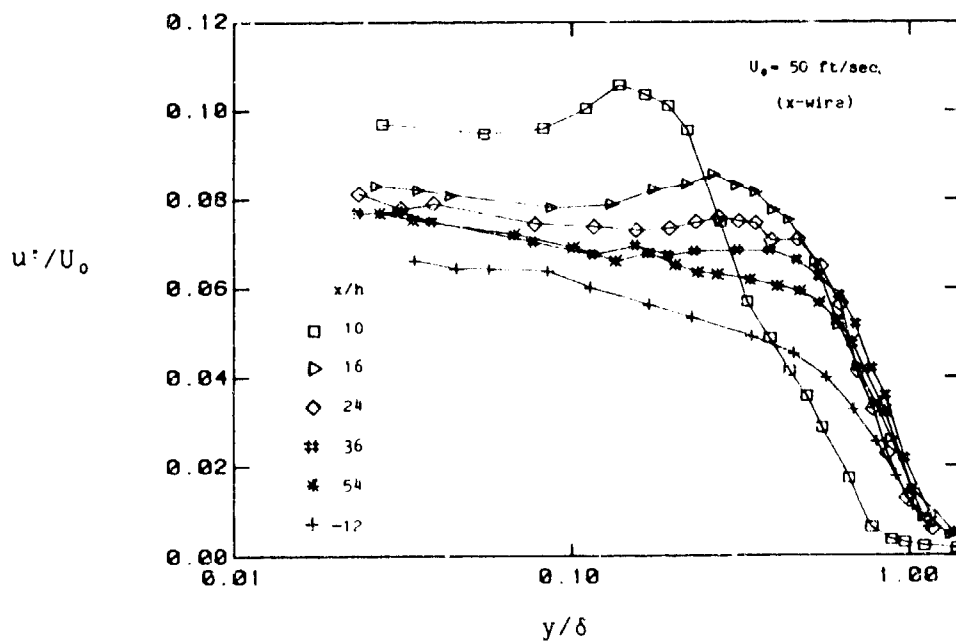


Figure 4.14 u'/U_0 Profiles at Downstream Locations (x-wire)

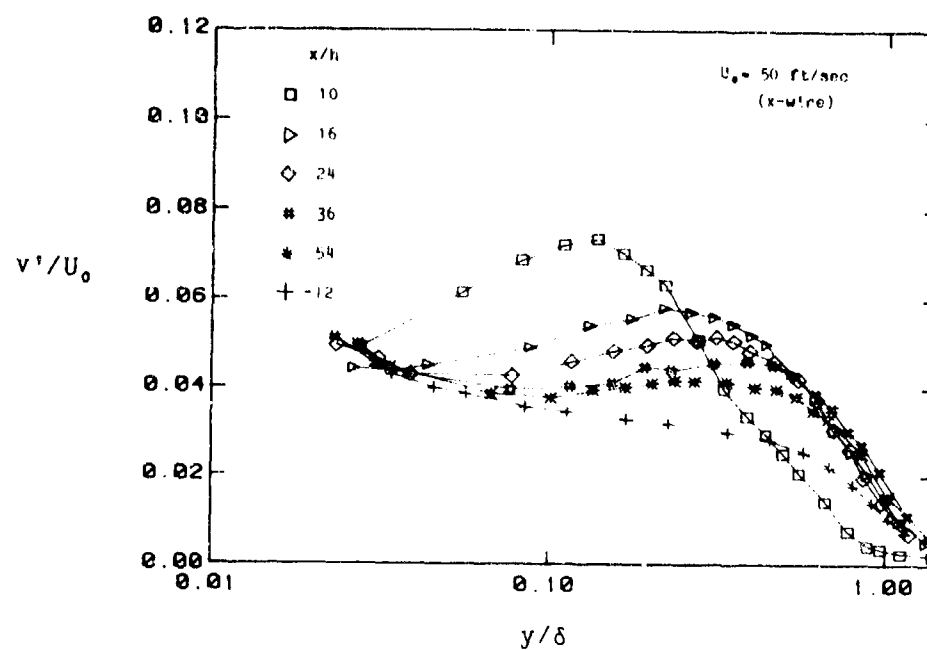


Figure 4.15 v'/U_0 Profiles at Downstream Locations

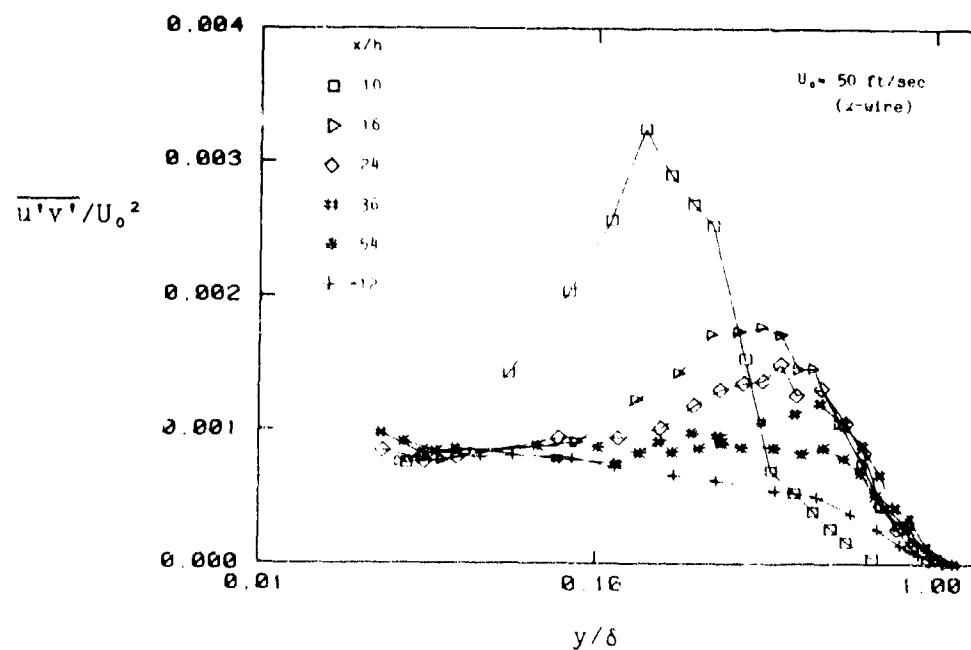


Figure 4.16 Turbulence Stress Profiles at Downstream Locations

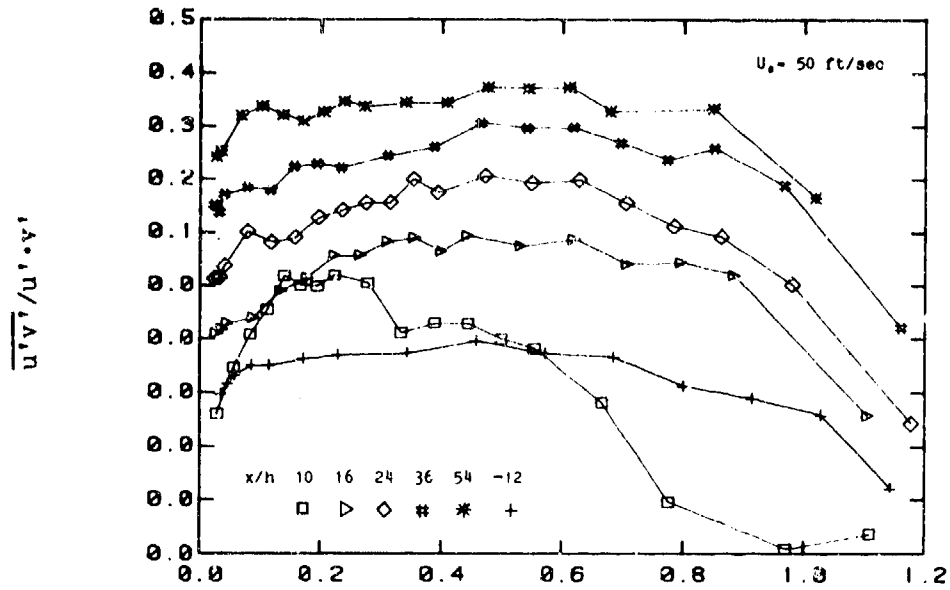


Figure 4.17 Turbulence Stress Correlation Coefficient Profiles

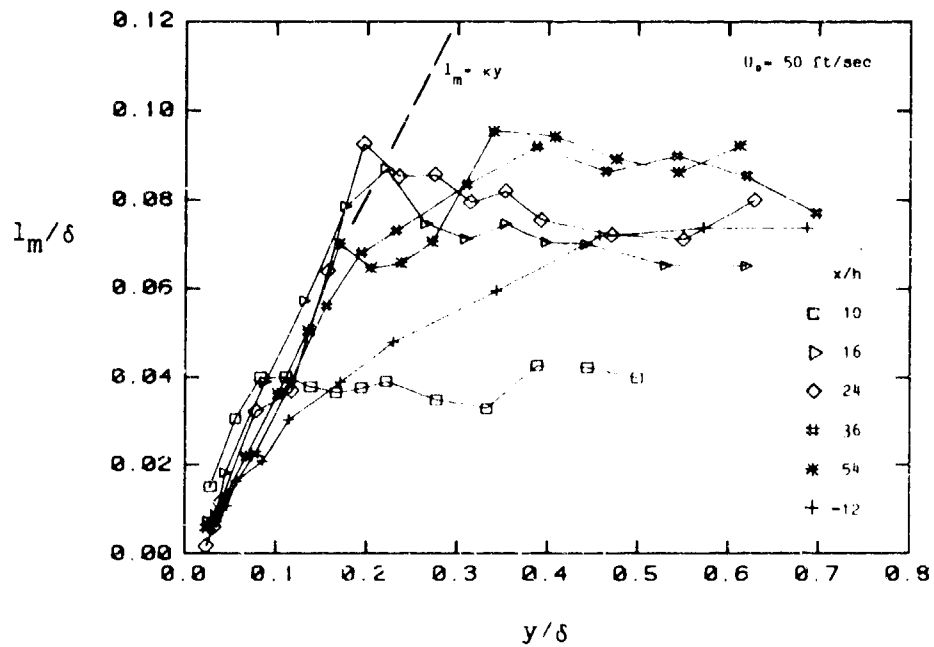


Figure 4.18 Mixing Length Profiles at Downstream Locations

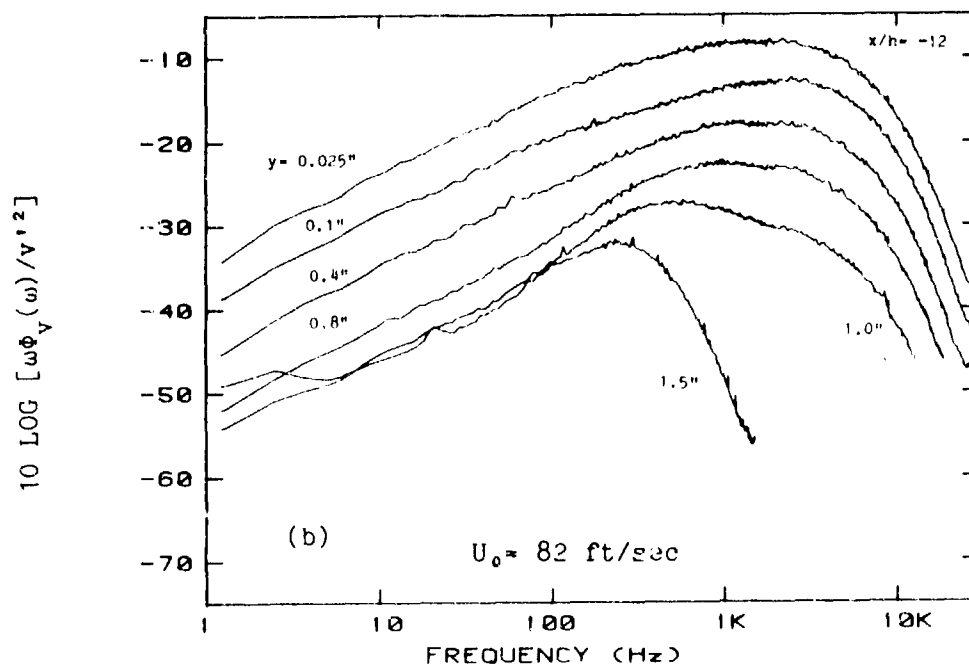
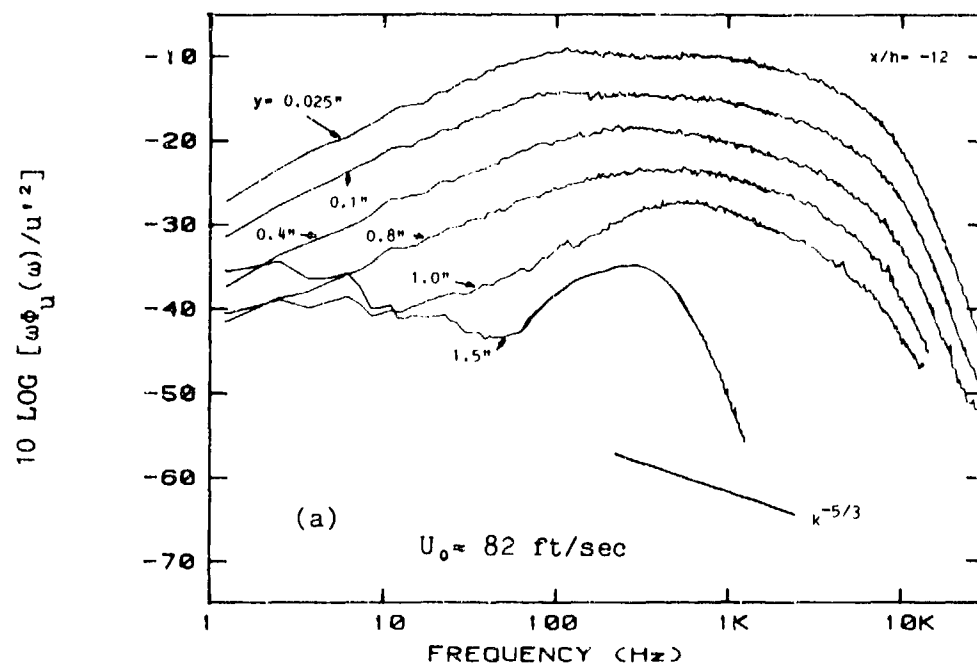


Figure 4.19 Velocity Spectra for Equilibrium Flow
(a) u spectra; (b) v spectra

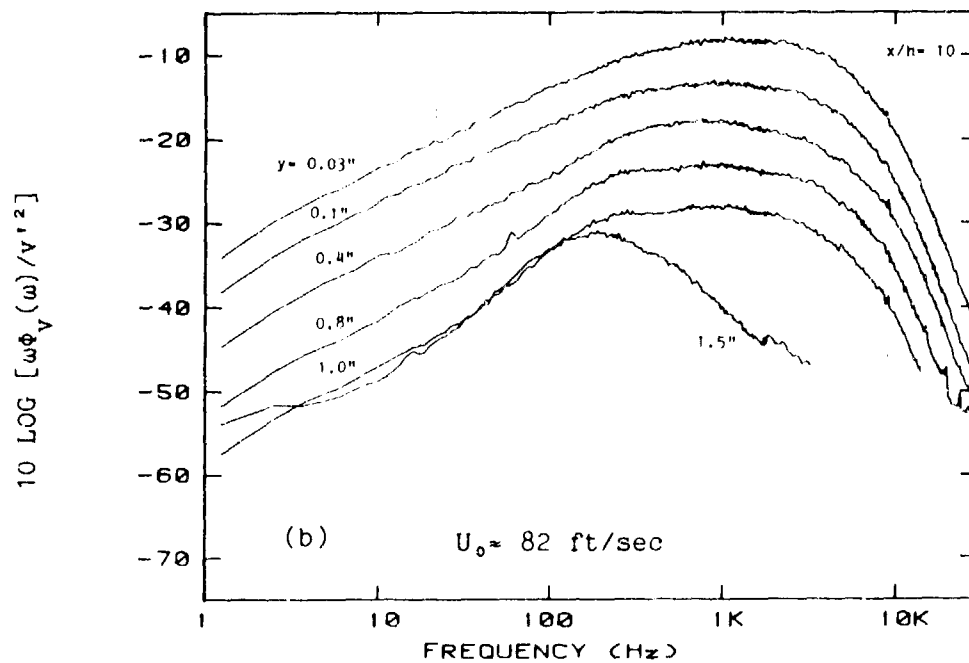
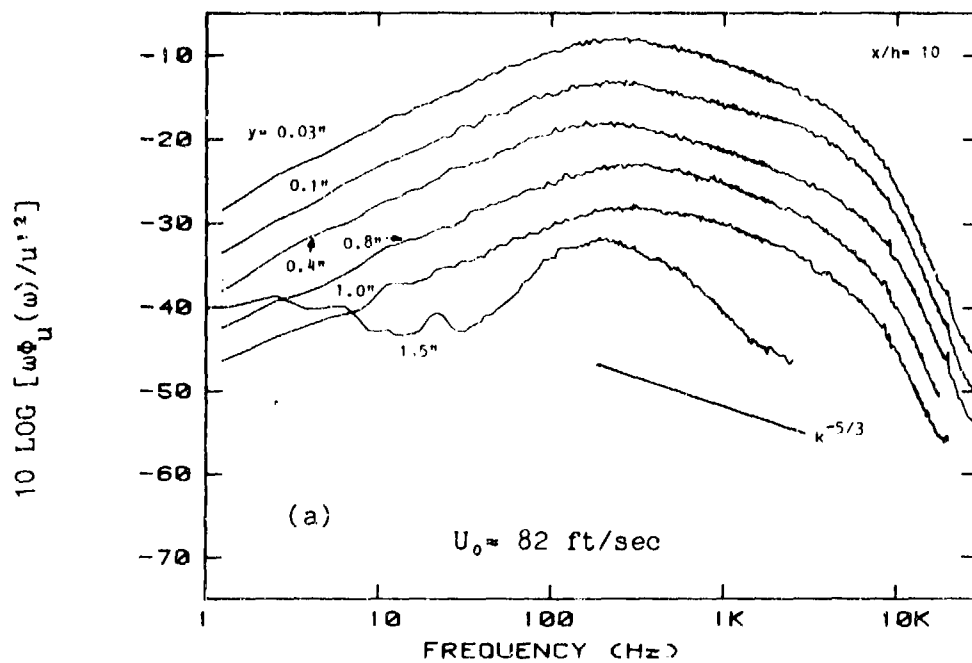


Figure 4.20 Velocity Spectra at Fixed Downstream Location ($x/h=10$)
 (a) u spectra; (b) v spectra

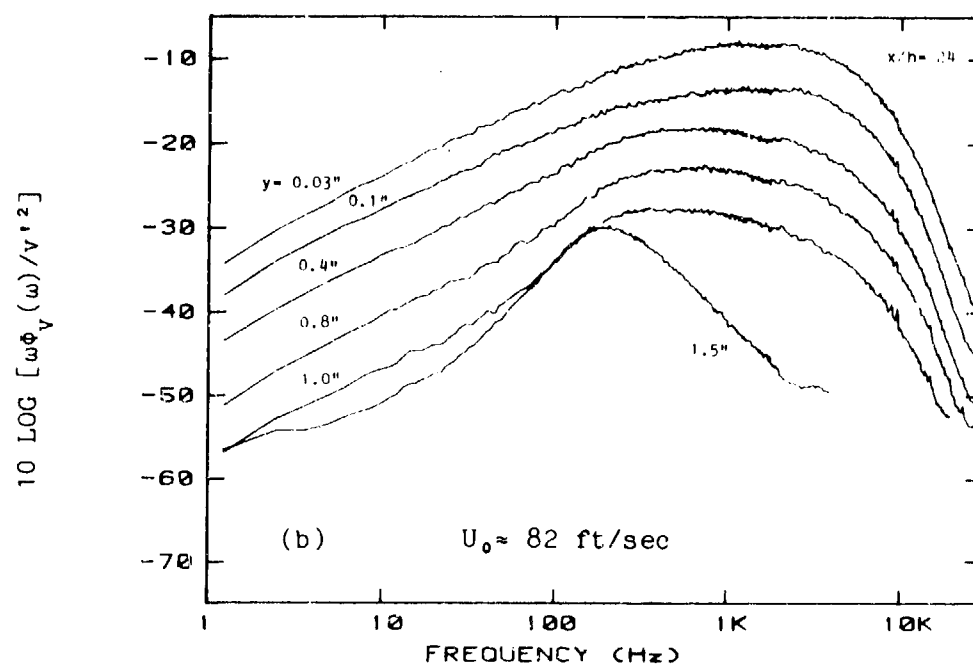
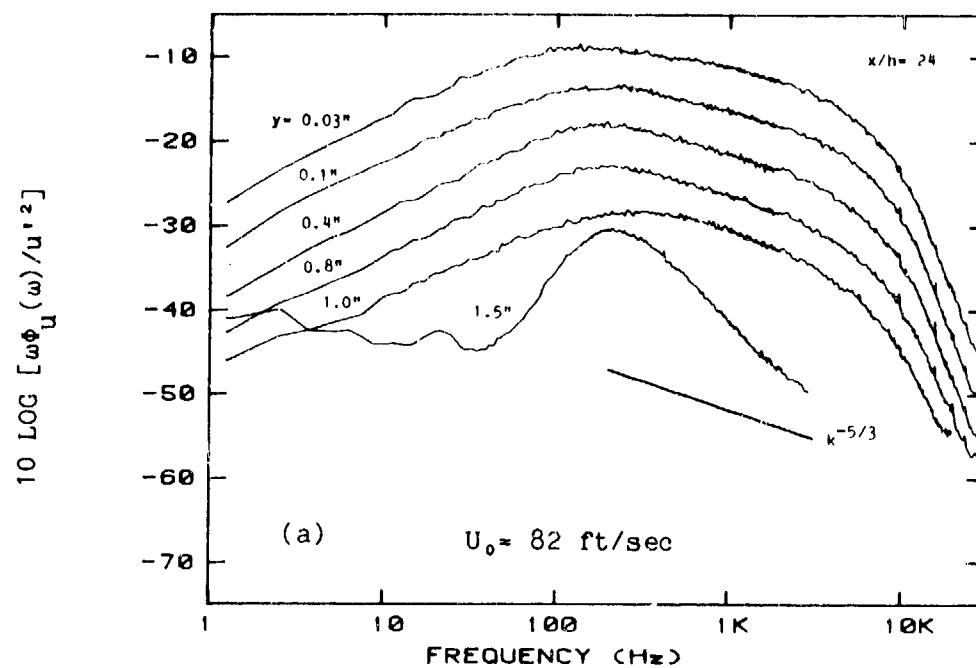


Figure 4.21 Velocity Spectra at Fixed Downstream Location ($x/h=24$)
(a) u spectra; (b) v spectra

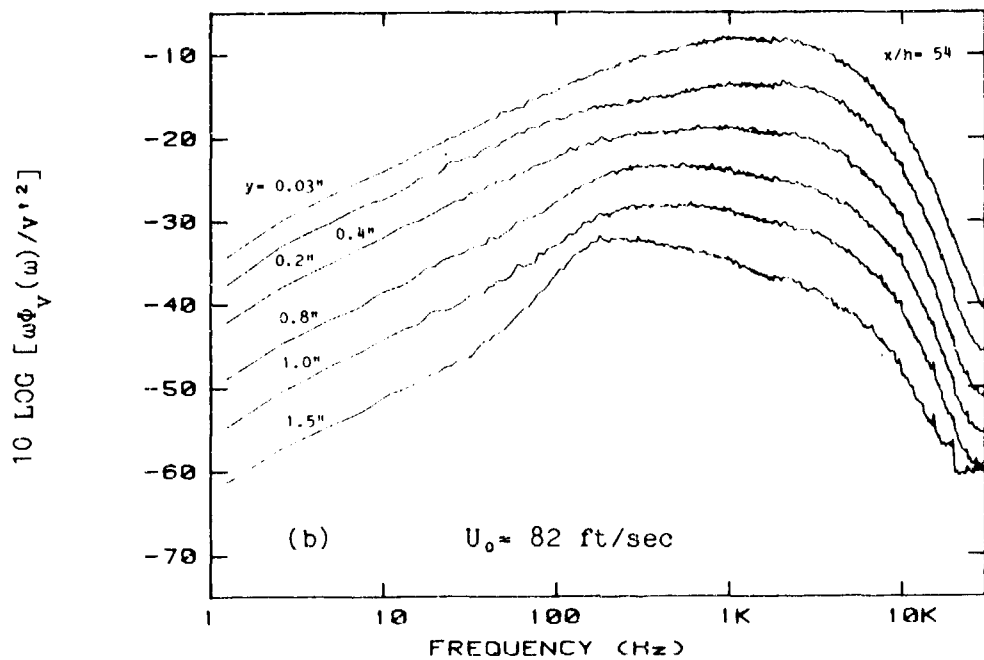
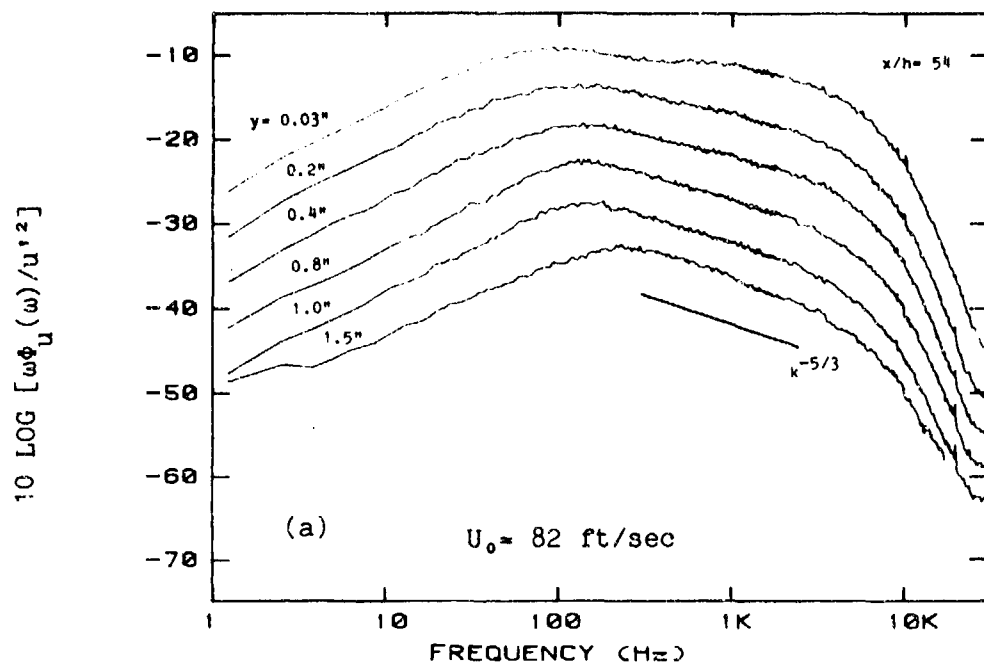


Figure 4.22 Velocity Spectra at Fixed Downstream Location ($x/h=54$)
 (a) u spectra; (b) v spectra

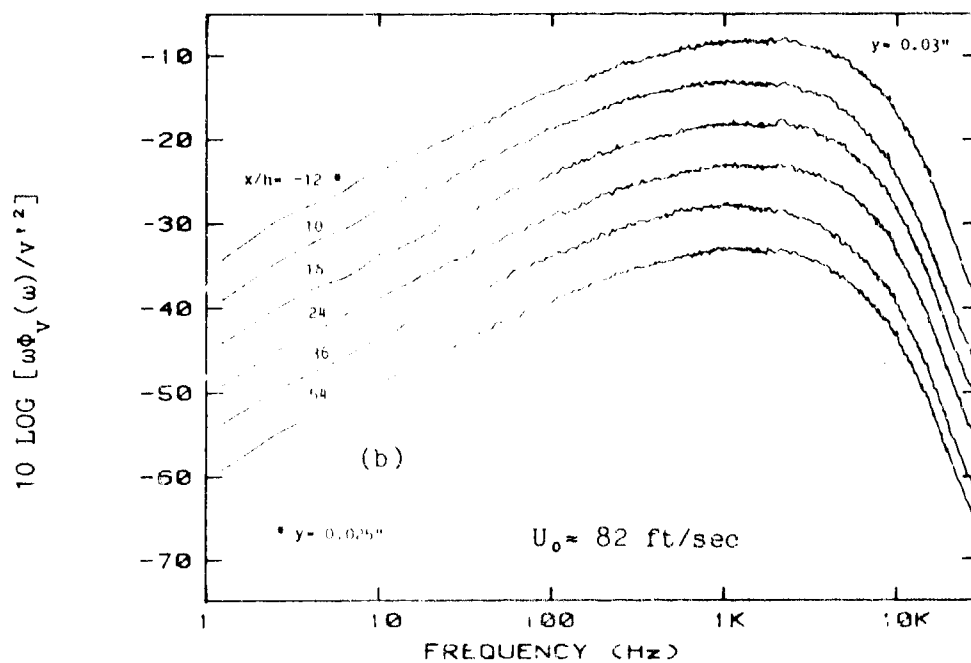
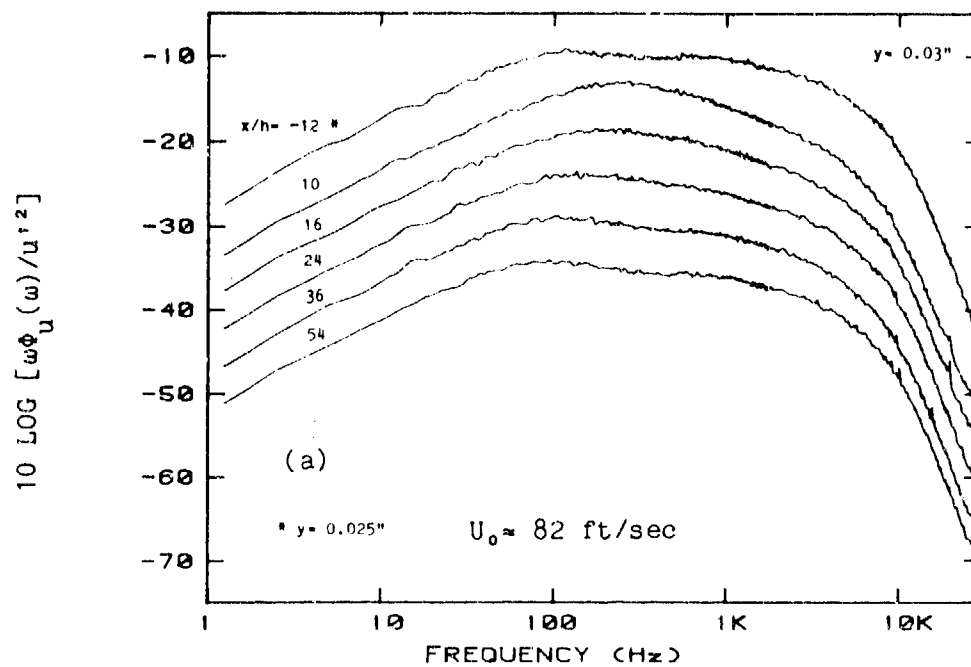


Figure 4.23 Velocity Spectra at Fixed Wall Position ($y=0.03$ -inch)
 (a) u spectra; (b) v spectra

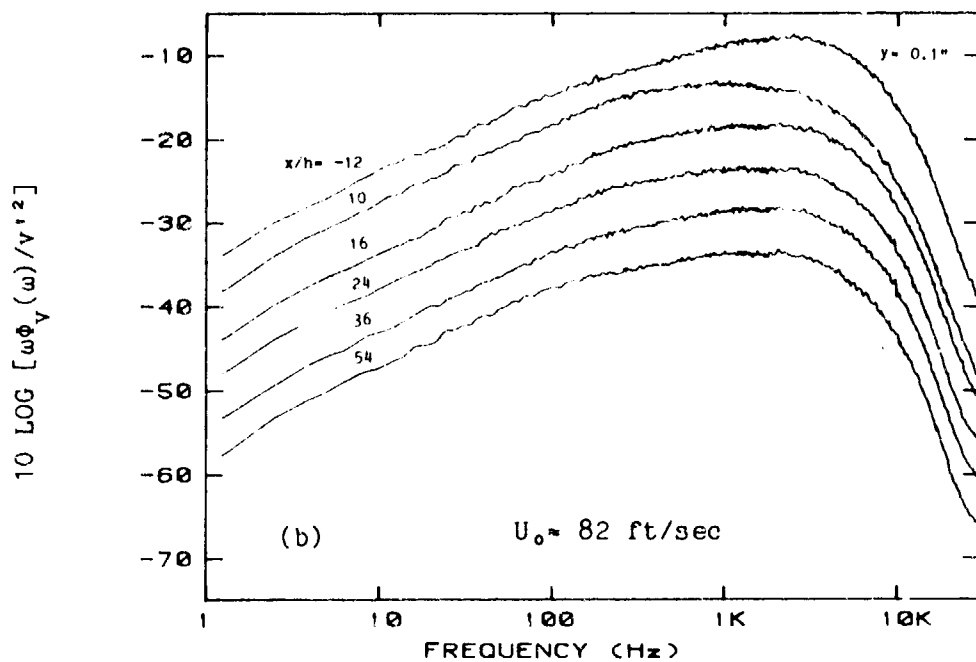
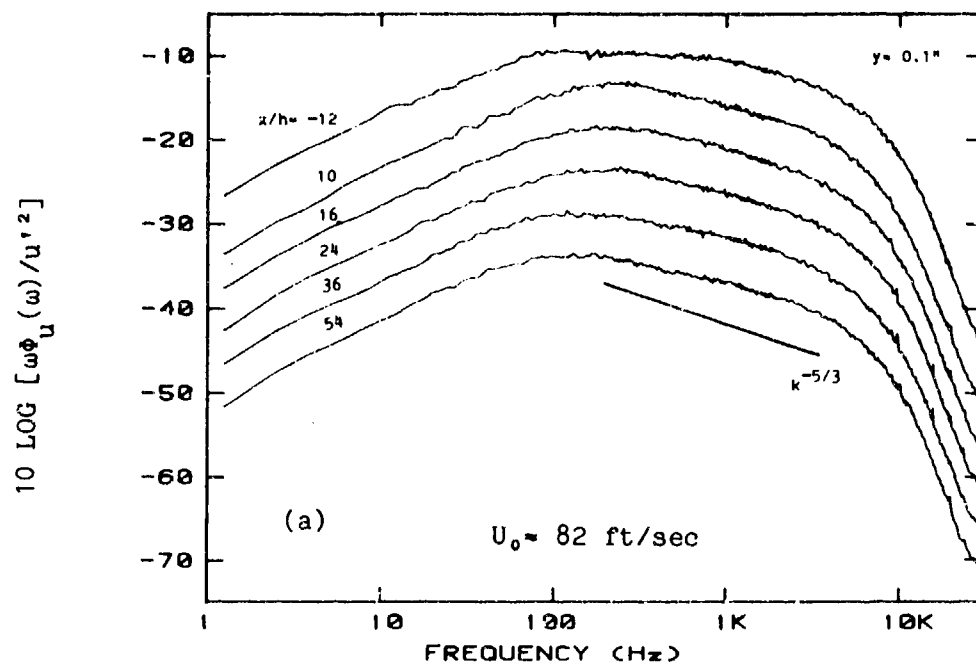


Figure 4.24 Velocity Spectra at Fixed Wall Position ($y=0.1$ -inch)
(a) u spectra; (b) v spectra

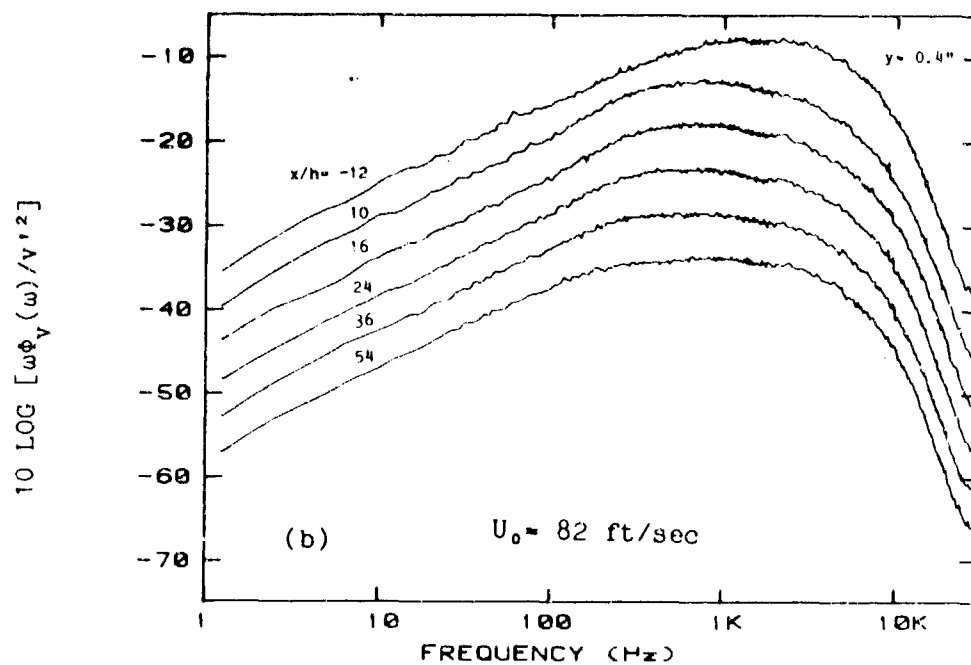
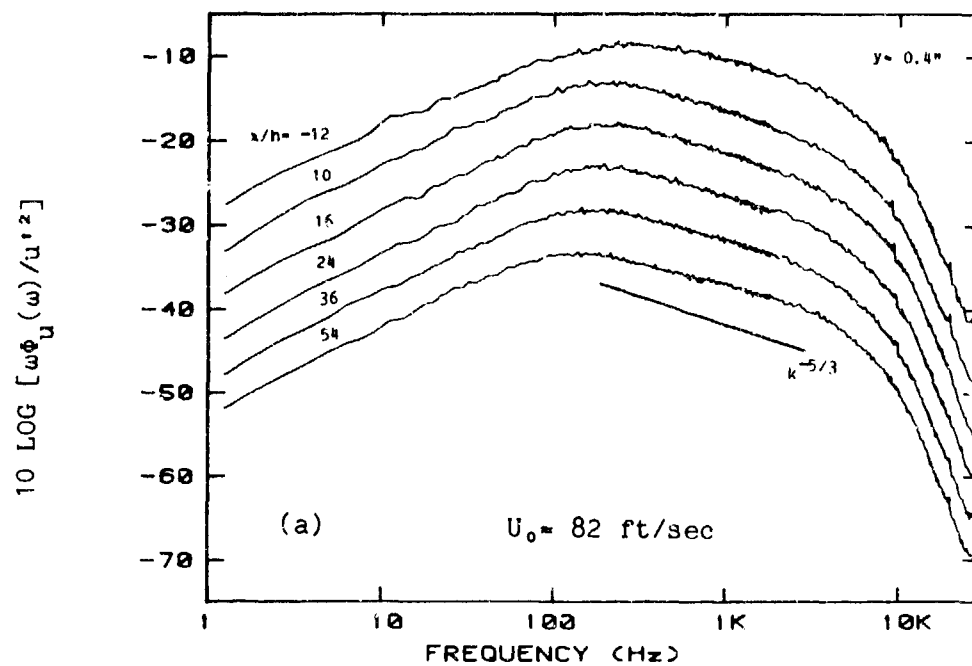


Figure 4.25 Velocity Spectra at Fixed Wall Position ($y=0.4$ -inch)
(a) u spectra; (b) v spectra

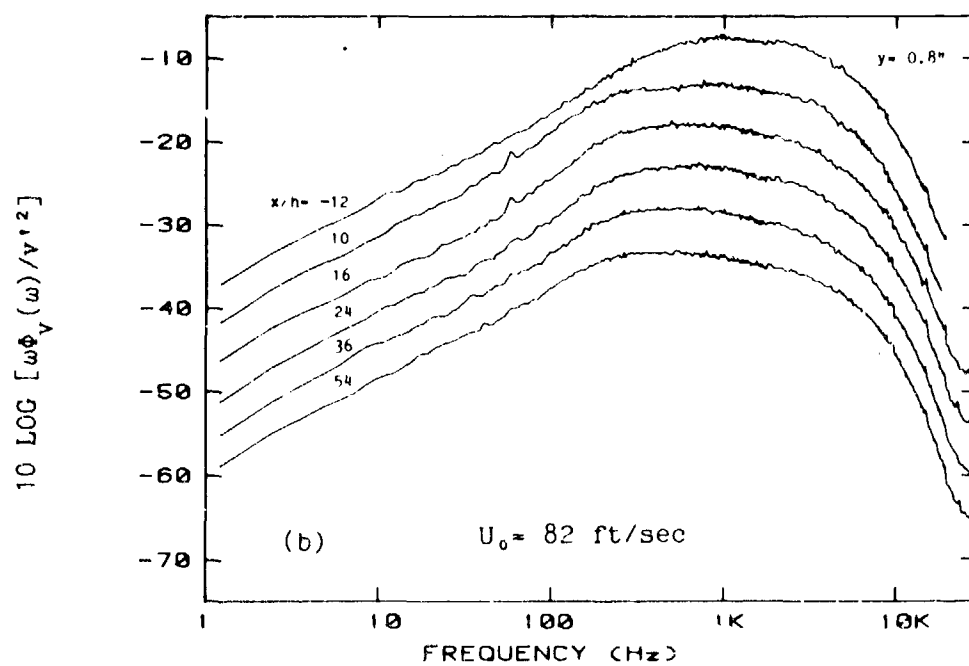
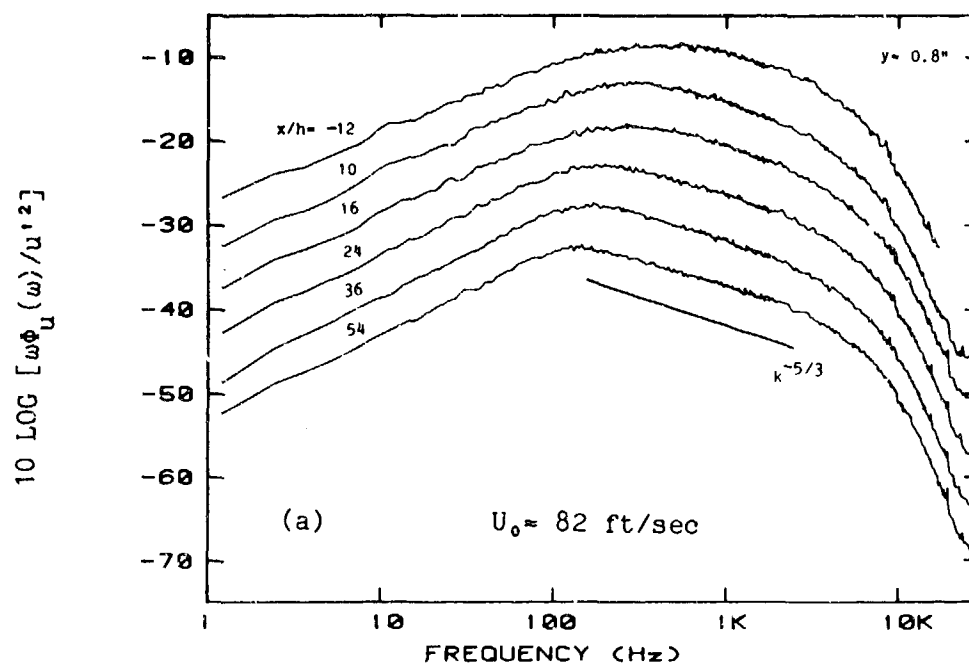


Figure 4.26 Velocity Spectra at Fixed Wall Position ($y=0.8$ -inch)
(a) u spectra; (b) v spectra

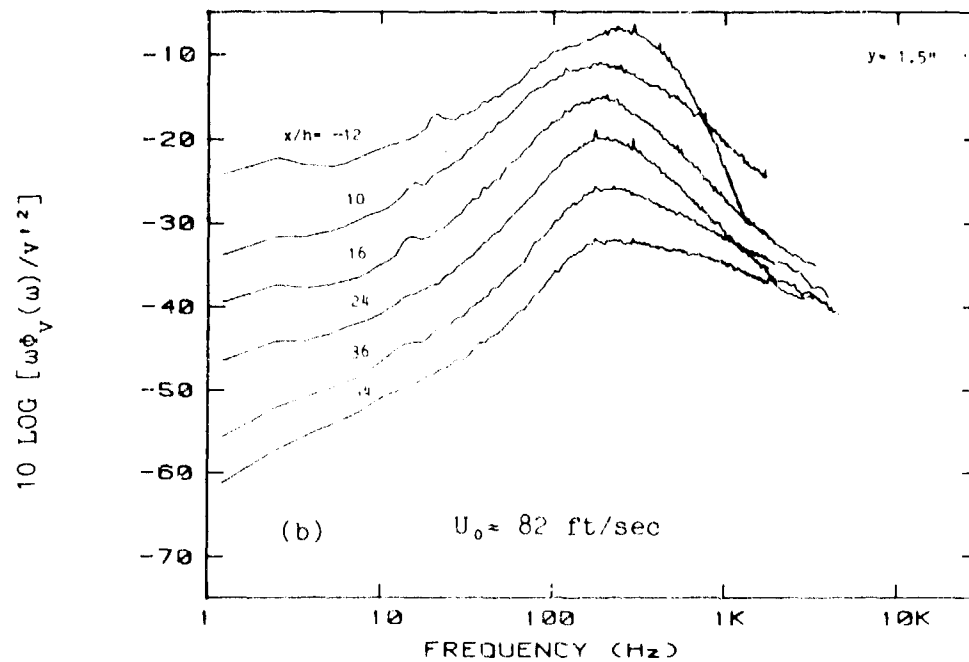
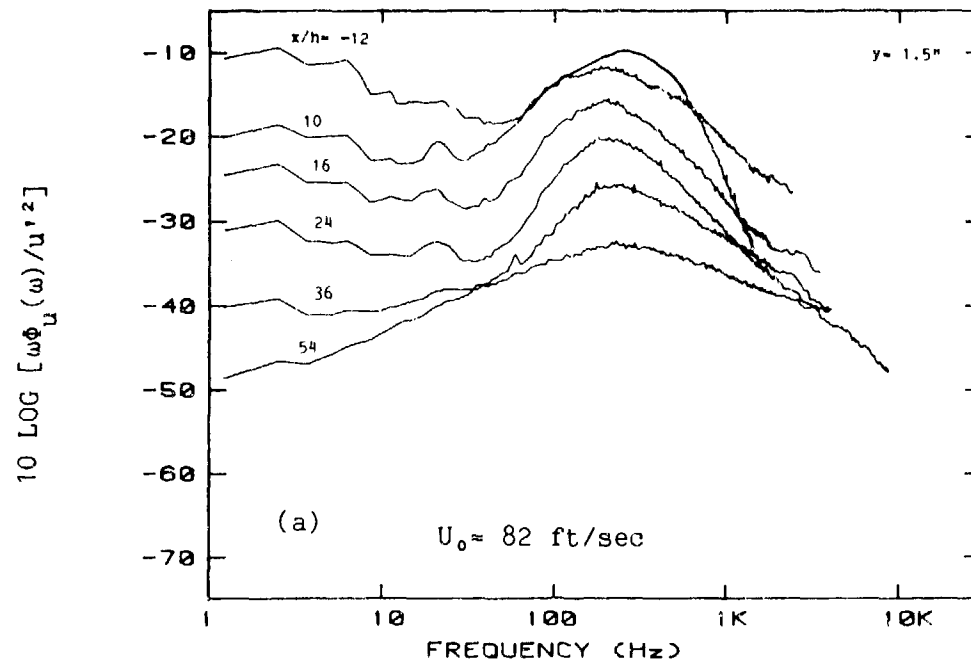


Figure 4.27 Velocity Spectra at Fixed Wall Position ($y=1.5\text{-inch}$)
 (a) u spectra; (b) v spectra

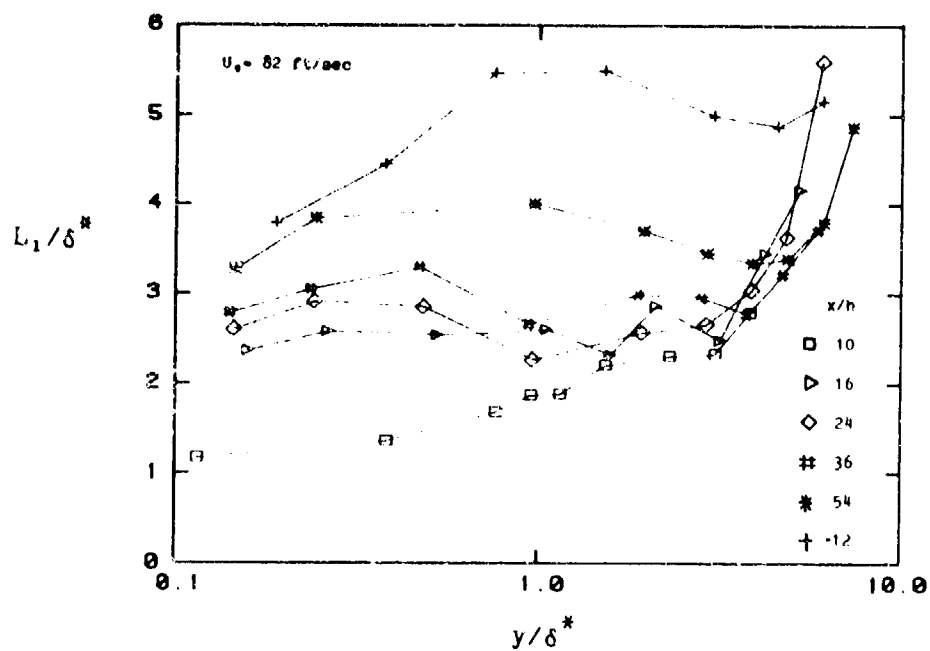


Figure 4.28(a) Profiles of Streamwise Integral Length Scale, L_1

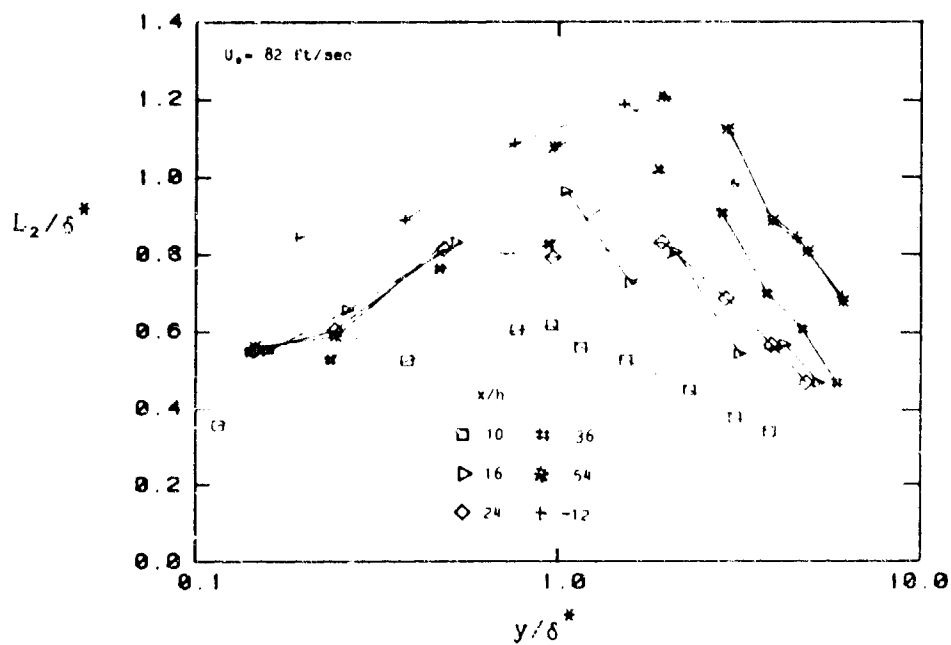


Figure 4.28(b) Profiles of Vertical Integral Length Scale, L_2

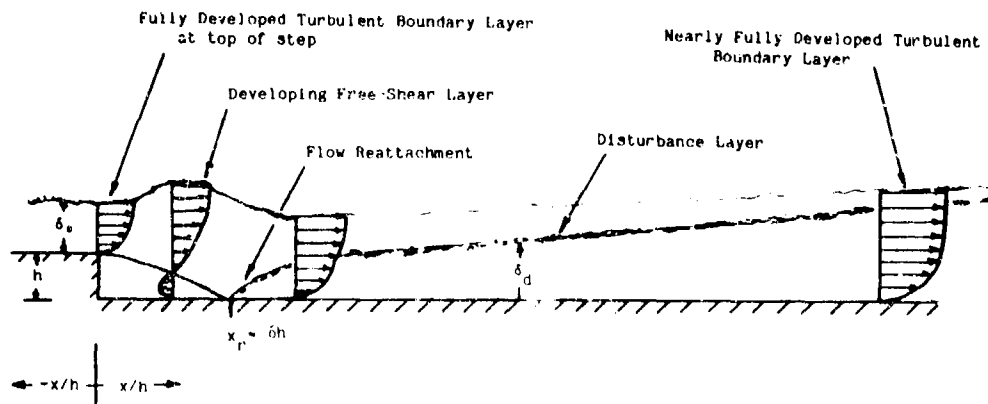


Figure 4.29 Downstream Propagation of Disturbance Layer

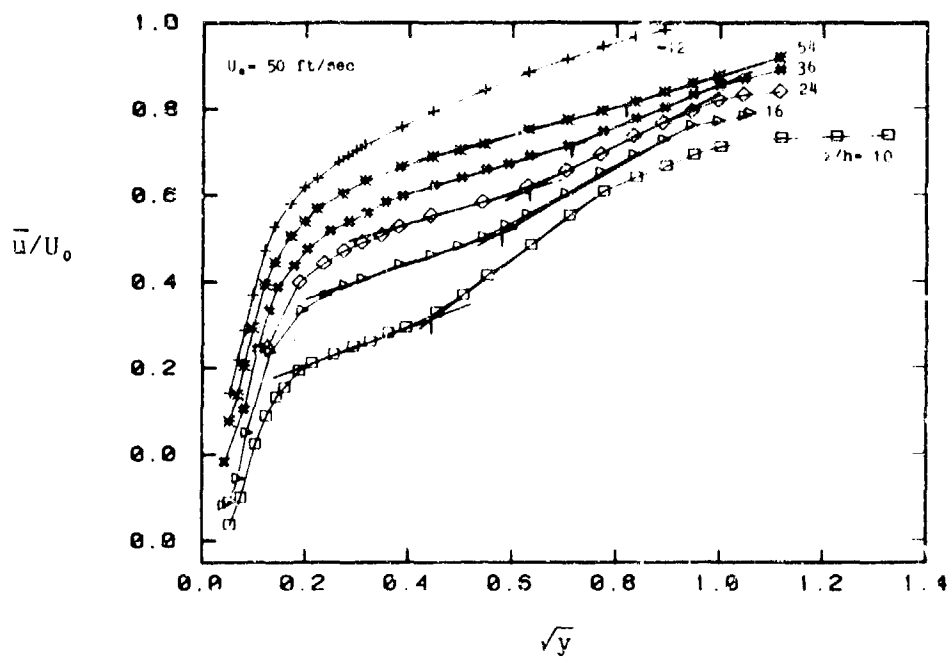


Figure 4.30 Mean Velocity Profiles Plotted Versus \sqrt{y}

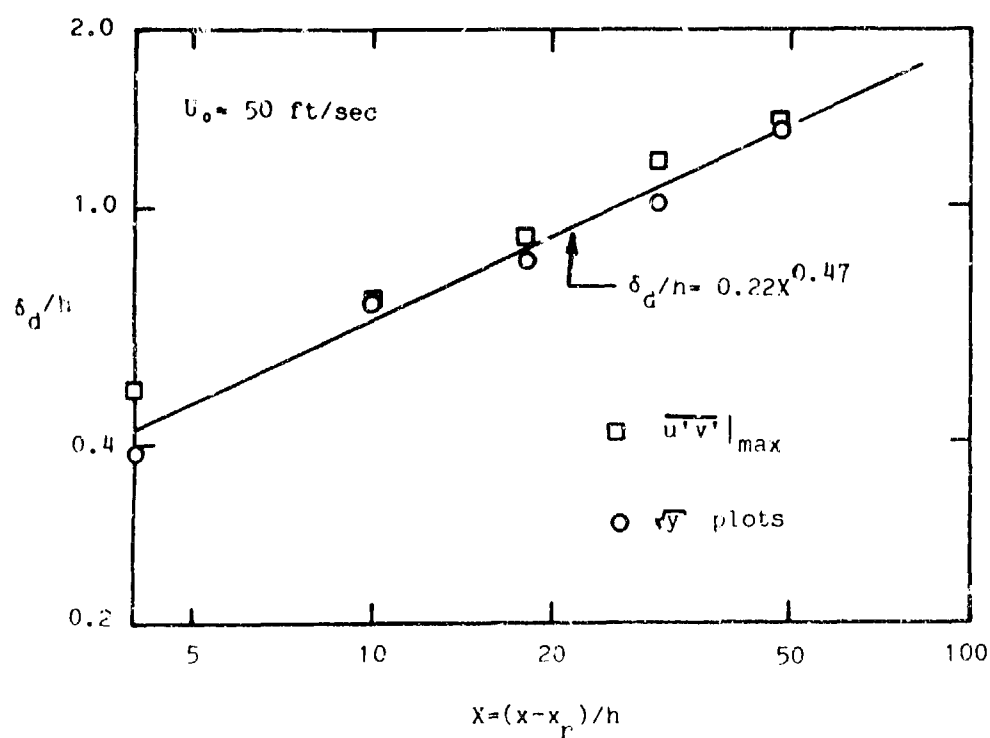


Figure 4.31 Location of Disturbance Layer

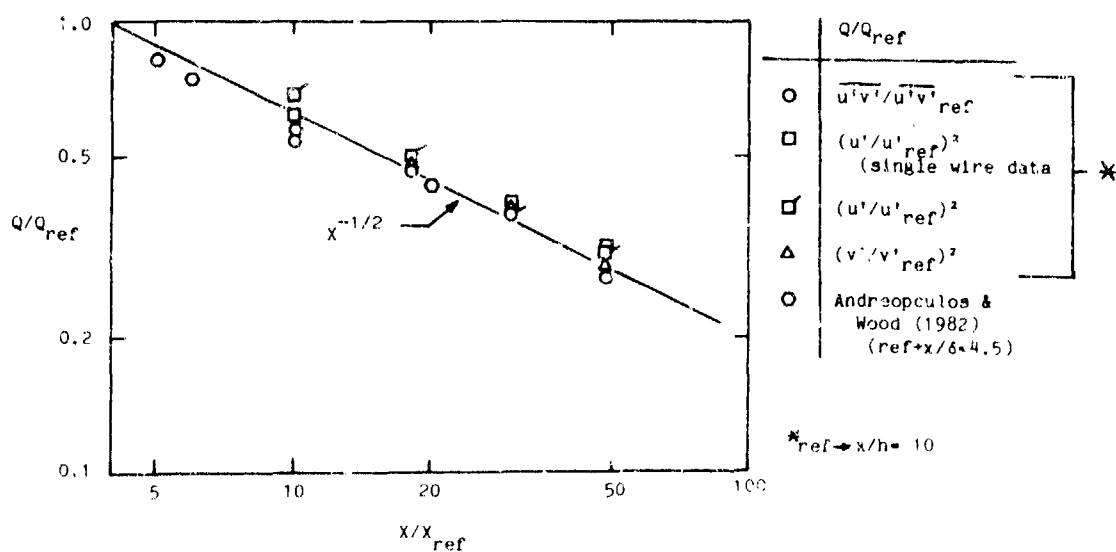


Figure 4.32 Decay of Disturbance Layer

CHAPTER 5

EXPERIMENTAL RESULTS FOR WALL PRESSURE FLUCTUATIONS

5.1 Introduction

This chapter presents the measurements made of the wall pressure fluctuations downstream of the reattachment point for flow over a backward-facing step. The purpose of these measurements is twofold. First, fluctuating wall pressures are a source of surface excitation that can lead to vibration and noise problems. A detailed knowledge of the spatial and temporal characteristics of the wall pressure field is needed to calculate surface response levels. This type of information is currently not available for a perturbed/relaxing flow field. Second, the relationship between the turbulence activity in the boundary layer and the fluctuations in surface pressure that are induced by this activity is not well understood. A question that arises is what in the flow field are the sources of pressure fluctuations. By investigating the wall pressures beneath a perturbed/relaxing boundary layer, which has unique and highly identifiable regions of turbulence activity, a better understanding of the organized structure within the boundary layer can be obtained.

Single point frequency spectra and two-point cross-spectral density measurements were made of the wall pressure field downstream of reattachment using flush-mounted pinhole pressure transducers. Data for both streamwise (longitudinal) and transverse (lateral) separations were obtained at $x/h=10, 16, 24, 36, 54$ and 72 as described in Chapter 3. Streamwise separations ranged from (approximately) $1/4$ -inch to 24-inch, and the transverse separations ranged from typically $1/4$ -inch to 3-inch. The streamwise extent of data obtained at $x/h=54$ and 72 was limited by the length of the tunnel test section. Data were obtained at two free-stream velocities, nominally 50 and 90 ft/sec. Velocity parameters at $x/h=72$ were taken to be approximately equal to those at $x/h=54$ since velocity data could not be obtained at $x/h=72$.

In addition to the non-equilibrium flow pressure measurements, cross-spectral measurements were also made of the pressure field for the (no step) equilibrium flow. These measurements were made with the

upstream transducer located 6-inches downstream of the location where the step normally would be located for the backward-facing step study. The equilibrium measurements were made along a line 1-inch above the test wall centerline in order to make use of pre-existing holes.

The cross-spectrum analysis procedures provided single-point frequency spectra for both transducers as well as the phase and magnitude of the cross-spectrum. For discussion purposes the magnitude of the cross-spectrum is expressed in terms of the coherence function and the phase is expressed as a convection velocity (for the streamwise measurements). Root-mean-square (RMS) values of the wall pressure fluctuations were obtained from integrations of the frequency spectra. The details of the procedures used to calculate the various spectral functions are given in Chapter 3.

The pressure data that were obtained are presented and discussed in three parts. First, a discussion of the RMS pressure measurements obtained for both the equilibrium and non-equilibrium flows is given. Secondly, a presentation and discussion of the equilibrium flow data is given, and finally the non-equilibrium data are presented and discussed.

5.2 Root-Mean-Square of Pressure Fluctuations

5.2.1 RMS Pressure Fluctuations

Root-mean-square values of the fluctuating wall pressures were obtained by numerically integrating the measured frequency spectra. By integrating the spectra from 50 Hz to 20,000 Hz it was possible to accurately eliminate the low frequency facility noise from the RMS values.

The values of RMS pressure that were obtained are shown in figure 5.1 normalized by dynamic head q . The value obtained for the equilibrium flow is shown as a line so comparisons can be made at all x/h locations. Data obtained in an earlier experiment, Farabee and Casarella (1984), are also shown for comparison. These additional data were obtained for flow over a 1/2-inch backward-facing step ($\delta_c/h=1.0$) mounted on a flat-plate fixture in a wind tunnel. These data are included for comparison to the current results as well as to show the variations in RMS pressure that are measured upstream of reattachment.

The two sets agree favorably well, particularly considering that they are measurements from two completely different facilities with different experimental configurations.

As discussed by Farabee and Casarella (1984) the RMS pressure levels are largest near reattachment and slowly decay in level downstream. Large values of RMS pressure at the location of flow reattachment are typical of many different types of reattaching flows as shown by Mabey (1972). The important features of figure 5.1, with regard to the current investigation, is the streamwise inhomogeneous nature of the wall pressures and the rather slow recovery rate of the RMS pressure to an equilibrium value. Even as far downstream as $x/h=72$, the RMS pressure is still larger than the equilibrium value.

Table 5.1 provides tabulated values of RMS pressures; the RMS data are given normalized by dynamic head and normalized by wall shear stress. Also tabulated in this table are values of the transducer diameter expressed in terms of viscous wall units ($d^+ = du^*/\nu$) and the diameter normalized by displacement thickness.

5.2.2 Resolution Errors in Pressure Measurement

To resolve the small scale, high frequency, components of the wall pressure fluctuations a "point size" transducer is needed. A transducer with a finite size will spatially average pressure components that are on the order of, or smaller than, the size of the transducer. This is the same problem discussed in the error analysis for the hot wire measurements. Pinhole microphones were used as a pressure transducer since they have a very small sensing area but still have a high sensitivity. Bull and Thomas (1976) questioned the validity of using pinhole transducers since disturbances can be generated by flow over the hole that exists in the boundary. It was suggested that the higher levels of RMS pressure that are reported using pinhole transducers are not due to better resolution of the small scale structures in the pressure field but are due to increased pressures generated by flow-hole disturbances.

Bull and Thomas (1976) compared RMS values of wall pressure fluctuations obtained with pinhole microphones and non-pinhole transducers and concluded that the higher values of RMS pressure

measured by the pinhole transducer were artificial, resulting from, most probably, disturbances created by flow over the hole in the boundary. Schewe (1983) measured wall pressure fluctuations with an especially small, non-pinhole, transducer and compared these results to those obtained by other investigators who also used non-pinhole transducers. Schewe did not include any pinhole measurements in his comparison due to the belief that pinhole measurements are in error. However, measurements obtained in this experiment with pinhole transducers agree quite well with the measurements of Schewe.

Figure 5 shows measured values of RMS pressure, normalized by dynamic head, plotted versus transducer diameter expressed in viscous wall units. This plot format is the same as that used by Schewe (1984) and by Bull and Thomas (1976). Included in figure 5.2 are their measurements. The current pinhole measurements agree quite well with the results of Schewe but the results of Bull and Thomas can be seen to be too low. The reason for these discrepancies is not known.

The details of the small scale structure of the wall pressure field are still not well understood. However, measurements with pinhole transducers do not appear to be in error as suggested by Bull and Thomas. Furthermore, the frequency region that is of interest in this study is below that effected by the type of transducer that is used.

5.3 Spectral Features of Wall Pressure Fluctuations for Equilibrium Flow

In this section spectral statistics for the equilibrium (no-step) boundary layer wall pressure fluctuations are presented. The purpose of obtaining these data was to provide pressure field statistics for a "classical" equilibrium flow boundary layer. These statistics will be used as a data base to which the statistics measured for the non-equilibrium flow will be compared.

5.3.1 Frequency Spectra

The single-point frequency spectra of the wall pressure fluctuations beneath the equilibrium flow boundary layer were measured at 51 and 93 ft/sec. Figure 5.3 shows the frequency spectra presented in dimensional form for these two speeds. Each spectrum is a composite

formed by assembling three individual spectra, each covering a different analysis range (500, 2000 and 20,000 Hz). Pressure spectra were obtained at many streamwise positions as part of the cross-spectral measurements for the equilibrium flow. The two spectra in figure 5.3 are representative of all the spectra that were measured. Over the streamwise range that was covered the spectra for the equilibrium flow were found to be spatially homogeneous. The low frequency end of the spectra are limited to 50 Hz by facility noise. The upper frequency range of the data is limited to 20,000 Hz by the Helmholtz resonance response of the pinhole microphone system (pertinent to the higher speed data). The very high frequency end of the 51 ft/sec spectrum was electrically contaminated and is not shown. The non-dimensionalized frequency spectra compare favorably with those reported in the literature.

Wall pressure fluctuations are produced by the turbulent velocity fluctuations that can occur throughout the boundary layer. By comparing the time and length scales that collapse the measured pressure spectra to the scales for a turbulent boundary layer, it is possible to identify specific regions in the boundary layer where pressure fluctuations are generated. As such, identification of global source regions can be made from the single-point frequency spectra. Additional information about the regions of the boundary layer that are primary sources of pressure fluctuations is obtained from the cross-spectral data as will be discussed later.

Figures 5.4-5.6 show the pressure spectra non-dimensionalized on three sets of boundary layer variables. Although detailed conclusions on the scaling dependence of the pressure fluctuations cannot be made from only two data curves, it is possible to identify specific scaling trends. Figure 5.4 shows the pressure spectra non-dimensionalized on the outer flow variables U_0 and δ^* , in the form

$$\frac{\phi_p(\omega)U_0}{q^2\delta^*} \quad \text{vs.} \quad \frac{\omega\delta^*}{U_0} \quad (5.1)$$

This scales the pressure fluctuations on dynamic head and uses a time scale, δ^*/U_0 , associated with the flow in the outer part of the boundary

layer. In figure 5.5 the spectra are made non-dimensional using combined inner-outer flow variables τ_0 (or τ_w), U_0 and δ^* , in the form

$$\frac{\phi_p(\omega)U_0}{\tau_0\delta^*} \quad \text{vs.} \quad \frac{\omega\delta^*}{U_0} \quad (5.2)$$

Again a time scale associated with the outer flow is used but now the magnitude of the pressures are normalized by the wall shear stress. The final set of non-dimensionalizing variables uses only the inner variables, τ_0 and u^* , which gives, as shown in figure 5.6,

$$\frac{\phi_p(\omega)u^{*2}}{\tau_0^2\nu} \quad \text{vs.} \quad \frac{\omega\nu}{u^{*2}} \quad (5.3)$$

where ν is the fluid kinematic viscosity. Inner variable scaling scales the magnitude of the pressure fluctuations on the wall shear stress and uses a time scale ν/u^{*2} , that is associated with turbulence activity in the inner layer of the boundary layer.

The low frequency components of the wall pressure field adequately scale on the outer flow variables (figure 5.4). This form of pressure scaling is common in the literature, primarily because the outer flow variables are relatively easy to obtain for a given experimental arrangement. However, the low frequency data collapses best using the combined inner-outer variable scaling as shown in figure 5.5. This shows the importance of the wall shear stress in establishing the magnitude of the low frequency pressure fluctuations. Outer variable scaling is related to combined inner-outer variable scaling by the factor C_f^2 ($\tau_0 = C_f q$). Neither outer variable nor combined inner-outer variable scaling holds for the high frequency portions of the pressure spectra.

Figure 5.6 shows that the high frequency pressure fluctuations scale exclusively on inner variables. The important term in the inner variable scaling that provides for a collapse of the two spectra is the time scale ν/u^{*2} . This scale is characteristic of time scales in the inner layer of the boundary layer. The magnitude of the high frequency pressure fluctuations are determined by the magnitude of the wall shear

stress, as were the low frequency fluctuations. The time scale of the high frequency pressure fluctuations is, however, much shorter than that for the low frequency fluctuations.

These variations in the scaling of the wall pressure spectra leads to the conjecture that the spectral sources of the wall pressure fluctuations are located in different regions of the boundary layer with the wall shear stress determining the overall level of pressure fluctuation for all regions. In summary, one concludes that there are two different time scales present in the pressure fluctuations and that these time scales are a result of pressure source terms being located in both the inner and the outer regions of the boundary layer.

The low frequency pressure fluctuations ($\omega\delta^*/U_0 \leq 2.0$) scale on an outer flow time scale δ^*/U_0 , showing that the source of these fluctuations is in the outer portion of the boundary layer. The high frequency fluctuations ($\omega\nu/u^{*2} > 0.4$ or $\omega\delta^*/U_0 > 4.0$) scale on a viscous time scale ν/u^{*2} , associated with turbulence activity in the inner layer of the boundary layer. This places the sources of high frequency pressure fluctuations near the wall. The above time scales could also be reinterpreted as a combination of a length and a velocity scale. The boundary layer displacement thickness δ^* and external flow velocity U_0 form the outer flow time scale δ^*/U_0 ; the viscous length scale ν/u^* and shear velocity u^* form the inner variable time scale ν/u^{*2} .

5.3.2 Cross-Spectral Measurements

Measurements of the two-point space-time statistics of the wall pressure field were obtained to provide a description of the spatial and convective characteristics of the pressure fluctuations. These results will be used to further examine the conclusions deduced from the single point spectra data. In particular, measurements of the pressure cross-spectral density can be interpreted to gain more insight into the eddy structure of the pressure fluctuations that compose the wall pressure field.

The cross-spectral properties of the wall pressure field are assumed to be separable into streamwise and transverse terms as suggested by Corcos (1962). The two-dimensional cross-spectrum, $\Phi_p(\omega, \xi)$, is thus given as

$$\Phi_p(\omega, \xi) = \Phi_p(\omega, \xi) \Phi_p(\omega, \eta)$$

where, $\Phi_p(\omega, \xi)$ is the streamwise spectrum, $\Phi_p(\omega, \eta)$ is the transverse spectrum and $\xi = (\xi, \eta)$ is the two-dimensional separation vector between measurement positions.

The relationship of the cross-spectrum to other statistical quantities is given in Chapter 3. The magnitude of the cross-spectrum is expressed in normalized form as the coherence function $\Gamma(\omega, \xi)$ (which is proportional to pressure spectrum as opposed to the square of the pressure spectrum). For streamwise separations the phase of the cross-spectrum is expressed as a convection velocity $U_c(\omega, \xi)/U_0$. The phase between transversely separated transducers is essentially zero and is not shown.

The cross-spectrum and single-point spectra were measured simultaneously. Measurements for 24 different streamwise separations were made ranging from a separation of 1/4-inch to 18-inch. Measurements for 12 transverse separations were made ranging from 1/4-inch to 3-inch. Data were obtained at 51 and 93 ft/sec. Data analysis was terminated after a $\Gamma(\omega) < .05$ was reached. When more than one frequency range was used, the spectral data from the different analysis ranges was assembled into a single spectrum (see Chapter 3).

In the presentations that follow only a select set of the separation data will be presented. The data that are not included are consistent with the data that are presented.

The measurements of wall pressure cross-spectral density, obtained with streamwise separations, are presented in figures 5.7-5.10 while measurements made with transverse separations are shown in figures 5.11 and 5.12. All these data are shown as continuous curves, for fixed separation distance, and are calculated directly from the measured coherence and phase spectra. For small separations each cross-spectral

curve consists of as many as 250 frequency points and for large separations each curve consists of as many as 50 points.

In the presentations that follow, first, the measurements of the streamwise coherence will be presented and discussed, and following that the measurements of the streamwise convection velocity will be given and discussed. Lastly, the transverse coherence measurements will be examined.

5.3.3 Streamwise Coherence

The coherence spectra measured for various streamwise separations are shown in figures 5.7 and 5.8 for 51 and 93 ft/sec, respectively. Values of $\Gamma(\omega, \xi)$ are plotted against the phase of the cross-spectrum $\Theta(\omega, \xi)$. For streamwise separations the cross-spectrum phase can be expressed as $\Theta(\omega, \xi) = -\omega\xi/U_c(\omega, \xi)$ which has certain physical meaning. With this the phase can be interpreted as a non-dimensional wavenumber, of the form $\Theta(\omega, \xi) = k_1\xi$, since $k_1 = \omega/U_c$. Hence, when the coherence is plotted in the above form it may be viewed as a measure of the decay of the dominant pressure producing eddies as observed in a frame of reference moving with the eddies.

Two specific trends are seen in the coherence plots for the equilibrium flow. The first, and most obvious, is the collapse of the high frequency portion of each plot onto a single universal curve for all separation distances. The second trend is the loss of the coherence that occurs at low frequency resulting in the low frequency region of each coherence curve falling below this universal curve. It will be shown later that the Strouhal number at which $\Gamma(\omega, \xi)$ deviates from the universal curve is nearly constant. Note that below this cutoff Strouhal number there is a greater loss of coherence for the larger separation distances.

The $\omega\xi/U_c(\omega, \xi)$ similarity that is shown by the collapse of the high frequency portions of the coherence plots to a universal curve has important physical significance. This is best illustrated by replacing $\omega\xi/U_c(\omega, \xi)$ with $k_1\xi$. This demonstrates that the various wavenumber components of the pressure field all lose the same amount of coherence in traveling a distance equal to their wavelength. Hence, all pressure

eddies in this region are similar when scaled by their wavelength and decay at the same rate.

Landahl (1967) calculated cross-spectral statistics for wall pressure fluctuations by modeling the turbulent shear flow as a waveguide and solving (using a non-homogeneous Orr-Sommerfeld equation) for the least damped modes of propagation. This analysis showed a similarity scaling behavior for the calculated coherence and his results compared favorably with the experimental results of Willmarth and Wooldridge (1962). Landahl suggested that in the log-law region of the boundary layer the only appropriate length scale for scaling turbulence eddies is the size of the eddy itself. This conclusion is in agreement with the interpretation that the log-law layer is a region where there is no specific length scale and as such the scale for a given eddy is the eddy size itself which leads to the similarity scaling $(\omega\xi/U_c(\omega,\xi)=k_1\xi)$.

Bull (1967) assumed that the wall pressure field coherence function, in the region of similarity scaling, followed the form of an exponential decay, given as

$$\Gamma(\omega,\xi)=\exp[-C_1|\omega\xi/U_c(\omega,\xi)|], \quad (5.4)$$

Bull used $C_1=0.1$ as the decay constant that best fit the streamwise coherence data. Assuming this approximation is valid, decay constants of 0.145 and 0.125 were obtained for the data in figures 5.7 and 5.8, respectively. Equation (5.4), using these decay constants, is shown for comparison in the appropriate figure. The loss of coherence in the similarity scaling region can be seen to follow an exponential decay law fairly well. Values of C_1 ranging from 0.1 to 0.19 are reported in the literature with the value of 0.11 being most common. Brooks and Hodgson (1981) report values of C_1 that decrease slightly with increasing free-stream velocity as do the values of C_1 for the current study.

The form of equation (5.4) shows that $\Gamma(\omega,\xi)$ is a measure of the memory of the wall pressure field as it convects downstream. The turbulence structures in the flow field that generate the wall pressure fluctuations are continually distorted by the dispersive action of the mean flow gradient as they convect downstream. This results in a loss

of coherence to both the turbulence structure and wall pressure field as they are convected downstream. A measure of the streamwise distance over which a pressure eddy remains coherent can be obtained from equation (5.4). Using $C_1=0.125$ in equation (5.4) it is found that a turbulent pressure eddy will decay to 1/10 its value in having traveled the distance of approximately three of its wavelengths. Interestingly, Blake (1984) points out that the values of C_1 obtained from the streamwise cross-spectrum measurements are very similar in value to those measured for the cross-spectrum of velocity fluctuations in the log-law region of a turbulent boundary layer.

The lack of similarity scaling (deviation from equation (5.4)) that occurs at low frequency for all coherence plots is also seen in the measurements reported by others, for example, Bull (1967), Brooks and Hodgson (1981), and Narayan and Plunkett (1985). However, the data of Blake (1970) does not show this breakdown in similarity scaling at low frequency. Additionally, the coherence data of Bull (1967) do not exhibit a peak at low frequencies as do the current measurements, but instead asymptotically approach a constant value of coherence with decreasing frequency. The presence of a peak in the coherence measurements is seen in the data of the others and is also predicted by the pressure field modeling of Chase (1983). The lack of similarity scaling that occurs at low frequency is actually a physical requirement of the wall pressure field as described below.

Assuming that equation (5.4) holds for all values of the similarity variable (all ξ and all ω) then $\Gamma(\omega, \xi)$ will go to unity as the similarity variable $\omega\xi/U_c(\omega, \xi) \rightarrow 0$. However, figures 5.7 and 5.8 show that $\Gamma(\omega, \xi)$ does not go to unity for small values of $\omega\xi/U_c(\omega, \xi)$. This discrepancy points out an interesting feature of the wall pressure field which requires that some re-interpretation of the measured cross-spectral data be made. This re-interpretation becomes crucial in understanding the non-equilibrium flow results.

To understand this discrepancy consider the two methods by which the $\omega\xi/U_c(\omega, \xi) \rightarrow 0$ limit can be obtained. $\omega\xi/U_c(\omega, \xi) \rightarrow 0$ can be obtained either by taking $\omega \rightarrow 0$ with a fixed value of ξ , or by $\xi \rightarrow 0$

with a fixed frequency. $\Gamma(\omega, \xi) \rightarrow 1$ as $\xi \rightarrow 0$ is a required result since for $\xi=0$ the cross-spectrum becomes the single-point auto-spectrum which has a unity value of coherence for all frequencies. On the other hand, if $\Gamma(\omega, \xi)$ were to approach unity as $\omega \rightarrow 0$, it would imply that the low frequency components of the pressure field are correlated over very long streamwise distances. This would require that the pressure source terms located in the boundary layer convect over large distances without being distorted by the mean velocity gradients of the flow. This violates physical reality and in fact does not occur. Instead, as the frequency approaches a zero value, even for finite separations, the coherence begins to decay.

In this study the cross-spectral measurements were obtained by holding ξ fixed and sweeping ω . Thus, a breakdown in similarity scaling at low frequency occurs as is physically required. This shows the effects of the inhomogeneity of the boundary layer. Results for the low frequency (low wavenumber) region will now be discussed.

Bull (1967) suggests that the wall pressure field is comprised of two groups of wavenumber components, one group that is of high wavenumber which lose coherence with $\omega\xi/U_c(\omega, \xi)$ similarity scaling, and a lower wavenumber group that lose coherence independently of wavenumber. Bull set the division between the two wavenumber groups as being where the coherence curves start deviating from a similarity scaling and found that this deviation occurs at roughly the same value of $\omega\delta^*/U_c(\omega, \xi)$ for each curve. This is consistent with a wavenumber independence behavior to the lower wavenumber group since $\omega\delta^*/U_c(\omega, \xi)$ can also be written as $k_1\delta^*$ assuming a Taylor's hypothesis holds. The low frequency coherence data obtained in the current investigation show a different behavior. Below the cutoff Strouhal number the coherence rapidly decreases with decreasing frequency. For these measurements the low frequency pressures are not wavenumber independent, as found by Bull.

The coherence data in figure 5.8 is replotted in figure 5.13 as a function of $\omega\delta^*/U_c(\omega, \xi)$ ($=k_1\delta^*$) which shows that the non-similarity scaling pressures peak and lose coherence at approximately the same value of $\omega\delta^*/U_c(\omega, \xi)$. The peaks in the coherence curves shift mildly

from a value of $\omega\delta^*/U_c(\omega,\xi)=0.35$ at $\xi/\delta^*=1.5$ to approximately 0.17 at $\xi/\delta^*=100$. Bull obtained a value of $\omega\delta^*/U_c(\omega,\xi)=0.35$ as point of demarcation between the two scaling groups using the value at which non-similar scaling begins. Although based on slightly different definitions, the cutoff Strouhal number obtained from figure 5.13 and that reported by Bull are quite similar. It seems that the size of the large scale pressure sources are limited by the boundary layer to $k_1\delta^*=0.17$. This corresponds to a streamwise wavelength of $\lambda=30\delta^*$. Similar results are also found for the lower speed data. Before proceeding it is noted that if a $U_c(\omega,\xi)=0.7$ is assumed then the peak in the coherence curves are found to occur at a value of $\omega\delta^*/U_c=0.25$.

As a check on the argument that $\Gamma(\omega,\xi)$ approaches unity as $\xi \rightarrow 0$ for fixed ω_0 , the 93 ft/sec coherence data were cross-plotted to obtain plots of $\Gamma(\omega_0,\xi)$. These plots of coherence are shown in figure 5.14 for selected values of frequency $f_0=\omega_0/2\pi$. Specific data points are marked with a symbol and a straight line connects each data point. The $\omega\delta^*/U_c(\omega,\xi)=0.35$ peaks in the coherence plots correspond to $f_0=250$ Hz. The square symbol is used for the coherence data with f_0 below 250 Hz and the 'x' for data above 250 Hz. Included in the figure is the line for an exponential decay law (equation (5.4)) using $C_1=0.125$ as obtained from figure 5.8. The high frequency curves ($f_0>400$ Hz) show a slight trend of a decreasing level of coherence with increasing frequency in the mid-region of the curves ($\omega_0\xi/U_c(\omega_0,\xi)=7.0$). This trend can be seen by comparing the 400 Hz curve to the 1500 Hz curve, both of which are indicated in the figure.

Clearly $\Gamma(\omega_0,\xi)$ approaches unity as $\omega_0\xi/U_c(\omega_0,\xi)$ approaches zero, for fixed frequency, as is required. However, the 100 and 200 Hz curves do not follow the general similarity trend, consistent with these data being in the wavenumber cutoff region. Although the curves for $f_0>250$ Hz all follow a similarity type behavior, the exponential decay constant (C_1) that best fits each curve increases slightly with increasing frequency. This shows that equation (5.4) is, at best, only a fair approximation for the pressure coherence in the similarity region.

5.3.4 Streamwise Convection Velocity

Before discussing the convection velocity data, a brief point about the computation of convection velocities is in order. As discussed in Chapter 2, the cross-spectra of the wall pressure field can be interpreted in terms of a wave-like behavior of the pressure fluctuations. The phase of the cross-spectrum is directly related to the convective velocity of the pressure fluctuation, given as

$$\theta(\omega, \xi) = -\omega \xi / U_c(\omega, \xi). \quad (5.5)$$

If $U_c(\omega, \xi)$ is assumed to be locally constant, that is $U_c(\omega, \xi) \approx U_c(\omega_0, \xi)$ over a small range of ω , then the slope of the phase can also be interpreted as a convection velocity,

$$U_c(\omega_0, \xi) = -\xi / [d\theta(\omega_0, \xi) / d\omega]. \quad (5.6)$$

Both relationships are (sometimes) used to calculate convection velocities. The advantage of using equation (5.6) is that $d\theta(\omega_0, \xi)$ can be evaluated over a sufficiently wide $d\omega$ range as to obtain smoothly varying values of $U_c(\omega, \xi)$. However, this pre-supposes that $U_c(\omega, \xi)$ is constant over that range. Since this may not be the case, particularly for the non-equilibrium flow, equation (5.5) was used to calculate $U_c(\omega, \xi)$ from the cross-spectral data.

The scatter that is present in the convection velocity data in figures 5.9 and 5.10 is a result of variations in the measured values of cross-spectrum phase. Errors in measured phase increase inversely with the level of coherence as given by equation (3.3).

Blake (1970) addressed the differences between group and phase velocity for wall pressure measurements. He showed that cross-spectrum measurements, if measured in a sufficiently small frequency bandwidth ($\Delta\omega/\omega$), provide a measure of the phase velocity of the frequency components of the pressure field. If, however, measurements are made with a wide frequency filter, then the phase measurements are related to the group velocity of the pressure field. Blake attributed filter bandwidth effects as the reason for the differences between his low frequency convection velocity results and those reported by Bull. The current measurements were made with a 2.4 Hz bandwidth for the data up to 500 Hz, a 9.7 Hz bandwidth for the data up to 2,000 Hz, and a 97 Hz bandwidth for the data up to 20,000 Hz (equivalent noise bandwidth).

Data were obtained in the three different analysis ranges in order to satisfy the small bandwidth requirement for all frequencies of interest. The term convection velocity and phase velocity will be used interchangeably.

Figures 5.9 and 5.10 show the values of pressure field phase velocity measured at 51 and 93 ft/sec, respectively, for streamwise separations ranging from $\xi/\delta^* = 1.5$ to $\xi/\delta^* = 100$. Phase velocity is presented as a function of the Strouhal number $\omega\delta^*/U_0$. With increasing ξ/δ^* the measured phase velocities increase for all values of $\omega\delta^*/U_0$. The overall trends are the same for both speeds. Discussions will center on the 93 ft/sec results (figure 5.10).

The variations in $U_c(\omega, \xi)/U_0$ with $\omega\delta^*/U_0$ are in qualitative agreement with the results of Blake (1970). The phase velocity initially increases with increasing frequency, reaches a maximum value at approximately $\omega\delta^*/U_0 = 0.3$, and then (for the smaller separations) decreases approaching an asymptotic value at high frequency. For separations greater than $\xi/\delta^* = 33$ a peak in convection velocity is no longer seen. The rapid decrease in phase velocity at low frequency is present in the data of Blake but is not present in the data of Bull. The data of Blake are too sparse to draw firm comparisons with the present data, but it appears as if the trend of increasing phase speed with increasing ξ/δ^* is present in his data.

The peak value of convection velocity that is measured for virtually all separations occurs at approximately a fixed value of $\omega\delta^*/U_0 = 0.3$. A suggested line is placed through the peak values of convection velocity in figure 5.10. Using an average convection velocity of $U_c = 0.77U_0$ places the line of maximum convection velocity at $\omega\delta^*/U_0 = 0.4$ or $k_1\delta^* = 0.4$, which is at essentially the same location as the peak in the coherence data. Hence, the wavenumber of the pressure eddies that have maximum phase velocity is close to the wavenumber at which maximum coherence is measured (figure 5.13). The peak phase velocity occurs within the wavenumber cutoff region of pressure fluctuations but occurs near the start of that region.

The validity of a Taylor's hypothesis for wall pressure fluctuations can be evaluated from the phase velocity data. For a Taylor's hypothesis to hold there must be a unique convection velocity that relates the wavenumber of a fluctuation to the frequency that it produces $k_1 = \omega / U_c(\omega)$. An assumption of this type has been freely assumed throughout the earlier discussions. Figure 5.10, for example, shows that this condition is not met exactly since for a fixed frequency the convection velocity varies with ξ/δ^* . The pressure field is thus characterized as being dispersive; fluctuations of nominally the same length scale convect at different velocities. This is illustrated in the work of Wills (1970) in which cross-spectral measurements were spatially transformed to give contour plots of $\phi_p(k_1, \omega)$.

Interpretation of pressure field data is greatly simplified by assuming the validity of a Taylor's hypothesis. Wills found that at constant frequency the range of measured phase velocities were normally distributed with a standard deviation of 14% of the average value. The errors that arise when a Taylor's hypothesis is used are thus small.

5.3.5 Transverse Coherence and Phase

Cross-spectrum measurements were obtained at 51 and 93 ft/sec for twelve transverse spacings. No convection in the transverse direction was measured ($\theta(\omega, \xi) \approx 0$). Plots of the transverse coherence versus the similarity variable $\omega\eta / U_c(\eta)$ were made where $U_c(\eta)$ was taken as the value of maximum convection velocity obtained for the streamwise convection measurements with a streamwise spacing equal to the transverse spacing ($U_c(\eta) = U_{cmax}(\omega, \xi = \eta)$). This selection of a convection velocity is quite arbitrary but provides a slightly better collapse on similarity variables than is obtained using the freestream velocity as the velocity scale. These data are shown in figures 5.11 and 5.12 for 51 and 93 ft/sec, respectively. Included in each figure is a suggested exponential fit of the form

$$\Gamma(\omega, \eta) = \exp[-C_2 |\omega\eta / U_c(\eta)|] \quad (5.7)$$

where $C_2 = 0.9$ for both data sets.

The general shape of the transverse coherence plots are similar to those reported by Bull (1967). As found for the streamwise coherence, at low frequency the curves deviate from a similarity scaling. This was not seen in the data of Blake (1970). Again one difference between the current measurements and those of Bull is the peak in the coherence measurements that is not seen in Bull's data. The maximum values of transverse coherence follow the same $\omega \delta^*/U_0$ trend as the streamwise measurements.

The wall pressures are coherent over a shorter transverse distance than streamwise distance, as is indicated by the larger exponential decay constant for the transverse data. Equation (5.7) shows that pressure eddies decay to 1/10 their value in a transverse distance of approximately 0.4 of the streamwise wavelength ($2\pi U_0/\omega$). The value of transverse decay constant obtained by Bull (1967) is 0.715. Blake (1970) does not specify a decay constant but shows that his transverse data agrees favorably with that of Bull. The reason for the larger decay constant in the current measurements is not known. However, the value of C_1 for both Bull and Blake was also smaller than that for the current measurements.

5.3.6 Discussion

As discussed earlier, one objective in measuring wall pressure fluctuations is to obtain a better understanding of what turbulence activity within the flow field produces surface pressure fluctuations. Simply stated, where in the flow are the source terms of the wall pressure fluctuations. The spectral measurements just presented provide a partial answer. Understanding the source terms for an equilibrium flow will help in interpreting the wall pressure measurements for the non-equilibrium flow.

The fluctuating wall pressures, as shown in Chapter 2, are a weighted integral of the velocity fluctuations that occur throughout the boundary layer. As such, a unique one-to-one correspondence between the wall pressure fluctuations and the velocity fluctuations at a specific location in the boundary layer does not exist. Instead, the best that can be said is that specific wall pressures are produced by turbulence activity in a particular "region" of the boundary layer.

Attempts at identifying pressure source regions assume that the length and velocity scales of the velocity field, where the pressure sources are located, match those of the pressure field. This amounts to primarily specifying that pressure sources are located at a position in the boundary layer y , where $U_c(\omega) = U(y)$. Additionally, the assignment of a turbulent structure in the boundary layer as a source of pressure fluctuations must be consistent with all of the measured spectral features of the wall pressure field.

The most notable features of the wall pressure field that were obtained from the cross-spectral measurements are now restated: (1) the single-point frequency spectrum scaled on combined inner-outer variables at low frequency ($\omega\delta^*/U_0 < 2.4$) and on inner variables at high frequency ($\omega\nu/U_0^2 > 0.4$); (2) the streamwise coherence consisted of two wavenumber groups, a higher wavenumber group that scaled on the similarity variable $\omega\xi/U_c(\omega, \xi)$, and a lower (cutoff) wavenumber group with a peak coherence at $\omega\delta^*/U_c(\omega, \xi) = 0.35$; (3) plots of convection velocity $U_c(\omega, \xi)/U_0$ versus $\omega\delta^*/U_0$ increased at low values of $\omega\delta^*/U_0$, reached a peak value at $\omega\delta^*/U_0 \approx 0.35$, and then decreased at higher values of $\omega\delta^*/U_0$ approaching an asymptotic value of $U_c(\omega, \xi)/U_0 \approx 0.65$. An additional feature to the convection velocity plots is the continual increase in convection velocity, at all frequencies, with increasing separation distance. Collectively, these features tend to identify more clearly the locations of the source terms. Each of these features will be further explored relative to their contribution to the pressure field.

Sources of Low Frequency Pressure Fluctuations

Figure 5.5 shows the frequency spectra scaled on combined inner-outer variables. The spectra peak at a value of $\omega\delta^*/U_0 \approx 0.3$. Below this peak the spectra have a nearly constant slope proportional to $\omega^{1/2}$. The extent of the $\omega^{1/2}$ region is limited by the low frequency limit (50 Hz) imposed by facility noise. Over the spectral region of $0.3 \leq \omega\delta^*/U_0 \leq 2.4$ the spectra follow a constant slope of $\omega^{-0.4}$ and similarly scale on combined inner-outer variables. Because of the low frequencies (hence large scales) that exist for $\omega\delta^*/U_0 \approx 0.3$ it is expected that the sources of these fluctuations are located in the outer region of the boundary

layer. This is supported by the convection velocity measurements. Peak convection velocities occur at about the frequency at which the spectra peak. Values of $U_c(\omega, \xi)/U_0$ range from 0.72 to 0.85 at $\omega\delta^*/U_0=0.3$. Hence, assuming $U(y)=U_c(\omega)$ this places the source of these pressure fluctuations at $350 < y^+ < 1000$ or $0.2 < y/\delta < 0.5$, which is in the outer region of the boundary layer thus explaining the success of the combined inner-outer variable scaling. This region produces the highest pressure levels. $\omega\delta^*/U_0=0.3$ is also the center Strouhal number for the wavenumber cutoff group of fluctuations that rapidly decay with decreasing frequency. The length scale for this Strouhal number is roughly $k_1\delta^*=0.3$ (or $\lambda=18\delta^*$).

The peak values of $U_c(\omega, \xi)/U_0$ appear to be directly associated with the maximum values of coherence. As $U_c(\omega, \xi)/U_0$ increases with increasing ξ , the peak in $\Gamma(\omega, \xi)$ shifts to lower values of $\omega\delta^*/U_0$ (figure 5.13). In turn, the inferred streamwise length scale for the pressure field also increases with increasing ξ . A range of streamwise length scales from $\lambda=18\delta^*$ to $30\delta^*$ are thus present in the outer region of the boundary layer.

Below $\omega\delta^*/U_0=0.3$, the convective phase velocity decreases rapidly indicating source positions nearer the wall. However, the length scales associated with these pressure fluctuations are increasing. This is demonstrated in figure 5.15 where $k_1\delta^*$ ($k_1=\omega/U_c(\omega, \xi)$) is plotted against $\omega\delta^*/U_0$ for each of the separations for the 93 ft/sec data. Note that $k_1\delta^*$ continually decreases with decreasing $\omega\delta^*/U_0$. The fact that the apparent source location moves closer to the wall as the scale of the fluctuation increases is contradictory to the general hypothesis that only small scale fluctuations exist near the wall. However, the analytical study of Panton and Linebarger (1974) supports this observation. They showed that the major contribution to the (one-dimensional) wavenumber spectrum of the wall pressure field at lower wavenumbers comes from the outer portion of the boundary layer. However, at the lowest wavenumbers the contribution from the outer region decreases and the major contribution comes from the log-law region of the boundary layer.

It appears as though the sources of the very large scale pressure fluctuations are physically limited in size by the boundary layer. When pressure source terms exceed the limit of the boundary layer cutoff the sources undergo excessively large levels of distortion. This distortion greatly reduces the coherence of the source resulting in lowered values of $\Gamma(\omega, \xi)$. This distortion could result in the effective center of the source being located nearer the wall thus giving decreased values of convection velocity. Both of these results are consistent with the trends in the low frequency data.

Before preceding a few additional comments about figure 5.15 are in order. Figure 5.15 is a form of a dispersion spectrum for the pressure field. The figure is a direct plot of the cross-spectrum phase that was measured (and unwrapped) for each separation. The slope of the curves gives the pressure field group velocity U_g defined as,

$$U_g = d\omega/dk_1, \quad (5.8)$$

$$(U_g/U_0 = d(\omega\delta^*/U_0)/d(k_1\delta^*)).$$

The validity of using Taylor's hypothesis is best demonstrated by this figure. Although $k_1\delta^*$ is a slowly varying function of $\omega\delta^*/U_0$, the spread in values of $\omega\delta^*/U_0$ at fixed values of $k_1\delta^*$ is sufficiently small that a single value could be used without much error. Hence, a Taylor's hypothesis is generally acceptable for the wall pressure field (at least for the wavenumbers and frequencies that are the major contributors to the pressure spectrum).

Sources of Mid- and High Frequency Pressure Fluctuations

Above $\omega\delta^*/U_0 = 0.3$, the wall pressure spectra (figure 5.5) follow a constant slope of $\omega^{-0.11}$ out to $\omega\delta^*/U_0 = 2.4$. Additionally, over this Strouhal number range the convective phase velocity (figures 5.9 and 5.10) asymptotically decreases to a value that is separation distance dependent and the pressure field coherence (figures 5.7 and 5.8) follows a similarity scaling behavior. Before proceeding, it should be noted that valid cross-spectrum data could only be obtained out to $\omega\delta^*/U_0 = 2.4$, with the smallest spacings, due to the loss of coherence that occurs for larger separations. This is illustrated by considering the following.

Take $r(\omega, \xi) \geq 0.1$ as being the limit for valid cross-spectral measurements. This coherence limit occurs at approximately $\omega \xi / U_c(\omega, \xi) = 20$ which can be expressed in terms of a $\omega \delta^* / U_0$ limit as

$$\omega \delta^* / U_0 = [\omega \xi / U_c(\omega, \xi)] * [U_c(\omega, \xi) / U_0] * [\delta^* / \xi].$$

Assuming a value of $U_c(\omega, \xi) / U_0 = 0.7$ gives the coherence limit as $\omega \delta^* / U_0 = 14 \delta^* / \xi$. As ξ / δ^* increases the highest value of $\omega \delta^* / U_0$ at which valid cross-spectra can be obtained decreases. Thus, the Strouhal number range of $0.3 \leq \omega \delta^* / U_0 \leq 2.4$ covers the range of measurements for which valid cross-spectral data could be obtained.

Values of convective phase velocity for this mid-frequency region vary from about $U_c(\omega, \xi) / U_0 = 0.8$, for the largest separations, to $U_c(\omega, \xi) / U_0 = 0.62$ for the smallest separations, which locates the pressure sources in the boundary layer between $y^+ = 150$ and $y^+ = 735$ ($y/\delta = 0.07$ to $y/\delta = 0.36$). This places the sources in the lower portion of the outer flow region or in the log-law region of the inner layer. Supporting this conclusion is the fact that over this frequency region the coherence follows a similarity scaling which is also indication that the pressure source terms are located in the log-law region of the boundary layer.

Bradshaw (1967) argues that the spectrum of pressure fluctuations generated by sources in the universal (log-law) region should scale as k_1^{-1} . The universal region is a region of overlap between pressures that scale on combined inner-outer variables and pressures that scale on inner variables. Panton and Linebarger (1974) discussed this issue and showed that the pressure spectrum in the overlap region must scale as k_1^{-1} . The form of the argument that is followed to show this scaling is a spectral equivalent of the arguments that are used to show a logarithmic scaling must hold for the mean velocity profile in the overlap region. Bradshaw points out that a frequency spectrum may exhibit a slightly weaker frequency scaling since $U_c(\omega)$ decreases with increasing ω and suggests an $\omega^{-5/6}$ as an expected scaling rate.

Considering the above discussion, the $\omega^{-0.4}$ scaling shown in figure 5.5 is considered to be indicative of a spectrum due to sources in the log-law region. Blake (1970) reports an $\omega^{-0.75}$ dependence to his

smooth wall pressure spectrum over a range of $\omega\delta^*/U_0$ from 0.4 to 8.0. Schewe (1983), who used extremely small pressure transducer (non-pinhole type) obtained data that do not show a spectral region that scales as ω^{-1} . Most reported pressure spectra data do not show a definite region of ω^{-1} scaling.

Above $\omega\delta/U_0=2.4$, the combined inner-outer variable scaling no longer holds. At higher frequencies the pressure spectrum scales on inner variables as shown in figure 5.6. Cross-spectral data could not be obtained in this frequency range. It is assumed, with the support of analytical models (Blake (1984)), that the pressure sources for these frequencies are in the inner layer. Measurements in this frequency range are subject to large errors due to transducer size effects. Blake (1984) suggests that the spectrum in this region should scale as ω^{-5} . A rough fit through the high frequency portion of the spectra in figure 5.6 gives a scaling of ω^{-6} .

5.4 Spectral Features of Wall Pressure Fluctuations for Non-Equilibrium Flow

5.4.1 Frequency Spectra

Single-point frequency spectra of the wall pressure fluctuations were obtained for an extensive number of streamwise positions. For each cross-spectrum that was measured single-point spectra were obtained for both transducers. For sake of clarity only spectra obtained at the upstream position of each cluster will be presented.

Figure 5.16 shows $\Phi_p(x/h, \omega)$ obtained at 90 ft/sec at each cluster position. The inhomogeneity of the wall pressure field is evident from this data. Not only is there a wide range of levels measured for any particular spectral component but the overall spectral shapes change with streamwise location. Included in this figure is the equilibrium flow spectrum. Similar results are also obtained for the 50 ft/sec spectra.

The features of the non-equilibrium spectra that differ from the equilibrium spectrum are the excess low frequency content and the depressed high frequency content. As shown by Farabee and Casarella (1985), the low frequency region is maximum at the point of flow

reattachment. Downstream of reattachment the low frequency region slowly reduces in magnitude as the flow undergoes relaxation and redevelopment. Even as far downstream as $x/h=72$ there is still an excess content to the low frequency fluctuations. Near reattachment the high frequency end of the pressure spectra are initially lower than the equilibrium flow spectrum. In the downstream direction the high frequency fluctuations increase in level and by $x/h=72$ are of the same level as the equilibrium spectrum (note that the equilibrium spectrum should be shifted down by 0.5 dB to adjust for the speed difference, i.e., assuming $\Phi_p(\omega)=U^3$ at low frequencies). Variations of the low frequency components with streamwise position are associated with the relaxation of the disturbance layer within the boundary layer while the high frequency variations are associated with the boundary layer redevelopment near the wall.

Identification of pressure source regions within the boundary layer can be made by evaluating the scaling dependence of the pressure spectra. Two issues arise; the scaling variables that collapse the spectra for the two speeds, at a fixed streamwise location, and, more importantly, the scaling variables that collapse the spectra measured at all streamwise locations. The former scaling variables do not provide much insight into the dependence of the pressure field on the non-homogeneous aspects of the flow field. However, the latter scaling variables provide valuable information as to what regions in the perturbed flow contain the wall pressure source terms.

For equilibrium flows the low frequency region was found to scale on combined inner-outer variables (τ_0 and U_0/δ^*). Spectra obtained at each x/h location at 90 ft/sec are shown in figure 5.17 non-dimensionalized using the combined inner-outer variables. The scaling parameters for the $x/h=72$ spectrum were assumed to be the same as measured at $x/h=54$ since flow field data were not obtained at $x/h=72$. Included in this figure is the equilibrium flow spectrum. Figure 5.18 shows the spectra obtained at $x/h=10$ and 72, for both 50 and 90 ft/sec, also plotted against the combined inner-outer variables. Combined inner-outer variable scaling accounts for speed effects but are not the variables on which the non-equilibrium pressures scale. With these

variables there is still a 12 dB spread in the non-dimensionalized spectra. Obviously, the pressure source terms for the low frequency portion of the spectrum do not scale on τ_0 , U_0 and δ^* for the perturbed flow.

Spectral analysis of wall pressure fluctuations downstream of various type of surface mounted irregularities have been reported by others; for example by Greshilov, Evtuchenko and Lyamshev (1967), by Fricke and Stevenson (1968), by Fricke (1971), and by Elswick (1972). Fricke (1971) non-dimensionalized wall pressure spectra, measured downstream of a surface fence, on outer variables using the step height as the length scale ($\Phi_p(\omega)U_0/q^2h$ vs. $\omega h/U_0$). The 90 ft/sec data were non-dimensionalized using these variables and are shown in figure 5.19. There is still about a 9 dB spread in spectral levels for the peak in the low frequency region. However, this form of frequency scaling aligns the peaks to nearly the same Strouhal number $\omega h/U_0 \approx 0.5$. The peak Strouhal number obtained by Fricke (1971) is $\omega h/U_0 \approx 0.3$ for the measurements downstream of reattachment. Greshilov et al. (1969), obtained a peak Strouhal number of approximately 0.7 for a ramp-like surface projection. In earlier work (Farabee and Casarella (1984)) the peak Strouhal number was found to decrease upstream of reattachment in much the same way the peak Strouhal number measured by Fricke (1971) decreased upstream of reattachment.

Failure of the above scaling variables to collapse the low frequency portion of the wall pressure spectra is not unexpected. The wall pressure spectra are markedly inhomogeneous and as such, scaling parameters that account for this feature are needed. The outer scaling of Fricke only accounts for variations in local free-stream velocity U_0 . The combined inner-outer variables account for τ_0 , U_0 and δ^* but a comparison of figures 4.8 and 4.10 to figure 5.1 shows that the variations in p_{RMS}/q are greater than those of τ_0 ($\tau_0 = C_f q$), U_0^3 and δ^* , hence, collapse on inner-outer variables will not be obtained. In Chapter 4 the inhomogeneity in the flow field was shown to be associated

with the presence of the disturbance layer. It thus seems logical to non-dimensionalize the pressure spectra on variables pertinent to the disturbance layer.

A pressure and time scale are needed in non-dimensionalizing the magnitude of the pressure fluctuations. The pressure scale will be taken as the maximum value of the turbulence Reynolds stress, $-\overline{\rho u'v'}$, that is measured in the disturbance layer. Instead of a specific time scale a ratio of length to velocity scales will be used. The length scale will be taken as the distance, δ_d , that the disturbance layer is away from the wall and the velocity scale will be taken as the mean velocity at this location ($U(\delta_d)$). For non-dimensionalization of the frequency the dimensionless group $\omega h/U_0$ will be used since it has already been shown to collapse the location of the low frequency peak. The pressure spectra non-dimensionalized on disturbance layer variables is given as

$$\frac{\Phi_p(\omega, x/h) U(\delta_d)}{(\overline{\rho u'v'})^2 \delta_d} \quad \text{vs.} \quad \frac{\omega h}{U_0} \quad (5.9)$$

The success of this non-dimensionalization of the inhomogeneous pressure field is demonstrated in figure 5.20. The total spread in peak spectral level, at low frequency, is less than 1.5 dB. This scaling can only be considered to hold up to $\omega h/U_0 \approx 1.5$. Deviations from this scaling occur first for the furthest downstream spectra but hold to higher values of $\omega h/U_0$ closer to reattachment. The selection of $\overline{\rho u'v'}$ as the scaling pressure term, as opposed to say $\overline{pu'^2}$ or $\overline{pv'^2}$, is immaterial in that all of the turbulence terms decay at the same rate with downstream position as shown by figure 4.32. In light of the discussions in Chapter 2, $\overline{pv'^2}$ would perhaps be a more appropriate choice. Clearly the disturbance layer is the source of the excess low frequency energy in the pressure spectra. The propagation of the disturbance layer across the boundary layer as it convects downstream produces the inhomogeneity in the wall pressure field. The pressure spectra will not return to an equilibrium condition until the disturbance layer is totally dissipated and this has been shown to require a downstream distance of well over $100h$.

slightly above the non-dimensional spectra. An increase in u^* of only 8% for the equilibrium spectrum would bring it in line with the single curve formed by the perturbed flow spectra. Considering the error bounds on the measurements of u^* and the strong influence of transducer spatial averaging effects in this region, the scaling of high frequency components on inner variables is quite successful.

5.4.2 Streamwise Coherence

Measurements of the streamwise coherence of the wall pressure field were made for a range of separations at each cluster position as described earlier. Figures 5.22-5.24 show the coherence measurements obtained at 90 ft/sec for streamwise locations $x/h=10$, 24 and 54, respectively. Each curve in these figures is obtained with a fixed value of separation. Measurements obtained at 50 ft/sec show the same behavior. At $x/h=54$ (figure 5.24) the largest separation that could be obtained was $\xi=10$ -inch.

Features of the streamwise coherence for the non-equilibrium flow are quite different from those for the equilibrium flow, as shown by comparing figures 5.22-5.24 to figures 5.7-5.8. The first feature to note is the overall high values of coherence that are measured. At $x/h=10$ (figure 5.22), with $\xi/\delta^*=0.96$ (the smallest streamwise separation), the highest level of coherence that is measured is 0.96 while for the equilibrium flow the highest level is 0.88. Additionally, at any given value of $\omega\xi/U_c(\omega,\xi)$ the maximum value of $\Gamma(\omega,\xi)$ that is measured for the non-equilibrium flow is larger than the value measured for the equilibrium. The second feature is the complete lack of a high frequency similarity scaling which occurs for the equilibrium flow. The last feature is the extended range of values of $\omega\xi/U_c(\omega,\xi)$ for which $\Gamma(\omega,\xi)$ measurements were obtained which occurs due to the higher values of measured coherence. Measurements for the equilibrium flow could only be obtained out to an $\omega\xi/U_c(\omega,\xi)=20$ before $\Gamma(\omega,\xi)$ decayed below 0.05 while for the non-equilibrium flow coherence measurements out to $\omega\xi/U_c(\omega,\xi)>40$ were obtained for several cluster positions.

Comparisons between figures 5.22 to 5.24 show that the streamwise coherence is non-homogeneous. The value of $\Gamma(\omega,\xi)$ that is obtained at a fixed value of $\omega\xi/U_c(\omega,\xi)$ depends on the streamwise position x/h . This

is illustrated in figure 5.25. In this figure $\Gamma(\omega, \xi)$ for each x/h position is represented by an envelope obtained by the upper bound of the composite of the coherence curves (such as figure 5.22). Included in figure 5.25 is the curve obtained for the similarity scaling region of the equilibrium flow data. The coherence envelopes for all of the non-equilibrium measurements are above that for the equilibrium flow. In going downstream from $x/h=10$ to $x/h=16$ the envelope increases slightly but then remains nearly constant at $x/h=16, 24$ and 36 . Further downstream the envelope decreases and at $x/h=72$ is rapidly approaching the envelope for the equilibrium measurements.

The non-homogeneity has been shown to be produced by the disturbance layer in the flow field. Near reattachment, at $x/h=10$, the disturbance layer is still readjusting to the distortions encountered at reattachment. Hence, the coherence of the pressure field induced by this layer is slightly reduced. Over the range of $x/h=10$ to 36 the pressure source terms in the disturbance layer convect downstream without much distortion. Although the disturbance layer was shown (figure 4.32) to decay at a rate $\sim x^{-1/2}$, a reduction in coherence will not occur unless this decay is accompanied by a distortion. The reduction in pressure field coherence for measurements beyond $x/h=36$ can be attributed to either distortion in the disturbance layer or to propagation of the disturbance layer to an outer boundary layer position where it is a less effective source of wall pressure fluctuations.

As discussed for the coherence data of the equilibrium flow, similarity variable scaling implies length scales which are independent of the flow field scales. The lack of similarity scaling that is seen for the non-homogeneous pressure field indicates the presence of specific length scales. The excess low frequency pressures seen in the frequency spectra is another indication of a constant length scale disturbance in the flow.

If the pressure field scales on similarity variables then plots of $\Gamma(\omega, \xi)$ versus $\omega \xi / U_c(\omega, \xi)$ will be the same for variations in either ω or ξ . This is not the case. Displaying data with fixed ξ , (display format for figures 5.22-5.24) is more direct since data is obtained as a

function of ω with fixed ξ . However, it is more illustrative to plot coherence measurements as a function of ξ for fixed values of ω_0 . This directly shows the spatial variations of the coherence data at a fixed frequency. Also, such plots are the spatial correlation function of the wall pressure obtained at a fixed frequency.

Coherence data plotted as $10 \cdot \log_{10} [\Gamma(x/h, \omega_0, \xi)]$ versus $\omega_0 \xi / U_c(\omega_0, \xi)$ are shown in figures 5.26-5.29 for frequencies $f_0 = \omega_0 / 2\pi = 200, 300, 500$ and 1000 Hz, respectively. These frequencies were selected to span the frequency range over which the wall pressures scaled on disturbance layer variables. Each curve is for a different value of x/h . The logarithmic coherence format was selected to allow a direct indication of the exponential decay rate (equation 5.4) for each curve.

Figure 5.26 shows $\Gamma(x/h, \omega_0, \xi)$ for the frequency of maximum pressure fluctuation (200 Hz). At all x/h locations the decay of $\Gamma(x/h, \omega_0, \xi)$ with ξ is essentially the same. This indicates that the source of the 200 Hz pressure fluctuations is an organized disturbance that convects downstream. The decay rate of the non-equilibrium flow is much less than the equilibrium flow. Figure 5.26 shows that the 200 Hz component decays to 1/10 its original value over a distance of approximately 7.3 of its streamwise wavelengths, while the equilibrium data decays in a distance of approximately 3 wavelengths.

These unique features to the coherence measurements require some discussion. Both Townsend (1976) and Tennekes and Lumley (1972) discuss the physical interpretation of correlation and spectral functions for turbulence. The "broadness" of a correlation function is inversely related to the width of the Fourier transformed function. So, a slowly decaying cross-spectrum (coherence) implies a narrow wavenumber spectrum, and vice versa. Hence, the wavenumber spectrum of the non-equilibrium pressure field should be narrower than the spectrum for the equilibrium pressures. This is consistent with the non-equilibrium pressure field being produced by an organized eddy structure resulting from the earlier free-shear layer. However, Townsend points out that the spectral width of a wavenumber-frequency spectrum is attributable to two effects; the real decay of turbulent eddies, as just discussed, and the variability of the convection velocity of the pressure field (as a

function of, say, wavenumber). So that, although the coherence function for the non-equilibrium pressure field decays slowly, implying a narrow wavenumber content, it may be broadened if the various frequency components have a wide range of phase speeds.

Coherence measurements for the 300 Hz component (figure 5.27) show more variation with streamwise location than does the 200 Hz component. The overall decay rate increases in the downstream direction. This indicates that the field is broadening as it convects downstream. At 300 Hz the decay rate is still less than that for the equilibrium field. At a frequency of 500 Hz (figure 5.28) all decay rates are approximately the same. The non-equilibrium pressure field is evolving at the same rate as the equilibrium. This is in spite of the fact that the pressure spectra levels are higher at 500 Hz (for all x/h) than the equilibrium spectrum.

At 1,000 Hz (figure 5.29) an interesting feature has emerged. Pressure fluctuations at the $x/h=10$ location decay faster than at any other location including the equilibrium case. Except for $x/h=10$ the decay rates are the same. This indicates that even though the pressure spectra levels at 1,000 Hz are highest at $x/h=10$ (figure 5.16) the sources of the pressure fluctuations are quite broad. Only limited sets (limited in range of ξ that could be measured) of data could be obtained at higher frequencies but the trends just described seem to continue at higher frequencies.

The low frequency cutoff, imposed by the boundary layer size, is also evident in the non-equilibrium coherence data. Figure 5.30 shows the low frequency portions of $\Gamma(\omega, \xi)$ plotted against $\omega \delta^*/U_0$ for the 90 ft/sec data set measured at $x/h=24$. This figure is representative of the measurements at each of the x/h locations. The roll-off in coherence is more pronounced for the non-equilibrium pressure field than for the equilibrium, as seen by comparing figure 5.30 to figure 5.9. In figure 5.30 the peak Strouhal number shifts from $\omega \delta^*/U_0=0.15$ for $\xi/\delta^*=1.2$ to a $\omega \delta^*/U_0=0.2$ for a $\xi/\delta^*=115$. The peaks in the coherence spectra occurs at approximately the same Strouhal number as the peak in the pressure spectrum (figure 5.17). Whether the coherence would peak

without the non-equilibrium effects being present is not known but the strength of the peak is surely aided by the non-equilibrium character of the flow field. The equilibrium coherence values peaked over the Strouhal number range of 0.17 to 0.3 for $\xi/\delta^*=100$ to $\xi/\delta^*=1.5$, respectively.

5.4.3 Convection Velocity

Values of convective phase velocity of the non-equilibrium pressure field were calculated from the phase of the cross-spectra measured at the six cluster positions. Figures 5.31-5.33 show the phase velocities measured for various separations (ξ/δ^*) at locations $x/h=10$, 24 and 54, respectively. The global trends in the data are similar to each other and to the trends in the equilibrium data. At low frequency the phase velocity increases with frequency, maximizes at some value of $\omega\delta^*/U_0$, and then decreases, reaching some asymptotic value that depends on the value of separation. Values of convection velocity, at a fixed frequency, increase with increasing separation distance. Although the convection data are globally similar there are important differences in the data obtained at each x/h locations.

At $x/h=10$ (figure 5.31) the convective phase velocities are lower than what are obtained further downstream or what are obtained for the equilibrium flow. Furthermore, at this position there is a wide variation in $U_c(\omega, \xi)/U_0$ with separation (ξ/δ^*) and only the smallest ξ/δ^* measurements show a local peak value of $U_c(\omega, \xi)/U_0$ with $\omega\delta^*/U_0$. Further downstream, at $x/h=24$ (figure 5.32), the convective phase velocities are higher and show a very pronounced local peak for most separations. At $x/h=54$ (figure 5.33) the measured phase velocities have increased even more and also show an even further pronounced local peak. These variations with x/h illustrate the degree of inhomogeneity of the perturbed wall pressure field.

Figures 5.34(a-c) show the convective phase data plotted for fixed frequencies $f_0=200$, 300 and 500 Hz, respectively. In each figure data obtained at each x/h location, as well as for the equilibrium flow, are shown plotted against separation distance ξ/δ^* . This figure shows the variation in convective velocity that occurs as a function of separation distance and streamwise position for a fixed frequency. The variations

in convection velocity measured with different separations for the perturbed flow result from two effects; variations arising from length scale filtering due to spacing between measurement points, and variations due to changes in the location of the disturbance layer in the boundary layer with streamwise position.

By interpreting the convective phase velocity measurements as specifying the location of the pressure sources in the boundary layer, the following description of the flow field, as a source of wall pressure fluctuations, can be given. Near reattachment ($x/h=10$, figure 5.31) pressure source terms, at a given frequency, are distributed over a wide range of the boundary layer. For example, at $x/h=10$ (figure 5.34(a)), with $f_0=200$ Hz, the convection velocity varies from approximately 0.55 (smallest ξ/δ^*) to 0.79 (largest ξ/δ^*). This implies that the 200 Hz pressure sources are distributed from a $y^+=180$ ($y/\delta^*=0.5$) to $y^+=700$ ($y/\delta^*=2.2$). The source for the small separation measurement is within the buffer layer while the source at $y^+=700$ is in the outer layer (for an equilibrium boundary layer). Further downstream the dominant pressure sources move away from the wall. Accompanied with this migration from the wall is the redevelopment of a viscous sublayer in the boundary layer. This reestablishes the high wavenumber, inner layer, pressure sources that are typical for an equilibrium flow. Far downstream the pressure sources are located further out in the boundary layer than where they would be found for an equilibrium flow. This feature is illustrated in figures 5.34(a-b) by comparing the values of $U_c(\omega, \xi)/U_0$ (for the same ξ/δ^* value) measured at each x/h position to the equilibrium value. The $f_0=200$ sources have reached the equivalent equilibrium boundary layer position by $x/h=16$ (for small ξ/δ^*) and the $f_0=300$ reaches the equilibrium position by $x/h=24$.

All of these features are consistent with the disturbance layer being the source of the lower frequency pressure fluctuations. The disturbance layer is near the wall at reattachment and propagates away from the wall as it convects downstream.

Figures 5.35(a) and (b) show a plot of $k_1 \delta^*$ versus $\omega \delta^*/U_0$ generated from the convection velocity data obtained at $x/h=10$ and 24, respectively. These figures are similar to that for the equilibrium flow (figure 5.15). The purpose of figures 5.35 is to show that the length scale of the pressure producing eddies continually increases with decreasing frequency even though the convective phase speeds may decrease. These figures also demonstrate the wavenumber breadth that exists at a given frequency. At $x/h=10$ (figure 5.35 (a)) there is a wider range of wavenumbers (i.e. wider range of values of U_c/U_0) than at $x/h=24$. A Taylor's hypothesis for the perturbed flow wall pressures is generally not valid due to this wide range of measured convection velocities for a fixed frequency. Plots in the form of figures 5.35 obtained for the data at $x/h=54$ are not shown but are nearly identical to the plots in figures 5.35(b) ($x/h=24$).

5.4.4 Transverse Coherence

Measurements of the transverse coherence of the non-equilibrium pressure field obtained at $x/h=10$, 24 and 54 are shown in figures 5.36-5.38, respectively. As for the equilibrium flow, no convection in the transverse direction was measured (nominally zero phase for transverse cross-spectrum measurements). An average velocity $U_{cb}=0.7U_0$ is used to form the similarity variable $\omega \eta/U_{cb}$ used in plotting the transverse coherence data.

Transverse coherence measurements exhibit the same lack of similarity variable scaling seen in the streamwise measurements. This non-similar scaling is not a result of using a fixed value of U_{cb} . The overall transverse coherence levels are higher than measured for the equilibrium flow.

Figures 5.39-5.41 show plots of transverse coherence as a function of transverse spacing for frequencies $f_0=200$, 300 and 500 Hz, respectively. Data at all x/h locations and for the equilibrium flow are included. Figure 5.39 shows that generally, at 200 Hz, the transverse coherence at $x/h=10$ is lower than at other downstream positions but is still larger than the equilibrium condition. The 300 Hz component of transverse coherence (figure 5.40) approaches the

equilibrium transverse coherence levels further downstream. At 500 Hz the coherence levels are all about equal to the equilibrium levels.

There is nothing specifically unique about the transverse coherence measurements that is not also seen in the streamwise coherence data.

5.4.5 Summary

As stated earlier the objective of obtaining spectral data of the non-equilibrium pressure field is twofold; first, since non-equilibrium flows are commonly encountered in practical flow situations a knowledge of the wall pressure fluctuations that are induced is needed in order to be able to predict structural response; second, by studying the details of both the turbulence flow field and the fluctuating wall pressures a better understanding of the process by which turbulent velocity fluctuations produce unsteady wall pressures will be obtained. Detailed discussions of the latter objective are deferred to the next Chapter which discusses further the relationships between velocity fluctuations and pressure fluctuations.

The most striking characteristic of the perturbed flow wall pressure field is that it is non-homogeneous. This is demonstrated most clearly in figure 5.6. Overall pressure levels are highest near reattachment and decrease in the streamwise direction. The pressure spectra have a band, centered at $\omega h/U_0 = 0.5$, of excess energy.

The source of the pressure field inhomogeneity was identified to be the disturbance layer that propagates through the boundary layer. The disturbance layer introduces a fixed length scale which alters the cross-spectral properties of the wall pressure field. The coherence of the wall pressure field is similarly non-homogeneous and is higher than what is found for an equilibrium flow. Additionally, there is no frequency region in which the coherence follows a similarity scaling. The convective phase velocities are also non-homogeneous and show characteristics that can be related to the location of the disturbance layer in the boundary layer.

Table 5.1 - Values of RMS Pressure

x/h	U_0 (ft/sec)	p/q	p/τ_0	du^*/v	d/δ^*
10	90	0.0020	9.63	47.6	0.120
10	50	0.0185	8.53	26.8	0.116
16	90	0.0141	4.38	56.0	0.164
16	50	0.0137	4.72	31.0	0.143
24	90	0.0116	3.83	57.0	0.150
24	50	0.0115	3.63	32.4	0.143
36	90	0.0106	3.50	57.0	0.147
36	50	0.0106	3.25	32.9	0.145
54	90	0.0098	2.99	59.5	0.152
54	50	0.0100	2.90	33.8	0.139
72	90	0.0099	3.00	59.5	0.152
72	50	0.0098	2.85	33.8	0.139
Eq. Flow	93	0.0092	3.20	58.2	0.185
Eq. Flow	51	0.0092	2.83	33.3	0.177

($d=0.032$ -inch)

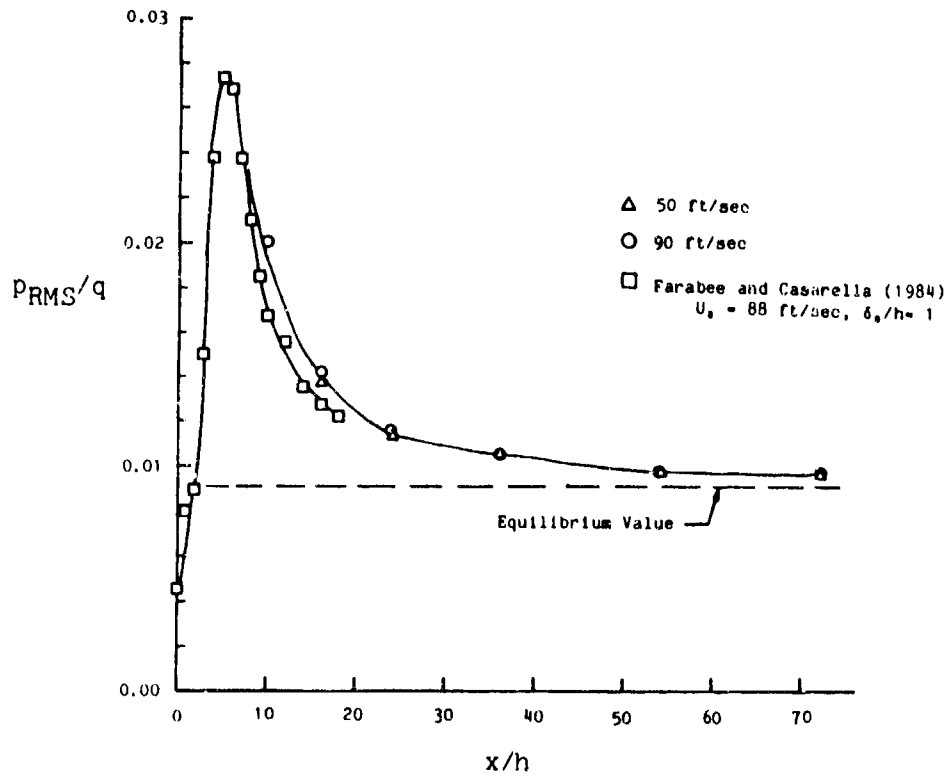


Figure 5.1 RMS Wall Pressure Fluctuations at Downstream Locations

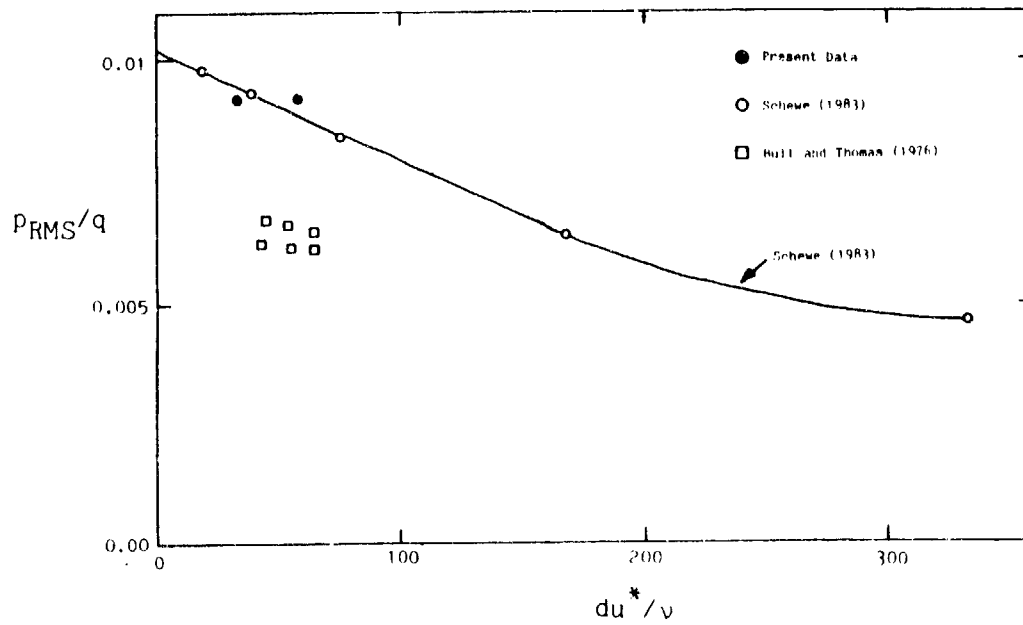


Figure 5.2 Comparison of RMS Pressure Fluctuations for Equilibrium Flows

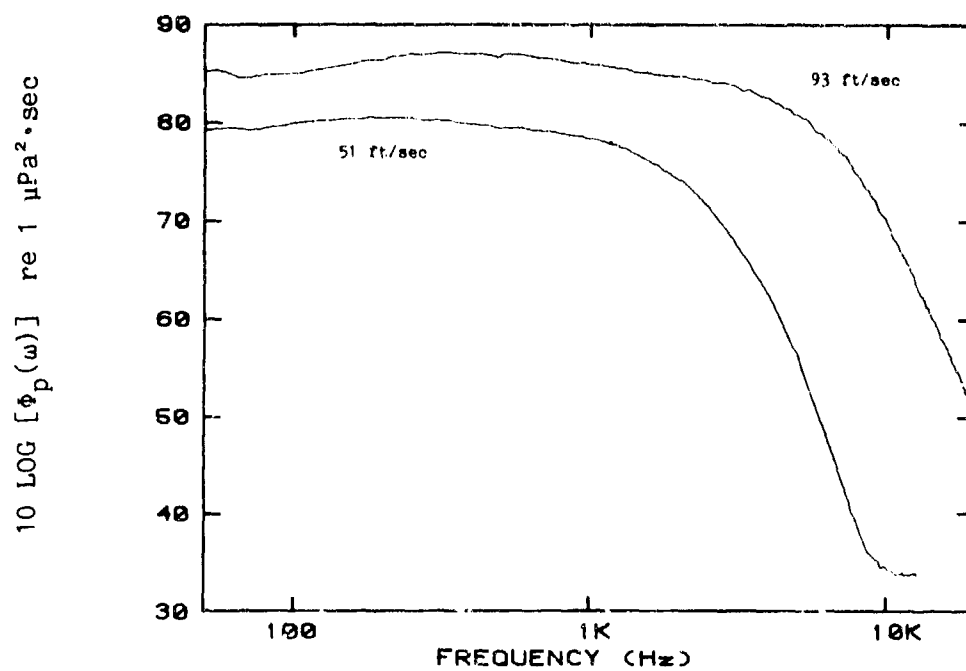


Figure 5.3 Wall Pressure Spectra For Equilibrium Flows

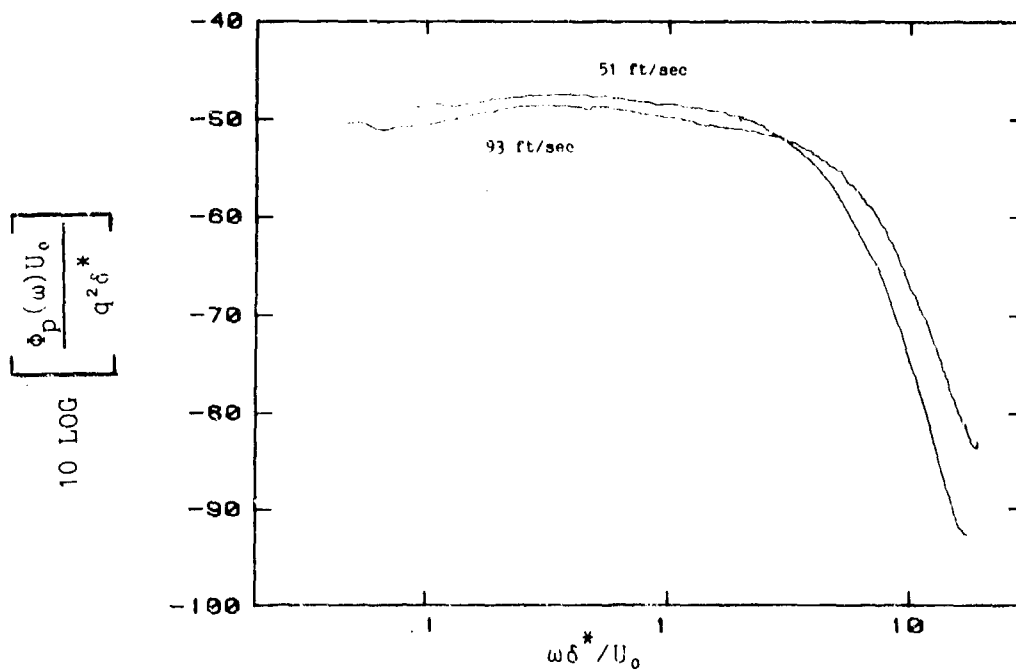


Figure 5.4 Wall Pressure Spectra Scaled on Outer Variables (Equilibrium Flow)

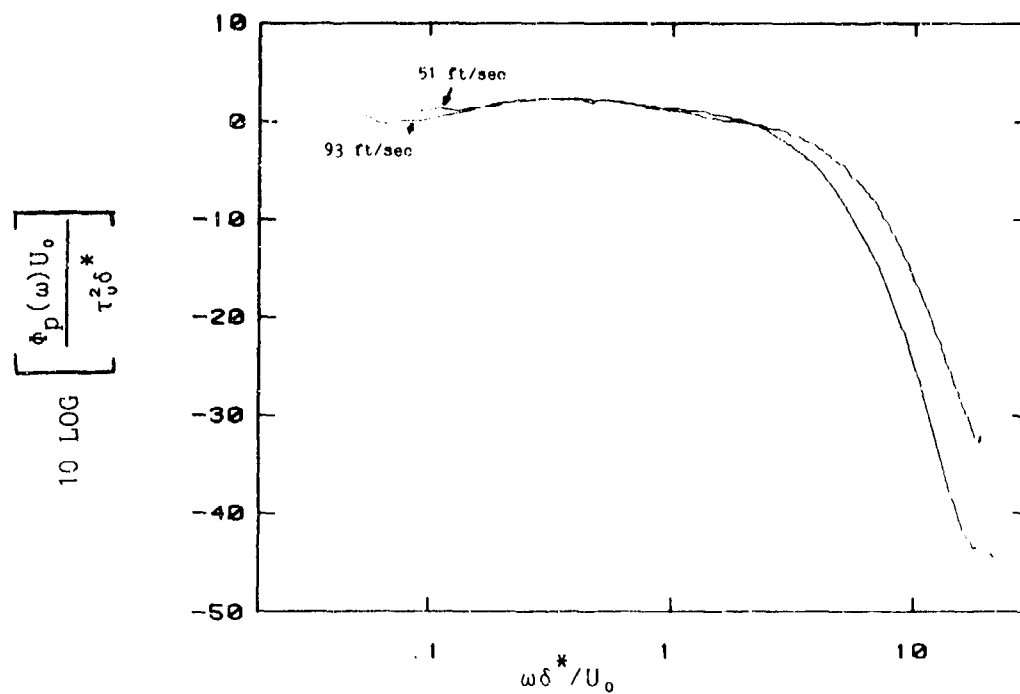


Figure 5.5 Wall Pressure Spectra Scaled on Inner-Outer Variables (Equilibrium Flow)

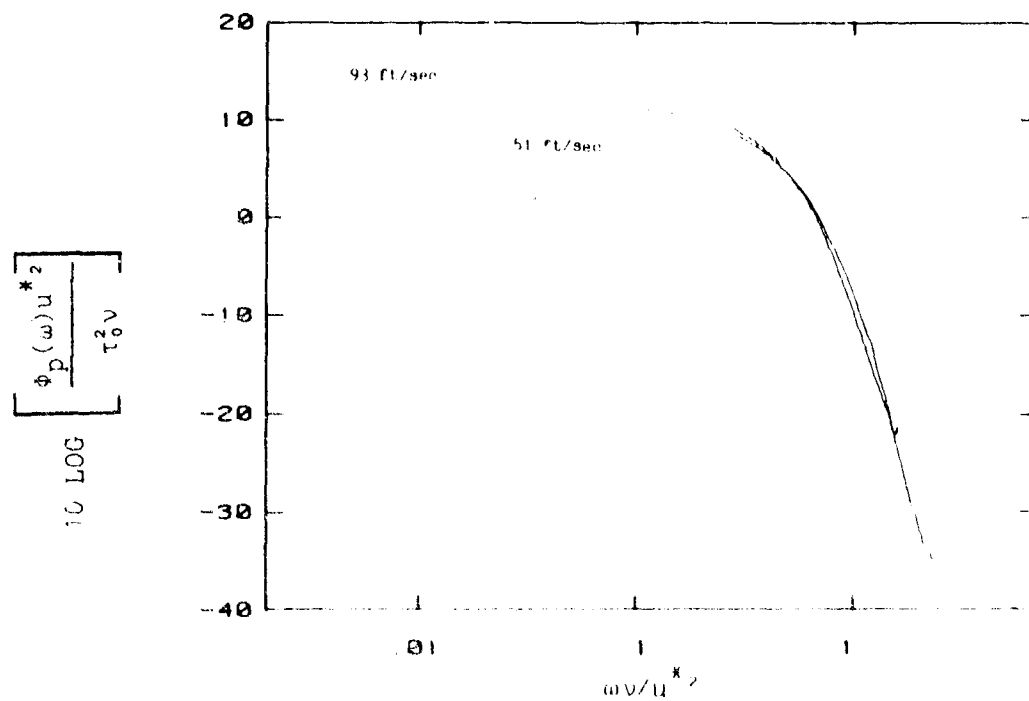


Figure 5.6 Wall Pressure Spectra Scaled on Inner Variables (Equilibrium Flow)

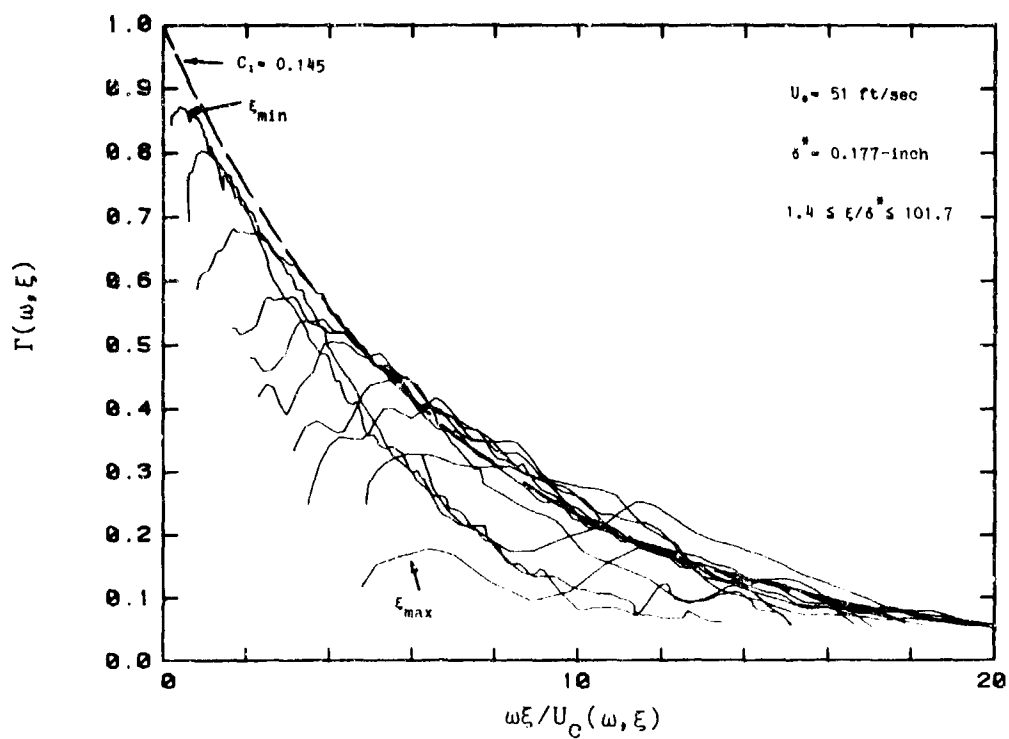


Figure 5.7 Streamwise Coherence for Equilibrium Flow ($U_0 = 51$ ft/sec)

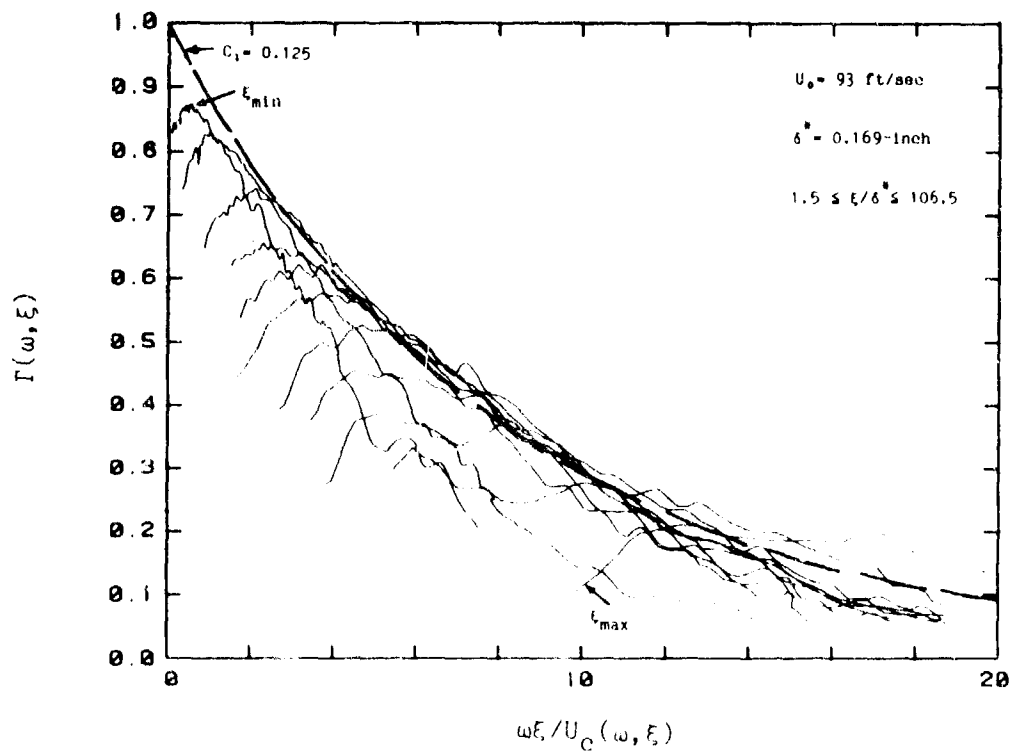


Figure 5.8 Streamwise Coherence for Equilibrium Flow ($U_0 = 93$ ft/sec)

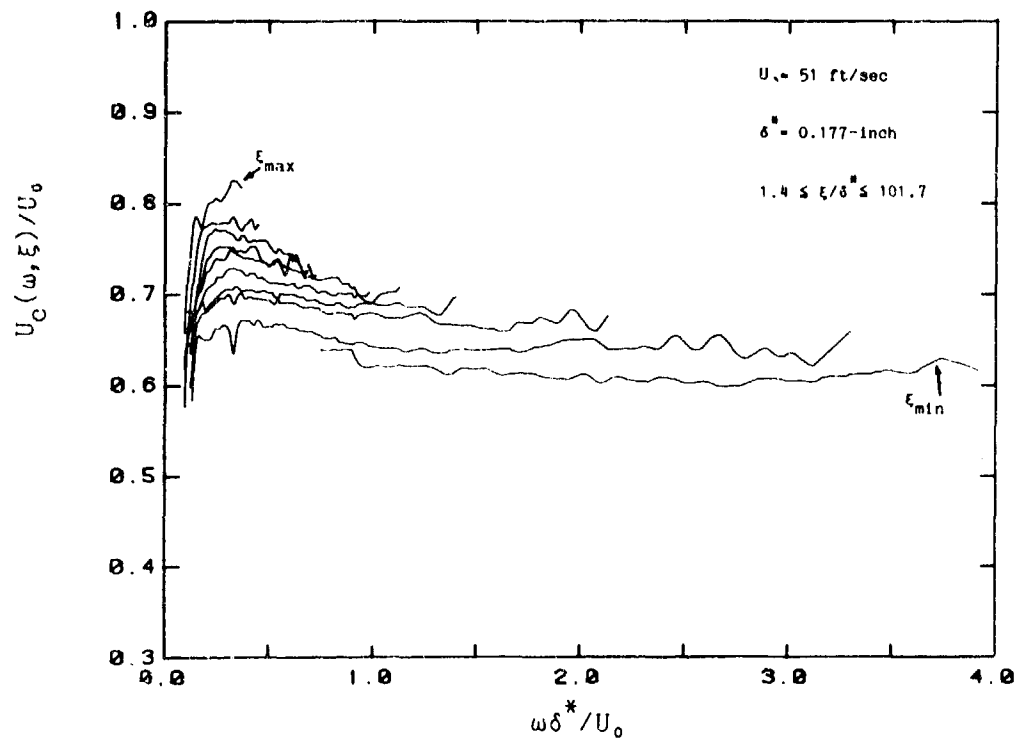


Figure 5.9 Convection Velocity for Equilibrium Flow
($U_0 = 51$ ft/sec)

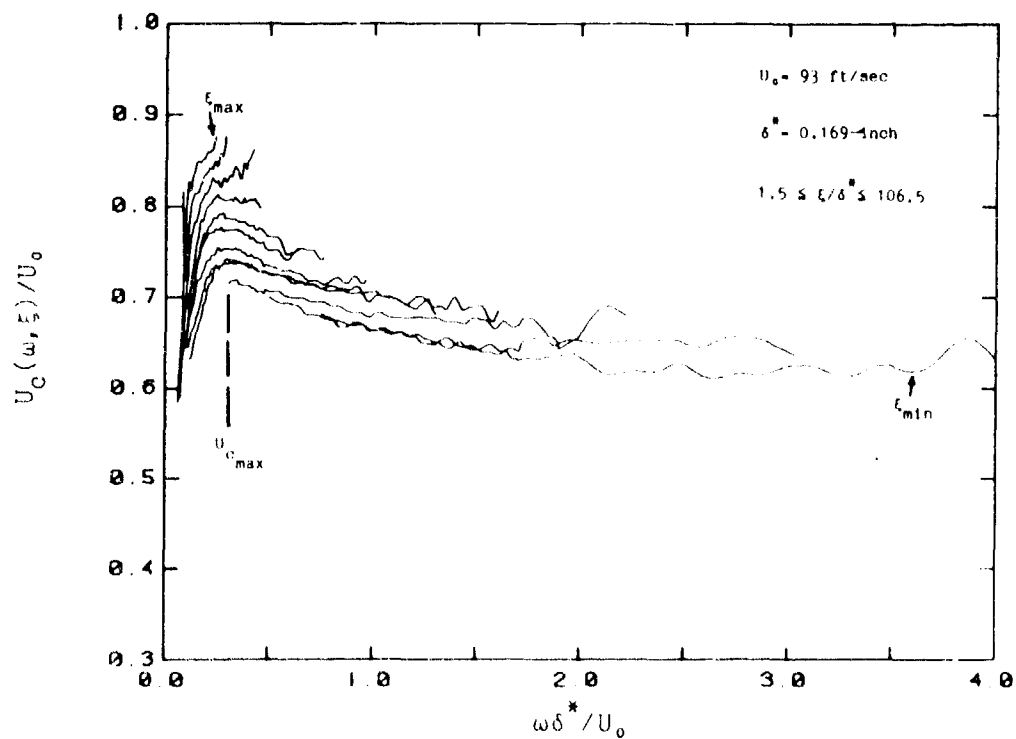


Figure 5.10 Convection Velocity for Equilibrium Flow
($U_0 = 93$ ft/sec)

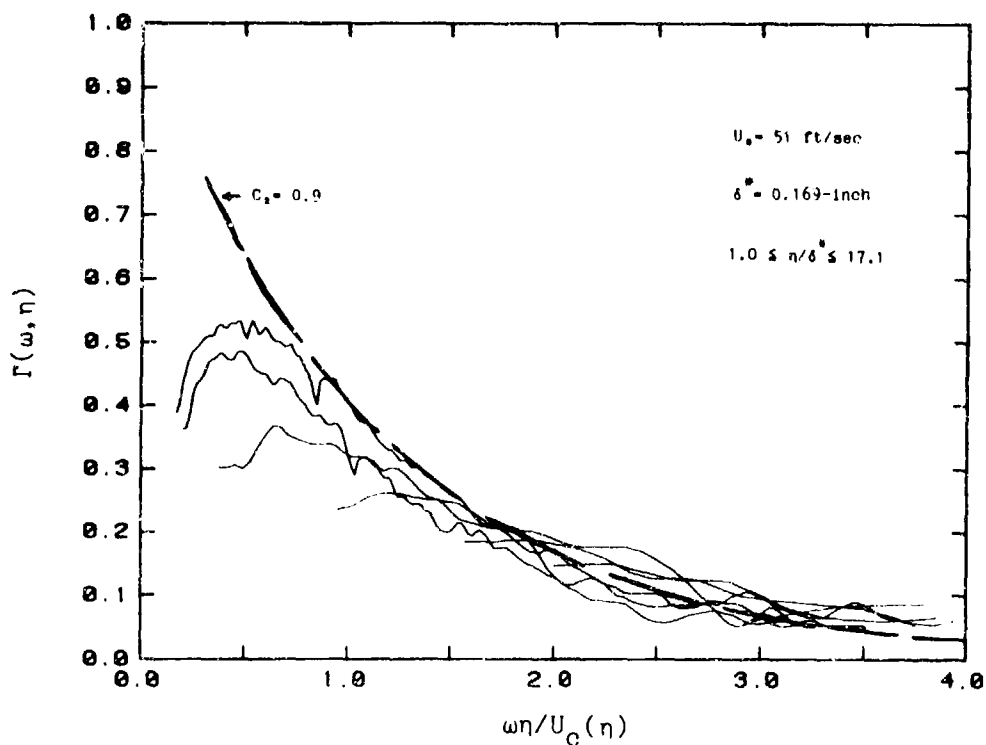


Figure 5.11 Spanwise Coherence for Equilibrium Flow
($U_0=51$ ft/sec)

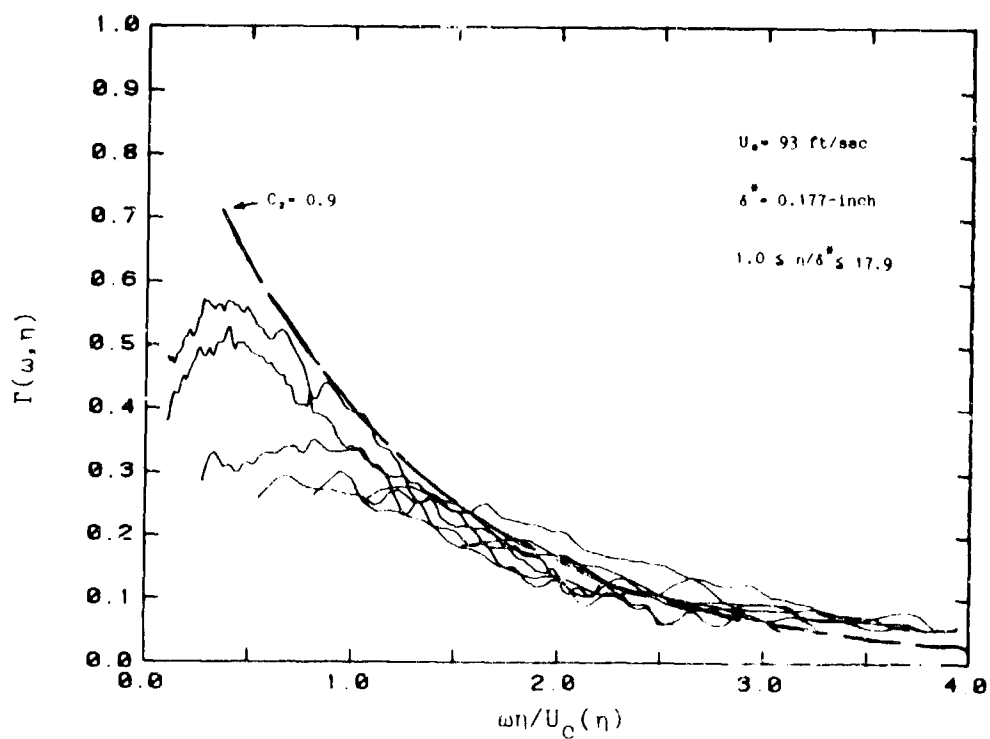


Figure 5.12 Spanwise Coherence for Equilibrium Flow
($U_0=93$ ft/sec)

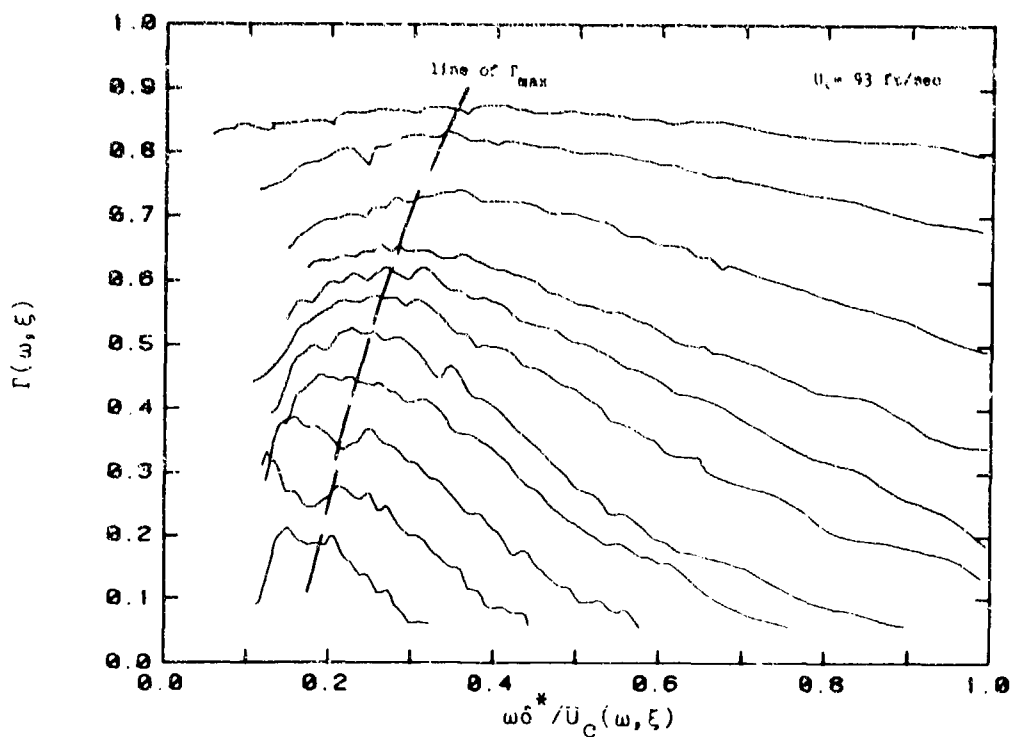


Figure 5.13 Streamwise Coherence versus $\omega\delta^*/U_c(\omega, \xi)$
(Equilibrium Flow)

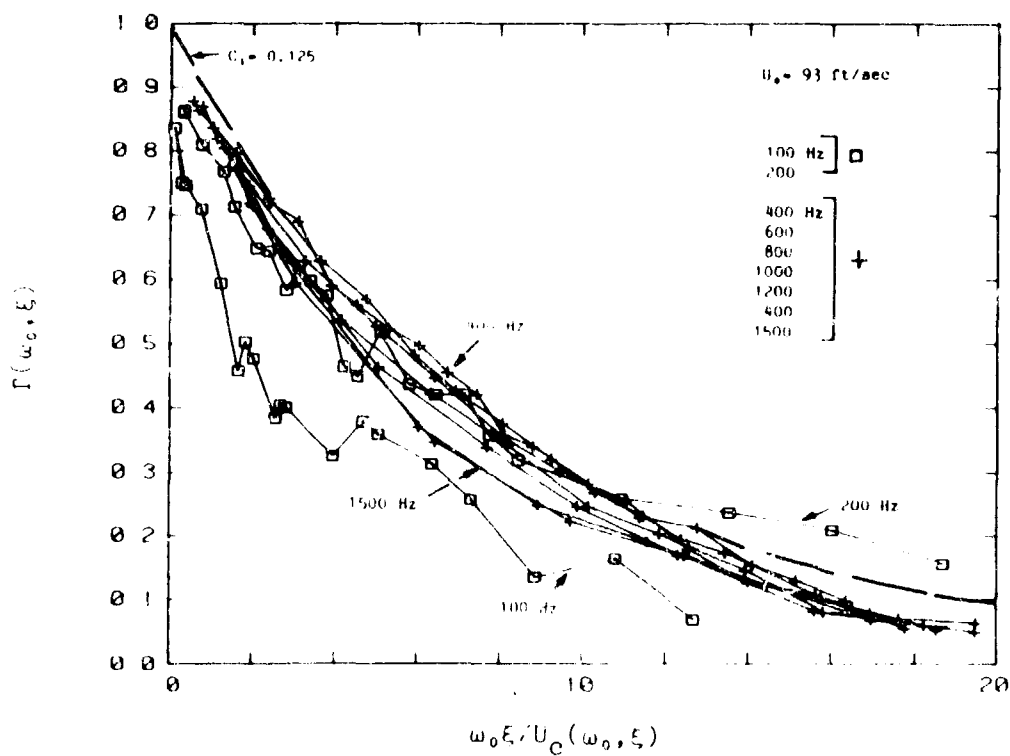


Figure 5.14 Streamwise Coherence for Selected Frequencies
(Equilibrium Flow)

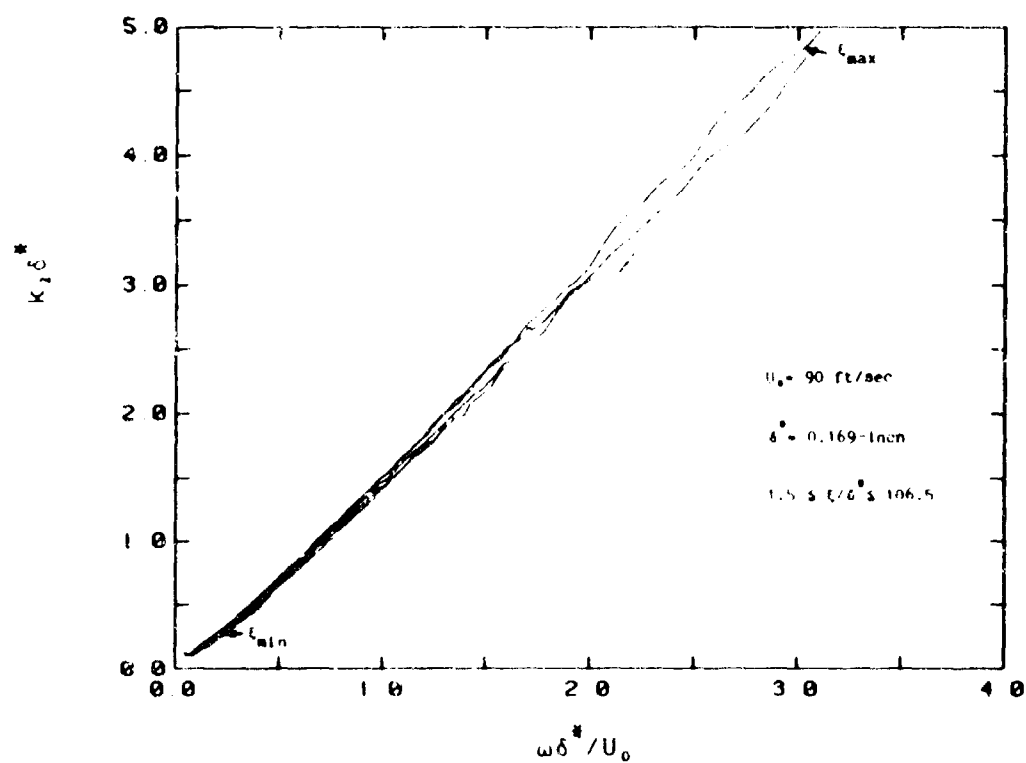


Figure 5.15 Plot of Dimensionless Wavenumber versus Strouhal Number (Equilibrium Flow)

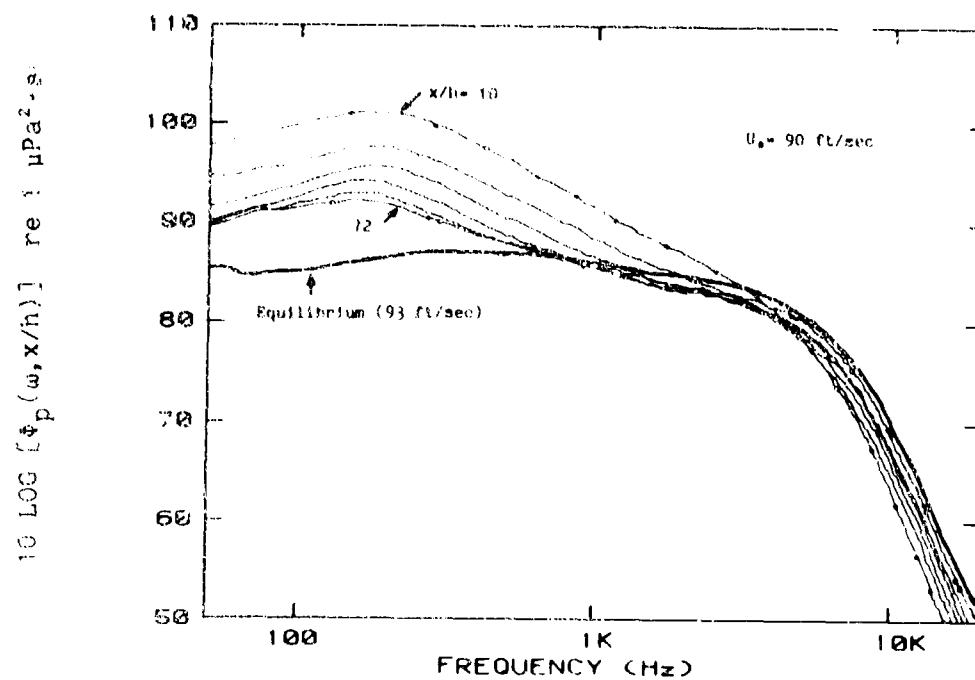


Figure 5.16 Wall Pressure Spectra at Downstream Locations

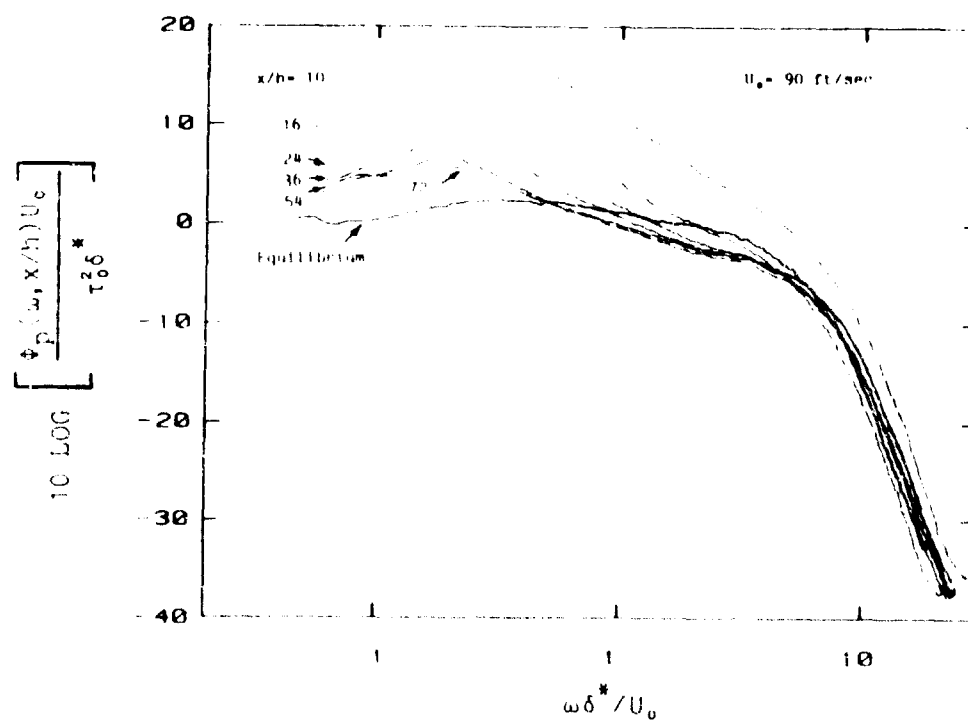


Figure 5.17 Wall Pressure Spectra Scaled on Inner-Outer Variables

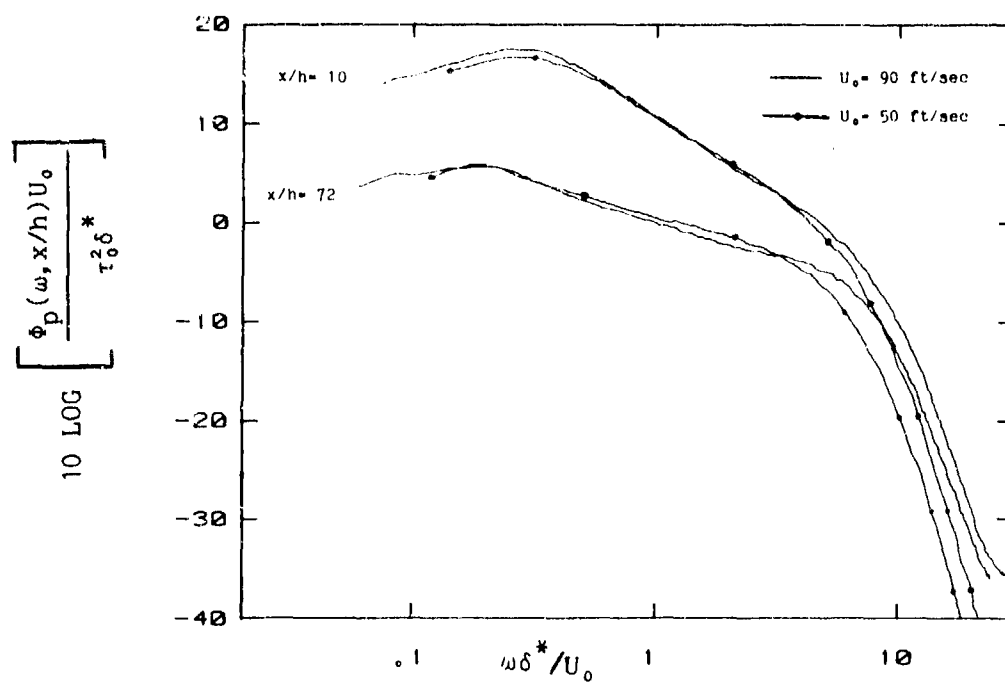


Figure 5.18 Collapse of Speed Variations for Wall Pressure Spectra Using Inner-Outer Variables

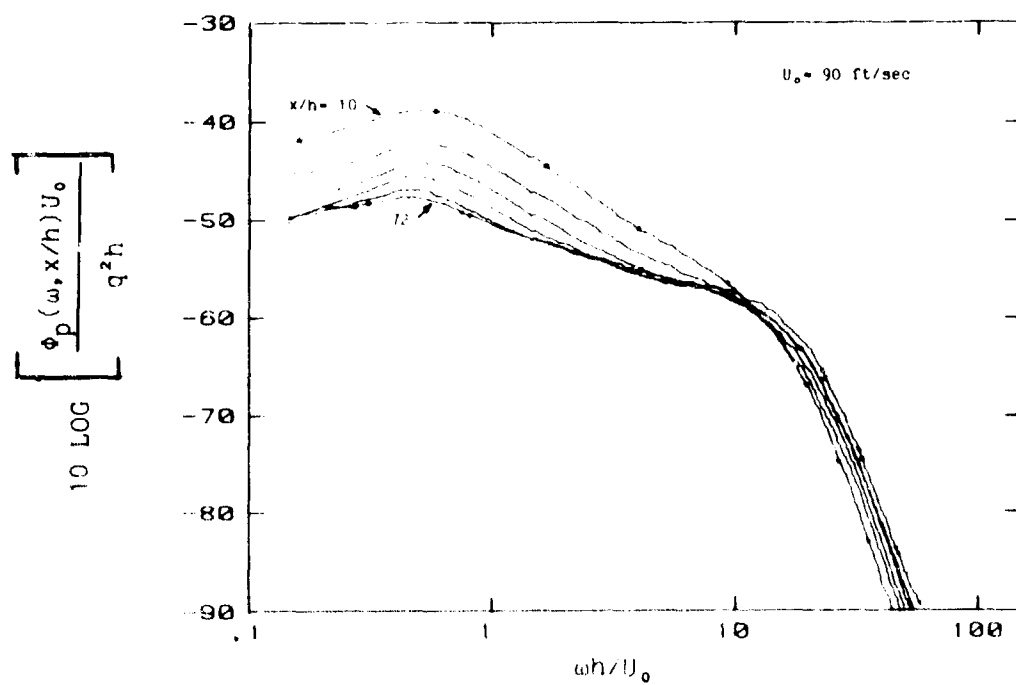


Figure 5.19 Wall Pressure Spectra Scaled on Step Variables

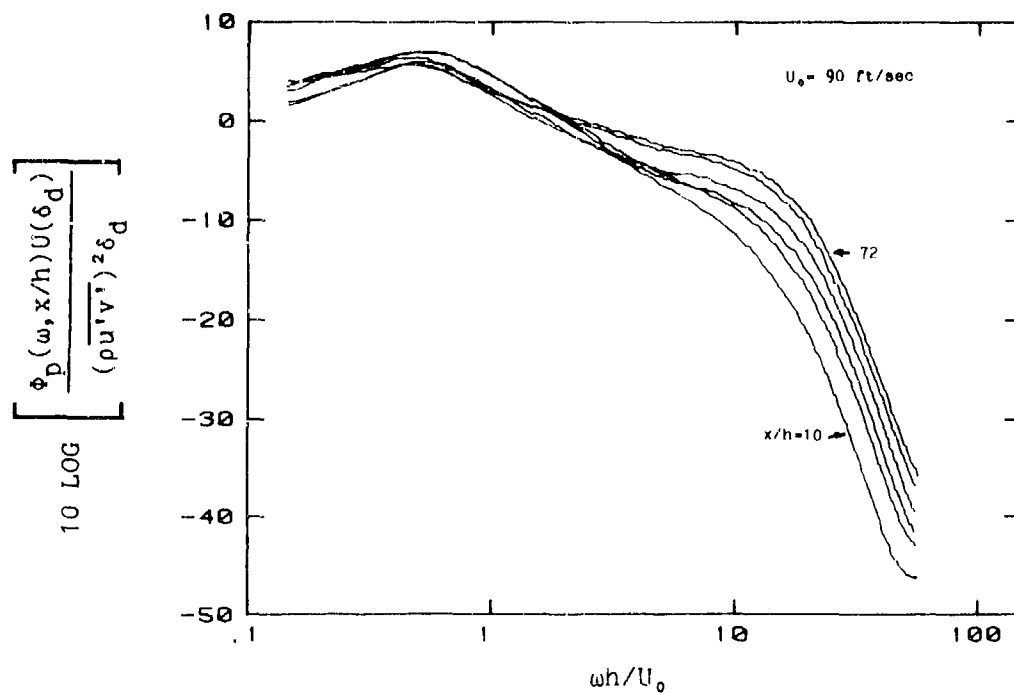


Figure 5.20 Wall Pressure Spectra Scaled on Disturbance Variables

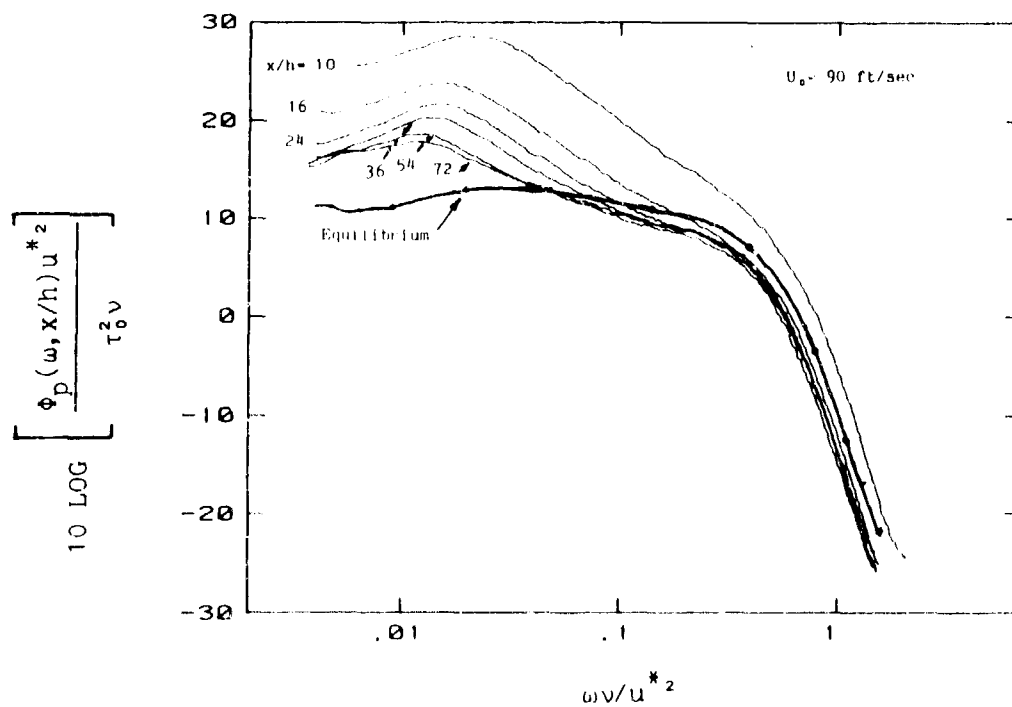


Figure 5.21 Wall Pressure Spectra Scaled on Inner Variables

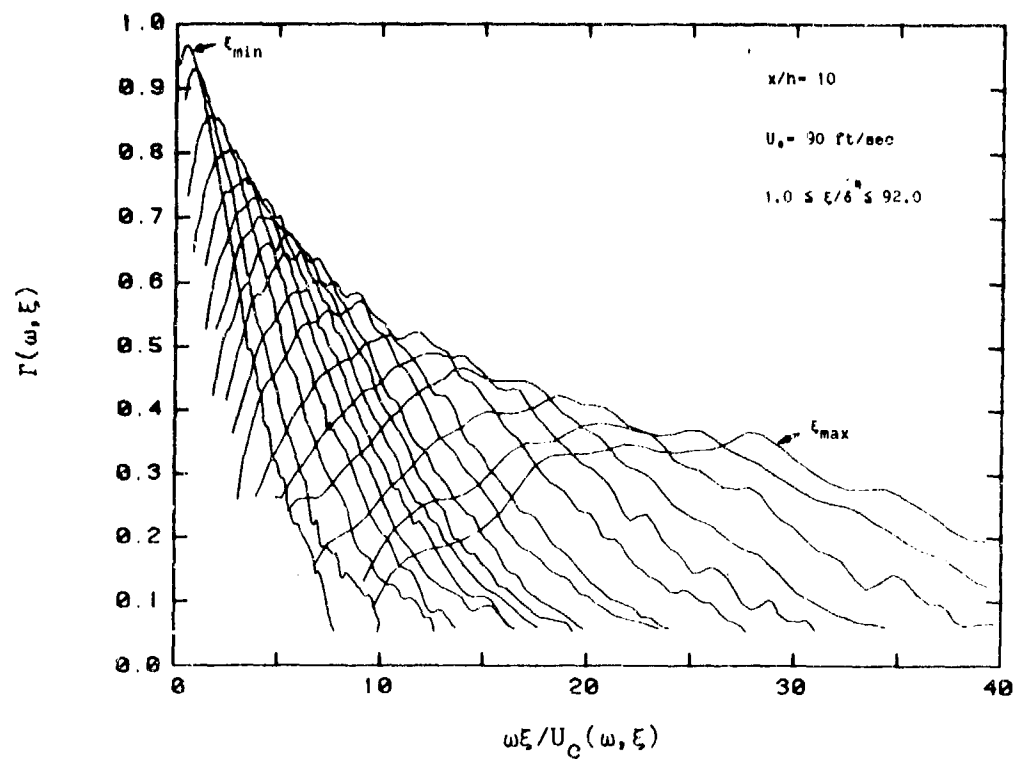


Figure 5.22 Streamwise Coherence at Downstream Location ($x/h=10$)

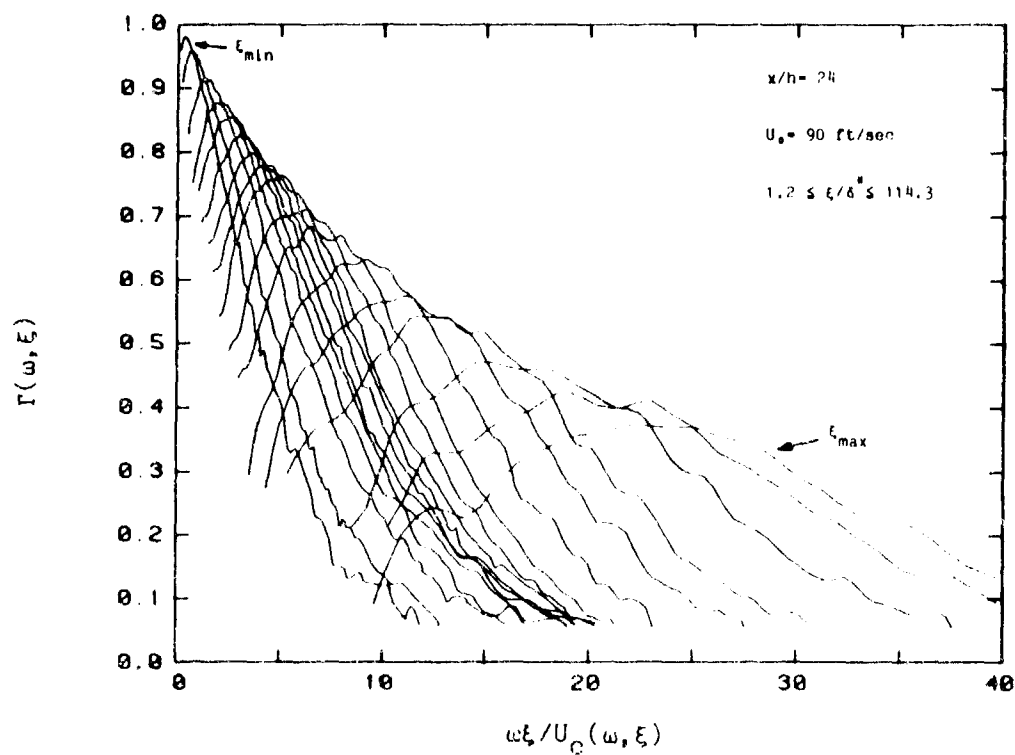


Figure 5.23 Streamwise Coherence at Downstream Location ($x/h=24$)

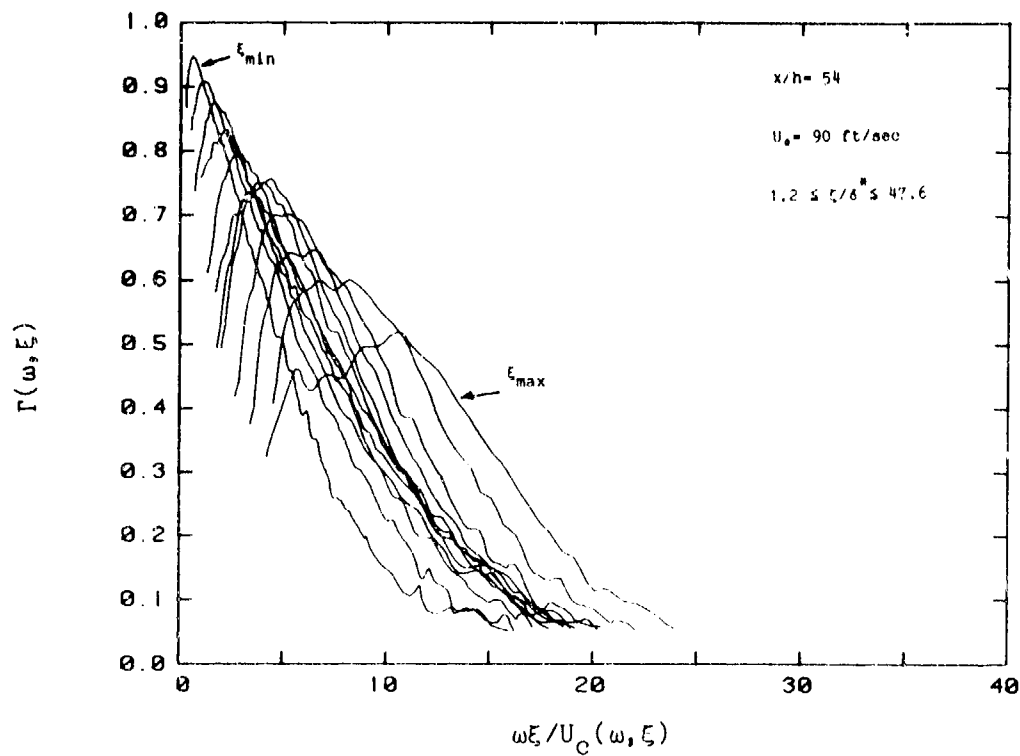


Figure 5.24 Streamwise Coherence at Downstream Location ($x/h=54$)

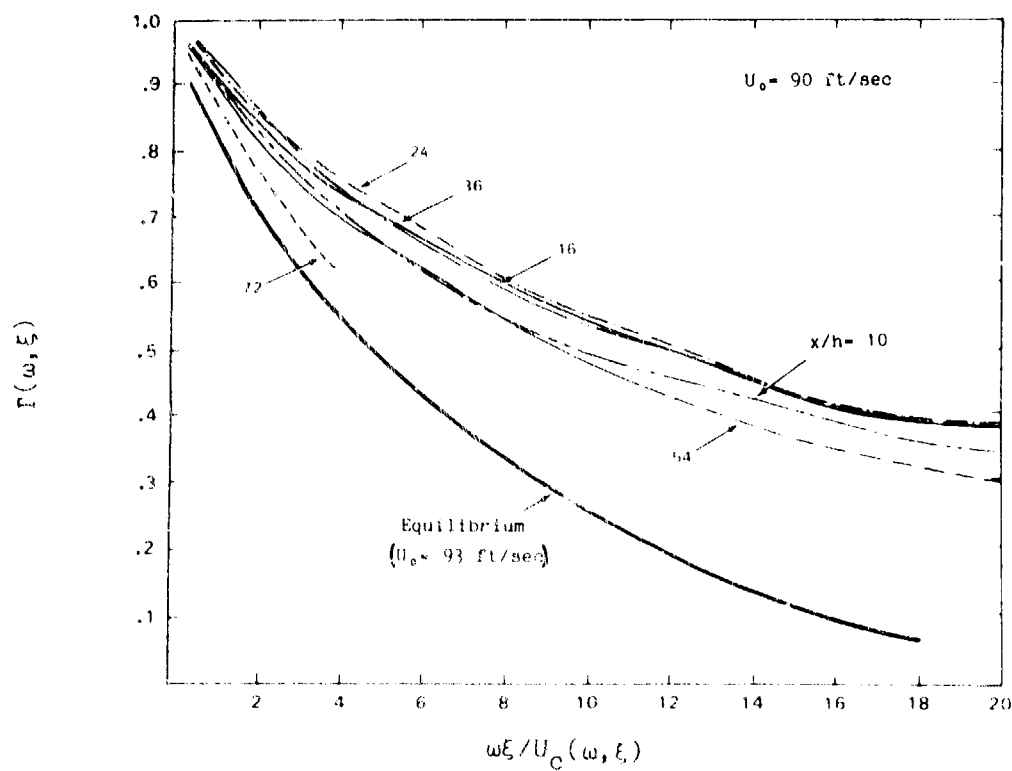


Figure 5.25 Comparison of Non-Equilibrium and Equilibrium Coherence Data

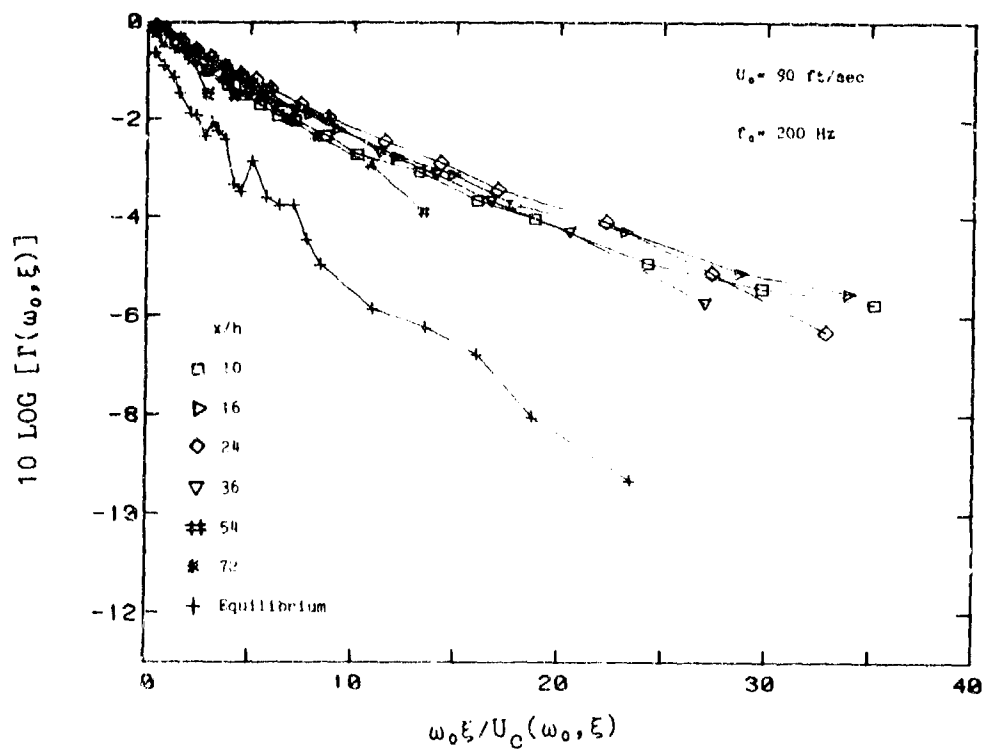


Figure 5.26 Streamwise Coherence for 200 Hz Component

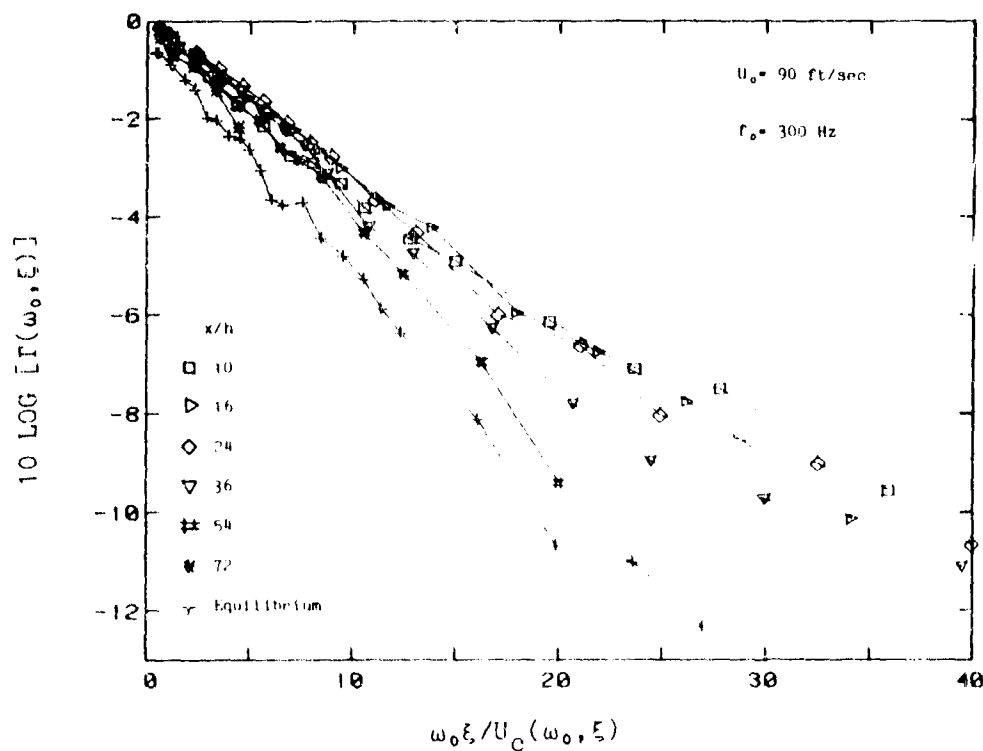


Figure 5.27 Streamwise Coherence for 300 Hz Component

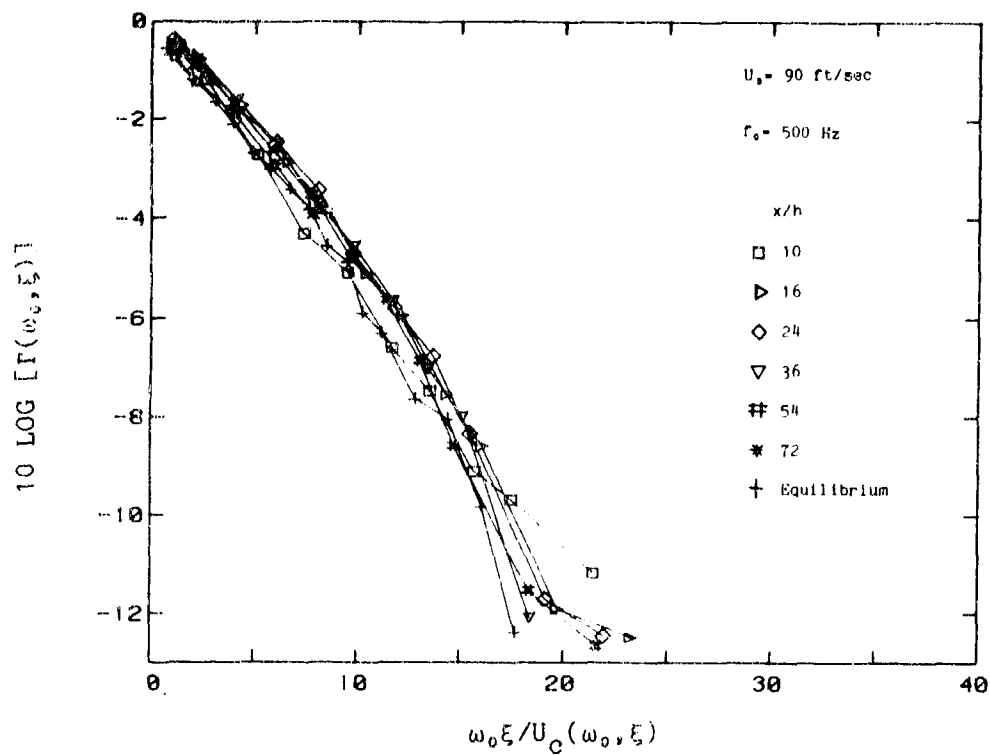


Figure 5.28 Streamwise Coherence for 500 Hz Component

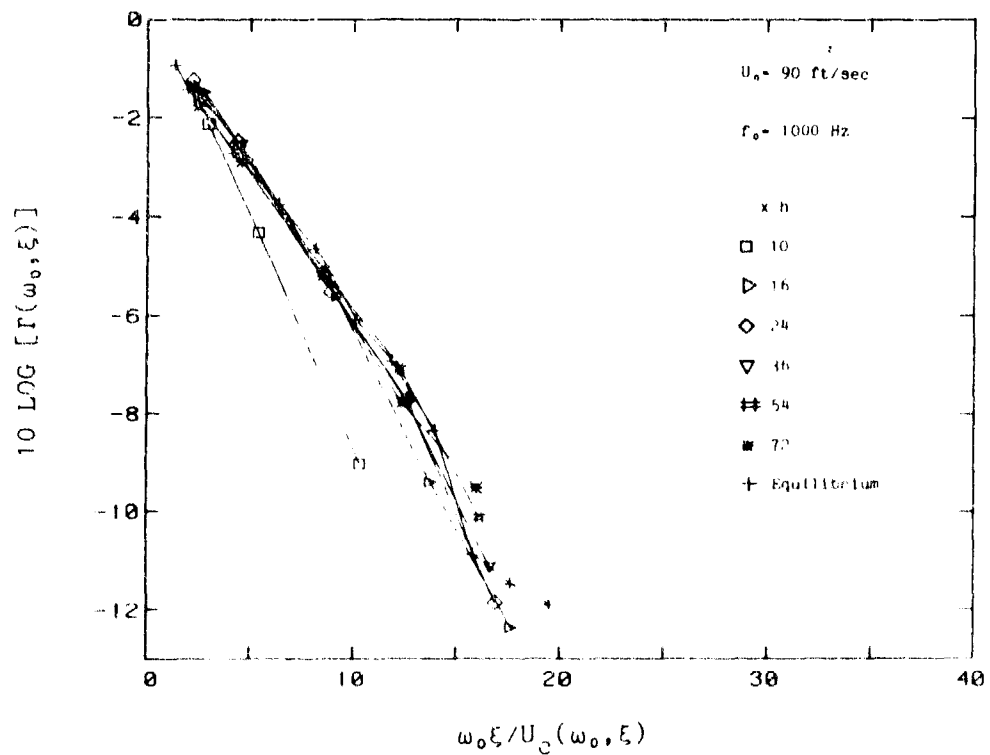


Figure 5.29 Streamwise Coherence for 1,000 Hz Component

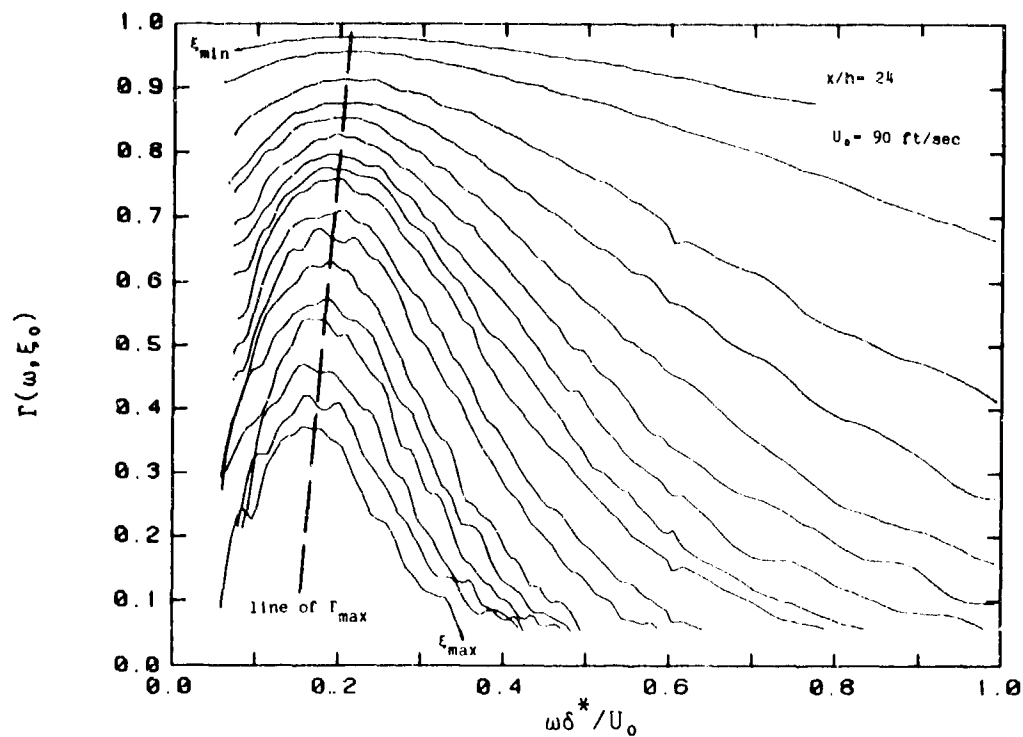


Figure 5.30 Streamwise Coherence versus Strouhal Number
(Non-Equilibrium Flow)

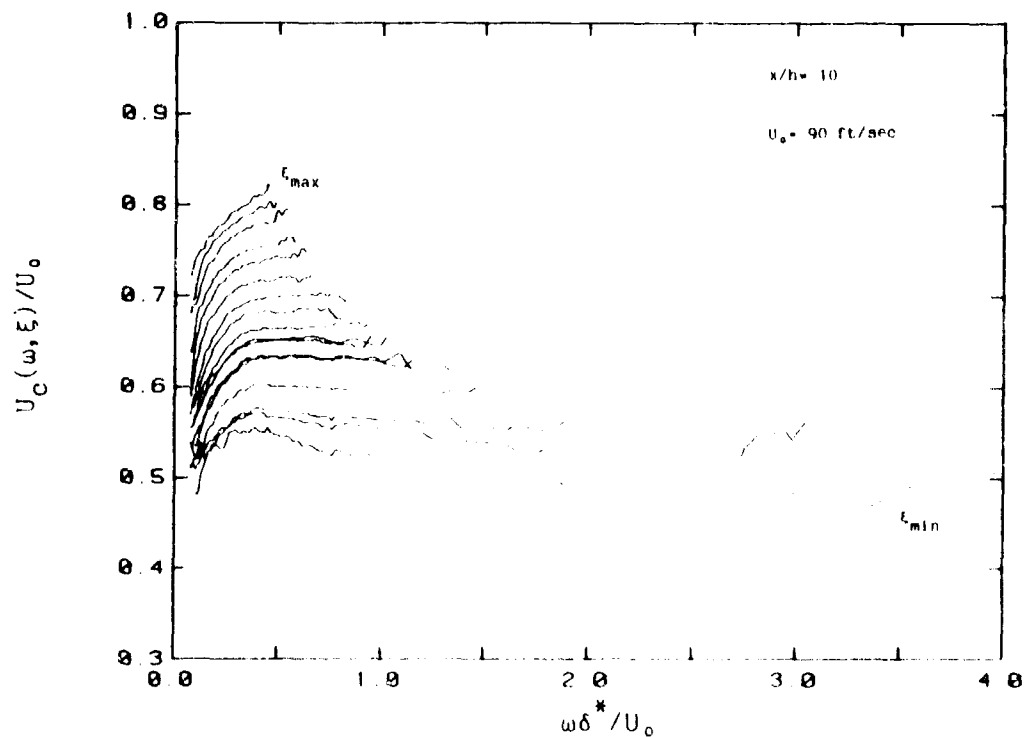


Figure 5.31 Convection Velocity at Downstream Location ($x/h=10$)

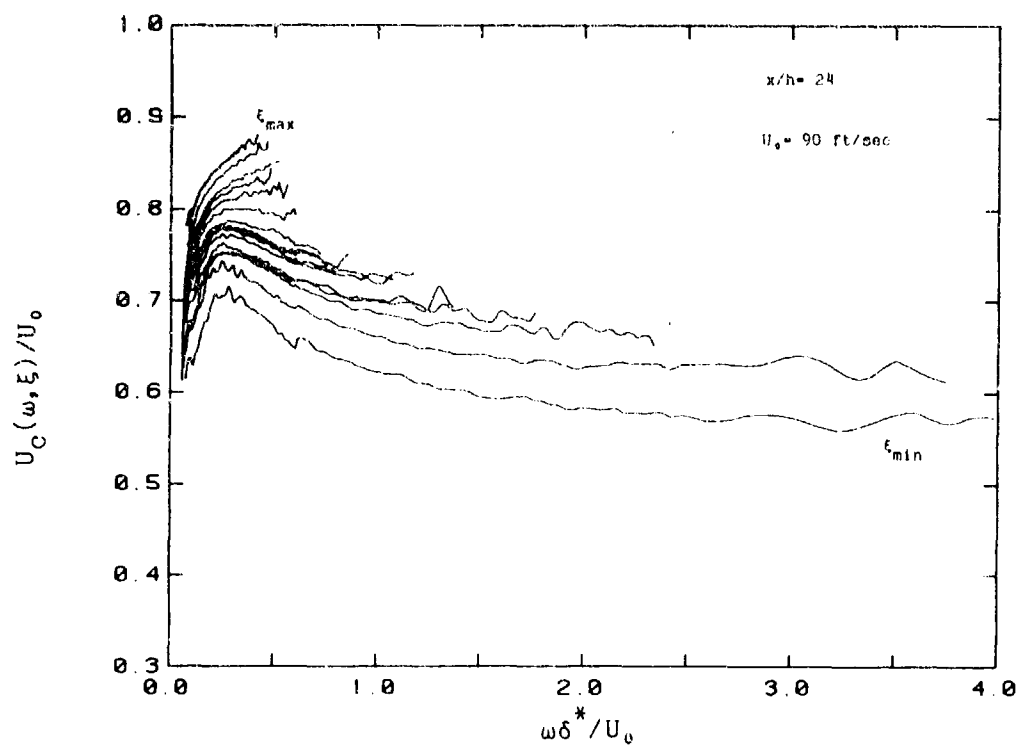


Figure 5.32 Convection Velocity at Downstream Location ($x/h=24$)

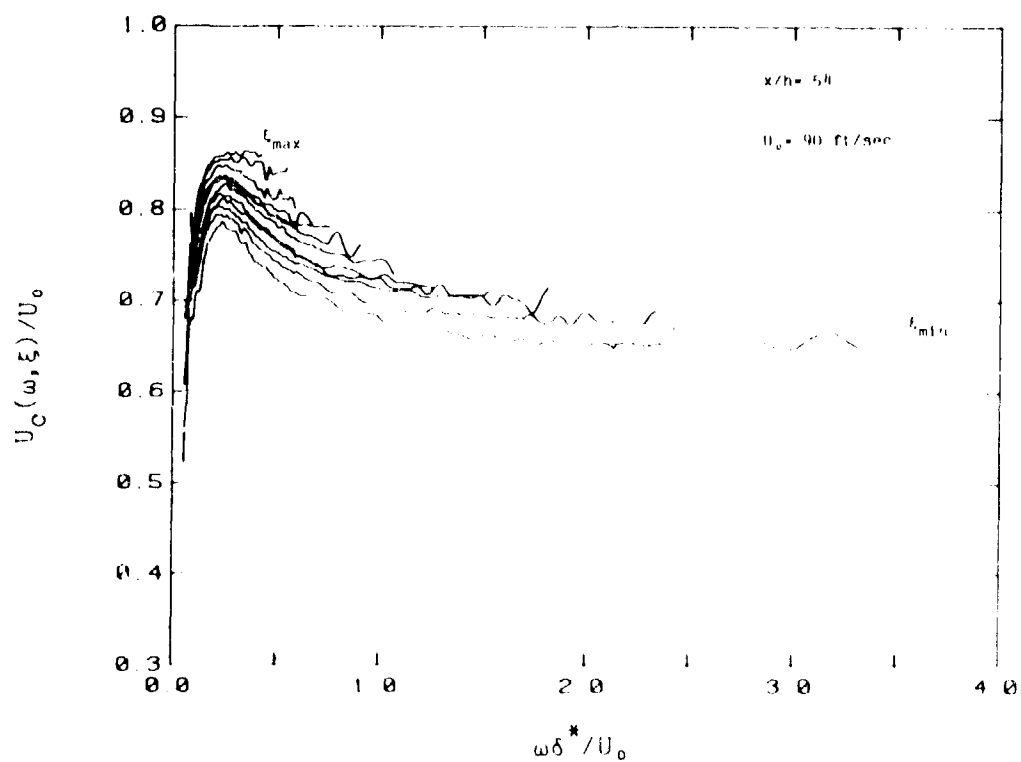


Figure 5.33 Convection Velocity at Downstream Location ($x/h=54$)

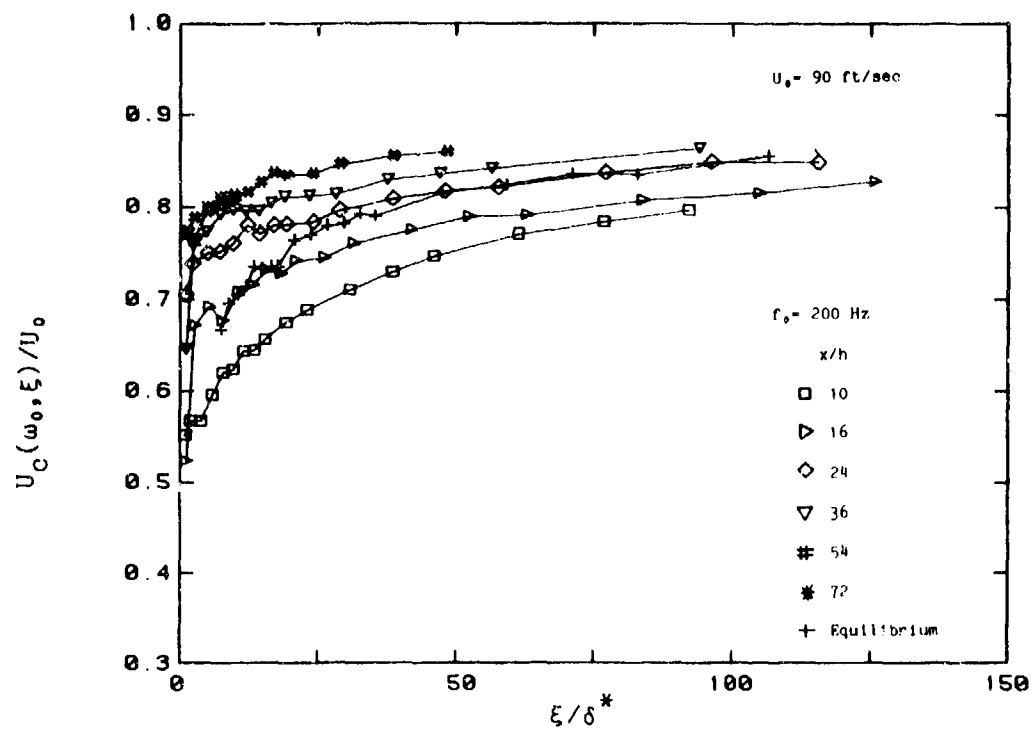


Figure 5.34(a) Convection Velocity for 200 Hz Component
(Non-Equilibrium Flow)

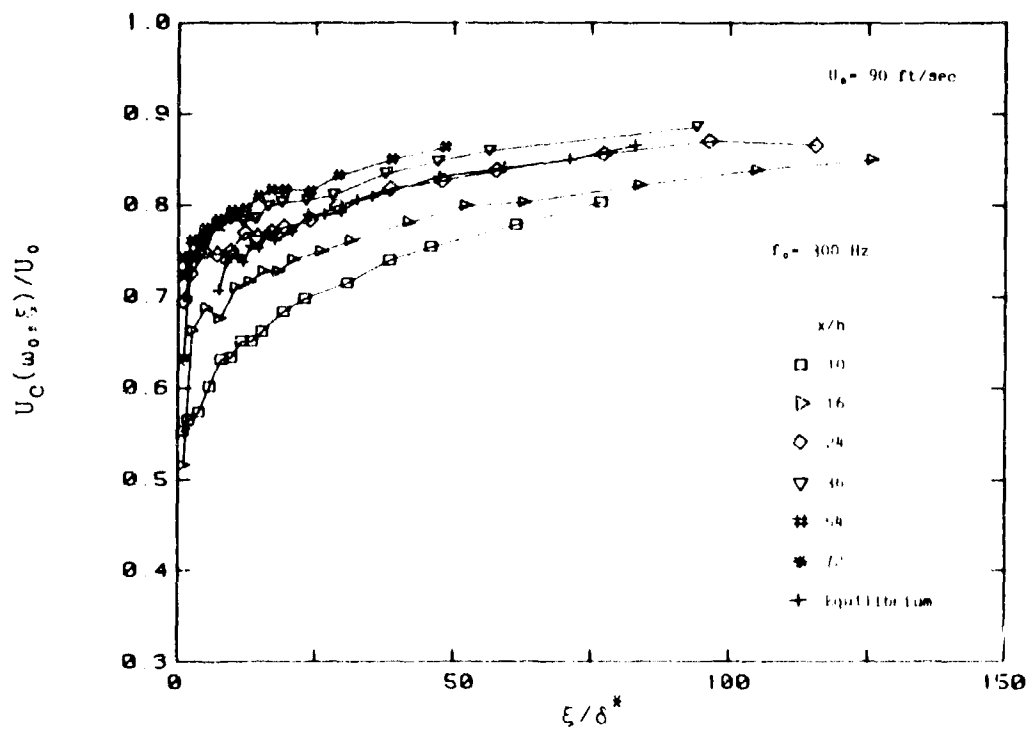


Figure 5.34(b) Convection Velocity for 300 Hz Component
(Non-Equilibrium Flow)

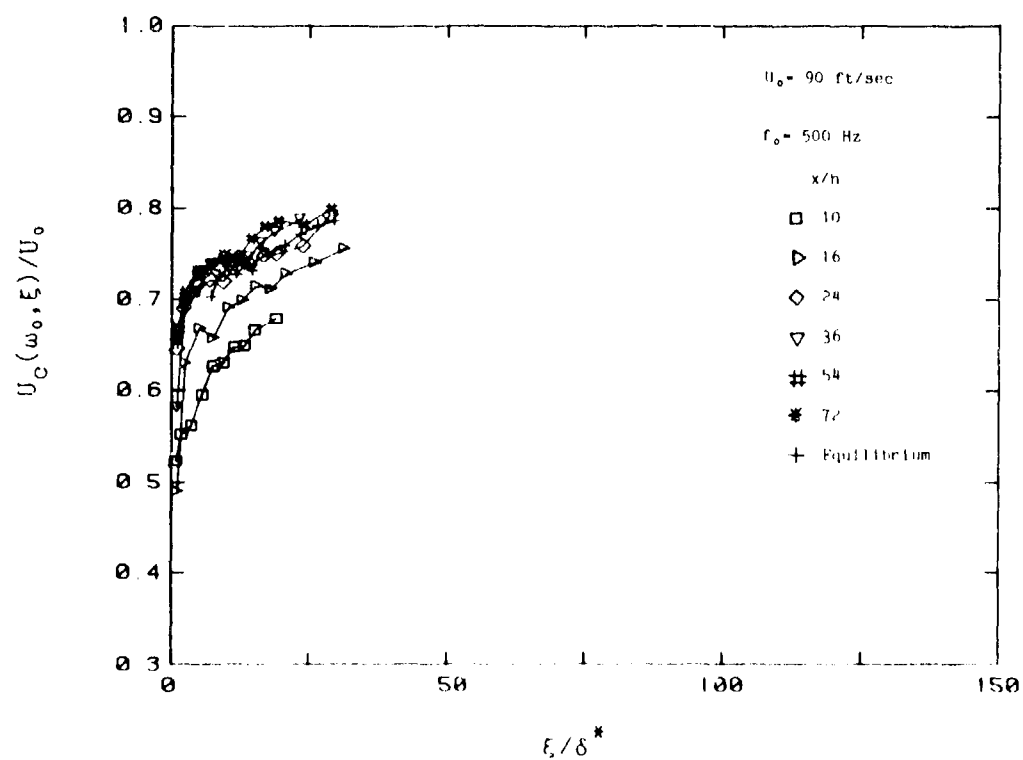


Figure 5.34(c) Convection Velocity for 500 Hz Component
(Non-Equilibrium Flow)

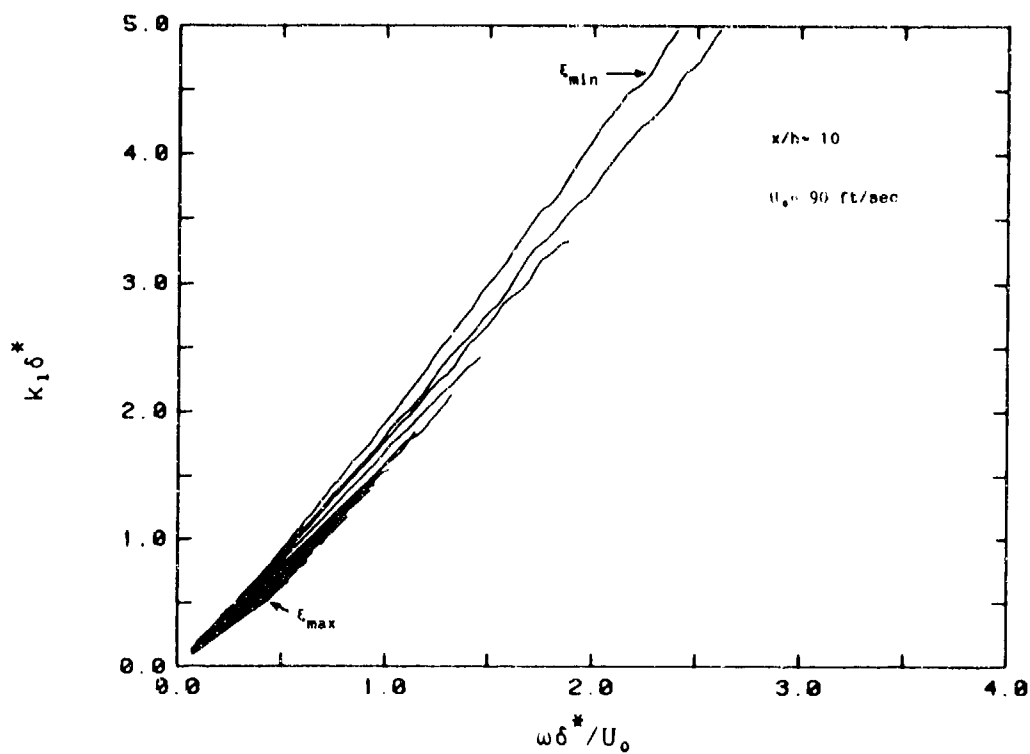


Figure 5.35(a) Dimensionless Wavenumber versus Strouhal Number at $x/h=10$ for Non-Equilibrium Flow

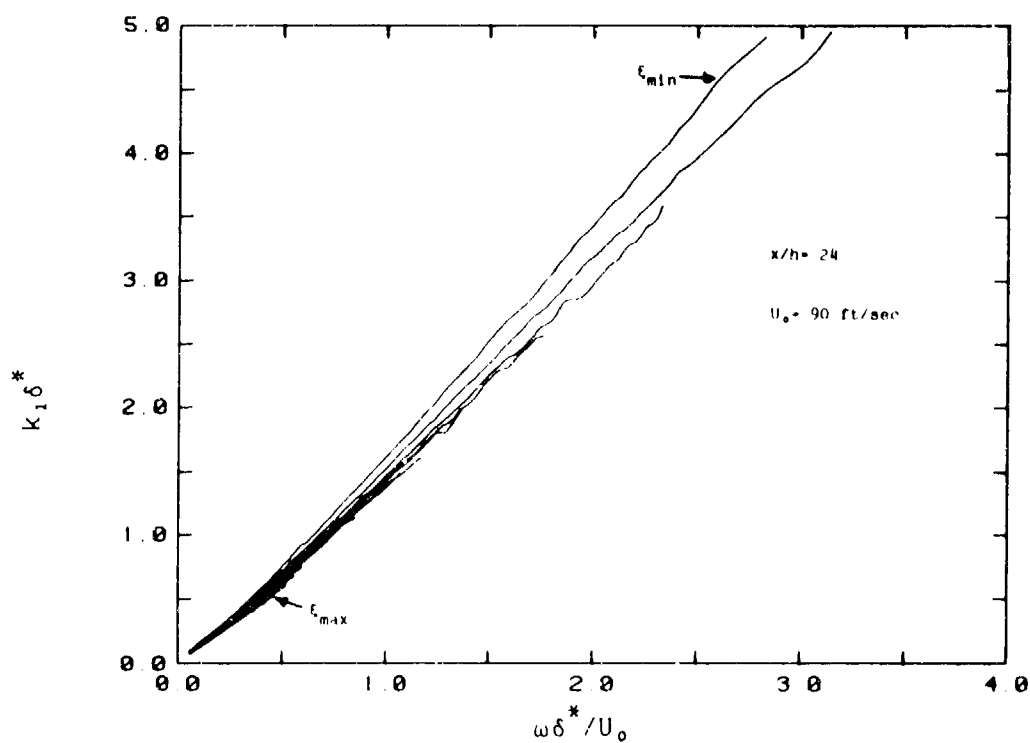


Figure 5.35(b) Dimensionless Wavenumber Versus Strouhal Number at $x/h=24$ for Non-Equilibrium Flow

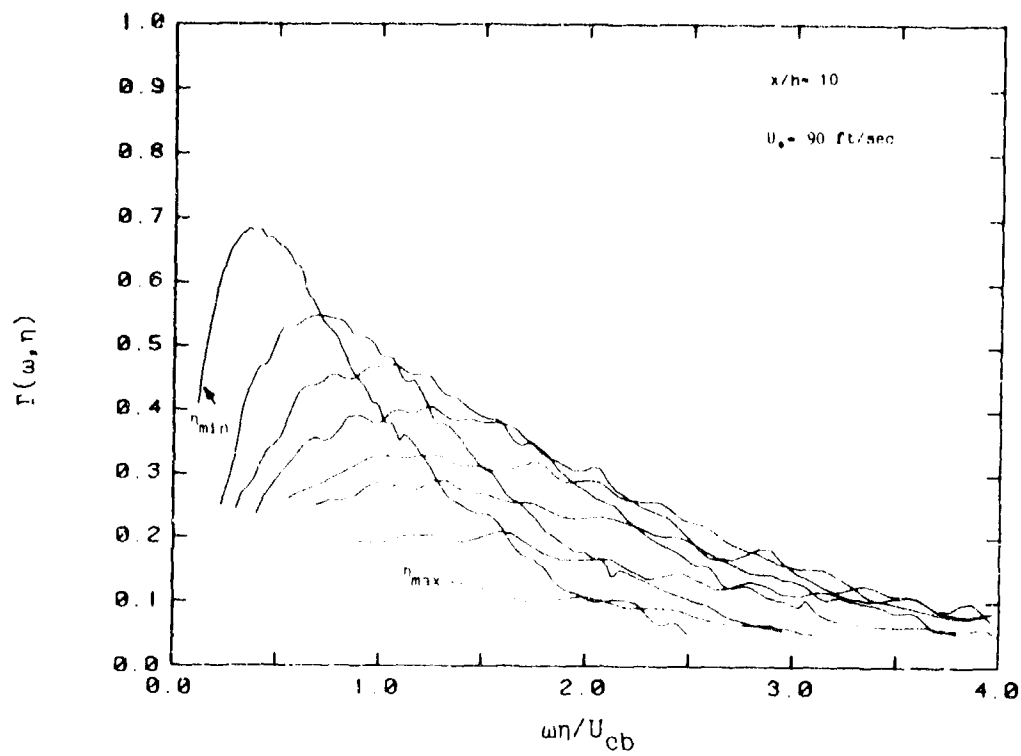


Figure 5.36 Spanwise Coherence at Downstream Location ($x/h=10$)

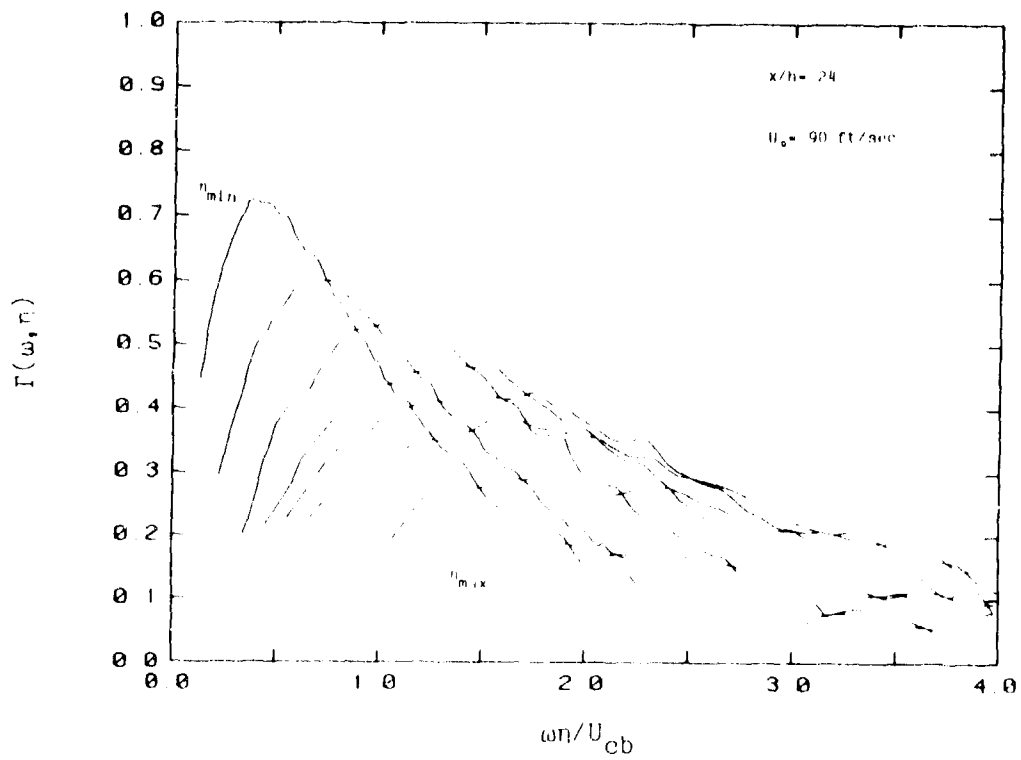


Figure 5.37 Spanwise Coherence at Downstream Location ($x/h=24$)

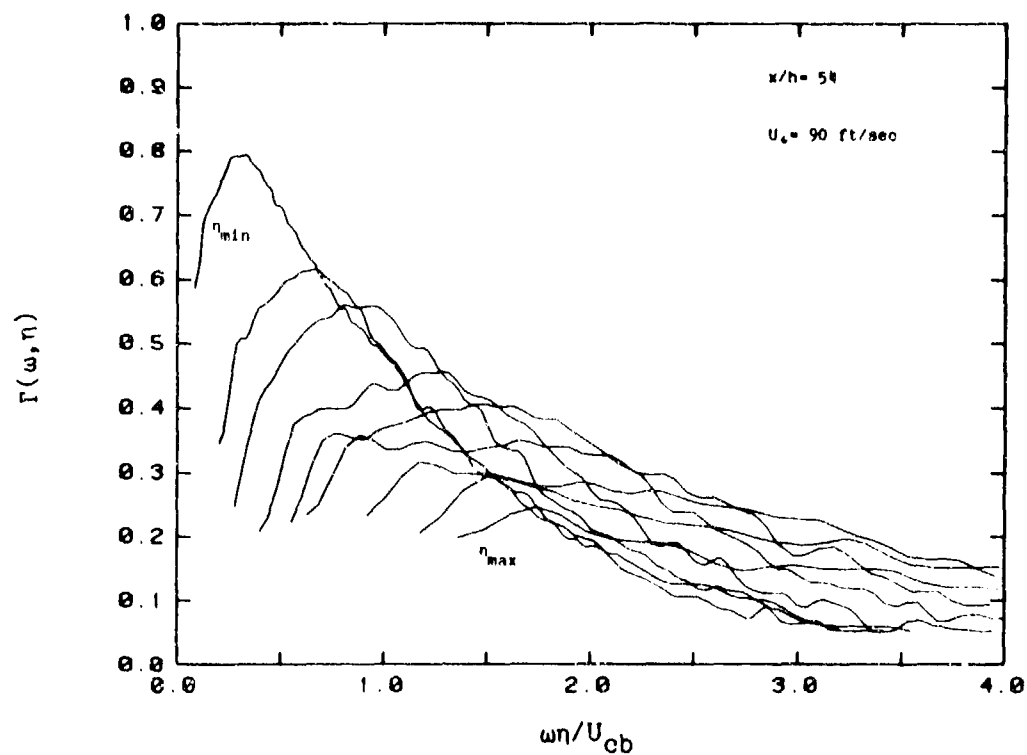


Figure 5.38 Spanwise Coherence at Downstream Location ($x/h=54$)

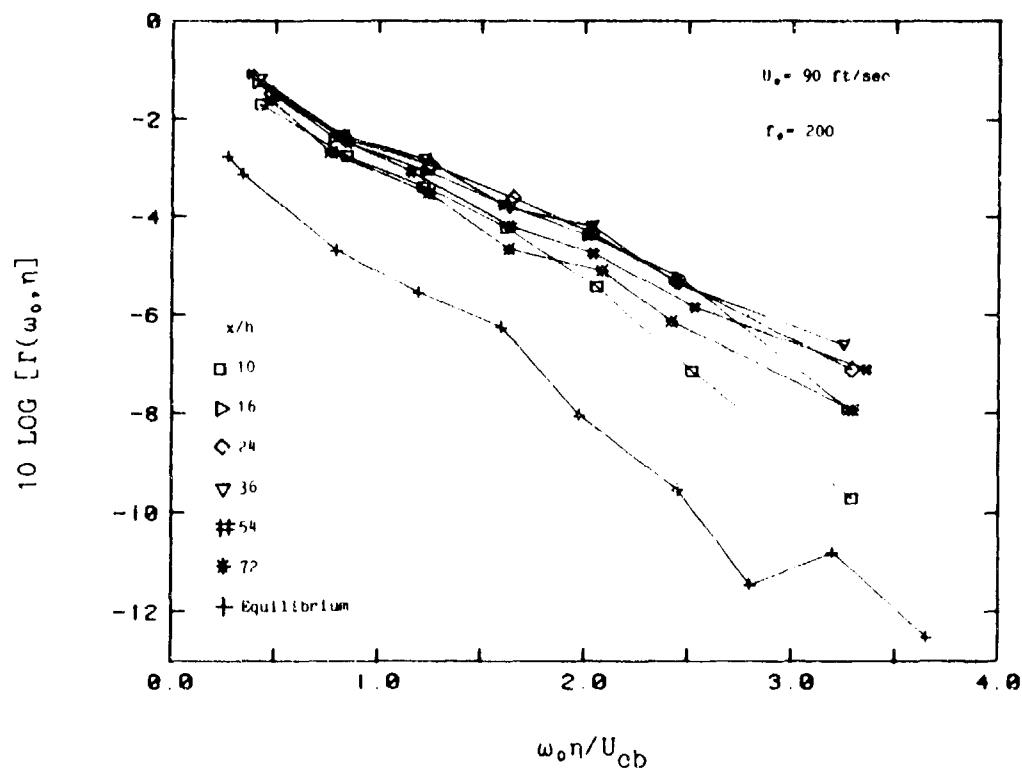


Figure 5.39 Spanwise Coherence for 200 Hz Component

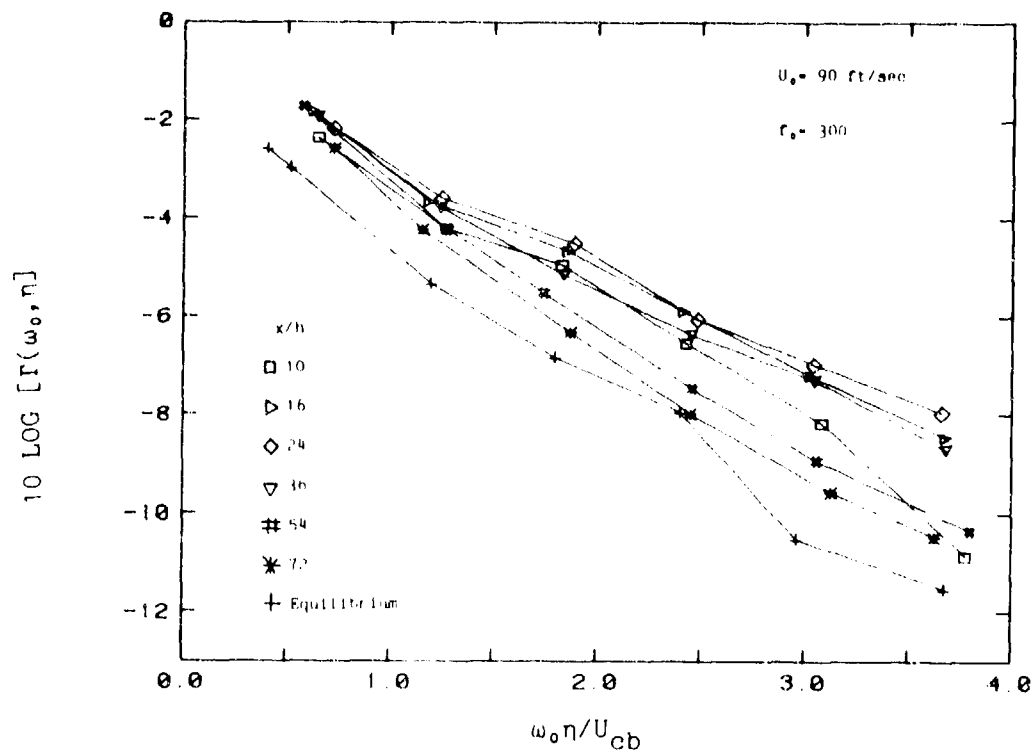


Figure 5.40 Spanwise Coherence for 300 Hz Component

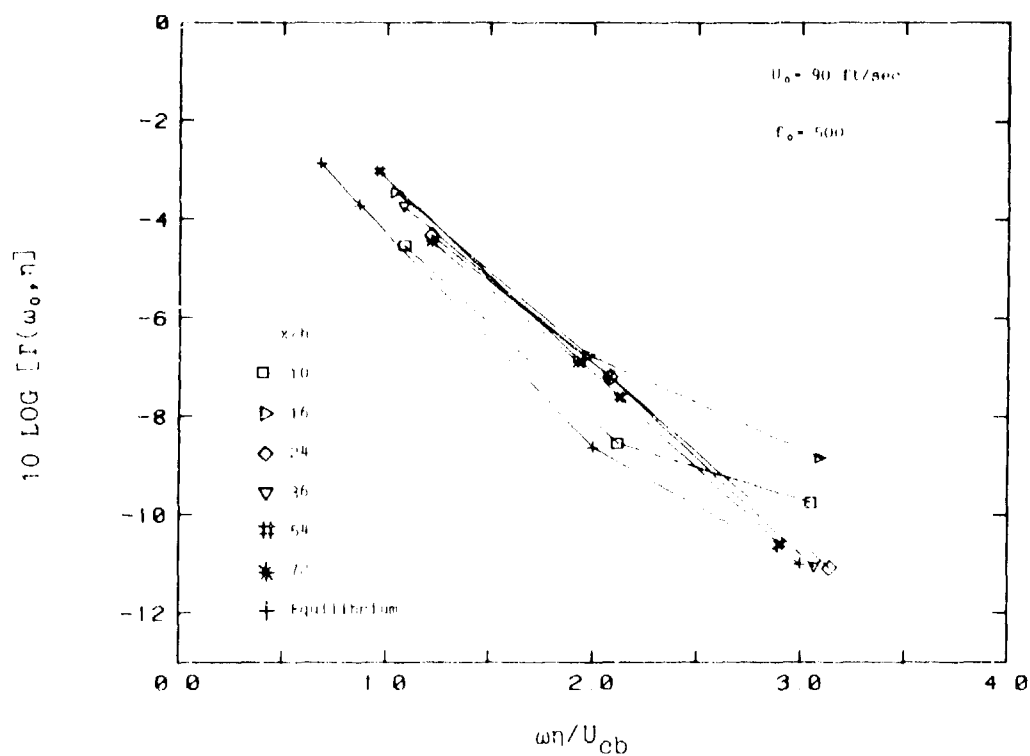


Figure 5.41 Spanwise Coherence for 500 Hz Component

CHAPTER 6

VELOCITY-PRESSURE RELATIONSHIPS

6-1 Introduction

One of the primary objectives of this research was to identify the regions of a boundary layer that are major contributors to wall pressure fluctuations. In Chapter 5 the velocity statistics presented in Chapter 4 were used to establish wall pressure scaling laws. This led to the identification of probable wall pressure source regions in the flow. These results, however, did not explicitly relate the turbulence data with the source terms for the wall pressure field.

In this Chapter the subject of wall pressure source region identification is re-addressed from two perspectives. First, the analytical developments of Chapter 2 will be used with the velocity statistics from Chapter 4 to identify regions in the boundary layer that are major contributors to wall pressure fluctuations. These results will be compared to the measured wall pressure statistics. Secondly, the relationship between the wall pressure field and boundary layer burst events, that are known to be the primary mechanism of Reynolds stress production, will be briefly reviewed.

6-2 Analytical Source Terms

In Chapter 2 a theoretical expression (equation (2.49)) for the wavenumber-frequency spectrum of wall pressure fluctuations was obtained and an interpretation of the various terms in the equation was given. The objective in this section is to further simplify this relationship, by making suitable analytical approximations, in order to obtain an expression that can be evaluated using the experimentally obtained results. Although strongly dependent on the assumed simplifying approximations, this final expression will be helpful in identifying wall pressure source regions in the boundary layer, particularly for the perturbed flow.

The starting point for this discussion is equation (2.49) which is rewritten here as equation (6.1),

$$\phi_p(\vec{k}, \omega) = 4\rho^2 (k_1/K)^2 \iint_0^\infty e^{-K(y+y')} \frac{dU}{dy} \frac{dU}{dy'} \quad (6.1)$$

$$\times R_2(y; y-y') \phi_v(\vec{k}, \omega, y) dy dy'.$$

To obtain an equation for the pressure frequency spectrum ($\phi_p(\omega)$) (6.1) is integrated over k_1 and k_3 ($\vec{k} = k_1, k_3$) in the manner given by equation (2.51). This gives

$$\phi_p(\omega) = 4\rho^2 \iint_{-\infty}^\infty (k_1/K)^2 \iint_0^\infty e^{-K(y+y')} \frac{dU}{dy} \frac{dU}{dy'} R_2(y; y-y') \quad (6.2)$$

$$\times \phi_v(\vec{k}, \omega, y) dy dy' dk_1 dk_3.$$

The unknown term in (6.2) is the vertical velocity cross-spectrum which, by equation (2.48), is written as a product of the vertical cross-correlation $R_2(y; y-y')$, and the planar wavenumber-frequency spectrum $\phi_v(\vec{k}, \omega, y)$ of the vertical velocity fluctuations.

Obtaining approximations for these two terms is the key aspect of all wall pressure field modeling efforts (see list of cited references at end of section 2.2). Attempts at approximating these terms for the non-equilibrium flow are further complicated by the complete lack of knowledge of the cross-spectral properties of the velocity field for a perturbed flow. However, since all that is sought is an expression that retains the rudimentary features of the wall pressure source terms, then simplifying approximations similar to those made for equilibrium flows will be used.

The approximations that are made to reduce (6.2) to an usable form are similar to those made by Blake (1971) in the analysis of wall pressure spectra from rough wall flows. The velocity wavenumber-frequency spectrum in (6.2) is assumed to have a separable form

$$\phi_v(\vec{k}, \omega) = v'^2 \phi_1(k_1) \phi_3(k_3) \phi_0(\omega - U_c k_1) \quad (6.3)$$

where $\phi_1(k_1)$ and $\phi_3(k_3)$ are independent wavenumber spectra describing the variations in the streamwise and transverse directions, respectively. $\phi_0(\omega - U_c k_1)$ is the moving axis spectrum which describes the frequency variations that occur in a reference frame moving with the

flow at the convective speed U_c . For frozen turbulence ϕ_0 is a delta function. The mean-square velocity fluctuation is factored out of the spectral functions and kept as a separate term. Blake (1964) suggests that the cross-correlation function be approximated by a weighted delta function,

$$R_2(y; y-y') = \Lambda(y)\delta(y-y') \quad (6.4)$$

where the weighting factor $\Lambda(y)$, remains as yet undefined but is assumed to be related to measured velocity statistics. By introducing (6.3) and (6.4) into (6.2) and assuming nearly frozen turbulence, allowing ϕ_0 to be written as a delta function, then the integrations over k_1 and y' can be made to obtain

$$\begin{aligned} \phi_p(\omega) = 4\rho^2 \int_{-\infty}^{\infty} (k_0/K)^2 \int_0^{\infty} e^{-2Ky} v'^2 (dU/dy)^2 \Lambda(y) \\ \times \frac{1}{U_c} \phi_1(\omega/U_c) \phi_3(k_3) dy dk_3 \end{aligned} \quad (6.5)$$

where $k_0 = \omega/U_c$, $k = \sqrt{k_0^2 + k_3^2}$, and $(1/U_c)\phi_1(\omega/U_c) = \phi_V^N(\omega) = \phi_V(\omega)/v'^2$ where $\phi_V^N(\omega)$ is the frequency spectrum of the vertical velocity fluctuations scaled on its mean-square value. The only unknown term in (6.5) is the transverse wavenumber spectrum ϕ_3 . Blake (1971) assumed that $\phi_3(k_3)$ has the somewhat general form of

$$\phi_3(k_3) = \frac{\lambda_3}{2\sqrt{\pi}} e^{-k_3^2 \lambda_3^2 / 4} \quad (6.6)$$

where λ_3 is a turbulence scale factor that is a function of wall position $\lambda_3 = \lambda_3(y)$. By introducing (6.6) into (6.5), the final integral becomes

$$\begin{aligned} \phi_p(\omega) = 4\rho^2 \int_{-\infty}^{\infty} (k_0/K)^2 \int_0^{\infty} \frac{1}{U_c} e^{-2Ky} v'^2 (dU/dy)^2 \Lambda(y) \\ \times \phi_1(\omega/U_c) \frac{\lambda_3}{2\sqrt{\pi}} e^{-k_3^2 \lambda_3^2 / 4} dy dk_3. \end{aligned} \quad (6.7)$$

Once the k_3 integration in (6.7) is performed, the remaining integrand is the wall pressure source distribution function.

Consider the k_3 integration in (6.7) separately by writing

$$\Phi_p(\omega) = 4\rho^2 \int_0^\infty \frac{1}{U_c} v'^2 (dU/dy)^2 \Lambda \Phi_v(\omega/U_c) I(\omega/U_c, y) dy \quad (6.8)$$

where,

$$I(\omega/U_c, y) = \frac{\lambda_3}{2\sqrt{\pi}} \int_{-\infty}^{\infty} \frac{k_0^2}{k_0^2 + k_3^2} e^{-2y\sqrt{k_0^2 + k_3^2}} e^{-k_3^2 \lambda_3^2 / 4} dk_3. \quad (6.9)$$

A solution to (6.9) can be obtained by evaluating the integral in separate high and low frequency regions (frequency is only a parameter in (6.9)). Low frequency is denoted by $\omega\lambda_3/U_c < 1$ and high frequency by $\omega\lambda_3/U_c > 1$. For both regions the dominant contribution comes from low (k_3) wavenumber components ($k_3/k_0 < 1$). In the high frequency region, with the assumption that $k_3 < k_0$, the integral for $I(\omega/U_c, y)$ is dominated by the second exponential term giving

$$I_H(\omega/U_c, y) = \frac{\lambda_3}{2\sqrt{\pi}} e^{-2k_0 y} \int_{-\infty}^{\infty} e^{-k_3^2 \lambda_3^2 / 4} dk_3 = e^{-2k_0 y}. \quad (6.10)$$

In the low frequency region the integral is again dominated by terms for which $k_3 < k_0$ and the integral can be approximated as

$$I_L(\omega/U_c, y) = \frac{\lambda_3}{2\sqrt{\pi}} e^{-2k_0 y} \int_{-\infty}^{\infty} \frac{k_0^2}{k_0^2 + k_3^2} dk_3 = \frac{k_0 \lambda_3 \sqrt{\pi}}{2} e^{-2k_0 y}. \quad (6.11)$$

With (6.10) and (6.11) equation (6.8) can be written as

$$\text{where } \Phi_p(\omega) = \int_0^\infty S_T S_{L,H} \Phi_v^N(\omega) e^{-2\omega y/U_c} dy, \quad (6.12)$$

$$S_T(y) = v'^2 (dU/dy)^2, \quad (6.13a)$$

$$S_L = C_L \Lambda \omega \lambda_3 / U_c \quad (\text{for } \omega \lambda_3 / U_c < 1), \quad (6.13b)$$

$$S_H = C_H \Lambda \quad (\text{for } \omega \lambda_3 / U_c > 1), \quad (6.13c)$$

and C_L and C_H are collected constants. In order to further evaluate (6.12) estimates of Λ and λ_3 must be established. The assumption by Blake (1984) that $\Lambda(y) \approx y$ will be used in evaluating (6.12). Since λ_3 is a turbulence scale factor it will be taken to be equal to the integral

length scale (L_2) obtained from the vertical velocity spectra. With these, equation (6.12) can be used as a description of the distribution of wall pressure source terms within the boundary layer.

Before any quantitative evaluations of (6.12) are made it is interesting to review the qualitative features of the terms in the equation. The $S_T(y)$ term is the primary source term for wall pressure fluctuations. Its functional form is a consequence of assuming that the mean shear-turbulence interaction term is the only source term in the original formulations. The form of the second term ($S_{L,H}$), depends on the frequency region of interest. At low frequency it contains an ω/U_c term that essentially comes from the streamwise derivative of the v component in the original source term. S_L also contains both the vertical correlation term and the transverse turbulence length scale (λ_3). For high frequencies only the vertical correlation term is present. The third term is the vertical velocity spectrum normalized by its mean-square value. This simply expresses the frequency distribution of the velocity fluctuations in the original source term. The last term is the exponential attenuation function. The effect of this term is the same as the exponential term discussed in Chapter 2. The contribution that a given velocity fluctuation makes to the wall pressure decreases exponentially with increasing frequency or wall distance. This term imposes the requirement that high frequency pressure fluctuations be generated by velocity terms near the wall.

Equation (6.12) will now be used to evaluate the distribution of wall pressure source terms within the boundary layer. One of the objectives in studying a perturbed flow was to investigate the wall pressures produced by a flow with an altered wall pressure source distribution. Hence, of particular interest is a comparison of the source terms for the equilibrium flow to those for the perturbed flow. In Chapter 5 it was shown that the major effect of the perturbed flow was to increase the low frequency levels of the wall pressure field. The low frequency levels still remain above the equilibrium levels as far downstream as the last measurement station ($x/h=72$). On the other hand, the high frequency components of wall pressure were initially elevated (at $x/h=10$) but by $x/h=16$ had returned to an equilibrium

(unperturbed) level. These observations suggest that in evaluating the distribution of wall pressure sources for the perturbed flow attention should be placed on the low frequency region of (6.12).

The low frequency form of (6.12) can be written in more convenient form as

$$\Phi_p(\omega) = C_L \int v'^2 (dU/dy)^2 \Lambda(y) \lambda_3(y) \frac{1}{U_c} \left[\frac{\omega \Phi_v(\omega)}{v'^2} \right] e^{-2\omega y/U_c} dy. \quad (6.14)$$

where

$$\left[\frac{\omega \Phi_v(\omega)}{v'^2} \right] = \tilde{\Phi}_v(\omega, y).$$

which is the form of dimensionless velocity spectrum used in Chapter 4. Again $\Lambda(y)=y$ and $\lambda_3(y)$ is taken to be the turbulence integral length scale for vertical velocity fluctuations. The plots of $\tilde{\Phi}_v(\omega, y)$, given in Chapter 4, show that, at least to first order, $\tilde{\Phi}_v(\omega, y)$ can be taken to be a universal function of ω and can be removed from the integral. To further simplify matters it can be assumed that for the frequencies of interest the exponential term is nearly unity (over the variable range of interest). With these approximations (6.14) can be written as

$$\Phi_p(\omega) = C_L \tilde{\Phi}_v(\omega) v'^2 (dU/dy)^2 L_2(y) y/U_c dy. \quad (6.15)$$

If U_c is taken to be the local mean velocity ($U(y)$) then the terms within the integral are frequency independent and describe the wall pressure source distribution in the boundary layer. For discussion purposes the integrand of (6.15) will be termed $S(y)$.

Equation (6.15) is now in a form that allows the source distribution of low frequency wall pressures for the perturbed and equilibrium flow to be compared. Figure 6.1 is a plot of $10 \cdot \log_{10}(S(y))$ versus y/δ^* for each of the streamwise positions for which velocity statistics were measured. The source term distributions for the perturbed flow are clearly different from that for the equilibrium flow. For the perturbed flow the distribution of source terms are markedly affected by the disturbance layer in the boundary layer.

The distribution for the equilibrium flow has its maximum value very near the wall and the levels rapidly decrease further away from the wall. This is consistent with the velocity statistics for an equilibrium flow; peak levels of turbulence occur at a $y^+ \approx 18$ and in the log-law region the gradient of the mean velocity is proportional to y^{-1} .

As has been discussed previously the flow characteristics at $x/h=10$ are unique compared to positions further downstream. This is also evident in the source term distribution. At $x/h=10$, $S(y)$ has a very pronounced peak showing the presence of a highly dominant source term at $y/\delta^* \approx 1$. Additionally there is no indication of an increase in the source term level closer to the wall as there is for all other measurement positions. The y/δ^* location of the peak in $S(y)$ corresponds to the location of the disturbance layer.

The source term distributions measured for $x/h > 10$ all follow a trend that is consistent with the trends in the turbulence intensity profiles. There is a near wall peak in $S(y)$ which rapidly decreases away from the near wall. Further out in the boundary layer, $S(y)$ shows a broad and more pronounced second peak that is a direct result of the highly turbulent disturbance layer in the flow. This primary peak in $S(y)$ decreases in level and moves further away from the wall in the downstream direction.

A number of qualitative aspects of the source term distributions shown in figure 6.1 should be noted. Although the second peak in $S(y)$ is generally lower in level than the near wall peak, the disturbance layer is still the primary source of (low frequency) wall pressures since the wall pressure is an integration of $S(y)$ over the extent of the boundary layer. Except for the distributions at $x/h=10$, all of the distributions for the perturbed flow are higher in level than the distribution for the equilibrium flow at comparable y/δ^* . This shows that flow disturbances that exist in the outer layer persist far downstream and can markedly influence the level of low frequency wall pressure fluctuations.

Since $S(y)$ is most strongly characterized by the v'^2 and $(dU/dy)^2$ terms, it is interesting to determine which term has more influence in dictating the shape of the $S(y)$ curves. Profiles of v'^2 are provided in

Chapter 4. Figure 6.2 shows plots of $20 \log_{10}(dU/dy)$, versus y/δ^* , obtained from the mean velocity profiles by the numerical differentiation technique describe in Chapter 4. Included in figure 6.2 is a line representing the value of dU/dy obtained assuming a log-law profile ($dU/dy = u^*/\kappa y$). The mean gradient of the equilibrium flow agrees well with the gradient for a log-law profile lending confidence in the accuracy of the numerical differentiation technique. At $y/\delta^* < 1$ dU/dy for the perturbed flow are parallel to, but below, dU/dy for the equilibrium flow. This trend was also present in the mixing length plots (figure 4.18). Generally, dU/dy for the perturbed flow are smaller than that for the equilibrium flow. Hence, the primary term in $S(y)$ is v'^2 .

A number of simplifying approximations were made which allowed (6.15) to be written in its relatively simple form. At the outset it was assumed that the flow was homogeneous in planes parallel to the wall. This is clearly not the case for a perturbed flow. The consequence of having a flow inhomogeneity is to provide a mechanism for wavenumber conversion which does not occur in a homogeneous flow. Attempts to account for an inhomogeneity term in the original formulization would simply further mask the role that velocity fluctuations play in generating wall pressures. Certain assumptions were made about the form of the vertical velocity cross-spectrum. Specifically, it was assumed that the vertical cross-correlation of the vertical velocity component increased linearly with wall distance. This assumption can lead to an underestimation of the contributions that come from the disturbance layer where the flow has a high degree of organized structure. The last assumption, leading to (6.15), is that the exponential term in (6.14) is nearly unity in the low frequency region. At a frequency of 200 Hz, which corresponds roughly to the peak in the perturbed flow wall pressure spectra, the exponential term is on the order of $e^{-0.5}$ at $y/\delta^* = 1$ and decreases exponentially with increasing wall distance. Included in figure 6.1 is a line representing this decay

term (using $\omega\delta^*/U_0 \approx 0.2$ and $U_c/U_0 \approx 0.7$). Even accounting for this decay term the disturbance layer is still a major contributor to the wall pressure field.

In summary, it was found in Chapter 5 that the low frequency wall pressure spectra for the perturbed flow scaled on the disturbance layer variables. This dependence is also predicted using an idealized analytical model for the velocity-wall pressure relationship. This comparison has helped provide validity to the use of (6.12) as a qualitative measure of the wall pressure source term locations in a boundary layer flow. From examination of (6.12) it can be seen that the primary pressure source term is $v'^2(dU/dy)^2$ and that the contribution a given term makes to the wall pressure field decreases exponentially with increasing frequency or wall distance. Hence, consistent with the observed scaling laws from Chapter 5, the sources of high frequency wall pressure fluctuations must be located near the wall while low frequency sources can be found further out in the boundary layer.

The frequency distribution of the wall pressure source terms scales differently between high and low frequencies. At low frequency the dependence is a function of the product of the exponential decay term and with the first spectral moment of the vertical velocity frequency spectrum. For high frequencies the wall pressure source term distribution is given by the product of the exponential decay term with the vertical velocity spectrum. Hence, the frequency spectrum of the vertical velocity determines the spectral content of the wall pressures. The final point is that the contribution a source term makes to the wall pressure is directly proportional to the vertical correlation distance of the source.

6.3 Burst Event Process

Since the realization, some 15 years ago, that the turbulence activity in the inner layer of a turbulent boundary layer is characterized, in part, by the presence of randomly occurring coherent "events," there has been extensive effort expended on trying to understand the specific role this activity plays in the turbulence process. The importance of this process in the maintenance of turbulence is illustrated by the measurements of Lu and Willmarth (1973)

who showed that nearly 80% of the turbulence Reynolds stress is a direct consequence of coherent motions. Unfortunately, to date the understanding of this process is still not clear. Review articles by Willmarth (1975) and Cantwell (1981) provide detailed accounts of what is currently known about these processes. For the purposes of this discussion no delineation will be made between the various phases or stages (streaks, sweeps, ejections, bursts, etc.) of a coherent motion, but all aspects will be globally referred to as a burst event.

With the importance of burst events to the turbulence production process being well accepted it follows to consider the role they play in the production of wall pressures. The studies of Burton (1974) and Thomas and Bull (1983) addressed specifically this question. Although Burton's study was inconclusive, the study of Thomas and Bull clearly show characteristic wall pressure fluctuation patterns which are associated with burst events.

Emmerling et al. (1973) found that the occurrence rate of zones of high-amplitude pressure fluctuations agreed well with the bursting frequencies predicted using either inner variable or outer variable scaling. The predicted values were not too dissimilar and they got slightly better agreement with the frequency predicted using the inner variable scaling. This shows a possible relationship between the burst event rate in the boundary layer and the large scale pressures at the wall. Similarly, if burst events are a primary source of wall pressure fluctuations, then the wall pressure spectrum may exhibit some feature that is characteristic of the bursting frequency.

To examine this issue the results of Blackwelder and Haritonidis (1983) are used to estimate the bursting frequency ω_b . They found that the bursting frequency scaled on inner variables (given as $\omega_b \nu / u_*^2 = 0.022$) and was nearly constant over a wide range of Reynolds numbers that span the Reynolds number range of the flow for the current investigation. A comparison of this bursting frequency to the frequencies for the wall pressure spectra in figure 5.6 show that ω_b ($f_b \approx 275$ Hz) is surprisingly close to the frequency at which the wall pressure spectrum is a maximum ω_m ($f_m \approx 350$ Hz). However, the wall

pressures in this frequency range were found to scale on the outer flow time scale δ^*/U_o (figure 5.5). Thus, although ω_m is in general agreement with ω_b the scaling behavior for the two differs. It is interesting to compare ω_m , obtained in figure 5.5 as $\omega\delta^*/U_o=0.3$, to the periodicity of the large-scale structure in the outer flow.

Hinze (1975) roughly estimates that turbulent bulges, characteristic of the outer flow structure, pass by a wall position with a recurrence frequency given by $\omega\delta^*/U_o=0.25$. This value is also very close to the frequency of peak spectral level but, more importantly, also scales on outer flow variables. Furthermore, the convection velocity data shows that the source of the wall pressure fluctuations at $\omega\delta^*/U_o=0.3$ come from the outer layer of the boundary layer. The conclusion is that although the bursting frequency is quite close to the frequency at which the wall pressure spectrum is a maximum, the two are not necessarily related. Instead, the frequency of peak pressures is more likely a consequence of the passage frequency of the large-scale structures in the outer flow.

However, it has been suggested that there may be an interdependence between the large-scale structure in the outer layer and the burst events near the wall which accounts for the similarity between the bursting frequency and the outer flow passage frequency. If this is true then the above scaling argument may no longer hold and it is possible that the spectral peak and the bursting frequency are related.

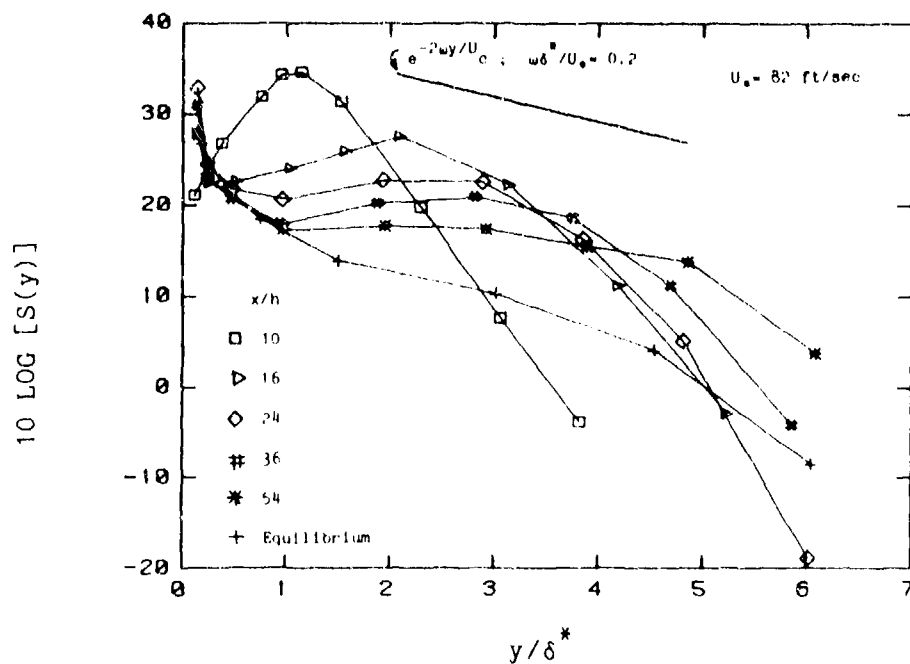


Figure 6.1 Source Term Distribution Within the Boundary Layer

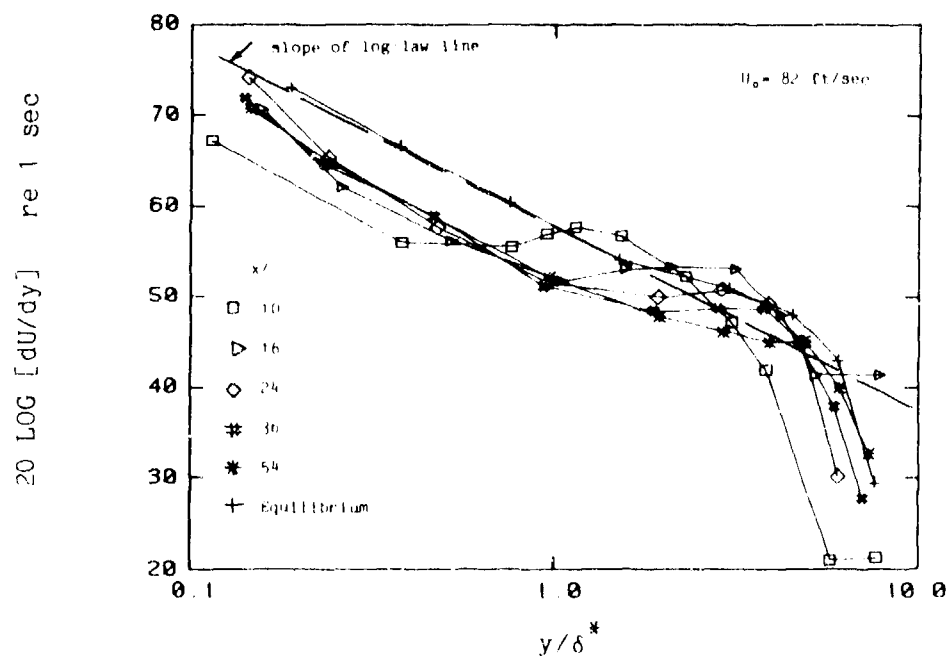


Figure 6.2 Mean Velocity Gradient Within the Boundary Layer

CHAPTER 7

SUMMARY AND CONCLUSIONS

7.1 Summary of Accomplishments

The overall objective of this research was to investigate the process by which turbulent boundary layers produce wall pressure fluctuations. The experimental approach consisted of measuring both single-point velocity statistics throughout the boundary layer and the cross-spectral statistics of the wall pressure field for both a fully developed equilibrium boundary layer and for a non-equilibrium turbulent boundary layer that was perturbed by passing over a backward-facing step. This perturbation to the flow introduced a highly energized disturbance layer close to the wall which was a primary contributor to low frequency wall pressure fluctuations. The disturbance layer propagated away from the wall and decayed in turbulence level as it convected downstream. This disturbance provided a flow in which the primary wall pressure source term was located at various regions of the boundary layer. By comparing the wall pressure statistics, measured at various downstream locations, to the properties of the disturbance layer it was possible to learn more about the role velocity fluctuations play in the production of wall pressures.

In addition to interpreting the wall pressure measurements to determine locations in the boundary layer for the probable wall pressure source terms, the statistical properties of the velocity field that were measured were used in an idealized analytical model for the wall pressure frequency spectrum to further confirm that the disturbance layer was the primary source of wall pressure fluctuations.

The data base that was obtained during this study is quite extensive. Velocity measurements consisted of mean velocity profiles, profiles of u' , v' , $\overline{u'v'}$, and velocity spectra of the u and v components of velocity. These data were obtained both upstream of the backward-facing step and at various downstream positions extending as far downstream as $x/h=54$. The wall pressure measurements were obtained in great detail. A very complete set of cross-spectral density measurements were obtained for the equilibrium flow and at various

positions downstream of the step. The farthest downstream position at which wall pressure measurements were made was $x/h=72$. Cross-spectrum measurements were obtained for streamwise and transverse separations (separate streamwise and transverse separations were used) ranging from a minimum separation of 1/4-inch to a maximum separation of 24-inch for the streamwise measurements and a maximum of 3-inch for the transverse measurements. All data are available on floppy disks in IBM PC format.

7.2 Major Conclusions

A summary of the major conclusions obtained from the interpretation and analysis of the experimental data follows:

Structure of the Flow

1. The separation and reattachment process places a region of highly turbulent flow near the wall; this region is termed the disturbance layer and is the remnants of the original mixing layer that was formed while a separated flow. The disturbance layer propagates away from the wall and decays in turbulence level as it convects downstream in a manner similar to the spreading and decay of a plane wake. At $x/h=10$ the disturbance layer is located at a $y/h \approx 0.5$ and at $x/h=54$ is located at $y/h=1.4$.

2. Near reattachment ($x_r/h=6$) the entire boundary layer is highly disturbed as characterized by the mean profiles at $x/h=10$. Within a short downstream distance ($x/h=16$) the near wall region of the attached boundary layer, extending out to the start of the log-law region, has recovered. Recovery of the outer flow region is, however, much slower. Full recovery will not occur until the disturbance layer has propagated all the way across the boundary layer. It is estimated that full recovery will not occur until an $x/h \approx 250$.

3. Spectra of the u component of velocity show the presence of the disturbance layer in the flow. u spectra measured in the vicinity of the disturbance layer display an extended region of $k^{-5/3}$ scaling indicative of a high Reynolds number flow. The vertical range within the boundary layer over which the $k^{-5/3}$ is observed is large. The reason for the extended $k^{-5/3}$ region is suggested to be a result of two effects; the first is an increase in the local turbulence Reynolds number due to the highly turbulent flow in the disturbance layer and the second is due to a shift to lower frequency (wavenumber) of the energy containing eddies which increases the extent of the inertial subrange of wavenumbers.

4. The spectra of the v component of velocity do not explicitly show the presence of the disturbance layer. Instead they are more characterized by variations in their spectral content that is a function of wall distance.

Features of the Wall Pressure Fluctuations

5. Levels of fluctuating wall pressure are very high near reattachment. The frequency spectra show that these high levels are associated with excess low frequency content. The levels decrease in the downstream direction, but even at $x/h=72$ the wall pressure spectrum has still not recovered to an equilibrium character.

6. The high frequency wall pressures were found to scale on inner flow variables (τ_0 and u^{*2}/ν) and this region was found to recover to an equilibrium condition quite rapidly. This places the source of high frequency wall pressure near the wall in the inner layer of the boundary layer.

7. The low frequency wall pressures showed dramatic variations in level with downstream position. However, they were found to scale on disturbance layer variables ($\overline{u'v'}$, $U(\delta_d)$, δ_d , h). Even at $x/h=72$, the low frequency portion of the wall pressure spectrum is higher than the equilibrium spectrum. Overall, the source of low frequency wall pressures is in the outer flow region.

8. The cross-spectral properties of the wall pressure field for the perturbed flow are quite different than those for an equilibrium flow. For the perturbed flow, the wall pressures remain coherent over much greater distances. This completely eliminates the similarity scaling that normally exists for the coherence. The convective phase velocities of the various frequency components are determined by the location of the disturbance layer in the flow.

9. For both the equilibrium and perturbed flows, it was found that the boundary layer acts to suppress pressure components below $\omega\delta^*/U_0=0.3$. Below this cutoff frequency both the coherence and convection velocity decrease rapidly. This cutoff frequency is also the location at which the wall pressure frequency spectrum is a maximum.

10. An idealized analytical model for the wall pressure frequency spectrum, which is a function of the measured velocity statistics, confirmed that the primary source for the low frequency wall pressures was the disturbance layer.

11. The occurrence rate (bursting frequency) for burst-events is quite close to the frequency at which the wall pressure spectrum is a maximum. However, the bursting frequency has been reported to scale on inner variables while the wall pressures clearly scale on the outer flow time scale at this low frequency. This essentially precludes the frequency of peak spectral level from being a direct result of the burst-event frequency in the flow.

7.3 Concluding Remarks

This investigation has provided interesting new insight into the process by which wall pressure fluctuations are produced by turbulent boundary layers. This information is of benefit not only to those interested in estimating the response of a surface to wall pressure excitation but also to the turbulence community as a whole in that the relationship between velocity fluctuations in the flow and wall pressure fluctuations is better understood. For many flow situations it is possible to monitor the wall pressure fluctuations, which is a non-intrusive measurement, to obtain an estimate of the turbulence activity and its organized structure in the flow field.

The data base that has been obtained for flow over a backward-facing step greatly extends that which is currently available by providing velocity data far downstream of the step where the flow is approaching a relaxation to the equilibrium state.

Information on the spectral properties of the wall pressure field for an equilibrium flow has been provided and these data extend the current knowledge. The very marked change in cross-spectral properties of the wall pressure field, below the boundary layer cutoff frequency ($\omega\delta^*/U_0 \approx 0.3$), has been demonstrated in detail. The cross-spectral data are of particularly high quality and extend over a very wide range of separation distances.

It has been shown that a flow disturbance can greatly alter not only the velocity statistics in the flow but also the resulting wall pressure fluctuations. Such a disturbance can persist far downstream before the flow completely relaxes back to an equilibrium state. Specific care must be taken to examine the upstream history of a turbulent boundary layer if either turbulent velocity or wall pressure calculations are to be made.

The final remark for this study is an overall summary; it has been shown that it is possible to obtain a good estimate of the location of wall pressure source terms in the flow, in spite of the fact that the wall pressures are an integrated effect of the velocity fluctuations throughout the boundary layer. This is particularly true for a perturbed flow but is still also valid for an equilibrium flow. This enhances the understanding of the interaction between velocity and pressure fluctuations.

REFERENCES

- Andreopoulos, J. and Wood, D.H., (1982), "The Response of a Turbulent Boundary Layer to a Short Length of Surface Roughness," *J. Fluid Mechanics*, Vol. 118, pp. 143-164.
- Antonia, R.A. and Luxton, R.E., (1971a), "The Response of a Turbulent Boundary Layer to an Upstanding Step Change in Surface Roughness," *Trans. of ASME, J. Basic Eng.*, Vol. 93, Series D, No. 1, pp. 22-34.
- Antonia, R.A. and Luxton, R.E., (1971b), "The Response of a Turbulent Boundary Layer to a Step Change in Surface Roughness. Part 1. Smooth to Rough," *J. Fluid Mechanics*, Vol. 48, Part 4, pp. 721-761.
- Antonia, R.A. and Luxton, R.E., (1972), "The Response of a Turbulent Boundary Layer to a Step Change in Surface Roughness. Part 2. Rough-to-Smooth," *J. Fluid Mechanics*, Vol. 53, Part 4, pp. 737-757.
- Batchelor, G.K., The Theory of Homogeneous Turbulence, Cambridge University Press, London (1967).
- Bendat, J.S. and Piersol, A.G., Random Data: Analysis and Measurement Procedures, Wiley-Interscience, New York (1971).
- Bendat, J.S. and Piersol, A.G., Engineering Applications of Correlation and Spectral Analysis, Wiley-Interscience, New York (1980).
- Bhattacharjee, S., Scheelke, B. and Troutt, T.R., (1985) "Modification of Vortex Interactions in a Reattaching Separated Flow," AIAA Paper 85-0555, Shear Flow Control Conference, Boulder, Colo.
- Blackwelder, R.F. and Haritonidis, J.H., (1983) "Scaling of the Bursting Frequency in Turbulent Boundary Layers," *J. Fluid Mechanics*, Vol. 132, pp. 87-103.
- Blake, W.K., (1970), "Turbulent Boundary-Layer Wall-Pressure Fluctuations on Smooth and Rough Walls," *J. Fluid Mechanics*, Vol. 44, Part 4, pp. 637-660.
- Blake, W.K., (1971), "Turbulent Velocity and Pressure Fields in Boundary-Layer Flows Over Rough Surfaces," *Proceed. of Symp. on Turbulence in Liquids*, Univ. of Missouri-Rolla, Oct. 1971 (published 1972).

- Blake, W.K., (1984), "Aero-Hydroacoustics for Ships," DTNSRDC Report 84/010, David Taylor Naval Ship Research and Development Center (June 1984).
- Bradshaw, P., (1967), "'Inactive' Motion and Pressure Fluctuations in Turbulent Boundary Layers," J. Fluid Mechanics, Vol. 30, Part 2, pp. 241-258.
- Bradshaw, P., An Introduction to Turbulence and Its Measurement, Pergamon Press, New York (1971).
- Bradshaw, P. and Wong, F.Y.F., (1972), "The Reattachment and Relaxation of a Turbulent Shear Flow," J. Fluid Mechanics, Vol. 52, Part 1, pp. 113-125.
- Brooks, T.F. and Hodgson, T.H., (1981), "Trailing Edge Noise Prediction From Measured Surface Pressures," J. Sound and Vibration, Vol. 78, No. 1, pp. 69-117.
- Bull, M.K., (1967), "Wall-Pressure Fluctuations Associated With Subsonic Turbulent Boundary Layer Flow," J. Fluid Mechanics, Vol. 28, Part 4, pp. 719-754.
- Bull, M.K. and Thomas A.S.W., (1976), "High Frequency Wall Pressure Fluctuations in Turbulent Boundary Layers," Physics of Fluids, Vol. 19, pp. 597-599.
- Bullock, K.J., Cooper, R.E. and Abernathy, F.H., (1978), "Structural Similarity in Radial Correlations and Spectra of Longitudinal Velocity Fluctuations in Pipe Flow," J. Fluid Mechanics, Vol. 88, Part 3, pp. 585-608.
- Burton, T.E., (1974), "The Connection Between Intermittent Turbulent Activity Near the Wall of a Turbulent Boundary Layer With Pressure Fluctuations at the Wall," Mass. Instit. of Tech., Acoustics and Vibration Lab., Rept. 70208-10 (June 1974).
- Cantwell, B.J., (1981), "Organized Motion in Turbulent Flow," Annual Review of Fluid Mechanics, Vol. 13, pp. 457-515.
- Champagne, F.H. and Sleicher, C.A., (1967), "Turbulence Measurements with Inclined Hot-wires. Part 2. Hot-wire Response Equations," J. Fluid Mechanics, Vol. 28, Part 1, pp. 177-182.
- Chandrsuda, C. and Bradshaw, P., (1981), "Turbulence Structure of a Reattaching Mixing Layer," J. Fluid Mechanics, Vol. 110, pp. 171-194.

- Chase, D.M., (1980), "Modeling the Wavevector-Frequency Spectrum of Turbulent Boundary Layer Wall Pressure," J. Sound and Vibration, Vol. 70, No. 1, pp. 29-67.
- Cherry, N.J., Hillier, R. and Latour, M.E.M., (1984), "Unsteady Measurements in a Separated and Reattaching Flow," J. Fluid Mechanics, Vol. 144, pp. 13-46.
- Cheun, B.S., Toy, N. and Moss, W.D., (1981), "The Effect of Upstream Boundary Layer Thickness Upon Flow Past a Backward-facing Step," Proceedings of the 7th Symposium on Turbulence, University of Missouri-Rolla (Sept. 1981).
- Clauser, F.H., (1956), "The Turbulent Boundary Layer," Advances in Applied Mechanics, Vol. 4, pp. 2-51, Academic Press.
- Cole III, J.E., (1985), "Sensitivity to Mean Flow Parameters of the Low Wavenumber Content of the Wall Pressure Under a Turbulent Boundary Layer," Report U-1205-333, Cambridge Acoustical Associates, Inc., (April 1985).
- Corcos, G.M., (1963), "Resolution of Pressure in Turbulence," J. Acoustical Soc. of Amer., Vol. 35, No. 2, pp. 192-199.
- Corcos, G.M., (1964), "The Structure of the Turbulent Pressure Field in Boundary-Layer Flows," J. Fluid Mechanics, Vol. 18, pp. 353-378.
- Dowling, A.P. and Ffowes Williams, J.E. Sound and Sources of Sound, Ellis Horwood Limited, Chichester, West Sussex, England (1983).
- Eaton, J.K. and Johnston, J.P., (1980), "Turbulent Flow Reattachment: An Experimental Study of the Flow and Structure Behind a Backward-facing Step," Report MD-39, Thermosciences Div., Dept. of Mechanical Engineering, Stanford University (Also Ph.D. Thesis of J.K. Eaton (1980) Stanford University).
- Eaton, J.K. and Johnston, J.P., (1981a), "A Review of Research on Subsonic Turbulent Flow Reattachment," AIAA Journal, Vol. 19, No. 9, pp. 1093-1100.
- Eaton, J.K. and Johnston, J.P., (1981b), "Low Frequency Unsteadiness of a Reattaching Turbulent Shear Layer," Proceedings of the 3rd International Symposium on Turbulent Shear Flows, Davis, Calif. (Sept. 1981).
- Eckelmann, H., (1974), "The Structure of the Viscous Sublayer and the Adjacent Wall Region in a Turbulent Channel Flow," J. Fluid Mechanics, Vol. 65, Part 3, pp. 439-459.

- Elliott, J.A., (1972), "Microscale Pressure Fluctuations Measured Within the Lower Atmospheric Boundary Layer," J. Fluid Mechanics, Vol. 53, Part 2, pp. 351-383.
- Elswick, R., (1976) Private Communication.
- Emmerling, R., Meier, G.E.A. and Dinkelacker, A., (1973), "Investigation of the Instantaneous Structure of the Wall Pressure Under a Turbulent Boundary Layer Flow," AGARD Conf. on Noise Mechanisms, CPP-131, Paper No. 24.
- Etheridge, D.W. and Kemp, P.H., (1978), "Measurements of Turbulent Flow Downstream of a Rearward-Facing Step," J. Fluid Mechanics, Vol. 86, Part 3, pp. 545-566.
- Farabee, T.M. and Casarella, M.J., (1984), "Effects of Surface Irregularity on Turbulent Boundary Layer Wall Pressure Fluctuations," ASME Journal of Vibration, Stress, and Reliability in Design, Vol. 106, pp. 343-350.
- Farabee, T.M. and Casarella, M.J., (1985), "Measurement of Fluctuating Wall Pressure for Separated/Reattached Boundary Layer Flows," ASME Winter Annual Meeting, Miami Beach, Fla., Nov. 17-22, NCA-Vol. 1, pp. 17-25.
- Ffowcs Williams, J.E., (1965), "Surface-Pressure Fluctuations Induced by Boundary-Layer Flow at Finite Mach Number," J. Fluid Mechanics, Vol. 22, Part. 3, pp. 507-519.
- Fricke, F.R., (1971), "Pressure Fluctuations in Separated Flows," J. Sound and Vibration, Vol. 17, No. 1, pp. 113-123.
- Fricke, F.R. and Stevenson, D.C., (1968), "Pressure Fluctuations in Separated Flow Region," J. Acoustical Soc. of Amer., Vol. 44, No. 5, pp. 1189-1200.
- Greshilov, E.M., Evtuchenko, A.V. and Lyamshev, L.M., (1969), "Spectral Characteristics of the Wall Pressure Fluctuations Associated with Boundary Layer Separation Behind a Projection on a Smooth Wall," Soviet Physics-Acoustics, Vol. 15, No. 1, pp. 29-34, (English Translation).
- Haj Hariri, H. and Akylas, T.R., (1985), "The Wall-Shear-Stress Contribution to Boundary-Layer Noise," Physics of Fluids, Vol. 28, No. 9, pp. 2727-2729.

- Hasan, M.A.Z., Casarella, M.J. and Rood, E.P., (1985), "An Experimental Study of the Flow and Wall Pressure Field Around a Wing-Body Junction," ASME Winter Annual Meeting, Miami Beach, Fla., Nov. 17-22, NCA-Vol. 1, pp. 89-95.
- Hinze, J.O., Turbulence, 2nd Edition, McGraw-Hill, New York (1975).
- Hubbard, H.H., (1957), "Some Experiments Related to the Noise From Boundary Layers," J. Acoustical Soc. of Amer., Vol. 29, No. 3, pp. 331-334.
- Hussain, A.K.M.F., (1983), "Coherent Structures - Reality and Myth," Physics of Fluids, Vol. 26, No. 10, pp. 2816-2850.
- Jorgensen, F.E., (1981), "Directional Sensitivity of Wire and Fiber-Film Probes," DISA Information No. 11, pp. 31-37.
- Kassab, S.Z., Derksen, R.W. and Azad, R.S., (1985), "Remarks on Stem Configuration of X-Array Hot-Wire Probes," Dantec Information No. 01, pp. 9-10 (June 1985).
- Kim, J., Kline, S.J. and Johnston, J.P., (1978), "Investigation of Separation and Reattachment of a Turbulent Shear Layer: Flow over a Backward-facing Step," Report MD-37, Thermosciences Div., Dept. of Mechanical Engineering, Stanford University.
- Klebanoff, P.S., (1955), "Characteristics of Turbulence in a Boundary Layer with Zero Pressure Gradient," NACA TN 1247.
- Kline, S.J., Reynolds, W.C., Schraub, F.A. and Runstadler, P.W., (1967), "The Structure of Turbulent Boundary Layers," J. Fluid Mechanics, Vol. 30, Part 4, pp. 741-773.
- Kraichnan, R.H., (1956), "Pressure Fluctuations in Turbulent Flow Over a Flat Plate," J. Acoustical Soc. of Amer., Vol. 28, No. 3, pp. 378-390.
- Landahl, M.T., (1967), "A Wave-Guide Model for Turbulence Shear Flow," J. Fluid Mechanics, Vol. 29, Part. 3, pp. 441-459.
- Lilley, G.M. and Hodgson, T.H., (1960), "On Surface Pressure Fluctuations in Turbulent Boundary Layers," AGARD Rpt. No. 276 (April 1960).
- Lu, S.S. and Willmarth, W.W., (1973), "Measurements of the Structure of the Reynolds Stress in a Turbulent Boundary Layer," J. Fluid Mechanics, Vol. 60, Part. 3, pp. 481-511.

- Mabey, D.G., (1972), "Analysis and Correlation of Data on Pressure Fluctuations in Separated Flow," J. Aircraft, Vol. 9, No. 9, pp. 642-645.
- Meecham, W.C. and Tavis, M.T., (1980), "Theoretical Pressure Correlation Functions in Turbulent Boundary Layers," Physics of Fluids, Vol. 23, No. 6, pp. 1119-1131.
- Morrison, W.R.B. and Kronauer, R.E., (1969), "Structural Similarity for Fully Developed Turbulence in Smooth Tubes," J. Fluid Mechanics, Vol. 39, Part 1, pp. 117-141.
- Moss, W.D. and Baker, S., (1980), "Re-Circulating Flows Associated with Two-Dimensional Steps," Aeronautical Quarterly, August 1980, pp. 151-172.
- Narayan, N. and Plunkett, R., (1985), "Pressure Cross Spectra in Turbulent Boundary Layers in Water," ASME Winter Annual Meeting, Miami Beach, Fla., Nov. 17-22, NCA-Vol. 1, pp. 97-103.
- Panton, R.L. and Linebarger, J.H., (1974), "Wall Pressure Spectra Calculations for Equilibrium Boundary Layer," J. Fluid Mechanics, Vol. 65, Part 2, pp. 261-287.
- Panton, R.L., Goldman, A.L., Lowery, R.L. and Reischman, M.M., (1980), "Low-Frequency Pressure Fluctuations in Axisymmetric Turbulent Boundary Layers," J. Fluid Mechanics, Vol. 97, Part 2, pp. 299-319.
- Perry, A.E. and Abell, C.J., (1975), "Scaling Laws for Pipe-Flow Turbulence," J. Fluid Mechanics, Vol. 67, Part 2, pp. 257-271.
- Pronchick, S.W., (1983), "An Experimental Investigation of the Structure of a Turbulent Reattaching Flow Behind a Backward-facing Step", Ph.D. Thesis, Dept. of Mechanical Engineering, Stanford University.
- Romanov, V.N., (1985), "Radiation of Sound From a Plate Excited by a Nonuniform Field of Random Forces," Sov. Phys. Acoust., 31(2), Mar-Apr. 1985, Amer. Inst. of Physics Translation.
- Samuel, A.E. and Joubert, P.N., (1974), "A Boundary Layer Developing in an Increasingly Adverse Pressure Gradient," J. Fluid Mechanics, Vol. 66, Part 3, pp. 481-505.
- Schewe, G., (1983), "On the Structure and Resolution of Wall-Pressure Fluctuations Associated with Turbulent Boundary-Layer Flow," J. Fluid Mechanics, Vol. 134, pp. 311-328.

- Schloemer, H.H., (1967), "Effects of Pressure Gradients on Turbulent Boundary-Layer Wall-Pressure Fluctuations," J. Acoustical Soc. of Amer., Vol. 42, No. 1, pp. 93-113.
- Smits, A.J. and Wood, D.H., (1985), "The Response of Turbulent Boundary Layers to Sudden Perturbations," Annual Review of Fluid Mechanics, Vol. 17, pp. 321-358.
- Smyth, R., (1979), "Turbulent Flow Over a Plane Symmetric Sudden Expansion," ASME, J. Fluids Engineering, Vol. 101, pp. 348-353.
- Strickland, J.H. and Simpson, R.L., (1975), "'Bursting' Frequencies Obtained from Wall Shear Stress Fluctuations in a Turbulent Boundary Layer," Physics of Fluids, Vol. 18, No. 3, pp. 306-308.
- Tani, I., Matsusaburo, I. and Komoda, H., (1961), "Experimental Investigation of Flow Separation Associated with a Step or a Groove," Report No. 364 (Vol. 27, No. 4), Aeronautical Research Institute, University of Tokyo.
- Tchen, C.M., (1954), "Transport Processes as Foundations of the Heisenberg and Obukhoff Theories of Turbulence," Physics Review, Vol. 93, No. 1, pp. 4-14.
- Tennekes, H. and Lumley, J.L., A First Course in Turbulence, The MIT Press, Cambridge, Mass. (1972).
- Thomas, A.S.W. and Bull, M.K., (1983), "On the Role of Wall-Pressure Fluctuations in Deterministic Motions in the Turbulent Boundary Layer," J. Fluid Mechanics, Vol. 128, pp. 283-322.
- Townsend, A.A., (1976), The Structure of Turbulent Shear Flow, 2nd Edition, Cambridge University Press, London (1976).
- Troutt, T.R., Scheelke, B. and Norman, T.R., (1984), "Organized Structures in a Reattaching Separated Flow Field," J. Fluid Mechanics, Vol. 143, pp. 413-427.
- Tutu, N.K. and Chevray, R., (1975), "Cross-wire Anemometry in High Intensity Turbulence," J. Fluid Mechanics, Vol. 71, Part 4, pp. 785-800.
- Vlasov, E.V., Ginevskii, A.S., Karavosov, R.K. and Frankfurt, M.O., (1979), "Statistical Characteristics of Pressure Fluctuations in the Flow-Separation Zone of a Plate Behind a Spoiler," Sov. Phys. Acoust., Vol. 25, No. 3, Amer. Inst. Physics Translation, pp. 208-211.

- Westphal, R.V., and Johnston, J.P., (1984), "Effect of Initial Conditions on Turbulent Reattachment Downstream of a Backward-facing Step," AIAA Journal, Vol. 22, No. 12, pp. 1727-1732.
- Willmarth, W.W. and Wooldridge, C.E., (1962), "Measurements of the Fluctuating Pressure at the Wall Beneath a Thick Turbulent Boundary Layer," J. Fluid Mechanics, Vol. 14, pp. 187-210. Corrigendum: J. Fluid Mechanics, Vol. 21, pp. 107-109.
- Willmarth, W.W. and Wooldridge, C.E., (1963), "Measurements of the Correlation Between the Fluctuating Velocities and the Fluctuating Wall Pressure in a Thick Turbulent Boundary Layer," AGARD Rept. No. 456.
- Willmarth, W.W. and Tu, B.J., (1967), "Structure of Turbulence in the Boundary Layer Near the Wall," Physics of Fluids Suppl., Vol. 10, pp. S134-S137.
- Willmarth, W.W., (1975), "Pressure Fluctuations Beneath Turbulent Boundary Layers," Annual Review of Fluid Mechanics, Vol. 7, pp. 13-38.
- Willmarth, W.W. and Sharma, L.K., (1984), "Study of Turbulent Structure with Hot Wires Smaller than the Viscous Length," J. Fluid Mechanics, Vol. 142, pp. 121-149.
- Wills, J.A.B., (1970), "Measurements of the Wave-Number/Phase Velocity Spectrum of Wall Pressure Beneath a Turbulent Boundary Layer," J. Fluid Mechanics, Vol. 45, Part 1, pp. 65-90.
- Yavuzhurt, S., (1984), "A Guide to Uncertainty Analysis of Hot-Wire Data," J. Fluids Engineering, Vol. 106, pp. 181-186.

APPENDIX A

HOT WIRE ERROR ANALYSIS

Correct interpretation of hot wire data requires a detailed knowledge of the response characteristics of the anemometry system to both the mean and fluctuating components of the flow field. The general approach is to perform a mean flow calibration and then assume that the calibration is also valid for the fluctuating velocity measurements. However, it is difficult to obtain unambiguous measurements of a given velocity component due to the quadratic response behavior of a hot wire. This requires a priori knowledge of the velocity field in order to correctly decompose the measurements. Added to these problems are the difficulties of trying to measure a spatial field with finite transducers. These issues have been widely discussed in the literature and only a limited discussion will be presented. First, a brief discussion will be given of the errors that arise due to finite transducer size limitations. Following that will be a more detailed discussion of the directional response of a hot wire. Finally, there will be a discussion of the possible sources of error for the measurements in this investigation.

Resolution Errors

The physical size of a measuring transducer is an important parameter that must be accounted for in interpreting fluctuating measurements. This is important for hot wire measurements not only in terms of spatial biasing by the sensitive portion of the wire but also in terms of the aerodynamic interference that the wire creates by its presence in the flow field. This second point was specifically addressed by Kassab et al. (1985) for anemometers that are similar to those used in this investigation.

Kassab et al. (1985) compared values of turbulence stresses measured with an in-line and two right-angled x-wire sensors for a turbulent boundary layer flow. The right-angle sensors that were studied are geometrically identical to the x-wire sensors used in the current investigation. They found that values of v'/U_0 and u'/U_0 were 5-10% lower for the right-angle probes than for the in-line probe.

Similarly, they found that the value of shear stress coefficient, $R_{12} = \overline{u'v'}/u'v'$, measured with the in-line probe was the same as is reported in the literature, however, the values of R_{12} obtained with the right-angle probe were 20% lower. They attributed these errors to aerodynamic interference resulting from flow over the probe support assembly. For the right-angle sensors the probe support is normal to the wall and in close proximity to the wires. It is interesting to note that values of v'/U_0 measured with the right-angle sensors rapidly increase near the wall while those measured with the in-line sensor follow the same behavior as the data by Klebanoff. This is the same trend seen in the v'/U_0 data for the current investigation.

Further resolution problems occur when the size of the transducer is of the same order as the spatial scales of the fluctuations. Since the hot wire output is actually an integration of the effects that occur over the sensitive portion of the sensing element it will not accurately resolve spatial variations that are smaller than the wire dimensions. A single wire anemometer, aligned parallel to the wall, integrates the u component over a spanwise length of the wire. An x -wire anemometer, aligned to measure u and v components, integrates velocity fluctuations over a wire length distance in a direction normal to the wall. Velocity gradients are largest in this direction. The physical dimensions of a x -wire also limit the minimum distance to the wall at which measurements can be made. In order to minimize these errors a very small x -wire is needed or, alternately, measurements in a thick boundary layer must be made. Examples of these two approaches are given by the studies of Willmarth and Sharma (1984), who used small x -wires, and by Eckelmann (1974) who made measurements in a thick boundary layer.

A part of the errors in the x -wire measurements are due to the effects discussed above. Klebanoff used a 3-inch thick boundary layer to obtain the often referenced turbulence data. Even the work of Kassab et al. (1985), which showed the existence of resolution errors, was made in an approximately 2-inch thick boundary layer. The onset boundary layer for the current investigation is 1-inch thick and at $x/\delta=10$, where the boundary layer was thickest, it was only 2-inch thick

(with fine scale structure that was more characteristic of a smaller boundary layer). The x-wire anemometer that was used had active sensor lengths of 0.05-inch. Based on the onset boundary layer this corresponds to wires that are 50 wall units long (lu^*/v), or about one half of a mixing length in dimension for the measurements further out in the boundary layer. While these problems explain the behavior at small wall distances and possibly explain errors at higher frequencies (small scales), there are additional errors that must be considered before a complete error estimate can be made.

Response Equations

The analysis that is presented follows that given by Jorgensen (1971) which was later used by Yavughurt (1984) in establishing a guide to hot wire uncertainty analysis.

The effective cooling velocity of a hot wire element can be expressed as

$$U_e^2 = U_w^2 + K_1^2 \cdot V_w^2 + K_2^2 \cdot W_w^2, \quad (A.1)$$

where the velocity terms U_w , V_w , and W_w are the velocity components expressed in the wire coordinates, shown in figure A.1. K_1 and K_2 are the sensitivities of the wire to flow in the V_w and W_w directions, respectively, and depend on wire geometry. Note the quadratic relationship between the effective cooling velocity and any of the individual velocity components.

Equation (A.1) is more useful when expressed in terms of velocities in a laboratory coordinate system. Using U , V , and W as the laboratory velocities equation (A.1) can be written as,

$$U_e^2 = A \cdot U^2 + B \cdot V^2 + C \cdot W^2 + D \cdot U \cdot V + E \cdot V \cdot W + F \cdot U \cdot W, \quad (A.2)$$

where,

$$A = \cos^2(\phi) + K_1^2 \cdot \sin^2(\phi) \quad (A.3)$$

$$B = (\sin^2(\phi) + K_1^2 \cdot \cos^2(\phi)) \cdot \cos^2(\theta) + K_2^2 \cdot \sin^2(\theta)$$

$$C = (\sin^2(\phi) + K_1^2 \cdot \cos^2(\phi)) \cdot \sin^2(\theta) + K_2^2 \cdot \sin^2(\theta)$$

$$D = (1 - K_1^2) \cdot \sin^2(\phi) \cdot \cos(\theta)$$

$$E = (\sin^2(\phi) + K_1^2 \cdot \cos^2(\phi) - K_2^2) \cdot \sin(\phi) \cdot \sin(\theta)$$

$$F = (1 - K_1^2) \cdot \sin^2(\phi) \cdot \sin(\theta).$$

The angles ϕ and θ are the azimuthal and polar angles, respectively, in spherical coordinates with the wire axis prescribing the polar axis.

With the assumptions,

$$U = U_0 + u'$$

$$V = v'$$

$$W = w'$$

$$\text{and } U_e = U_{em} + u'_e$$

equation (A.2) can be expanded to give

$$U_{em} = A^{-.5} \cdot U_0 + O(2) \quad (A.4)$$

$$u'_e = A^{-.5} \cdot u' + (.5 \cdot D \cdot A^{-.5}) \cdot v' + (.5 \cdot F \cdot A^{-.5}) \cdot w' + [D \cdot^5] \cdot [(u' \cdot v') \cdot^5 + [(5 \cdot D \cdot F / A)^{-.5}] \cdot [(v' \cdot w') \cdot^5] + [F \cdot^5] \cdot [(u' \cdot w') \cdot^5] + O(3) \quad (A.5)$$

where $O(2)$ and $O(3)$ denote terms of order 2 and 3, respectively. These neglected higher order terms constitute an error that is generally small enough to be dropped.

Single wire measurements are made with the wire placed horizontal to the wall, aligned normal to the flow. This orientation gives $\theta=0$, and $\phi=0$, for which equations (A.3) give $A=1$, $B=K_1^2$, $C=K_2^2$, and $D=E=F=0$. With these values equations (A.5) become

$$U_{em} = U_0 + O(2) \quad (A.6)$$

and

$$u'_e = u' + O(2)$$

which shows that the error terms for a horizontal wire are quite low. Yavuzhurt (1984) calculated the errors in the U_{em} and u'_e by estimating the $O(2)$ terms in equations (A.6) using the data from Klebanoff and found that the total errors were less than 1-1.5% (assuming $K_1=0.2$ and $K_2=1.02$).

For x-wire measurements two wires are placed at $A_1=45^\circ$, and $A_2=\pm 90^\circ$. This gives for the two wires

$$A = B = (1+K_1^2)/2 \quad (A.7)$$

$$C = K_2^2$$

$$\pm D = \pm (1-K_1^2)$$

$$E = F = 0$$

Thus for either wire

$$U_e = A^{-.5} \cdot U_0 + O(2) \quad (A.8)$$

and for each wire

$$u_{e_1}' = A \cdot 5 \cdot u' + [.5 \cdot D \cdot A \cdot 5] \cdot v' + 0(2)$$

$$u_{e_2}' = A \cdot 5 \cdot u' - [.5 \cdot D \cdot A \cdot 5] \cdot v' + 0(2)$$

where terms of $0(3)$ and above are neglected.

Estimates of the u and v components of velocity are obtained by summing the subtracting, respectively, the two wire signals. This gives,

$$U_s = U_{e_1} + U_{e_2} = 2 \cdot A \cdot 5 \cdot U_0 \quad (A.9)$$

$$u_{e_s}' = u_{e_1}' + u_{e_2}' = 2 \cdot A \cdot 5 \cdot u'$$

and
$$u_{e_d}' = u_{e_1}' - u_{e_2}' = [D/A \cdot 5] \cdot v' ,$$

therefore,
$$\overline{u'}/U_0 = \overline{u_{e_s}'} / U_s + 0(2) \quad (A.10)$$

$$\overline{v'}/U_0 = [(2 \cdot A/D) \cdot \overline{u_{e_d}'}] / U_s + 0(2)$$

and
$$\overline{u'v'}/U_0^2 = [2 \cdot A/D] \cdot [\overline{u_{e_s}' \cdot u_{e_d}'}] / U_s^2 + 0(3).$$

Equations (A.10) are normally used in obtaining u' , v' , and $\overline{u'v'}$ data from cross wire anemometers. For example, a simple analog sum of the two signals with them first in phase and then with them out of phase will give the u' and v' components as given by equations (A.10).

Deviations From Cosine Cooling

Measurements of u'/U_0 have an error term that is simply the error in the measurement of the sum of the two signals while the errors for measurements of v'/U_0 and $\overline{u'v'}/U_0^2$ have a similar error with along with a term due to the factor $2A/D$. For crossed wire anemometers

$$2A/D = [1 + K_1^2] / [1 - K_1^2]. \quad (A.11)$$

The value of tangential sensitivity K_1 , of a hot wire element is primarily a function of the length-to-diameter ratio of the wire and the angle of the flow relative to the wire. Jorgensen (1971) measured K_1 for different types of wires over a range of inflow angles. For the wire that most closely matches the one used in the current investigation the value of K_1 for an angle of 45° is $K_1=0.3$. This is close to the value reported by others as well. With this value the correction factor in equation (A.11) is

$$2A/D = 1.2$$

which means that the measurements of v'/U_0 and $\overline{u'v'}/U_0^2$ uncorrected for

tangential cooling are 20% too low. Champagne and Sleicher (1967) performed a more detailed analysis of this and derived a slightly different equation for the v'/U_0 term their results give the same approximate value for the error term.

Additional Errors

The above errors arise due to deviation from the cosine law for cooling which is assumed for the wire response function. Additional errors occur due to the effect of the w component of velocity, contributions from higher order terms that were neglected in the derivations of the wire transfer functions (equations (A.8)), and from rectification of the hot wire signal that occurs when the signal crosses zero (which is not a problem for single horizontal wires so long as $u' < U_0$, but is a problem with slanted or x -wires). These errors increase dramatically with the turbulence intensity of the flow. Again, however, the u'/U_0 measurement is least effected by these errors. Tutu and Chevray (1975) estimated the magnitude of the errors that occur from these effects and found that they are not large at low turbulence intensities but become quite large at high levels of turbulence intensity. They quote that errors of 28% in measured correlation ($\overline{u'v'}$) can occur when the turbulence intensity is 35%, and these errors are above those due to deviations from the cosine law for cooling. The errors due to the w component and higher order terms are similar to those calculated by Yavuzkurt (1984).

Sources of Errors in Current Measurements

The errors described above could account for the lower levels of v'/U_0 and $\overline{u'v'}/U_0$ that are measured but do not account for the lower u'/U_0 levels. The errors in u' that result from the x -wire data reduction program were checked by synthesizing x -wire signals using a random (white) noise generator to simulate velocity fluctuations and a dc voltage source for the mean flow. A signal, representing one of the x -wire elements was formed by summing the random and dc voltages, and the other signal was formed by inverting the random noise before summing with the dc voltage. This provided signals representing a flow field with $V=0$ and $\overline{u'v'}=u' \cdot v'$ (correlation coefficient of 1). The

dc voltage was set to a level typical of the output of the linearizer when the wire was in the outer flow region and the ratio of R.M.S. to dc voltage was set to approximately 0.01 to simulate a low turbulence intensity flow ($\approx 1\%$ turbulence intensity). This provided a check of the complete analysis system starting at the A/D's. The computed values of u'/U_0 , v'/U_0 , and $\overline{u'v'}/U_0$ were in error by less than 2%.

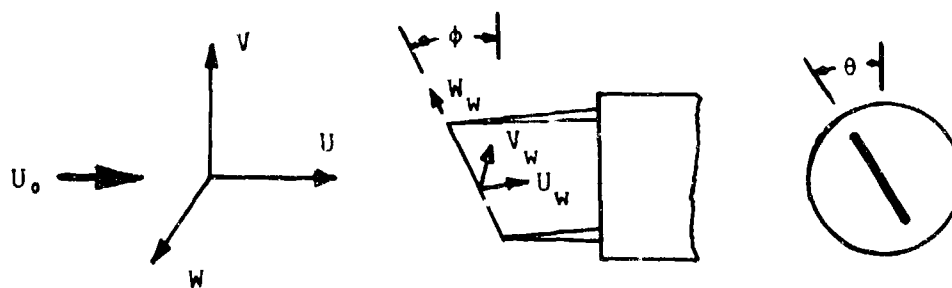
As a further check, the frequency spectra of the u' and v' components were integrated to obtain mean-square values. These values were compared to the values computed by the analysis program. The u' and v' signals that were used for the spectral analysis were formed by an analog sum and subtraction of the x-wire signals (output of linearizers) using a TSI Model 1015C correlator. This system is completely independent of the computer system. The agreement between these two methods of measurement is good. Figure A.2 shows a comparison of turbulence intensity profiles (u'/U_0 and v'/U_0) obtained at $x/h=10$ using both methods. This figure is representative of the results obtained at all locations. The errors that exist in the turbulence measurements must be attributable to a cause unrelated to the computational methods used.

A DISA Model 55P63 x-wire was used for the two component turbulence stress measurements. Cold resistances of 3.70 and 3.38 ohms were measured for wires A and B, respectively. The x-wire was aligned to the flow so that wire A faced upstream at an angle of 45 degrees to the wall and wire B downstream at an angle of 45 degrees. With this orientation a positive V component means flow away from the wall. The wires were operated at an 80% overheat ratio using DISA Model 55M10 bridges. Linearization was obtained using DISA Model 55D10 linearizers. The wires were linearized by positioning the x-wire in the potential flow region of the tunnel, aligned so that each wire was at a 45 degree angle with the mean flow. The bridge voltages that were measured over a range of flow speeds from 82 ft/sec (typical $u/U_0=1.0$) to 25 ft/sec ($u/U_0=0.3$) were found to differ by less than 0.3%.

The calculated exponent for both wires was 2.05. This exponent was used as an initial linearization exponent in each linearizer and then adjusted slightly to obtain a 2:1 linearizer voltage ratio for a 2:1

velocity ratio. A comparison of the performance of the two linearizers was made by injecting known voltages into each linearizer simultaneously and then comparing output voltages. Voltages typical of the bridge voltages were used. The linearizers output amplifiers were adjusted to give the same output voltage at an input voltage equivalent to $u/U_0=1.0$. The linearizer output voltages differed by less than 1% at an input voltage level equivalent to $u/U_0=0.5$ and differed by less than 3% at $u/U_0=0.3$.

These comparisons and checks indicate that the differences between the u'/U_0 measured with the x-wire and the single wire anemometers are primarily due to resolution errors associated with the finite size of the x-wire anemometer. Other unknown errors in misalignment could also possibly be present such as an undetected angle variation of the hot wire with the mean flow as the hot wire was traversed to the wall and back out.



Laboratory Coordinate System

Wire Coordinate System

Figure A.1 Hot Wire Geometry and Velocity Components

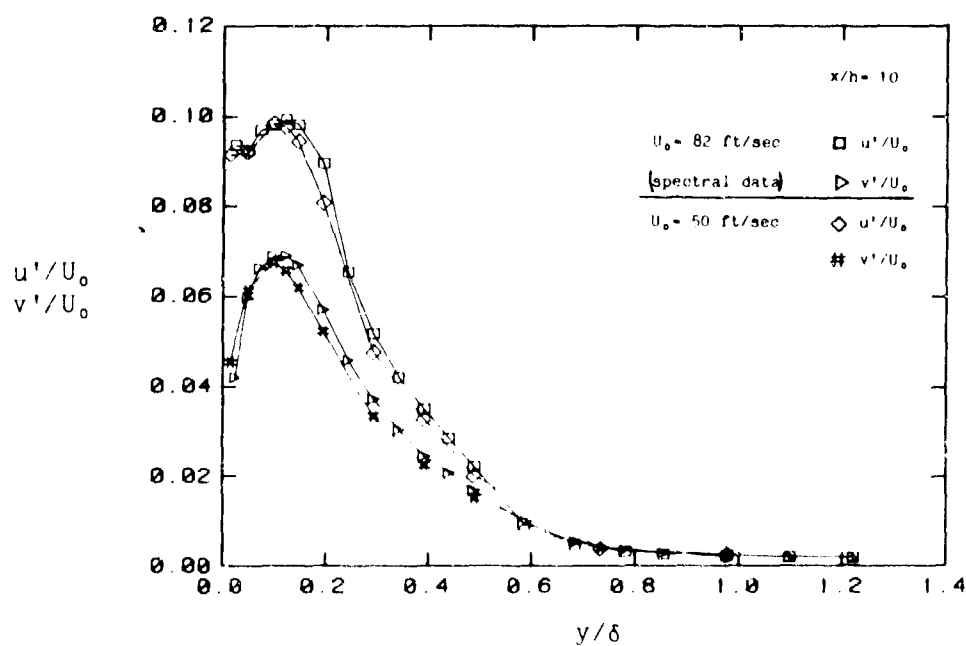


Figure A.2 Comparison of Turbulence Intensities from Integrated Velocity Spectra to Results from Hot Wire Analysis Program

APPENDIX B

TABULATED PROFILE DATA

Single Wire

&

X-Wire

Equilibrium Flow
U₀=50.9 (ft/sec)

$\delta = 1.097\text{-inch} \parallel \delta' = 0.177\text{-inch} \parallel \theta = 0.128\text{-inch} \parallel H=1.38$
 $U^*/U_0=0.040 \parallel C_F=3.255 \times 10^{-3} \parallel C_{FM}=3.229 \times 10^{-3} \parallel G=6.828$

$y(\text{inch})$	y/δ	U/U_0	U^*/U_0	C_F	C_{FM}	G
0.000	0.000	0.000	0.000	0.000	0.000	0.000
0.003	0.003	0.122	0.030	0.037	0.037	0.037
0.004	0.004	0.164	0.071	0.053	0.053	0.053
0.005	0.005	0.210	0.106	0.066	0.066	0.066
0.006	0.006	0.262	0.141	0.085	0.085	0.085
0.007	0.007	0.308	0.164	0.091	0.091	0.091
0.008	0.008	0.357	0.195	0.099	0.099	0.099
0.009	0.009	0.399	0.227	0.092	0.092	0.092
0.010	0.010	0.456	0.258	0.098	0.098	0.098
0.012	0.012	0.495	0.285	0.095	0.095	0.095
0.013	0.013	0.536	0.303	0.089	0.089	0.089
0.014	0.014	0.568	0.320	0.086	0.086	0.086
0.015	0.015	0.589	0.339	0.082	0.082	0.082
0.016	0.016	0.605	0.357	0.079	0.079	0.079
0.017	0.017	0.624	0.375	0.076	0.076	0.076
0.018	0.018	0.635	0.392	0.078	0.078	0.078
0.019	0.019	0.642	0.408	0.078	0.078	0.078
0.020	0.020	0.651	0.424	0.076	0.076	0.076
0.022	0.022	0.672	0.456	0.074	0.074	0.074
0.024	0.024	0.692	0.487	0.072	0.072	0.072
0.026	0.026	0.706	0.516	0.069	0.069	0.069
0.028	0.028	0.724	0.544	0.068	0.068	0.068
0.030	0.030	0.744	0.571	0.064	0.064	0.064
0.032	0.032	0.766	0.598	0.058	0.058	0.058
0.034	0.034	0.788	0.624	0.053	0.053	0.053
0.036	0.036	0.812	0.649	0.047	0.047	0.047
0.038	0.038	0.837	0.674	0.042	0.042	0.042
0.040	0.040	0.862	0.699	0.035	0.035	0.035
0.042	0.042	0.888	0.724	0.027	0.027	0.027
0.044	0.044	0.912	0.749	0.020	0.020	0.020
0.046	0.046	0.937	0.774	0.010	0.010	0.010
0.048	0.048	0.962	0.799	0.002	0.002	0.002
0.050	0.050	0.988	0.824	0.004	0.004	0.004
0.052	0.052	1.000	0.849	0.002	0.002	0.002
0.054	0.054	1.000	0.874	0.002	0.002	0.002
0.056	0.056	1.000	0.899	0.002	0.002	0.002
0.058	0.058	1.000	0.924	0.002	0.002	0.002
0.060	0.060	1.000	0.949	0.002	0.002	0.002
0.062	0.062	1.000	0.974	0.002	0.002	0.002
0.064	0.064	1.000	0.999	0.002	0.002	0.002
0.066	0.066	1.000	1.000	0.002	0.002	0.002
0.068	0.068	1.000	1.000	0.002	0.002	0.002
0.070	0.070	1.000	1.000	0.002	0.002	0.002
0.072	0.072	1.000	1.000	0.002	0.002	0.002
0.074	0.074	1.000	1.000	0.002	0.002	0.002
0.076	0.076	1.000	1.000	0.002	0.002	0.002
0.078	0.078	1.000	1.000	0.002	0.002	0.002
0.080	0.080	1.000	1.000	0.002	0.002	0.002
0.082	0.082	1.000	1.000	0.002	0.002	0.002
0.084	0.084	1.000	1.000	0.002	0.002	0.002
0.086	0.086	1.000	1.000	0.002	0.002	0.002
0.088	0.088	1.000	1.000	0.002	0.002	0.002
0.090	0.090	1.000	1.000	0.002	0.002	0.002
0.092	0.092	1.000	1.000	0.002	0.002	0.002
0.094	0.094	1.000	1.000	0.002	0.002	0.002
0.096	0.096	1.000	1.000	0.002	0.002	0.002
0.098	0.098	1.000	1.000	0.002	0.002	0.002
0.100	0.100	1.000	1.000	0.002	0.002	0.002
0.102	0.102	1.000	1.000	0.002	0.002	0.002
0.104	0.104	1.000	1.000	0.002	0.002	0.002
0.106	0.106	1.000	1.000	0.002	0.002	0.002
0.108	0.108	1.000	1.000	0.002	0.002	0.002
0.110	0.110	1.000	1.000	0.002	0.002	0.002
0.112	0.112	1.000	1.000	0.002	0.002	0.002
0.114	0.114	1.000	1.000	0.002	0.002	0.002
0.116	0.116	1.000	1.000	0.002	0.002	0.002
0.118	0.118	1.000	1.000	0.002	0.002	0.002
0.120	0.120	1.000	1.000	0.002	0.002	0.002
0.122	0.122	1.000	1.000	0.002	0.002	0.002
0.124	0.124	1.000	1.000	0.002	0.002	0.002
0.126	0.126	1.000	1.000	0.002	0.002	0.002
0.128	0.128	1.000	1.000	0.002	0.002	0.002
0.130	0.130	1.000	1.000	0.002	0.002	0.002
0.132	0.132	1.000	1.000	0.002	0.002	0.002
0.134	0.134	1.000	1.000	0.002	0.002	0.002
0.136	0.136	1.000	1.000	0.002	0.002	0.002
0.138	0.138	1.000	1.000	0.002	0.002	0.002
0.140	0.140	1.000	1.000	0.002	0.002	0.002
0.142	0.142	1.000	1.000	0.002	0.002	0.002
0.144	0.144	1.000	1.000	0.002	0.002	0.002
0.146	0.146	1.000	1.000	0.002	0.002	0.002
0.148	0.148	1.000	1.000	0.002	0.002	0.002
0.150	0.150	1.000	1.000	0.002	0.002	0.002
0.152	0.152	1.000	1.000	0.002	0.002	0.002
0.154	0.154	1.000	1.000	0.002	0.002	0.002
0.156	0.156	1.000	1.000	0.002	0.002	0.002
0.158	0.158	1.000	1.000	0.002	0.002	0.002
0.160	0.160	1.000	1.000	0.002	0.002	0.002
0.162	0.162	1.000	1.000	0.002	0.002	0.002
0.164	0.164	1.000	1.000	0.002	0.002	0.002
0.166	0.166	1.000	1.000	0.002	0.002	0.002
0.168	0.168	1.000	1.000	0.002	0.002	0.002
0.170	0.170	1.000	1.000	0.002	0.002	0.002
0.172	0.172	1.000	1.000	0.002	0.002	0.002
0.174	0.174	1.000	1.000	0.002	0.002	0.002
0.176	0.176	1.000	1.000	0.002	0.002	0.002
0.178	0.178	1.000	1.000	0.002	0.002	0.002
0.180	0.180	1.000	1.000	0.002	0.002	0.002
0.182	0.182	1.000	1.000	0.002	0.002	0.002
0.184	0.184	1.000	1.000	0.002	0.002	0.002
0.186	0.186	1.000	1.000	0.002	0.002	0.002
0.188	0.188	1.000	1.000	0.002	0.002	0.002
0.190	0.190	1.000	1.000	0.002	0.002	0.002
0.192	0.192	1.000	1.000	0.002	0.002	0.002
0.194	0.194	1.000	1.000	0.002	0.002	0.002
0.196	0.196	1.000	1.000	0.002	0.002	0.002
0.198	0.198	1.000	1.000	0.002	0.002	0.002
0.200	0.200	1.000	1.000	0.002	0.002	0.002

Equilibrium Flow
U₀=93.3 (ft/sec)

$\delta = 1.095\text{-inch} \parallel \delta' = 0.169\text{-inch} \parallel \theta = 0.124\text{-inch} \parallel H=1.36$
 $U^*/U_0=0.038 \parallel C_F=2.867 \times 10^{-3} \parallel C_{FM}=2.871 \times 10^{-3} \parallel G=6.936$

$y(\text{inch})$	y/δ	U/U_0	U^*/U_0	C_F	C_{FM}	G
0.000	0.000	0.000	0.000	0.000	0.000	0.000
0.003	0.003	0.167	0.040	0.043	0.043	0.043
0.004	0.004	0.229	0.056	0.047	0.047	0.047
0.005	0.005	0.286	0.073	0.050	0.050	0.050
0.006	0.006	0.336	0.090	0.052	0.052	0.052
0.007	0.007	0.387	0.107	0.054	0.054	0.054
0.008	0.008	0.409	0.124	0.055	0.055	0.055
0.009	0.009	0.427	0.141	0.056	0.056	0.056
0.010	0.010	0.447	0.158	0.057	0.057	0.057
0.012	0.012	0.497	0.185	0.058	0.058	0.058
0.013	0.013	0.529	0.202	0.059	0.059	0.059
0.014	0.014	0.559	0.219	0.060	0.060	0.060
0.015	0.015	0.579	0.236	0.061	0.061	0.061
0.016	0.016	0.599	0.253	0.062	0.062	0.062
0.017	0.017	0.617	0.270	0.063	0.063	0.063
0.018	0.018	0.630	0.287	0.064	0.064	0.064
0.019	0.019	0.642	0.304	0.065	0.065	0.065
0.020	0.020	0.656	0.321	0.066	0.066	0.066
0.022	0.022	0.682	0.357	0.067	0.067	0.067
0.024	0.024	0.707	0.393	0.068	0.068	0.068
0.026	0.026	0.735	0.429	0.069	0.069	0.069
0.028	0.028	0.761	0.465	0.070	0.070	0.070
0.030	0.030	0.787	0.501	0.071	0.071	0.071
0.032	0.032	0.812	0.537	0.072	0.072	0.072
0.034	0.034	0.837	0.573	0.073	0.073	0.073
0.036	0.036	0.862	0.609	0.074	0.074	0.074
0.038	0.038	0.888	0.645	0.075	0.075	0.075
0.040	0.040	0.912	0.681	0.076	0.076	0.076
0.042	0.042	0.937	0.717	0.077	0.077	0.077
0.044	0.044	0.962	0.753	0.078	0.078	0.078
0.046	0.046	0.988	0.789	0.079	0.079	0.079
0.048	0.048	1.000	0.825	0.080	0.080	0.080
0.050	0.050	1.000	0.861	0.081	0.081	0.081
0.052	0.052	1.000	0.897	0.082	0.082	0.082
0.054	0.054	1.000	0.933	0.083	0.083	0.083
0.056	0.056	1.000	0.969	0.084	0.084	0.084
0.058	0.058	1.000	1.005	0.085	0.085	0.085
0.060	0.060	1.000	1.041	0.086	0.086	0.086
0.062	0.062	1.000	1.077	0.087	0.087	0.087
0.064	0.064	1.000	1.113	0.088	0.088	0.088
0.066	0.066	1.000	1.149	0.089	0.089	0.089
0.068	0.068	1.000	1.185	0.090	0.090	0.090
0.070	0.070	1.000	1.221	0.091	0.091	0.091
0.072	0.072	1.000	1.257	0.092	0.092	0.092
0.074	0.074	1.000	1.293	0.093	0.093	0.093
0.076	0.076	1.000	1.329	0.094	0.094	0.094
0.078	0.078	1.000	1.365	0.095	0.095	0.095
0.080	0.080	1.000	1.401	0.096	0.096	0.096

$x/h=12$
 $U_0=50.5$ (ft/sec)

$\delta=0.874$ -inch || $\delta^* = 0.130$ -inch || $\theta = 0.097$ -inch || $H=1.34$
 $u/U_0=0.043$ || $C_F=3.778 \times 10^{-3}$ || $C_{FM}=3.712 \times 10^{-3}$ || $G=5.838$

y (inch)	y/δ	U/U_0	U/U_0^*	yU/U_0	U^2/U_0^2
0.000	0.000	0.000	0.000	0.00	0.000
0.003	0.003	0.140	3.224	3.42	0.047
0.005	0.006	0.279	5.049	5.70	0.072
0.007	0.008	0.286	5.597	7.98	0.085
0.010	0.011	0.369	8.484	11.40	0.096
0.015	0.017	0.411	10.831	17.10	0.100
0.020	0.022	0.527	12.129	22.80	0.093
0.030	0.034	0.579	13.325	34.20	0.087
0.040	0.045	0.618	14.224	45.51	0.081
0.050	0.057	0.639	14.702	57.01	0.076
0.070	0.080	0.677	15.566	79.81	0.073
0.080	0.091	0.691	15.896	91.21	0.073
0.090	0.103	0.704	16.206	102.61	0.072
0.100	0.114	0.716	16.481	114.02	0.071
0.150	0.171	0.755	17.439	171.02	0.067
0.200	0.229	0.793	18.236	228.03	0.063
0.300	0.343	0.843	19.399	342.05	0.057
0.400	0.457	0.883	20.314	456.06	0.051
0.500	0.572	0.915	21.050	570.08	0.046
0.600	0.686	0.943	21.703	684.09	0.043
0.700	0.800	0.965	22.273	798.11	0.040
0.800	0.915	0.981	22.590	912.12	0.030
0.900	1.029	0.993	22.827	1026.14	0.012
1.000	1.143	0.997	22.940	1140.15	0.007
1.500	1.715	0.997	22.945	1710.23	0.003
2.000	2.286	0.996	22.909	2280.30	0.003
3.000	3.430	0.991	22.975	3420.45	0.003

$x/h=12$
 $U_0=81.5$ (ft/sec)

$\delta=0.918$ -inch || $\delta^* = 0.132$ -inch || $\theta = 0.101$ -inch || $H=1.31$
 $u/U_0=0.041$ || $C_F=3.378 \times 10^{-3}$ || $C_{FM}=3.377 \times 10^{-3}$ || $G=5.776$

y (inch)	y/δ	U/U_0	U/U_0^*	yU/U_0	U^2/U_0^2
0.000	0.000	0.000	0.000	0.00	0.000
0.002	0.002	0.139	3.390	3.84	0.041
0.004	0.004	0.284	5.683	7.33	0.068
0.006	0.007	0.324	7.872	10.81	0.080
0.008	0.009	0.393	9.568	14.30	0.082
0.009	0.010	0.413	10.061	16.05	0.084
0.010	0.011	0.441	10.734	17.79	0.084
0.013	0.014	0.490	11.933	23.02	0.081
0.018	0.020	0.541	13.170	31.74	0.077
0.023	0.025	0.573	13.944	40.47	0.074
0.033	0.036	0.611	14.871	57.91	0.071
0.043	0.047	0.632	15.379	75.35	0.069
0.053	0.058	0.654	15.917	92.79	0.069
0.063	0.069	0.674	16.412	110.23	0.067
0.073	0.080	0.686	16.702	127.69	0.066
0.083	0.091	0.698	16.904	145.12	0.066
0.093	0.102	0.710	17.288	162.56	0.065
0.103	0.112	0.722	17.557	180.00	0.065
0.128	0.140	0.746	18.154	223.61	0.064
0.153	0.167	0.763	18.560	267.21	0.062
0.203	0.221	0.792	19.272	354.42	0.059
0.303	0.330	0.837	20.373	528.85	0.054
0.403	0.439	0.875	21.294	703.27	0.048
0.503	0.548	0.909	22.114	877.62	0.042
0.603	0.657	0.938	22.820	1052.11	0.036
0.703	0.766	0.960	23.366	1226.52	0.029
0.803	0.875	0.978	23.808	1400.95	0.019
0.903	0.984	0.989	24.063	1575.37	0.011
1.003	1.093	0.995	24.214	1749.79	0.007
1.503	1.637	0.994	24.179	2621.90	0.003
2.003	2.182	0.997	24.255	3494.01	0.002
3.003	3.271	1.002	24.380	5238.22	0.002

$x/h = 10$
 $U_0 = 50.4$ (ft/sec)

$\delta = 1.804$ -inch || $\delta^* = 0.269$ -inch || $\theta = 0.176$ -inch || $H = 1.53$

$u/U_0 = 0.033$ || $C_f = 2.167 \times 10^{-3}$ || $C_{fm} = 2.370 \times 10^{-3}$ || $G = 10.461$

y (inch)	y/δ	u/U_0	u^*/U_0	yu^*/v	u^2/U_0
0.000	0.000	0.000	0.000	0.00	0.000
0.003	0.002	0.035	2.597	2.59	0.027
0.006	0.003	0.148	4.506	5.13	0.058
0.011	0.006	0.273	8.290	9.50	0.091
0.016	0.009	0.338	10.268	13.81	0.096
0.021	0.012	0.383	11.624	18.13	0.100
0.026	0.014	0.404	12.270	22.45	0.097
0.036	0.020	0.444	13.494	31.08	0.097
0.046	0.026	0.462	14.028	39.72	0.097
0.066	0.037	0.461	14.625	56.99	0.095
0.086	0.048	0.499	15.167	74.25	0.099
0.106	0.059	0.511	15.515	91.52	0.103
0.131	0.073	0.531	16.132	113.11	0.104
0.156	0.086	0.544	16.581	134.69	0.106
0.206	0.114	0.578	17.556	177.87	0.114
0.256	0.142	0.618	18.774	221.04	0.117
0.306	0.170	0.663	20.130	264.21	0.115
0.406	0.225	0.734	22.310	350.55	0.107
0.506	0.280	0.804	24.425	436.89	0.085
0.606	0.336	0.858	26.075	523.23	0.059
0.706	0.391	0.891	27.253	609.58	0.051
0.806	0.447	0.917	27.865	695.92	0.041
0.906	0.502	0.943	28.655	782.26	0.034
1.006	0.558	0.962	29.239	868.60	0.026
1.256	0.696	0.982	29.834	1084.46	0.010
1.506	0.835	0.986	29.948	1300.31	0.005
1.756	0.973	0.990	30.066	1516.17	0.004
2.006	1.112	0.991	30.119	1732.03	0.004
3.006	1.666	0.999	30.349	2595.45	0.004

$x/h = 10$
 $U_0 = 82.0$ (ft/sec)

$\delta = 2.048$ -inch || $\delta^* = 0.261$ -inch || $\theta = 0.179$ -inch || $H = 1.47$

$u/U_0 = 0.032$ || $C_f = 2.109 \times 10^{-3}$ || $C_{fm} = 2.253 \times 10^{-3}$ || $G = 9.880$

y (inch)	y/δ	u/U_0	u^*/U_0	yu^*/v	u^2/U_0
0.000	0.000	0.000	0.000	0.00	0.000
0.005	0.002	0.204	6.279	6.34	0.081
0.007	0.003	0.259	7.965	9.71	0.087
0.012	0.006	0.367	11.297	16.65	0.095
0.017	0.008	0.404	12.446	23.59	0.094
0.022	0.011	0.433	13.340	30.53	0.094
0.027	0.013	0.448	13.800	37.47	0.093
0.037	0.018	0.471	14.498	51.35	0.092
0.047	0.023	0.485	14.939	65.22	0.092
0.067	0.033	0.505	15.546	92.98	0.093
0.087	0.042	0.523	16.093	120.73	0.096
0.107	0.052	0.536	16.519	148.49	0.098
0.132	0.064	0.550	16.923	183.18	0.102
0.157	0.077	0.570	17.554	217.86	0.105
0.207	0.101	0.600	18.481	287.26	0.109
0.257	0.125	0.632	19.450	356.65	0.113
0.307	0.150	0.674	20.760	426.04	0.110
0.407	0.199	0.749	23.058	564.81	0.102
0.507	0.248	0.814	25.076	703.59	0.079
0.607	0.296	0.861	26.517	842.36	0.056
0.707	0.345	0.897	27.611	981.14	0.045
0.807	0.394	0.921	28.348	1119.91	0.038
0.907	0.443	0.942	29.022	1258.69	0.031
1.007	0.492	0.959	29.525	1397.46	0.025
1.257	0.614	0.980	30.193	1744.40	0.008
1.507	0.736	0.985	30.334	2091.34	0.004
1.757	0.858	0.986	30.364	2438.28	0.003
2.007	0.980	0.990	30.500	2785.22	0.003
3.007	1.468	0.997	30.707	4172.97	0.002

x/h = 16
U_∞ = 50.6 (ft/sec)

δ = 1.131-inch || δ' = 0.219-inch || θ = 0.150-inch || H = 1.46
u/U_∞ = 0.038 || C_f = 2.909 × 10⁻³ || C_{fm} = 2.756 × 10⁻³ || G = 5.203

y (inch)	y/δ	u/U _∞	u'/U _∞	yv/u	u'/U _∞
0.000	0.000	0.000	0.000	0.00	0.000
0.002	0.002	0.081	2.128	2.01	0.019
0.003	0.003	0.089	2.330	3.01	0.031
0.005	0.004	0.143	3.758	5.02	0.056
0.008	0.007	0.248	6.499	8.03	0.088
0.018	0.016	0.436	13.434	18.08	0.099
0.038	0.034	0.532	13.958	38.16	0.092
0.058	0.051	0.569	14.913	58.24	0.088
0.078	0.069	0.590	15.473	78.33	0.089
0.098	0.087	0.606	15.879	98.41	0.086
0.148	0.131	0.637	16.714	148.62	0.090
0.198	0.175	0.661	17.319	198.83	0.091
0.248	0.219	0.680	17.840	249.04	0.095
0.293	0.263	0.703	18.423	299.25	0.097
0.348	0.308	0.730	19.135	349.46	0.097
0.398	0.352	0.755	19.798	399.67	0.097
0.498	0.440	0.803	21.062	500.09	0.090
0.598	0.529	0.852	22.351	600.50	0.076
0.698	0.617	0.892	23.393	700.92	0.062
0.798	0.705	0.927	24.315	801.34	0.050
0.898	0.794	0.961	25.198	901.76	0.038
0.998	0.882	0.971	25.463	1002.18	0.031
1.098	0.971	0.984	25.601	1102.60	0.022
1.123	0.993	0.989	25.943	1127.70	0.019
1.498	1.324	1.001	26.255	1504.27	0.006

x/h = 16
U_∞ = 82.2 (ft/sec)

δ = 1.015-inch || δ' = 0.191-inch || θ = 0.135-inch || H = 1.41
u/U_∞ = 0.038 || C_f = 2.914 × 10⁻³ || C_{fm} = 2.677 × 10⁻³ || G = 7.591

y (inch)	y/δ	u/U _∞	u'/U _∞	yv/u	u'/U _∞
0.000	0.000	0.000	0.000	0.00	0.000
0.001	0.001	0.124	3.248	2.45	0.046
0.002	0.002	0.145	3.799	4.08	0.062
0.005	0.004	0.226	5.920	7.35	0.092
0.006	0.006	0.305	8.000	10.62	0.097
0.010	0.009	0.392	10.259	15.52	0.096
0.014	0.014	0.461	12.068	23.69	0.093
0.019	0.015	0.507	13.275	31.85	0.091
0.030	0.029	0.556	14.571	48.19	0.086
0.039	0.039	0.578	15.139	64.53	0.084
0.049	0.049	0.597	15.531	80.86	0.085
0.060	0.059	0.605	15.837	97.20	0.084
0.080	0.078	0.625	16.371	129.87	0.085
0.090	0.088	0.636	16.654	146.20	0.084
0.099	0.098	0.643	16.853	162.54	0.086
0.149	0.147	0.671	17.574	244.22	0.087
0.200	0.196	0.687	18.009	325.90	0.088
0.300	0.295	0.732	19.189	489.25	0.093
0.399	0.393	0.779	20.420	652.61	0.093
0.500	0.492	0.827	21.662	815.96	0.087
0.599	0.590	0.875	22.931	979.32	0.074
0.699	0.689	0.918	24.051	1142.68	0.061
0.800	0.787	0.949	24.956	1306.03	0.047
0.900	0.886	0.964	25.375	1469.39	0.037
1.000	0.984	0.989	25.913	1632.75	0.027
1.500	1.477	1.006	26.352	2449.53	0.005

$x/h = 24$
 $U_0 = 50.2$ (ft/sec)

$\delta = 1.275$ -inch || $\delta' = 0.219$ -inch || $\theta = 0.157$ -inch || $H = 1.40$
 $u^*/U_0 = 0.040$ || $C_F = 3.168 \times 10^{-3}$ || $C_{FM} = 2.997 \times 10^{-3}$ || $C = 7.120$

y (inch)	y/δ	u/U_0	u^*/U_0	yu^*/ν	u^*/U_0
0.000	0.000	0.000	0.000	0.00	0.000
0.016	0.013	0.395	9.922	16.65	0.100
0.036	0.028	0.548	13.759	37.46	0.093
0.056	0.044	0.591	14.952	56.27	0.084
0.076	0.060	0.620	15.568	79.07	0.082
0.096	0.075	0.639	16.060	99.88	0.079
0.121	0.095	0.655	16.467	125.89	0.079
0.146	0.115	0.676	16.995	151.91	0.080
0.196	0.154	0.702	17.635	203.93	0.079
0.296	0.232	0.733	18.415	307.97	0.081
0.396	0.311	0.769	19.327	412.02	0.082
0.496	0.389	0.806	20.261	516.06	0.082
0.596	0.468	0.844	21.201	620.11	0.076
0.696	0.546	0.886	22.266	724.16	0.068
0.796	0.624	0.917	23.035	828.20	0.060
0.896	0.703	0.944	23.714	932.25	0.050
0.996	0.781	0.970	24.379	1036.29	0.034
1.096	0.860	0.982	24.668	1140.34	0.024
1.240	0.977	0.990	24.862	1296.40	0.014
1.496	1.174	0.993	24.950	1556.52	0.007
1.996	1.566	0.994	24.980	2076.74	0.004
2.996	2.350	1.000	25.136	3117.20	0.004

$x/h = 24$
 $U_0 = 81.4$ (ft/sec)

$\delta = 1.199$ -inch || $\delta' = 0.208$ -inch || $\theta = 0.155$ -inch || $H = 1.34$
 $u^*/U_0 = 0.039$ || $C_F = 3.031 \times 10^{-3}$ || $C_{FM} = 2.879 \times 10^{-3}$ || $C = 6.521$

y (inch)	y/δ	u/U_0	u^*/U_0	yu^*/ν	u^*/U_0
0.000	0.000	0.000	0.000	0.00	0.000
0.003	0.003	0.180	4.614	4.95	0.074
0.005	0.004	0.253	6.489	8.25	0.100
0.008	0.007	0.345	8.865	13.21	0.098
0.010	0.015	0.507	13.035	29.71	0.086
0.038	0.032	0.593	15.221	62.73	0.078
0.058	0.048	0.627	16.110	95.75	0.079
0.078	0.065	0.648	16.637	128.76	0.077
0.098	0.082	0.666	17.099	161.78	0.076
0.123	0.103	0.683	17.538	203.05	0.075
0.148	0.123	0.698	17.926	244.32	0.077
0.198	0.165	0.719	18.461	326.86	0.075
0.298	0.248	0.754	19.370	491.93	0.077
0.398	0.332	0.783	20.107	657.01	0.078
0.498	0.415	0.818	21.017	822.09	0.077
0.598	0.499	0.855	21.959	987.17	0.074
0.698	0.582	0.889	22.828	1152.25	0.068
0.798	0.665	0.918	23.588	1317.33	0.061
0.898	0.749	0.947	24.328	1482.40	0.048
0.998	0.832	0.970	24.919	1647.48	0.034
1.098	0.916	0.983	25.255	1812.56	0.023
1.248	1.041	0.993	25.502	2060.18	0.013
1.498	1.249	0.994	25.525	2472.87	0.006
1.998	1.666	0.993	25.500	3298.27	0.003
2.998	2.500	0.997	25.613	4949.05	0.003

$x/h = .36$ $U_0 = 81.7 \text{ (ft/sec)}$ $\delta = 1.389\text{-inch} \parallel \delta^+ = 0.213\text{-inch} \parallel \theta = 0.161\text{-inch} \parallel H = 1.33$ $u^+ / U_0 = 0.039 \parallel C_f = 3.033 \times 10^{-3} \parallel C_{fm} = 2.904 \times 10^{-3} \parallel G = 6.338$									
$y \text{ (inch)}$	y/δ	U/U_0	U/u^+	U/u^+	yu^+ / ν	u^+ / U_0			
0.000	0.000	0.000	0.000	0.000	0.00	0.000			0.000
0.002	0.001	0.127	3.258		3.32	0.043			0.043
0.007	0.005	0.296	7.613		11.60	0.097			0.097
0.012	0.009	0.421	10.817		19.89	0.092			0.092
0.017	0.012	0.492	12.637		28.18	0.087			0.087
0.022	0.016	0.525	13.471		36.47	0.084			0.084
0.032	0.023	0.573	14.710		53.04	0.078			0.078
0.042	0.030	0.597	15.334		69.62	0.074			0.074
0.062	0.045	0.628	16.126		102.77	0.076			0.076
0.082	0.059	0.654	16.783		135.92	0.075			0.075
0.102	0.073	0.677	17.378		169.07	0.073			0.073
0.127	0.091	0.691	17.750		210.51	0.073			0.073
0.152	0.109	0.710	18.230		251.95	0.073			0.073
0.202	0.145	0.724	18.591		334.83	0.070			0.070
0.252	0.181	0.746	19.160		417.71	0.070			0.070
0.302	0.217	0.761	19.539		500.59	0.069			0.069
0.352	0.253	0.780	20.022		583.47	0.068			0.068
0.402	0.289	0.793	20.373		666.35	0.069			0.069
0.502	0.361	0.819	21.036		832.10	0.068			0.068
0.602	0.433	0.844	21.673		997.86	0.067			0.067
0.702	0.505	0.874	22.454		1163.62	0.066			0.066
0.802	0.578	0.902	23.166		1329.38	0.061			0.061
0.902	0.650	0.929	23.865		1495.13	0.053			0.053
1.002	0.722	0.954	24.488		1660.89	0.046			0.046
1.102	0.794	0.966	24.808		1826.65	0.035			0.035
1.252	0.902	0.983	25.237		2075.29	0.023			0.023
1.502	1.082	0.995	25.546		2489.68	0.010			0.010
2.002	1.442	0.995	25.563		3318.47	0.005			0.005
3.002	2.162	0.999	25.565		4976.05	0.003			0.003

$x/h = .36$ $U_0 = 50.4 \text{ (ft/sec)}$ $\delta = 1.293\text{-inch} \parallel \delta^+ = 0.216\text{-inch} \parallel \theta = 0.150\text{-inch} \parallel H = 1.36$ $u^+ / U_0 = 0.040 \parallel C_f = 3.271 \times 10^{-3} \parallel C_{fm} = 3.165 \times 10^{-3} \parallel G = 6.502$									
$y \text{ (inch)}$	y/δ	U/U_0	U/u^+	U/u^+	yu^+ / ν	u^+ / U_0			
0.000	0.000	0.000	0.000	0.00	0.00	0.000			0.000
0.002	0.002	0.080	1.981		2.12	0.016			0.016
0.007	0.005	0.203	5.024		7.43	0.076			0.076
0.012	0.009	0.343	8.490		12.73	0.101			0.101
0.017	0.013	0.432	10.689		18.04	0.100			0.100
0.022	0.017	0.486	12.025		23.35	0.099			0.099
0.032	0.025	0.536	13.250		33.96	0.092			0.092
0.042	0.032	0.574	14.203		44.57	0.087			0.087
0.062	0.048	0.616	15.241		65.80	0.081			0.081
0.082	0.063	0.638	15.777		87.02	0.078			0.078
0.102	0.079	0.658	16.270		108.24	0.078			0.078
0.127	0.098	0.682	16.865		134.77	0.079			0.079
0.152	0.118	0.696	17.216		161.30	0.078			0.078
0.202	0.156	0.722	17.844		214.37	0.075			0.075
0.252	0.195	0.739	18.267		267.43	0.074			0.074
0.302	0.234	0.757	18.727		320.49	0.073			0.073
0.352	0.272	0.772	19.082		373.55	0.073			0.073
0.402	0.311	0.790	19.539		426.61	0.073			0.073
0.502	0.388	0.814	20.126		532.73	0.073			0.073
0.602	0.466	0.847	20.946		638.85	0.072			0.072
0.702	0.543	0.877	21.680		744.97	0.069			0.069
0.802	0.620	0.903	22.326		851.09	0.065			0.065
0.902	0.698	0.931	23.028		957.22	0.058			0.058
1.002	0.775	0.955	23.619		1063.34	0.047			0.047
1.102	0.852	0.969	23.965		1169.46	0.038			0.038
1.252	0.969	0.989	24.445		1328.64	0.022			0.022
1.502	1.162	0.996	24.620		1593.95	0.012			0.012
2.002	1.549	0.995	24.609		2124.55	0.007			0.007
3.002	2.322	0.999	24.696		3185.77	0.006			0.006

$x/h = 54$
 $U_0 = 82.1 \text{ (ft/sec)}$
 $\delta = 0.206\text{-inch} \parallel \theta = 0.160\text{-inch} \parallel H = 1.28$
 $u/U_0 = 0.041 \parallel C_p = 3.289 \times 10^{-3} \parallel C_{fm} = 3.110 \times 10^{-3} \parallel G = 5.447$

y (inch)	y/δ	U/U ₀	U/u	u/u	y ⁺ /y	u'/U ₀
0.000	0.000	0.000	0.000	0.000	0.00	0.000
0.002	0.002	0.176	4.348	4.33	4.33	0.051
0.005	0.003	0.268	6.611	7.80	7.80	0.078
0.006	0.004	0.364	8.971	11.27	11.27	0.087
0.010	0.006	0.454	11.197	16.47	16.47	0.087
0.015	0.009	0.516	12.716	25.14	25.14	0.085
0.019	0.013	0.546	13.469	33.80	33.80	0.082
0.030	0.019	0.587	14.461	51.14	51.14	0.078
0.039	0.026	0.617	15.225	68.48	68.48	0.075
0.049	0.032	0.641	15.795	85.81	85.81	0.075
0.074	0.038	0.672	16.574	129.15	129.15	0.074
0.099	0.065	0.699	17.248	172.49	172.49	0.073
0.149	0.097	0.728	17.945	259.17	259.17	0.070
0.200	0.130	0.752	18.539	345.85	345.85	0.068
0.249	0.162	0.769	18.966	432.53	432.53	0.066
0.300	0.195	0.786	19.383	519.21	519.21	0.064
0.400	0.260	0.812	20.032	692.57	692.57	0.063
0.500	0.325	0.836	20.626	865.92	865.92	0.063
0.600	0.390	0.861	21.224	1039.28	1039.28	0.061
0.700	0.455	0.878	21.642	1212.64	1212.64	0.060
0.800	0.520	0.899	22.156	1386.00	1386.00	0.056
0.900	0.586	0.914	22.538	1559.36	1559.36	0.054
1.249	0.651	0.938	23.126	1732.71	1732.71	0.049
1.499	0.813	0.971	23.941	2166.11	2166.11	0.036
1.999	0.976	0.989	24.394	2599.51	2599.51	0.019
3.000	1.302	0.997	24.592	3466.30	3466.30	0.006
	1.953	0.999	24.637	5199.88	5199.88	0.003

$x/h = 54$
 $U_0 = 50.5 \text{ (ft/sec)}$
 $\delta = 0.225\text{-inch} \parallel \theta = 0.171\text{-inch} \parallel H = 1.31$
 $u/U_0 = 0.042 \parallel C_p = 3.449 \times 10^{-3} \parallel C_{fm} = 3.315 \times 10^{-3} \parallel G = 5.763$

y (inch)	y/δ	U/U ₀	U/u	u/u	y ⁺ /y	u'/U ₀
0.000	0.000	0.000	0.000	0.000	0.00	0.000
0.003	0.002	0.125	3.001	3.28	3.28	0.043
0.005	0.003	0.186	4.477	5.47	5.47	0.064
0.007	0.005	0.253	6.094	7.65	7.65	0.084
0.010	0.007	0.342	8.227	10.93	10.93	0.097
0.015	0.010	0.442	10.636	16.40	16.40	0.099
0.020	0.014	0.494	11.907	21.97	21.97	0.097
0.030	0.020	0.555	13.362	32.50	32.50	0.090
0.040	0.027	0.588	14.162	43.73	43.73	0.084
0.050	0.034	0.618	14.873	54.66	54.66	0.080
0.075	0.051	0.653	15.727	82.00	82.00	0.077
0.100	0.068	0.683	16.448	109.33	109.33	0.075
0.150	0.102	0.714	17.203	163.99	163.99	0.074
0.200	0.136	0.739	17.784	218.65	218.65	0.071
0.250	0.170	0.753	18.136	273.32	273.32	0.069
0.300	0.204	0.767	18.461	327.98	327.98	0.069
0.400	0.272	0.802	19.306	437.31	437.31	0.066
0.500	0.340	0.824	19.833	546.64	546.64	0.068
0.600	0.408	0.844	20.323	655.96	655.96	0.064
0.700	0.476	0.865	20.834	765.29	765.29	0.065
0.800	0.544	0.889	21.407	874.52	874.52	0.061
0.900	0.612	0.910	21.904	983.95	983.95	0.057
1.000	0.680	0.927	22.335	1093.27	1093.27	0.054
1.250	0.849	0.968	23.310	1366.59	1366.59	0.038
1.500	1.019	0.992	23.899	1639.91	1639.91	0.018
2.000	1.359	0.995	23.965	2186.55	2186.55	0.006
3.000	2.039	0.997	24.006	3279.82	3279.82	0.003

$x/h = -2$, $z/h = 0$
 $U_0 = 50.4$ (ft/sec)

$\delta = 0.759$ -inch || $\delta^* = 0.114$ -inch || $\theta = 0.084$ -inch || $H = 1.36$
 $u^*/U_0 = 0.044$ || $C_F = 3.950 \times 10^{-3}$ || $C_{FM} = 3.738 \times 10^{-3}$ || $G = 5.915$

y (inch)	y/δ	U/U_0	U^*/U_0	y_u/y_v	u^*/U_0
0.000	0.000	0.000	0.000	0.00	0.000
0.003	0.004	0.135	3.047	3.50	0.044
0.005	0.006	0.207	4.549	5.64	0.070
0.010	0.013	0.383	8.607	11.67	0.102
0.015	0.019	0.483	10.869	17.51	0.100
0.020	0.025	0.537	12.073	23.35	0.098
0.025	0.032	0.582	13.110	29.19	0.094
0.035	0.044	0.677	14.107	40.86	0.085
0.045	0.057	0.655	14.737	52.54	0.082
0.065	0.082	0.687	15.466	75.88	0.076
0.085	0.108	0.716	16.114	99.23	0.071
0.105	0.133	0.736	16.553	122.58	0.073
0.130	0.165	0.761	17.122	151.77	0.070
0.155	0.196	0.774	17.422	186.95	0.068
0.205	0.260	0.807	18.153	239.33	0.066
0.225	0.323	0.837	18.835	287.70	0.061
0.305	0.386	0.855	19.247	356.07	0.059
0.355	0.450	0.875	19.683	414.44	0.057
0.405	0.513	0.893	20.084	472.82	0.053
0.455	0.576	0.908	20.444	531.19	0.048
0.505	0.640	0.924	20.795	589.56	0.048
0.505	0.766	0.953	21.439	706.31	0.041
0.705	0.893	0.976	21.954	823.05	0.034
0.805	1.020	0.992	22.332	939.80	0.025
0.905	1.147	1.002	22.546	1056.54	0.017

$x/h = -2$, $z/h = 6$
 $U_0 = 50.4$ (ft/sec)

$\delta = 0.724$ -inch || $\delta^* = 0.109$ -inch || $\theta = 0.079$ -inch || $H = 1.37$
 $u^*/U_0 = 0.044$ || $C_F = 3.919 \times 10^{-3}$ || $C_{FM} = 3.741 \times 10^{-3}$ || $G = 6.095$

y (inch)	y/δ	U/U_0	U^*/U_0	y_u/y_v	u^*/U_0
0.000	0.000	0.000	0.000	0.00	0.000
0.004	0.006	0.169	3.822	4.65	0.058
0.009	0.012	0.338	7.633	10.46	0.097
0.014	0.019	0.455	10.283	16.28	0.102
0.019	0.026	0.526	11.871	22.09	0.101
0.024	0.033	0.567	12.809	27.91	0.093
0.029	0.040	0.594	13.414	33.72	0.090
0.039	0.054	0.630	14.228	45.35	0.084
0.049	0.068	0.656	14.820	56.97	0.081
0.069	0.095	0.693	15.664	80.23	0.075
0.089	0.123	0.714	16.121	103.48	0.075
0.109	0.150	0.727	16.433	126.74	0.073
0.134	0.185	0.760	17.160	155.80	0.070
0.159	0.219	0.779	17.603	184.87	0.068
0.209	0.288	0.814	18.391	243.01	0.065
0.259	0.358	0.841	18.990	301.14	0.061
0.309	0.427	0.862	19.473	359.28	0.058
0.359	0.496	0.883	19.952	417.41	0.055
0.409	0.565	0.902	20.384	475.55	0.053
0.459	0.634	0.920	20.777	533.69	0.050
0.509	0.703	0.935	21.125	591.82	0.046
0.609	0.841	0.964	21.766	708.09	0.040
0.709	0.979	0.987	22.295	824.36	0.031
0.809	1.117	1.005	22.713	940.64	0.020

$x/h = 54$, $z/h = 5$
 $U_0 = 50.4$ (ft/sec)

$\delta = 1.360$ -inch || $\delta^* = 0.207$ -inch || $\theta = 0.155$ -inch || $H = 1.33$
 $u/U_0 = 0.0u_1$ || $C_f = 3.409 \times 10^{-3}$ || $C_{fm} = 3.317 \times 10^{-3}$ || $G = 6.028$

y (inch)	y/δ	U/U_0	U/u_1	yu/v	u^2/U_0
0.000	0.000	0.000	0.000	0.00	0.000
0.003	0.002	0.162	3.934	2.71	0.061
0.008	0.006	0.250	6.056	8.13	0.085
0.013	0.009	0.385	9.333	13.54	0.101
0.018	0.013	0.468	11.341	18.96	0.101
0.028	0.020	0.538	13.041	29.50	0.095
0.037	0.028	0.582	14.090	40.53	0.088
0.057	0.042	0.618	14.977	62.30	0.082
0.078	0.057	0.645	15.621	83.97	0.082
0.097	0.072	0.659	16.200	105.64	0.080
0.123	0.090	0.690	16.718	132.73	0.076
0.148	0.108	0.703	17.021	159.82	0.077
0.198	0.145	0.739	17.890	213.99	0.077
0.248	0.182	0.757	18.346	268.17	0.072
0.298	0.219	0.775	18.779	322.34	0.073
0.348	0.256	0.792	19.194	376.52	0.071
0.398	0.292	0.804	19.487	430.69	0.070
0.498	0.366	0.825	19.974	539.04	0.070
0.598	0.439	0.854	20.695	647.40	0.068
0.698	0.513	0.879	21.299	755.75	0.065
0.798	0.587	0.905	21.923	864.10	0.063
0.898	0.660	0.924	22.374	972.45	0.060
0.997	0.734	0.948	22.958	1080.80	0.052
1.098	0.807	0.965	23.367	1189.15	0.046
1.248	0.918	0.986	23.888	1351.68	0.035
1.498	1.101	0.994	24.072	1622.55	0.018
1.998	1.463	0.998	24.169	2164.31	0.008
2.998	2.205	0.999	24.203	3247.81	0.007

$x/h = -2$, $z/h = -6$
 $U_0 = 50.5$ (ft/sec)

$\delta = 0.709$ -inch || $\delta^* = 0.104$ -inch || $\theta = 0.076$ -inch || $H = 1.36$
 $u/U_0 = 0.0u_5$ || $C_f = 3.987 \times 10^{-3}$ || $C_{fm} = 3.813 \times 10^{-3}$ || $G = 5.976$

y (inch)	y/δ	U/U_0	U/u_1	yu/v	u^2/U_0
0.000	0.000	0.000	0.000	0.00	0.000
0.003	0.004	0.129	2.880	3.52	0.040
0.005	0.007	0.205	4.600	5.87	0.068
0.010	0.014	0.380	8.506	11.74	0.099
0.015	0.021	0.488	10.918	17.61	0.103
0.025	0.035	0.579	12.963	29.35	0.091
0.035	0.049	0.625	14.000	41.09	0.086
0.055	0.078	0.680	15.228	64.56	0.079
0.075	0.106	0.706	15.810	88.04	0.076
0.095	0.134	0.731	16.376	111.52	0.074
0.120	0.169	0.754	16.878	140.87	0.072
0.145	0.205	0.779	17.452	170.21	0.071
0.195	0.275	0.813	18.209	228.91	0.066
0.245	0.346	0.837	18.755	287.60	0.062
0.295	0.416	0.859	19.248	346.30	0.060
0.345	0.487	0.883	19.776	404.99	0.057
0.395	0.557	0.903	20.226	463.69	0.053
0.445	0.628	0.920	20.505	522.38	0.050
0.495	0.698	0.940	21.042	581.08	0.047
0.595	0.840	0.966	21.626	698.46	0.040
0.695	0.981	0.988	22.120	815.85	0.032
0.795	1.122	1.002	22.439	933.24	0.023

$x/h = 54$, $z/h = -6$
 $U_0 = 50.4$ (ft/sec)

$\delta = 1.397$ -inch || $\delta^* = 0.218$ -inch || $\theta = 0.162$ -inch || $H = 1.34$

$u^*/U_0 = 0.041$ || $C_F = 3.366 \times 10^{-3}$ || $C_{Fm} = 3.220 \times 10^{-3}$ || $G = 6.222$

y (inch)	y/δ	U/U_0	U/U_0^*	yu^*/U_0	u^*/U_0
0.000	0.000	0.000	0.000	0.00	0.000
0.003	0.002	0.081	1.962	3.23	0.022
0.006	0.006	0.240	5.845	8.62	0.081
0.018	0.013	0.463	11.278	19.39	0.104
0.028	0.020	0.541	13.174	30.16	0.094
0.048	0.034	0.600	14.617	51.70	0.086
0.068	0.049	0.637	15.514	73.24	0.080
0.088	0.063	0.651	15.877	94.78	0.081
0.113	0.081	0.678	16.514	121.70	0.078
0.138	0.099	0.701	17.091	148.63	0.078
0.168	0.135	0.723	17.632	202.48	0.074
0.238	0.170	0.746	18.161	256.33	0.075
0.288	0.206	0.764	18.617	310.18	0.074
0.338	0.242	0.777	18.944	364.03	0.071
0.388	0.278	0.793	19.324	417.87	0.069
0.488	0.349	0.820	19.987	525.57	0.067
0.588	0.421	0.840	20.474	633.27	0.067
0.688	0.493	0.860	20.974	740.97	0.068
0.788	0.564	0.890	21.705	848.67	0.064
0.888	0.636	0.905	22.069	956.37	0.061
0.988	0.707	0.932	22.710	1064.07	0.055
1.088	0.779	0.949	23.139	1171.77	0.049
1.238	0.886	0.973	23.719	1335.32	0.038
1.488	1.065	0.998	24.328	1602.57	0.021
1.988	1.423	1.000	24.384	2141.07	0.009

$x/h = 54$, $z/h = 0$
 $U_0 = 50.4$ (ft/sec)

$\delta = 1.627$ -inch || $\delta^* = 0.219$ -inch || $\theta = 0.166$ -inch || $H = 1.32$

$u^*/U_0 = 0.041$ || $C_F = 3.442 \times 10^{-3}$ || $C_{Fm} = 3.313 \times 10^{-3}$ || $G = 5.856$

y (inch)	y/δ	U/U_0	U/U_0^*	yu^*/U_0	u^*/U_0
0.000	0.000	0.000	0.070	0.00	0.000
0.001	0.001	0.098	2.362	1.63	0.034
0.006	0.004	0.193	4.650	7.08	0.073
0.011	0.007	0.345	8.316	12.52	0.093
0.017	0.010	0.442	10.659	17.96	0.100
0.026	0.016	0.537	12.932	28.85	0.095
0.036	0.022	0.575	13.853	39.74	0.087
0.057	0.035	0.626	15.067	61.52	0.082
0.076	0.047	0.654	15.765	83.29	0.080
0.096	0.059	0.671	16.165	105.07	0.080
0.121	0.075	0.694	16.731	132.29	0.077
0.146	0.090	0.703	16.941	159.51	0.078
0.197	0.121	0.730	17.556	213.95	0.074
0.246	0.152	0.755	18.189	268.39	0.072
0.297	0.182	0.768	18.522	322.82	0.072
0.346	0.213	0.784	18.891	377.26	0.070
0.397	0.244	0.798	19.240	431.70	0.070
0.497	0.305	0.826	19.506	540.58	0.068
0.597	0.367	0.848	20.243	649.46	0.066
0.696	0.428	0.874	21.077	758.34	0.064
0.796	0.490	0.898	21.634	867.22	0.061
0.896	0.551	0.918	22.128	976.09	0.059
0.996	0.612	0.942	22.702	1084.37	0.053
1.097	0.674	0.954	22.991	1193.85	0.048
1.246	0.766	0.973	23.454	1357.17	0.036
1.496	0.920	0.988	23.806	1629.36	0.020
1.996	1.227	0.995	23.989	2173.76	0.008
2.997	1.842	0.999	24.090	3262.54	0.006

$x/h = -12$
 $U_0 = 50.6 \text{ ft/sec}$

$y(\text{inch})$	U/U_0	u'/U_0	v'/U_0	u'^2v'/U_0^3
0.000	0.3000	0.0000	0.0000	0.000E+00
0.030	0.6816	0.0663	0.0426	0.836E-03
0.040	0.7075	0.0644	0.0395	0.804E-03
0.050	0.7206	0.0643	0.0382	0.816E-03
0.075	0.7517	0.0638	0.0353	0.791E-03
0.100	0.7742	0.0602	0.0342	0.723E-03
0.150	0.8120	0.0562	0.0326	0.665E-03
0.200	0.8339	0.0534	0.0316	0.625E-03
0.300	0.8744	0.0491	0.0298	0.547E-03
0.400	0.9090	0.0453	0.0281	0.504E-03
0.500	0.9396	0.0400	0.0253	0.376E-03
0.600	0.9693	0.0328	0.0220	0.264E-03
0.700	0.9909	0.0256	0.0178	0.142E-03
0.800	1.0080	0.0180	0.0138	0.716E-04
0.900	1.0109	0.0111	0.0103	0.295E-04
1.000	1.0106	0.0065	0.0071	0.562E-05
1.500	1.0135	0.0025	0.0024	-1.145E-05
2.000	1.0102	0.0020	0.0019	-1.140E-05
4.000	1.0014	0.0018	0.0017	0.865E-07

$x/h = -12$
 $U_0 = 82.1 \text{ ft/sec}$

$y(\text{inch})$	U/U_0	u'/U_0	v'/U_0	u'^2v'/U_0^3
0.000	0.0000	0.0000	0.0000	0.000E+00
0.030	0.6726	0.0565	0.0344	0.610E-03
0.040	0.6865	0.0566	0.0330	0.634E-03
0.050	0.7034	0.0564	0.0320	0.575E-03
0.075	0.7277	0.0556	0.0309	0.590E-03
0.100	0.7541	0.0546	0.0303	0.555E-03
0.150	0.7821	0.0525	0.0290	0.561E-03
0.200	0.8123	0.0497	0.0281	0.512E-03
0.300	0.8458	0.0453	0.0271	0.462E-03
0.400	0.8788	0.0402	0.0248	0.373E-03
0.500	0.9039	0.0362	0.0225	0.320E-03
0.600	0.9362	0.0301	0.0196	0.209E-03
0.700	0.9560	0.0245	0.0161	0.123E-03
0.800	0.9763	0.0163	0.0126	0.531E-04
0.900	0.9885	0.0099	0.0093	0.188E-04
1.000	0.9912	0.0054	0.0061	0.198E-05
1.500	0.9932	0.0021	0.0020	-7.87E-06
2.000	0.9986	0.0019	0.0018	0.379E-08
4.000	0.9959	0.0021	0.0020	-4.47E-07

x/h = 10
U_∞ = 50.4 ft/sec

y (inch)	U/U _∞	u'/U _∞	v'/U _∞	u'v'/U _∞ ²
0.000	0.0000	0.0000	0.0000	0.000E+00
0.050	0.5230	0.0970	0.0489	0.758E-03
0.100	0.5619	0.0949	0.0612	0.143E-02
0.150	0.5923	0.0960	0.0685	0.203E-02
0.200	0.6103	0.1005	0.0719	0.256E-02
0.250	0.6244	0.1057	0.0733	0.324E-02
0.300	0.6302	0.1036	0.0700	0.290E-02
0.350	0.6281	0.1011	0.0664	0.268E-02
0.400	0.7522	0.0956	0.0629	0.252E-02
0.500	0.8182	0.0750	0.0507	0.154E-02
0.600	0.8633	0.0570	0.0395	0.702E-03
0.700	0.9010	0.0488	0.0333	0.536E-03
0.800	0.9321	0.0415	0.0292	0.397E-03
0.900	0.9492	0.0359	0.0250	0.269E-03
1.000	0.9700	0.0288	0.0205	0.166E-03
1.100	0.9937	0.0174	0.0142	0.448E-04
1.200	1.0022	0.0066	0.0075	-0.161E-06
1.600	1.0052	0.0038	0.0042	-0.169E-05
1.750	1.0053	0.0031	0.0035	-0.965E-06
2.000	1.0047	0.0023	0.0024	-0.345E-06
2.500	1.0038	0.0018	0.0019	-0.254E-06

x/h = 10
U_∞ = 85.7 ft/sec

y (inch)	U/U _∞	u'/U _∞	v'/U _∞	u'v'/U _∞ ²
0.000	0.0000	0.0000	0.0000	0.000E+00
0.050	0.5413	0.0935	0.0417	0.685E-03
0.100	0.5751	0.0923	0.0594	0.132E-02
0.150	0.6083	0.0967	0.0661	0.206E-02
0.200	0.6304	0.0974	0.0687	0.248E-02
0.250	0.6633	0.0942	0.0688	0.275E-02
0.300	0.7055	0.0981	0.0667	0.260E-02
0.400	0.7673	0.0893	0.0567	0.202E-02
0.500	0.8261	0.0651	0.0456	0.101E-02
0.600	0.8650	0.0514	0.0369	0.649E-03
0.700	0.8956	0.0418	0.0302	0.381E-03
0.800	0.9212	0.0349	0.0243	0.231E-03
0.900	0.9417	0.0284	0.0206	0.154E-03
1.000	0.9614	0.0221	0.0166	0.636E-04
1.200	0.9760	0.0090	0.0095	0.164E-05
1.400	0.9832	0.0045	0.0051	-0.205E-05
1.600	0.9859	0.0031	0.0035	-0.130E-05
1.750	0.9894	0.0026	0.0027	-0.557E-06
2.000	0.9893	0.0022	0.0021	-0.222E-06
2.250	0.9939	0.0019	0.0018	-0.174E-06
2.500	0.9940	0.0018	0.0017	-0.155E-06

$x/h = 16$
 $U_0 = 50.7 \text{ ft/sec}$

$y(\text{inch})$	U/U_0	U'/U_0	V'/U_0	$U'V'/U_0^2$
0.000	0.0000	0.0000	0.0000	0.000E+00
0.030	0.9814	0.0831	0.0439	0.768E-03
0.040	0.9993	0.0622	0.0435	0.779E-03
0.050	0.9106	0.6609	0.0448	0.931E-03
0.100	0.8466	0.0782	0.0488	0.915E-03
0.150	0.6684	0.0790	0.0537	0.123E-02
0.200	0.5905	0.0823	0.0554	0.143E-02
0.250	0.7013	0.0835	0.0577	0.172E-02
0.300	0.7294	0.0856	0.0568	0.174E-02
0.350	0.7535	0.0831	0.0557	0.177E-02
0.400	0.7822	0.0816	0.0541	0.172E-02
0.450	0.8040	0.0775	0.0517	0.146E-02
0.500	0.8283	0.0753	0.0497	0.147E-02
0.600	0.8716	0.0658	0.0431	0.106E-02
0.700	0.9144	0.0517	0.0375	0.751E-03
0.800	0.9420	0.0422	0.0302	0.433E-03
0.900	0.9668	0.0340	0.0252	0.294E-03
1.000	0.9824	0.0261	0.0203	0.159E-03
1.250	0.9984	0.0046	0.0097	0.474E-05
1.500	0.9937	0.0045	0.0049	-0.261E-05
2.000	0.9944	0.0023	0.0024	-0.452E-06
2.500	0.9973	0.0019	0.0018	-0.317E-06

$x/h = 16$
 $U_0 = 86.0 \text{ ft/sec}$

$y(\text{inch})$	U/U_0	U'/U_0	V'/U_0	$U'V'/U_0^2$
0.000	0.0000	0.0000	0.0000	0.000E+00
0.030	0.6021	0.0741	0.0390	0.841E-03
0.040	0.6151	0.0723	0.0391	0.616E-03
0.050	0.6292	0.0739	0.0403	0.621E-03
0.100	0.6610	0.0753	0.0404	0.856E-03
0.150	0.6808	0.0756	0.0503	0.105E-02
0.200	0.7042	0.0792	0.0535	0.130E-02
0.250	0.7198	0.0799	0.0550	0.159E-02
0.300	0.7449	0.0792	0.0541	0.158E-02
0.350	0.7630	0.0801	0.0531	0.159E-02
0.400	0.7449	0.0792	0.0541	0.158E-02
0.450	0.8012	0.0765	0.0508	0.155E-02
0.500	0.8273	0.0724	0.0474	0.140E-02
0.600	0.8707	0.0609	0.0416	0.985E-03
0.700	0.9086	0.0467	0.0334	0.573E-03
0.800	0.9345	0.0375	0.0276	0.341E-03
0.900	0.9567	0.0288	0.0228	0.207E-03
1.000	0.9710	0.0209	0.0179	0.998E-04
1.250	0.9869	0.0076	0.0084	0.106E-05
1.500	0.9884	0.0042	0.0046	-0.203E-05
2.000	0.9927	0.0031	0.0031	-0.975E-06
2.500	0.9942	0.0024	0.0024	-0.421E-06
3.000	0.9957	0.0019	0.0017	-0.184E-06

$x/h = 24$
 $U_0 = 50.6 \text{ ft/sec}$

y (inch)	U/U_0	U^*/U_0	V^*/U_0	U^*V^*/U_0^2
0.500	0.0000	0.0000	0.0000	0.000E+00
0.630	0.5753	0.0813	0.0492	0.853E-03
0.640	0.6028	0.0779	0.0462	0.769E-03
0.650	0.6262	0.0791	0.0427	0.799E-03
0.660	0.6468	0.0744	0.0423	0.948E-03
0.670	0.6767	0.0738	0.0456	0.948E-03
0.680	0.7247	0.0730	0.0460	0.102E-02
0.690	0.7387	0.0735	0.0493	0.119E-02
0.700	0.7560	0.0749	0.0511	0.131E-02
0.710	0.7761	0.0759	0.0504	0.136E-02
0.720	0.7873	0.0750	0.0513	0.137E-02
0.730	0.8015	0.0746	0.0503	0.150E-02
0.740	0.8317	0.0706	0.0481	0.127E-02
0.750	0.8656	0.0710	0.0458	0.132E-02
0.760	0.8931	0.0648	0.0417	0.106E-02
0.770	0.9285	0.0564	0.0372	0.837E-03
0.780	0.9570	0.0474	0.0305	0.448E-03
0.790	0.9774	0.0329	0.0260	0.266E-03
0.800	0.9920	0.0229	0.0195	0.130E-03
0.810	1.0051	0.0130	0.0140	0.367E-04
0.820	1.0090	0.0061	0.0068	-2.39E-05
0.830	0.9979	0.0029	0.0030	-5.00E-06
0.840	0.9955	0.0022	0.0021	-3.65E-06

$x/h = 24$
 $U_0 = 86.4 \text{ ft/sec}$

y (inch)	U/U_0	U^*/U_0	V^*/U_0	U^*V^*/U_0^2
0.500	0.0000	0.0000	0.0000	0.000E+00
0.630	0.6188	0.0727	0.0422	0.833E-03
0.640	0.6453	0.0716	0.0388	0.589E-03
0.650	0.6601	0.0725	0.0383	0.747E-03
0.660	0.7098	0.0710	0.0402	0.838E-03
0.670	0.7303	0.0722	0.0436	0.909E-03
0.680	0.7509	0.0713	0.0463	0.985E-03
0.690	0.7656	0.0722	0.0483	0.111E-02
0.700	0.7822	0.0729	0.0494	0.125E-02
0.710	0.7910	0.0723	0.0490	0.134E-02
0.720	0.8082	0.0733	0.0484	0.131E-02
0.730	0.8429	0.0711	0.0474	0.138E-02
0.740	0.8739	0.0666	0.0444	0.117E-02
0.750	0.9054	0.0615	0.0401	0.972E-03
0.760	0.9394	0.0486	0.0338	0.639E-03
0.770	0.9591	0.0404	0.0291	0.428E-03
0.780	0.9785	0.0282	0.0228	0.199E-03
0.790	0.9984	0.0113	0.0128	0.114E-04
0.800	1.0022	0.0056	0.0061	-2.51E-05
0.810	1.0010	0.0038	0.0040	-1.07E-05
0.820	1.0007	0.0030	0.0029	-5.17E-06
0.830	1.0011	0.0025	0.0024	-5.51E-06
0.840	0.9997	0.0023	0.0020	-2.20E-06

x/h = 36
U₀ = 50.7 ft/sec

y (inch)	U/U ₀	V/U ₀	U'V'/U ₀ ²
0.000	0.0000	0.0000	0.000E+00
0.030	0.5592	0.0770	0.983E-03
0.040	0.5938	0.0774	0.924E-03
0.050	0.6150	0.0750	0.865E-03
0.060	0.6293	0.0704	0.786E-03
0.070	0.6370	0.0676	0.753E-03
0.080	0.6393	0.0696	0.711E-03
0.090	0.6362	0.0674	0.687E-03
0.100	0.6248	0.0683	0.663E-03
0.110	0.6079	0.0685	0.645E-03
0.120	0.5872	0.0685	0.625E-03
0.130	0.5640	0.0663	0.604E-03
0.140	0.5399	0.0625	0.584E-03
0.150	0.5124	0.0579	0.562E-03
0.160	0.4819	0.0519	0.538E-03
0.170	0.4495	0.0449	0.512E-03
0.180	0.4158	0.0359	0.483E-03
0.190	0.3839	0.0258	0.452E-03
0.200	0.3494	0.0108	0.416E-03
0.210	0.3134	0.0040	0.375E-03
0.220	0.2745	0.0026	0.330E-03

x/h = 36
U₀ = 86.2 ft/sec

y (inch)	U/U ₀	V/U ₀	U'V'/U ₀ ²
0.000	0.0000	0.0000	0.000E+00
0.030	0.5982	0.0691	0.731E-03
0.040	0.6259	0.0699	0.695E-03
0.050	0.6477	0.0705	0.788E-03
0.060	0.7036	0.0685	0.701E-03
0.070	0.7303	0.0668	0.771E-03
0.080	0.7528	0.0668	0.882E-03
0.090	0.7705	0.0653	0.854E-03
0.100	0.7808	0.0665	0.991E-03
0.110	0.7938	0.0643	0.982E-03
0.120	0.8073	0.0647	0.995E-03
0.130	0.8209	0.0629	0.969E-03
0.140	0.8318	0.0643	0.112E-02
0.150	0.8606	0.0631	0.104E-02
0.160	0.8848	0.0603	0.934E-03
0.170	0.9097	0.0560	0.806E-03
0.180	0.9334	0.0502	0.687E-03
0.190	0.9580	0.0407	0.436E-03
0.200	0.9746	0.0330	0.269E-03
0.210	0.9804	0.0235	0.150E-03
0.220	0.9888	0.0190	0.868E-04
0.230	0.9964	0.0090	0.434E-05
0.240	0.9961	0.0040	-0.122E-05
0.250	0.9990	0.0025	-0.352E-06

x/h = 54
U₀ = 50.5 ft/sec

y' (inch)	U/U ₀	u'/U ₀	v'/U ₀	u' ² v'/U ₀ ³
0.000	0.0000	0.0000	0.0000	0.000E+00
0.040	0.5983	0.0762	0.0494	0.918E-03
0.050	0.6294	0.0754	0.0442	0.842E-03
0.100	0.5959	0.0721	0.0382	0.884E-03
0.150	0.7325	0.0692	0.0374	0.876E-03
0.200	0.7564	0.0661	0.0391	0.832E-03
0.250	0.7705	0.0679	0.0399	0.840E-03
0.300	0.7898	0.0652	0.0408	0.871E-03
0.350	0.8057	0.0635	0.0414	0.913E-03
0.400	0.8136	0.0630	0.0413	0.877E-03
0.500	0.8401	0.0619	0.0412	0.879E-03
0.600	0.8637	0.0604	0.0399	0.832E-03
0.700	0.8783	0.0593	0.0395	0.876E-03
0.800	0.9083	0.0566	0.0378	0.795E-03
0.900	0.9294	0.0529	0.0346	0.683E-03
1.000	0.9493	0.0479	0.0329	0.517E-03
1.250	0.9836	0.0323	0.0249	0.268E-02
1.500	0.9992	0.0148	0.0152	0.370E-04
2.000	1.0009	0.0054	0.0060	-0.315E-05
2.500	0.9981	0.0032	0.0034	-0.105E-05

x/h = 54
U₀ = 85.9 ft/sec

y' (inch)	U/U ₀	u'/U ₀	v'/U ₀	u' ² v'/U ₀ ³
0.000	0.0000	0.0000	0.0000	0.000E+00
0.040	0.6007	0.0663	0.0397	0.735E-03
0.050	0.6255	0.0663	0.0368	0.673E-03
0.100	0.6859	0.0654	0.0336	0.688E-03
0.150	0.7168	0.0628	0.0344	0.726E-03
0.200	0.7441	0.0615	0.0349	0.666E-03
0.250	0.7602	0.0597	0.0354	0.669E-03
0.300	0.7770	0.0599	0.0373	0.766E-03
0.350	0.7880	0.0599	0.0378	0.769E-03
0.400	0.7992	0.0592	0.0382	0.823E-03
0.450	0.8153	0.0577	0.0386	0.800E-03
0.500	0.8300	0.0581	0.0383	0.859E-03
0.500	0.8517	0.0561	0.0386	0.859E-03
0.700	0.8738	0.0565	0.0380	0.874E-03
0.800	0.8899	0.0530	0.0367	0.753E-03
0.900	0.9168	0.0511	0.0342	0.702E-03
1.000	0.9338	0.0478	0.0322	0.623E-03
1.250	0.9691	0.0319	0.0243	0.248E-03
1.500	0.9884	0.0169	0.0167	0.652E-04
2.000	0.9964	0.0057	0.0065	-0.412E-06
2.500	0.9970	0.0031	0.0031	-0.211E-06

INITIAL DISTRIBUTION

Copies

2 DARPA
 1 Library
 1 TTO/A. Ellinthorpe

8 CHONR
 1 Library
 1 ONR 200B
 1 ONR 280/ACSAS Project
 1 ONR 4250A/R. Fitzgerald
 4 ONR 32
 1 A. Kushner
 1 M. Reischman
 1 R. Whitehead
 1 C. Lee

2 NAVSEA
 1 Library
 1 SEA 55N/A. Paladino

4 NRL
 1 Library
 3 Code 5844
 1 R. Hansen
 1 R. Handler
 1 M. Horne

1 UNSA/S. Elder

1 NAVPGSCOL/Library

1 NOSC/Library

10 NUSC, New London
 1 Library
 1 Code 10/W. Von Winkle
 1 Code 323/W. Strawderman
 3 Code 3233
 1 R. Elswick
 1 S. Ko
 1 H. Schloemer
 1 Code 3241/W. Keith
 2 Code 3292
 1 C. Sherman
 1 B. Buehler
 1 Code 5100/C. Wagner

1 NUSC, Newport/Library

Copies

12 DTIC

1 AFOSR

1 NASA Scientific and Technical Information Facility

5 NASA, Langley
 1 Library
 1 T. Brooks
 1 D. Bushnell
 1 J. Hardin
 1 L. Maestrello

2 NASA, Lewis
 1 Library
 1 M. Goldstein

1 NBS/Technical Library

1 Brown University/J. Liu

2 U. of California, Berkeley
 1 Dept of Mech. Engineering
 1 Dept of Naval Architecture

1 U. of California, Los Angeles/
 W. Meecham

2 California Inst. of Tech./Engr. Sciences Dept
 1 Library
 1 T. Wu

1 Case Western Reserve U./Dept of Mech. Engr.

2 Cornell U./School of Mech. & Aerospace Engr.
 1 Library
 1 J. Lumley

2 Florida Atlantic U./Dept of Ocean Engr.
 1 Library
 1 S. Dunn

Copies

- 1 Georgia Inst. of Tech./School of Mech. Engr.
- 2 The Johns Hopkins U./Applied Physics Laboratory
 - 1 Library
 - 1 S. Corrsin
- 1 Harvard U./Div. of Engr. and Applied Physics/R. Kronauer
- 1 U. of Houston/Dept of Mech. Engr./A.K.M.F. Hussain
- 1 Illinois Inst. of Tech./Dept of Mechanics & Mechanical & Aerospace Engr./H. Nagib
- 1 U. of Iowa/Inst. of Hydraulic Research
- 2 Lehigh U./Dept of Mech. Engr. & Mechanics
 - 1 D. Rockwell
 - 1 C. Smith
- 1 U. of Maryland, College Park/Dept of Mech. Engr./J. Wallace
- 1 U. of Maryland, Baltimore/C. von Kerczek
- 2 Massachusetts Inst. of Tech.
 - 1 J. Haritonidis
 - 1 P. Leehey
- 2 U. of Michigan
 - 1 Dept of Aerospace Engr./W. Willmarth
 - 1 Dept of Engr. Mech./Library
- 2 Michigan State U./Mech. Engr. Dept
 - 1 Library
 - 1 R. Falco

Copies

- 4 U. of Minnesota
 - 3 St. Anthony Falls Hydraulic Lab.
 - 1 Library
 - 1 R. Arndt
 - 1 R. Plunkett
 - 1 Dept of Electrical Engr./R. Lambert
- 1 North Carolina State U./Center for Sound and Vibration/T. Hodgson
- 1 U. of Notre Dame/Dept of Aerospace & Mech. Engr.
- 4 Pennsylvania State U./Applied Research Laboratory
 - 1 Library
 - 1 R. Henderson
 - 1 C. Burroughs
 - 1 G. Lauchle
- 1 Princeton U./Dept of Mech. and Aero. Engr./A. Smits
- 1 Purdue U./W. Tiederman
- 1 U. of Rhode Island/Dept of Mech. & Ocean Engr./F. White
- 2 U. of Southern California
 - 1 Dept of Aerospace Engr.
 - 1 R. Blackwelder
- 5 Stanford U.
 - 1 Dept of Mech. Engr.
 - 1 Research Institute/Library
 - 3 Thermosciences Dept
 - 1 J. Eaton
 - 1 S. Kline
 - 1 W. Reynolds
- 1 U. of Texas, Austin/Dept of Mech. Engr./R. Panton

Copies

2 Virginia Polytechnic Institute
 1 Dept of Engr. Science
 & Mech.
 1 Dept of Aero. & Ocean Engr./
 R. Simpson

1 Bendix Corp./F. DeMetz

5 Bolt, Beranek & Newman, Inc.
 1 J. Barger
 1 K. Chandiramani
 1 P. Jameson
 1 N. Martin
 1 M. Howe

2 Cambridge Acoustical Assc.
 1 Library
 1 J. Cole

1 Chase, Inc./D. Chase

1 Donanco, Inc./D. Ross

1 Engineering & Science Associates,
 Inc./J. Shen

3 Flow Research Company
 1 R. Cooper
 1 M. Gad-el-Hak
 1 J. Duncan

1 General Dynamics, Electric Boat
 Division/Library

1 Gould Defense System/J. Meng

1 Hersh Acoustical/A. Hersh

1 Lockheed, Georgia/A. Thomas

1 McDonnell Douglas, Corp./F. Roos

1 Newport News Shipbuilding and
 Drydock Co./Library

1 Poseidon Research/S. Crow

1 Planning Systems Inc./V. Kolhi

Copies

4 ORI, Inc.
 1 R. Hoglund
 1 T. Bell
 1 R. Veglio-Laurin
 1 J. Witting

1 Stevens Inst. of Tech./Davidson
 Laboratory

CENTER DISTRIBUTION

Copies	Code	Name
1	01	R. Metrey
1	15	W. Morgan
1	1504	V. Monacella
1	154	J. McCarthy
1	1542	T. Huang
1	1543	E. Rood
1	19	M. Sevik
1	1901	M. Strasberg
1	1902	G. Maidanik
1	1904	R. Stefanowicz
1	1905.1	W. Blake
1	1905.2	W. Reader
1	1905.3	D. Feit
1	1906	R. Biancardi
1	1930.1	W. Hoover
1	1930.2	J. Lee
1	1932	J. Cummings
1	1933	C. Sherwood
1	1933	R. Wasserman
1	194	F. Archibald
1	1940.1	K. Lewis
1	1940.2	R. Waterhouse
1	1940.3	M. Casarella

Copies	Code	Name
1	1942	D. Arguez
1	1942	S. Fisher
1	1942	L. Chandler
1	1942	M. Diemer
1	1942	T. Farabee
1	1942	F. Geib
1	1942	T. Griffin
1	1942	Y. Hwang
1	1942	M. Kim
1	1942	E. Leibolt
1	1942	P. Mahoney
1	1942	P. McGlade
1	1942	P. Shang
1	1942	M. Stockman
1	1942	L. Tarazek
1	1942	P. Zacolla
1	1944	J. Gershfeld
1	1944	C. Kincely
1	1944	L. Maga
1	1944	T. Mathews
1	1944	E. Skiko
1	1961	B. Douglas
1	1961	Y. Liu
1	1961	L. Cole
1	1965	J. Neimiec
10	5211.1	Reports Distribution
1	522.1	TIC (C)
1	522.2	TIC (A)

CHAPTER 1. THE UNITED STATES OF AMERICA

1. THE UNITED STATES OF AMERICA IS A FEDERAL REPUBLIC, COMPOSED OF FIFTY STATES, THE DISTRICT OF COLUMBIA, AND THE TERRITORIES OF ALASKA AND HAWAII. THE UNITED STATES OF AMERICA IS A DEMOCRATIC COUNTRY, WHERE THE PEOPLE ARE SOVEREIGN.

2. THE UNITED STATES OF AMERICA IS A COUNTRY WHERE THE PEOPLE ENJOY THE RIGHTS OF FREEDOM OF SPEECH, RELIGION, AND ASSEMBLY. THE UNITED STATES OF AMERICA IS A COUNTRY WHERE THE PEOPLE ENJOY THE RIGHTS OF LIFE, LIBERTY, AND THE PURSUIT OF HAPPINESS.

3. THE UNITED STATES OF AMERICA IS A COUNTRY WHERE THE PEOPLE ENJOY THE RIGHTS OF EQUALITY AND JUSTICE. THE UNITED STATES OF AMERICA IS A COUNTRY WHERE THE PEOPLE ENJOY THE RIGHTS OF FAIRNESS AND HONOR. THE UNITED STATES OF AMERICA IS A COUNTRY WHERE THE PEOPLE ENJOY THE RIGHTS OF DIGNITY AND RESPECT. THE UNITED STATES OF AMERICA IS A COUNTRY WHERE THE PEOPLE ENJOY THE RIGHTS OF FREEDOM AND JUSTICE.